SURVEY OF NEUTRON SPECTROSCOPIC FACTORS AND ASYMMETRY DEPENDENCE OF NEUTRON CORRELATIONS IN TRANSFER REACTIONS

By

Hiu Ching Lee

A DISSERTATION

Submitted to
Michigan State University
In partial fulfillment of the requirements
For the degree of

DOCTOR OF PHILOSOPHY

Physics and Astronomy

2010

ABSTRACT

SURVEY OF NEUTRON SPECTROSCOPIC FACTORS AND ASYMMETRY DEPENDENCE OF NEUTRON CORRELATIONS IN TRANSFER REACTIONS

By

Hiu Ching Lee

Transfer reactions have been used as an experimental tool to obtain abundant spectroscopic information for stable nuclei in the past half-century. With the advance of high intensity radioactive beams, transfer reactions can be used in the same spirit to explore the structures of exotic nuclei, where dramatic changes in nuclear structure have been observed near the drip lines.

This thesis work is partly motivated by the revived interest in transfer reactions using rare isotope beams. The first part of this dissertation describes the survey of spectroscopic factors extracted from an extensive amount of data on single neutron (*p*,*d*) and (*d*,*p*) transfer reactions on stable isotopes from Lithium to Nickel. Utilizing the global optical model potential, Chapel-Hill 89, and the conventional single-particle geometry in the adiabatic distorted wave approximation (ADWA) model, the measured ground-state and most excited-state neutron spectroscopic factors for nuclei with $3 \leq Z \leq 28$ agree with the predictions from large-basis-shell-model to better than 30%. The established systematics provides an essential framework to analyze the structural information obtained from transfer reactions for both stable and exotic nuclei. The suppression of spectroscopic factors from shell model values due to nucleon-nucleon correlations is explored by using different optical model parameters and single nucleon bound state geometry. For most nuclei, the neutron ground-state spectroscopic factors are

reduced by about 30% compared to large-basis-shell-model predictions if the ADWA reaction model uses transferred-neutron bound state and microscopic Jeukenne, Lejeune and Mahaux (JLM) nucleon-target optical potential geometries constrained by Hartree-Fock calculations. The magnitude of reduction is similar to that obtained in (*e,e'p*) measurements near the closed shells.

The neutron-proton asymmetry dependence of the reduction in the spectroscopic factor is related to the neutron-neutron and neutron-proton correlations. The experimental efforts in this dissertation are dedicated to the study of the asymmetry dependence of neutron correlations through spectroscopic factor measurements using (*p,d*) neutron transfer reactions with proton-rich ^{34}Ar and neutron-rich ^{46}Ar radioactive beams in inverse kinematics. The kinematically complete experiments use a high resolution silicon strip array to detect the deuterons in coincidence with the recoil residues detected in a mass spectrometer. The experimental results show little reduction of the ground-state neutron spectroscopic factor of the proton-rich nucleus ^{34}Ar compared to that of neutron-rich ^{46}Ar. The results suggest that correlations, which generally reduce such spectroscopic factors, do not depend strongly on the neutron-proton asymmetry of the nucleus in this isotopic region. The results are consistent with the systematics established from the extensive studies of spectroscopic factors from transfer reactions. They are, however, contradictory to the strong dependence obtained in knockout reactions. Our new results pose intriguing questions about the reaction mechanisms of transfer and knockout reactions as well as the nature of neutron correlations in nuclei with extreme isospin asymmetry.

to my parents (Hiu Ying Chan and Kwong Ming Lee)

and my sister (Hiu Man Betty Lee)

Acknowledgements

First and foremost, I would like to express my deepest appreciation to my Ph.D supervisor Professor Betty Tsang for her invaluable guidance and continuing support throughout my graduate studies. Her powerful insight and leadership as well as persistence to accomplish goals in the intellectual ways are essential to the completion of this dissertation. The wisdom, enthusiasm and determination I learned from her have profound influence on my future career and personal life. I would also like to express my heartiest gratitude to her for giving me encouragement and numerous opportunities during these years.

Much gratitude goes to Professor William G. Lynch for countless fruitful discussions and patience. His intellects and critical observation as well as deep understanding of Physics are invaluable to me. I am sincerely thankful to all the members in HiRA group, including the former HiRA post-docs Drs. Vladimir Henzl and Daniela Henzlova and fellow graduate students Dan Coupland, Micha Kilburn, Andy Rogers, Alisher Sanetullaev and Mike Youngs. Their experimental skills and working attitudes are remarkable. The experiment could not be accomplished without their hard work. I am especially indebted to Andrew Rogers. His great help from setting up the experiment to addressing endless problems I experienced in the beginning of data analysis are highly appreciated.

I would like to acknowledge the contributions from all the collaborators. The productive collaborations led to the success of this experiment. I would like to thank to Dr. Daniel Bazin at NSCL, Dr. Zhiyu Sun at Institute of Modern Physics in China, Prof.

Robert Charity and Prof. Lee Sobotka at Washington University, Dr. Sylvie Hudan at Indiana University, Prof. Michael Famiano at Western Michigan University, Dr. Mark Wallace at LANL, Dr. Dan Shapira at ORNL, Dr. Bill Peters and Patrick O'Malley at Rutgers University, Kyle Schmitt and Dr. Andy Chae at University of Tennessee and Hoi Kit Cheung at Chinese University of Hong Kong.

Many thanks go to the excellent support from the incredible NSCL staff members. I appreciate the help from John Yurkon of the detector laboratory, Len Morris, Craig Snow and Renan Fontus of the design group, Jim Vincent of electronics group, Ron Fox of the computer group, Andrew Thulin of vacuum group, Dr. David Sanderson for laser alignment measurements and all the machine shop staff. In addition, A1900 people including Drs. Mauricio Portillo, Marc Hausmann, Tom Ginter have always been extremely helpful. Their great help made the experiment possible.

The extensive studies of spectroscopic factors (SF) could not be achieved without the following people. Dr. Xiaodong Liu (a former NSCL graduate student of Prof. Betty Tsang) developed a systematic framework to extract consistent experimental SFs, which is the foundation of my dissertation. Shi Chun Su and Jiayan Dai at the Chinese University of Hong Kong came to NSCL in summer and reanalyzed massive amounts of existing experimental data to obtain SFs for a wide range of nuclei. Special thanks to Shi Chun Su for developing a powerful and user-friendly database to organize all the data and calculations. Scott Warrant maintained and improved such a fantastic database. Prof. Mihai Horoi at Central Michigan University calculated the theoretical SFs with full fp shell-model space and Dr. Hang Liu formerly at NSCL used the high performance

computing (HPC) systems in MSU for large-basis shell model calculations. Angelo Signoracci performed the SF calculations for ^{46}Ar nucleus. I greatly appreciate their work. In additional, I would also like to thank Prof. B. Alex Brown and Prof. Jeff Tostevin for the use of the programs Oxbash and TWOFNR.

I would like to express my sincere thanks to Professor Pawel Danielewicz for giving me the opportunities to get involved in his theoretical project from which I have benefited a lot. His deep intuition, great ability to visualize interactions in nature and brilliant ideas are admirable. I deeply appreciate his opening the window for me to another piece of elegant Physics world.

I am grateful to Prof. B. Alex Brown, Prof. Edward Brown, Prof. William G. Lynch and Prof. Chien-Peng Yuan for reading my dissertation and serving on my guidance committee. Their generous advice and suggestions on the thesis are greatly appreciated.

I would also acknowledge other members and visitors of the HiRA group including Dr. Zbigniew Chajecki, Dr. Franck Delaunay, Dr. Tilak Kumar Ghosh, Rachel Hodges, Dr. Sergei Lobastov, Fei Lu, Michal Mocho, DanYang Pang, Patrick Quarterman and Jack Winkelbauer for their support and help as well as friendship. Many thanks to Rachel Hodges and Dr. Tilak Kumar Ghosh for reading my thesis and giving suggestions.

I would like to personally thank the Physics Department of the Chinese University of Hong Kong, where I did my Bachelor degree, and Prof. Ming Chung Chu for offering me the opportunity to participate the Summer Undergraduate Research Experience

(SURE) program and work with Prof. Betty Tsang (who became my Ph.D advisor) at NSCL during the summer in my senior year. It was all because of the fantastic research experience at NSCL and excellent supervision of Prof. Betty Tsang that summer, I started to be fascinated with nuclear physics and decided to pursue a doctorate degree in this field.

I would also like to thank Dr. Chueh-an Hsieh who has been my wonderful roommate for more than 4 years during our graduate studies. I deeply appreciate her understanding, sharing and invaluable friendship.

Last, but not least, my deepest gratitude goes to my parents Hiu Ying Chan and Kwong Ming Lee for always being there to give me unconditional support and believing in me. Many thanks to my sister Hiu Man (Betty) Lee for being such a wonderful sister and friend always deeply caring about and understanding me. The love I have received from my family is the main source of power in my pursuit of graduate study and my entire life.

TABLE OF CONTENTS

LIST OF TABLES

LIST OF FIGURES

Images in this dissertation are presented in color

Chapter 1

Introduction

1.1 Nucleon correlation in shell structure and spectroscopic factor

One of the basic aims of fundamental science is to understand the properties of matters that make up the universe. All terrestrial substances are composed of atoms. At the core of an atom, surrounded by electrons, lies the nucleus. Protons and neutrons are the basic building blocks of the nucleus. Properties of all isotopes are determined by the number of protons and neutrons. The number of protons in a nucleus (Z) establishes the chemical identity of the element. A variety of isotopes of a specific element are formed from different numbers of neutrons (N). The possible N/Z ratio of an isotope depends on the nature of the nuclear force which binds the protons and neutrons in the nucleus. About 300 stable isotopes, with large binding energies, exist in nature.

Figure 1.1 displays the chart of the nuclei with proton number and neutron number [ISF]. The region with black squares represents the stable isotopes, called the valley of stability. As the N/Z ratio decreases (proton-rich) or increases (neutron-rich), compared to the stable isotopes the nuclei are unstable and decay towards the valley of stability. These observed short-lived exotic isotopes are shown in green in Figure 1.1.

One of the ultimate goals in nuclear physics is to determine the limits within which nucleus can exist or the exact positions of the proton and neutron drip lines in the nuclear chart. Since the nucleosynthesis processes, for instance *r*- and *rp*-process, take place in regions of extreme N/Z ratios as indicated in Figure 1.1 [Wal81,Cow91,Sch98],

understanding the properties of exotic nuclei near the drip lines is of critical importance and would offer new glimpses into the origin of the elements in the universe.

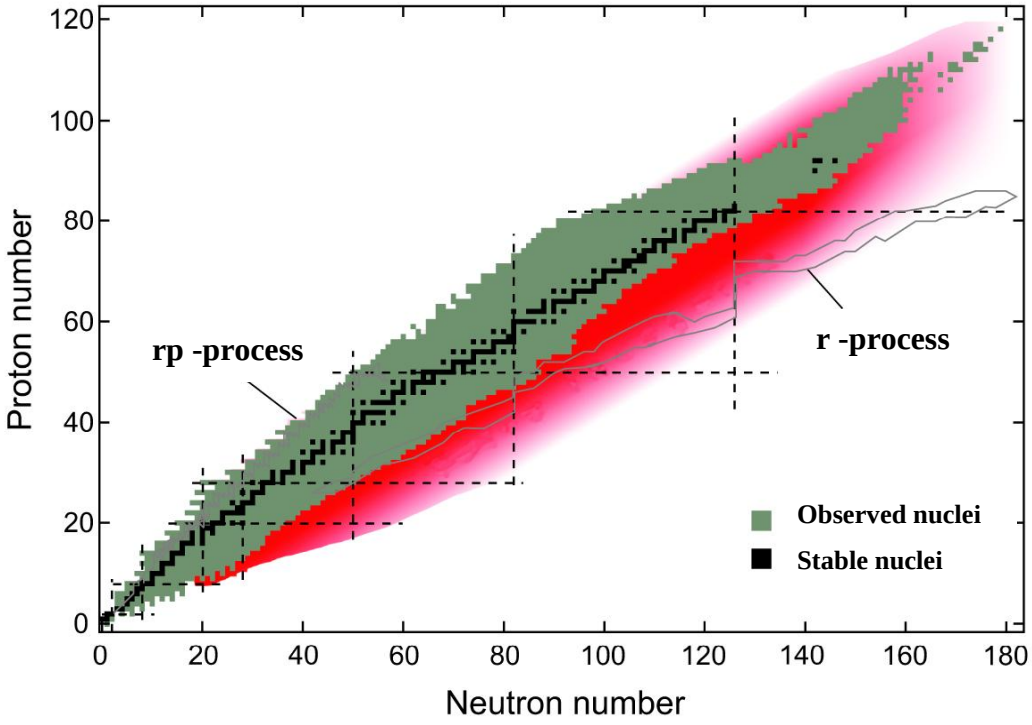

Figure 1.1: Chart of the nuclei with proton number and neutron number. Stable isotopes are shown in black while the observed unstable nuclei are shown in green. Dashed lines indicate the conventional magic numbers. Nuclei relevant in the astrophysical *rp*- and *r*- processes are also indicated (adopted from [ISF]).

In 1930s, the gross feature of nuclear binding energies for stable isotopes was successfully described by the Bethe-Weizsacker Formula [Boh75]. This simple macroscopic approach based on the liquid drop model includes the volume, surface, Coulomb, pairing and proton-neutron symmetry effects in a nucleus. A systematic comparison of experimental nuclear binding energies to predictions reveals periodic deviations where unusual stabilities arise from nuclei with numbers of neutrons or protons at 8, 20, 28, 50, 82 and 126 [Mye66,Boh75]. Such observation can be

satisfactorily explained by the shell model of atomic nuclei proposed by Mayer and Jensen [May60], for which they shared the 1963 Nobel Prize for Physics. The shell model has been immensely robust and successful in describing both systematic and specific features of nuclear structures. The simplest shell model, often called the Independent Particle Model (IPM), requires each nucleon to occupy a single-particle eigenstate in the nuclear spherical mean-field potential from the core. The mean-field is usually described by a harmonic oscillator or Woods-Saxon potential [May60,Cas90,Pre93]. This model neglects any correlations in the motions of particles outside the core or residual interactions between the valence single particles and the core. Protons and neutrons fill the eigenstates independently. Each nucleon state is characterized by its single-particle energy and quantum numbers (n,l,j), where n is associated with the number of nodes of the radial wave function, and l and j are the orbital and total angular momenta. The maximum occupancy in each neutron (proton) eigenstate is ($2j+1$) neutron (proton) [May60,Cas90,Pre93]. With a strong spin-orbit force included in the nuclear spherical mean-field potential from the core, the shell model produces significant energy gaps at the magic numbers of 8, 20, 28, 50, 82 and 126 (Figure 1.2) [Bro05,May60,Cas90,Pre93]. Stable nuclei with proton or neutron numbers corresponding to a magic number exhibit stability and natural abundance. This simple shell model also gives the correct ordering of the single-particle orbits for stable isotopes as shown in Figure 1.2. In addition, it reasonably describes the nuclear static and dynamic properties of low-lying states in spherical stable nuclei and serves as a foundation of the more sophisticated modern shell model development [Bro01].

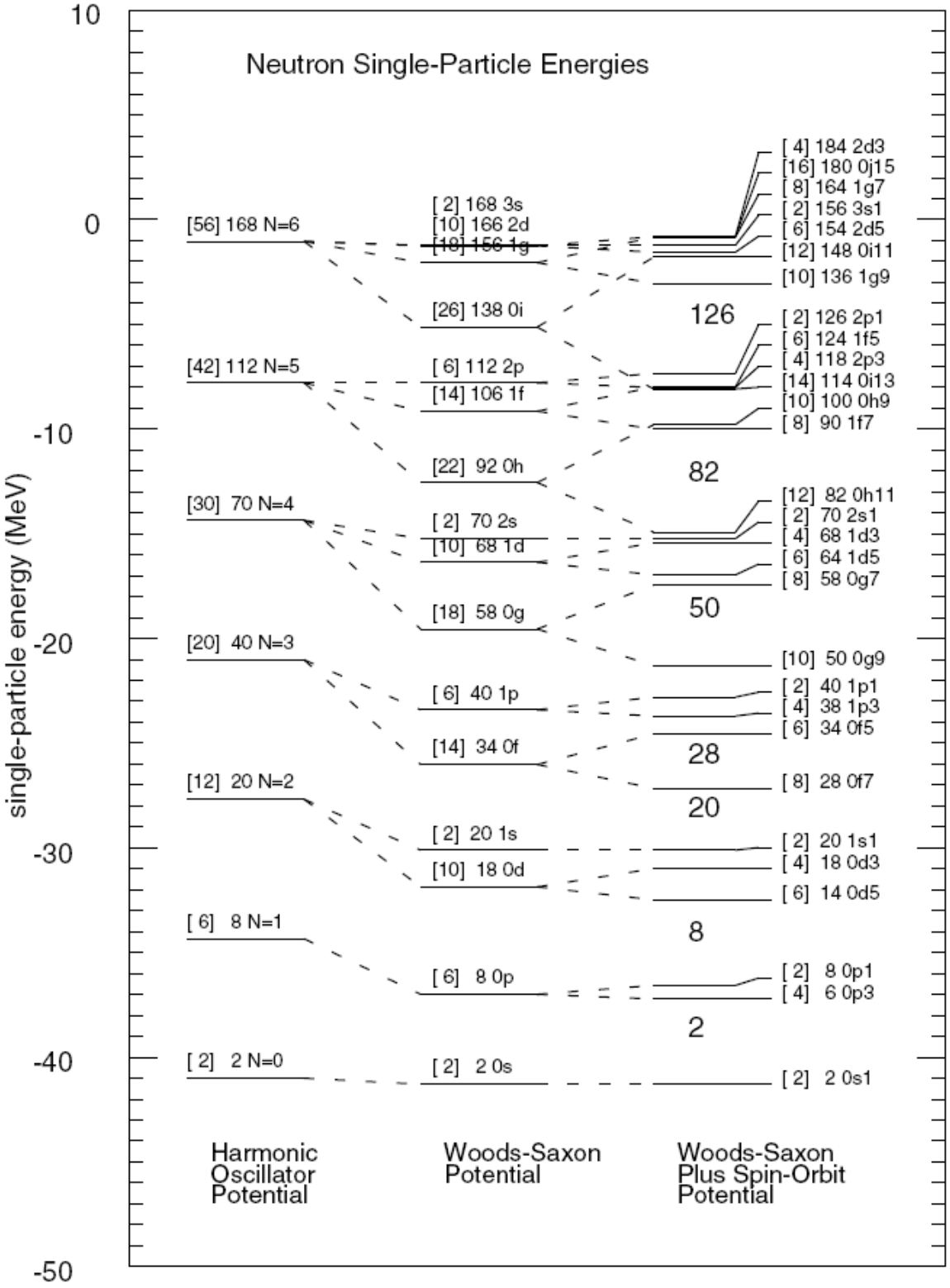

Figure 1.2: Nuclear shell structure [Bro05].

Although the mean-field model provides a basic framework to understand nuclear structure, a complete description of nuclei requires consideration of the nucleon-nucleon (*N*-*N*) correlations which modify the nuclear wave functions. The short-range component of the correlation in nuclei originates from the strong repulsion of nucleons at very short distances. Such repulsive force extends the momentum components of the nucleon wave functions to very high energy single-particle orbits and modify the compressibility of nuclei and nuclear matter [Akm98,Dic08]. The long-range component of the correlation arises from the attractive interactions between valence nucleons. This induces collective modes and pairing correlations within nuclei and leads to the coupling of nucleon orbits to low-lying collective excitations and giant resonances [Gol99]. The correlated interplay between the single-particle and collective dynamics spreads the single particle strength over a large range in excitation energy [Dic04,Dic08].

One signature of correlations is the fractional occupation of single-particle orbitals. The total occupancy of a single-particle state is not directly observable, but it can be quantified by the spectroscopic factor (SF). The SF probes the overlap between many-body wave functions of the initial and final states and measures the degree of single-nucleon overlap for a state in the specific transition [Aus70]. It characterizes the structure of nuclear states and connects experimental results to theoretical nuclear structure calculations. The measurement of (*e,e'p*) reactions on nuclei near closed proton shells is one well-known example of using SFs to investigate the effects of correlations. Results show that the absolute experimental proton SF values are reduced systematically by 30-40% compared to the mean-field theory of the Independent Particle Model [Pan97,

Kra01]. This observation suggests that significant contributions of *N-N* interactions are absent in the Independent Particle Model descriptions [Pan97,Dic04,Bar09].

The large-basis shell-model approach has been developed to include some of the *N-N* correlations in the nuclear structure studies [Bro01]. To account for the shortcomings in an approximation with a one-body mean-field potential, a two-body nucleon-nucleon interaction V_{NN} is employed in the Hamiltonian:

$$H = \sum_{\mathrm{i}} (\frac{\vec{p_{\mathrm{i}}}^2}{2m}) + \sum_{\mathrm{i<j}} V_{\mathrm{NN}}(\vec{r_{\mathrm{i}}} - \vec{r_{\mathrm{j}}}) \qquad (1.1)$$

Because of the difficulties in obtaining the exact solution in such a many-body aspect, a single-particle spherical potential is introduced to approximate the Hamiltonian into two terms as an independent particle moving in an effective average potential $H^{(0)}$ and residual interactions $H^{(1)}$.

$$H = \sum_{\mathrm{i}} \left[\frac{\vec{p_{\mathrm{i}}}^2}{2m} + U(\vec{r_{\mathrm{i}}})\right] + \left[\sum_{\mathrm{i<j}} V_{NN}(\vec{r_{\mathrm{i}}} - \vec{r_{\mathrm{j}}}) - \sum_{\mathrm{i}} U(\vec{r_{\mathrm{i}}})\right] = H^{(0)} + H^{(1)} \qquad (1.2)$$

Consequently nucleons in a nucleus can be grouped into the core part and the valence part, where the core part is completely occupied. Starting from the core and observed single-particle state, the residual two-body interaction in the Hamiltonian is adjusted to describe other properties of nuclei in a given valence space. By approximating the configuration mixing with a basis of nucleon quasi-particle orbits, the effective-interaction theories of current shell models can describe much of the long-range component of the interactions [Bro01,Dic04]. Limited by the dimension space, the valence nucleon Hilbert space has to be truncated in the calculations. This confines the

description of long-range correlations in the vicinity only near the Fermi surfaces. Currently available residual interactions provide satisfactory descriptions for the light to medium mass nuclei in *sp*-, *sd*- and *pfg*- shell regions [Cau05]. The correlations that arise from short-range and long-range with coupling to vibrational excitations are beyond the effective interactions employed in the current effective-interaction shell models. Progress with other theoretical approaches to describe full nucleon correlations is being made [Dic04,Ste06,Bar09-3].

The results from (*e,e'p*) clearly indicate the absence of nucleon correlations in the mean field model descriptions for nuclei near the closed shell. Understanding the correlations and the single-particle structure in nuclei with large proton-neutron asymmetry becomes compelling. With the advent of radioactive beam facilities, nuclei far from the stability line with large neutron or proton excess can be investigated. It has been observed that the nucleon correlations play a prominent role in the breakdown of the conventional magic numbers with the appearance of new "magic" numbers and new ordering of single-particle states and exotic modes of excitations for exotic nuclei [Sor08]. For instance, new shell gaps and magic numbers appear at N=14, 16 instead of N=8, 20 for neutron-rich nuclei in the *sd*-shell, and the swapping of $s_{1/2}$ and $d_{5/2}$ single-particle states at N=16 for Oxygen isotopes [Sor08]. To study the evolutions in the nuclear structure from the valley of stability toward the drip lines, it is essential to investigate the roles of the proton-neutron asymmetry dependence of the mean field and the long- and short-range correlations. Many experimental approaches provide insight about such evolutions. For instance, one can measure the variations of effective single particle energies which illustrate the monopole interaction effect that acts between

proton-neutron spin-orbit partners [Gau06, Sig07]. Another approach is to investigate the asymmetry dependence of single-particle occupancies [Gad08]. Both approaches require accurate determination of spectroscopic factors.

1.2 Spectroscopic factors from transfer reactions

Direct reaction is a powerful probe of single-particle structures. With minimum rearrangement of the nucleons during collisions, direct reaction involves a few degrees of freedom. In the past half century, reaction theories have been developed to allow determination of spectroscopic factors which quantify the nucleon occupancies and degrees of correlations in the single-particle wave functions. In addition to transfer reactions, there are two other experimental techniques to extract spectroscopic factors. Firstly, the electron-induced proton knockout reaction (*e,e'p*) which was developed to measure the spectroscopic factors of proton single-particle hole states in well-bound nuclei in the 1980's [Kra01]. The results from (*e,e'p*) reactions indicate 30-40% depletion of occupancy attributed to the nucleon correlations. Even though it is believed that reaction theory is more exact and that electrons probe the interior of the wave functions, neutron removal and particle-state cannot be studied by electron scattering. In addition, this technique can be applied to study only stable isotopes due to lack of rare isotope targets. To extend the systematic studies to exotic isotopes, considerable progresses in both theories and experimental techniques in single-nucleon knockout reactions using fast beams have been made in the last decade [Han03, Tos04]. The low beam intensity requirement of only an order of 10^2 particles-per-second at incident energy above 50 MeV/u offer a powerful approach to systematically study the hole-state spectroscopic

factors for exotic nuclei [Han03, Tos04, Gad08]. Knockout reactions suggest a systematic trend of spectroscopic factors and nucleon correlations.

The main source of spectroscopic factor information for stable nuclei in the past half century is from transfer reactions. Compared to (*e,e'p*) and one-nucleon knockout reactions, transfer reactions probe both particle- and hole-states exclusively for stable as well as exotic nuclei. Beam energies used in transfer reactions can vary from a few MeV to a hundred MeV per nucleon depending on the experimental purposes. With the recent revived interest of transfer reactions due to the availability of radioactive beams, it is essential to review and understand the existing theoretical reaction models of transfer reactions, and develop a systematic framework to extend the study of the nuclear structures from stable to exotic nuclei.

One-nucleon transfer reactions such as (*p,d*), (*d,p*), (*d,n*), (^{3}*He,d*) and (*d,*^{3}*He*) are frequently used to probe correlations and properties of single-particle wave functions and the degree to which the nuclear state is a pure single-particle state. The angular distributions of the emitted *d* or *p* are characteristic of the angular momentum of the transferred nucleon. For two-nucleon transfers such as (*p,t*) and (*t,p*), the transferred angular momentum is shared between two transferred nucleons and therefore the correlations of nuclear structure govern the strength of the reaction. This important feature provides a means to probe nuclear correlations between two nucleons which is not accessible to one-nucleon transfer reactions [Aus07,Tan08]. The two-nucleon transfer reaction can also be used to study unbound states in exotic nuclei which are restricted in one-nucleon transfer techniques [Suz09]. However the applicability of the two-nucleon transfer reactions is limited by the complications in the reaction theories and low reaction

rates. Similarly, multi-nucleon transfer reactions may be a useful tool for studies of correlations [Aus07]. Unfortunately, there is not yet a well developed theory to describe the data. This thesis is dedicated to single-nucleon transfer reactions which have more well developed theories and extensive existing data.

For one-nucleon transfer reactions, the description of the reaction mechanism generally utilizes the distorted wave Born approximation (DWBA) [Sat80,Gle04, Aus70]. The differential cross section is proportional to the square of transition amplitude, which can be described by two main factors as shown in Equation 1.3. S_{lj} is the spectroscopic factor which is determined by the wave functions of nuclear states involved but independent of the kinematics; $B_l^{m_l}$ contains the reaction dynamics information through the overlap of the wave functions of the relative motions and the wave function of the transfer nucleon [Aus70, Sat80, Gle04].

$$\frac{d\sigma}{d\Omega} \propto |T_{\alpha\beta}|^2 \propto \sum_{ljm_l} S_{lj} |B_l^{m_l}|^2 \qquad (1.3)$$

Since S_{lj} reflects the nature of wave functions, it provides a means for comparison between experiments and theories. The experimental spectroscopic factor in a transfer reaction is obtained by taking the ratios of the experimental cross sections to the predicted cross sections from the reaction model [Aus70,Sat80,Gle04]. Extraction of meaningful and reliable spectroscopic factors is essential through accurate descriptions of reaction theory. As discussed in Chapter 2, non-locality and finite-range DWBA calculations are developed for realistic descriptions of kinematics. The calculations also require optical model potentials to construct the distorted waves of incoming and

outgoing reaction channels and the inputs of the bound-state radial wave functions of the transferred particle.

However, a survey of the published spectroscopic factors for certain nuclei shows that they are not consistent. It is not unusual to find published spectroscopic factors for a particular nucleus that fluctuate by a factor of two as demonstrated in Figure 1.3 for the ground-state spectroscopic factors of ^{41}Ca extracted from ^{40}Ca(d,p)^{41}Ca reactions. Similarly, one can often find that published spectroscopic factor values for the same reaction by different authors agree within uncertainties, even though the data used to extract them are not in agreement [Lee07]. Many of the difficulties in the past extractions of spectroscopic factors have been associated with ambiguities in the optical model parameterizations which are used in the DWBA model to construct the distorted waves of incoming and outgoing reaction channels. Geometries of the bound-state radial wave functions of the transferred particle are strongly correlated to the magnitudes of the spectroscopic factors [Aus70,Sat80,Gle04]. In addition, the deuteron breakup effects have been found to be important in the calculated angular distributions and deduced spectroscopic factors [Joh70]. The inconsistencies in spectroscopic factor extractions hinder the use of transfer reactions from studying evolution of nuclear structures, such as the shell evolution along the isotopic or isotonic chains. Therefore it is crucial to develop a systematic approach to extract consistent and reliable relative spectroscopic factors from transfer reactions.

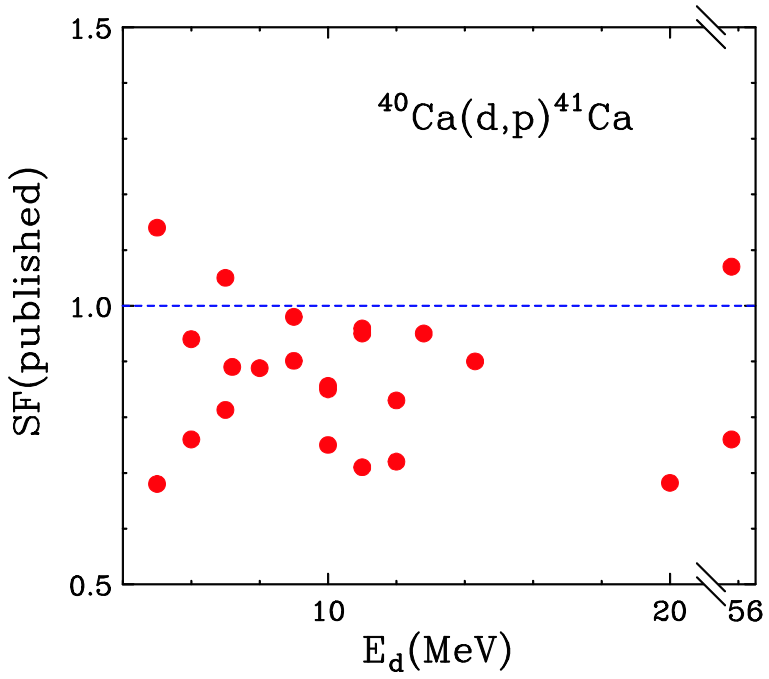

Figure 1.3: Fluctuations in the published ground-state spectroscopic factors of ^{41}Ca extracted from ^{40}Ca(d,p) ^{41}Ca reactions.

A consistent three-body analysis of neutron transfer reaction data involving minimal assumptions has been developed for (*p*,*d*) and (*d*,*p*) transfer reactions [Liu04, Liu05]. The methodology uses Adiabatic Distorted-wave Born approximation (ADWA), an extension of DWBA theory with the Johnson-Soper (JS) adiabatic approximation to the neutron, proton, and target three-body system [Joh70] taking into account the effect of deuteron break up. To avoid the ambiguity in optical potentials obtained from individual best fits to elastic scattering data, global nucleon optical model potentials or microscopic potentials are applied consistently at all incident energies and target nuclei. Additionally, a consistent set of input parameters for the reaction mechanism and single-particle bound state is adopted in the cross-section calculations [Liu04, Liu05, Lee07].

One may argue that it would be better to fit the experimental elastic scattering data at the same incident energy by adjusting the parameters in optical model potentials for nucleon transfer reaction. This, however, does not seem to result in an overall improved description, mainly because data at a single incident energy do not lead to an unambiguous determination of the nuclear optical potential. Instead, it is more appropriate to use elastic scattering data measured over many energies to obtain a global optical potential that can be used without the need for an additional measurement of elastic scattering for a particular transfer reaction [Per76]. Such practice becomes desirable when a large range of beam energies and nuclei is needed in systematic studies or when radioactive beams are involved where beam time for elastic scattering is often not available.

The systematic ADWA analysis approach has been proven to sufficiently remove the long-standing ambiguities in the cross-section calculations and give consistent spectroscopic factors for ^{12}C(d,p)^{13}C and ^{13}C(p,d)^{12}C reactions [Liu04,Liu05]. To examine the possibility of using such a consistent approach for a global study of nuclear structure using spectroscopic factors, the first part of this dissertation is dedicated to the systematic comparisons of an extensive amount of single neutron (p,d) and (d,p) transfer reaction cross-section data on stable isotopes from Lithium to Nickel, obtained in the past 40 years, to the angular distributions calculated in the ADWA model [Tsa05,Lee06,Lee07,Tsa09,Lee09]. This large-scale survey utilizes the existing data to extract meaningful spectroscopic factors and establishes reliable systematics in the ground-state and excited-state spectroscopic factors. This provides an essential framework for studying nuclear structures using transfer reactions.

1.3 Motivation of present experiment

Based on the consistent ADWA framework, the comprehensive analyses of transfer reaction data described in Chapter 2 suggest that the reduction factors *Rs*, the ratio of the experimental spectroscopic factor (SF) to prediction, are independent of the neutron binding energy for stable nuclei within statistical errors [Tsa05, Lee06]. The reduction factor quantifies the percentage of correlation absent in the shell model descriptions. To understand the regions of extreme *N/Z*, the experimental efforts of this dissertation focus on the measurements of (*p,d*) neutron transfer reactions involving proton-rich ^{34}Ar and neutron-rich ^{46}Ar beams. These measurements were done in inverse kinematics to extract the experimental neutron SFs for ^{34}Ar and ^{46}Ar. The difference between neutron and proton separation energy ($\Delta S=Sn-Sp$ for neutron SF; $\Delta S=Sp-Sn$ for proton SF), which characterizes the asymmetry dependence of the relative shift for the neutron and proton Fermi surface, is 12.41 MeV and -10.03 MeV for ^{34}Ar and ^{46}Ar respectively. This significantly expands the separation energy difference of isotopes investigated. In previous global studies the maximum ΔS is 7.31 MeV with a few measurements at ΔS smaller than -10 MeV. The ^{34}Ar results would highlight the correlation's effects in the proton-rich regime [Lee10].

Large suppression (up to 75%) in SF values compared to shell model predictions for strongly bound valence nucleons has been observed in one-nucleon knockout reactions [Gad08] as represented as solid triangles in Figure 1.4. In particular, the neutron reduction factor *Rs* of ^{34}Ar is smaller by a factor of 2 compared to that of ^{46}Ar [Gad04-2, Gad05]. This suggests that the valence nucleon of the deficient nucleon species is much

more strongly correlated compared to those of the excess nucleon species [Gad08]. The trend of strong suppression experienced by the deeply bound nucleon is not found in the spectroscopic factors obtained in transfer reactions [Tsa05,Lee06] or (*e,e'p*) measurements [Kra01] for nuclei close to stability, where the (*e,e'p*) results are shown as open circles in Figure 1.4. The large asymmetry dependence of correlations in knockout reactions, however, has not been explained by theories or other global analyses [Bar09-1,Bar09-2,Bar09-3,Cha06,Cha07]. For example, the dispersive optical model (DOM) analysis of elastic-scattering and bound-level data on Ca isotopes ($^{40\text{-}49}$Ca) suggests weak asymmetry dependence of proton correlations, where the change in proton SF magnitude from ^{40}Ca to ^{48}Ca is about 10% [Cha06,Cha07].

The present measurements of the (*p,d*) reaction on proton-rich ^{34}Ar and neutron-rich ^{46}Ar provide the opportunity to compare the asymmetry dependence of correlation obtained from transfer and knockout reactions [Lee10]. The conclusion from the present transfer reaction experiments investigates the compatibility of different experimental techniques and reaction theories for a unified description of the nature of correlations and the underlying physics.

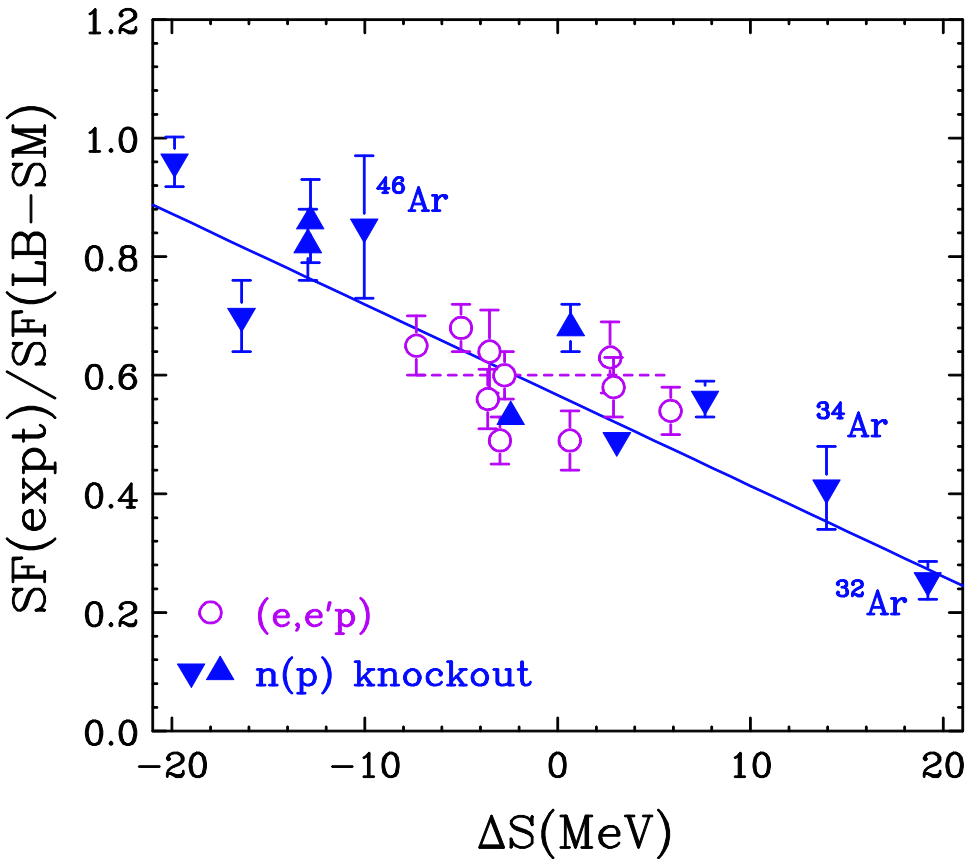

Figure 1.4: Reduction factor (*Rs*) as a function of the difference of neutron and proton separation energies (*ΔS*). The open circles and closed triangles denote the *Rs* obtained from (*e,e'p*) and knockout reaction measurements respectively. The solid line is the averaged *Rs* from (*e,e'p*) reaction data, while the dashed line is the best fit of *Rs* from the knockout reaction data.

1.4 Organization of Dissertation

This dissertation is organized in the following way. Chapter 2 introduces the methodology to extract spectroscopic factors systematically using published angular distributions of (*p*,*d*) and (*d*,*p*) transfer reactions. This chapter also presents a survey of deduced ground- and excited-state spectroscopic factors of *Z*=3-28 nuclei. The systematics of spectroscopic factors is used to provide checks of the residual interactions and Hilbert spaces used in the current nuclear structure calculations. Chapter 3 focuses on the experiments of the $p(^{34,36,46}\mathrm{Ar},d)$ transfer reactions performed at NSCL. This is followed by the descriptions of the calibrations and data analysis in Chapter 4. Chapter 5 presents the cross section and spectroscopic factor extractions for these measurements as well as the associated uncertainties. In this chapter, the ^{34}Ar and ^{46}Ar data are compared to large-basis shell-model predictions and the discussion of the underlying physics is given in great detail. The summary and conclusions are given in Chapter 6.

Chapter 2

Spectroscopic factors from transfer reactions

Spectroscopic factors (SF) quantify the nature and occupancy of the single-particle orbits in a nucleus. Measurements of spectroscopic factors therefore provide quantitative information about the single particle structure of nuclei in the shell model. In our present work, we extract the neutron spectroscopic factors of nucleus B in the reactions of B(*p*,*d*)A and A(*d*,*p*)B, where nucleus B is considered to be composed of the core A plus the valence neutron n. The overlap integral between the wave function of one state in nucleus A and another in B provides the theoretical neutron spectroscopic factor of nucleus B, which are usually calculated using shell models. The ratio of the measured cross sections divided by the cross sections calculated with a reaction model defines the experimental SF for transfer between these states.

Since 1960, (*p*,*d*), (*d*,*p*) and other single nucleon transfer reactions have been extensively used to extract spectroscopic information for single nucleon orbits. However, the published SF values in the literatures for a particular nucleus often varied widely, more than a factor of 2 in the case of ^{40}Ca(*d*,*p*)^{41}Ca reaction as shown in Figure 1.3, for instance, reflecting uncertainties and ambiguities introduced by the choice of optical model parameters and bound state potential parameters employed in the reaction models [Liu04, Lee07]. To allow comparisons of the experimental spectroscopic factors with theoretical predictions over a broad range of nuclei, we have adopted a systematic and consistent approach involving minimal assumptions and have reanalyzed the existing

transfer reactions data. A priori, transfer reactions do not yield absolute spectroscopic factors as the analysis depends on other input parameters such as the geometry of the neutron bound state wave function as well as the optical potentials used in the reaction model. However, if the analysis utilizes a consistent set of parameters, the relative spectroscopic factors can be determined reliably. It should be emphasized that relative normalized SF values are sufficient to study the evolution of nuclear structure; while the absolute normalization in SF magnitude is only required to determine how much correlation remove the single-particle strengths from the Hilbert space in which the shell model states are degenerated.

This chapter explains the basic principles of both transfer reaction model and shell structure model. The methodology of extracting consistent experimental SFs with minimum assumptions is also demonstrated here. The comparisons of the experimental SFs to the shell-model predictions as well as to the other SF compilations are presented and the underlying physics is discussed. The results shown in this section have been published in several papers [Tsa05, Lee06, Lee07, Tsa09, Lee09].

2.1 Reaction theory

The mechanism of direct transfer reactions ($A+a \rightarrow B+b$) can be described by the distorted-wave Born approximation (DWBA). In this theory, the reaction is regarded as a perturbation in the elastic scattering that induces a transition to occur between two channels. The relative motions are governed by an optical potential. The resulting waves, distorted from the inelastic scattering plane wave, are used to obtain the approximate transition amplitude which is a nuclear overlap function. The model calculates the

differential cross sections. It is important to note that the DWBA theory is based on the assumptions that the reaction is a one-step direct process and the interaction which drives the reaction is weak enough for the reaction to be treated in the first-order perturbation theory. Adiabatic approximation can be incorporated in the DWBA framework to take into account the influence of deuteron break-up. Such approach is designated as adiabatic distorted-wave Born Approximation (ADWA). This subsection presents the DWBA formalism and the use of adiabatic approximation in ADWA. Many global optical potentials have been developed over the past years. Among them, two well determined and widely used optical-model potentials derived using global and microscopic approaches respectively are introduced in this chapter.

2.1.1 Adiabatic Distorted-Wave Born Approximation (ADWA)

The basis of the distorted-wave Born approximation for direct transfer reactions ($A+a \rightarrow B+b$) is the distorted-wave transition amplitude which is expressed as Equation 2.1[Aus70,Sat80,Jac70,Kra01].

$$\begin{aligned} \mathrm{T}_{\alpha\beta}^{\mathrm{DW}} &= \langle \chi_{\beta}^{(-)}(\overrightarrow{k_\beta}, \overrightarrow{r_\beta})\, \psi_B \psi_b \,|V_\alpha - U_\alpha|\, \psi_A \psi_a\, \chi_{\alpha}^{(+)}(\overrightarrow{k_\alpha}, \overrightarrow{r_\alpha})\rangle \\ &= \int d\vec{r}_\beta \int d\vec{r}_\alpha \chi_{\beta}^{(-)*}\left(\overrightarrow{k_\beta}, \overrightarrow{r_\beta}\right) \langle Bb|V_\alpha - U_\alpha|Aa\rangle\ \chi_{\alpha}^{(+)}\left(\overrightarrow{k_\alpha}, \overrightarrow{r_\alpha}\right) \end{aligned} \qquad (2.1)$$

where α (β) is the entrance (exit) channel with projectile (ejectile) a(b) and target (final) nucleus A(B) and $\overrightarrow{r_\alpha}$ ($\overrightarrow{r_\beta}$) is the relative coordinates between projectile a and A nucleus (between b and B). V_α is the interaction between the projectile, a, and the target nucleus. $\psi_A(\psi_B)$ is the internal wave function of the projectile (target) nucleus. And $\chi_{\alpha}^{(+)}(\overrightarrow{k_\alpha}, \overrightarrow{r_\alpha})$ is the solution of the Schrodinger equation for the incoming particle with

the distorting potential U_α in channel α. The exact wave function of the system is described by a product of the internal wave functions of the outgoing particle ψ_b, the residual nucleus ψ_{B} and a function $\chi_\beta^{(-)}(\overrightarrow{k_\beta}, \overrightarrow{r_\beta})$ associated with the elastic scattering of the outgoing particle from the final nucleus B. It is a common practice to assume that the term of $V_\alpha - U_\alpha$ can be replaced by the interaction between the transferred nucleon and the projectile nucleus V_{an}.

The nuclear matrix element $\langle Bb|V_\alpha - U_\alpha|Aa\rangle$, with integration performed over all coordinates independent of $\overrightarrow{r_\alpha}$ and $\overrightarrow{r_\beta}$, can be expanded into the nuclear overlap integral as shown in Equation 2.2 , which carries single-particle state information (*n*,*l*,*j*,*m*), and into the overlap function between the projectile and ejectile as presented in Equation 2.3. Eventually the transition amplitude can be expressed in Equation 2.4 and the differential cross section is proportional to the square of the transition amplitude [Kra01].

$$\int d\zeta_B \, \psi_B^*(\zeta_B) \, \psi_A(\zeta_B, \vec{R}) = \sum_{nljm} \langle J_B \, j \, M_B \, m | J_A \, M_A \rangle \sqrt{S_{nlj}} \, \Phi_{nljm}(\vec{R}) \quad (2.2)$$

$$f(\vec{r}) = \langle \psi_b^*(\zeta_a, \vec{r}) | V_{an}(\vec{r}) | \psi_a(\zeta_a) \rangle \quad (2.3)$$

$$T_{\alpha\beta}^{DW} \propto$$

$$\sum_{nljm} \sqrt{S_{nlj}} \int d\vec{r}_\beta \int d\vec{r}_\alpha \chi_\beta^{(-)*}(\overrightarrow{k_\beta}, \overrightarrow{r_\beta}) \, \Phi_{nljm}(\vec{R}) \, f(\vec{r}) \chi_\alpha^{(+)}(\overrightarrow{k_\alpha}, \overrightarrow{r_\alpha}) \quad (2.4)$$

where $\langle J_B \, j \, M_B \, m | J_A \, M_A \rangle$ is a Clebsch-Gordon coefficient, $\sqrt{S_{nlj}}$ is the spectroscopic amplitude and $\Phi_{nljm}(\vec{R})$ is the normalized single-article wave function and ζ is the internal coordinate.

For more realistic descriptions of the reaction mechanism, the optical potential should be non-local, which means that the wave function at a point is affected within the range of non-local potential. This directly affects the wave functions of the projectile and ejectile in the region where the transfer takes place. The nonlocality corrections have been obtained by fitting the experimental data [Per62]. In addition, interactions among protons and neutrons exist in a finite range. Without such consideration in the calculations, the contributions coming from the nuclear interior are over-emphasized. The effect of finite-range of the interaction for deuteron can be taken into account approximately using local energy approximation (LEA) [But64].

With the small separation energy of 2.224 MeV, deuteron breaks up easily in the field of core nucleus especially at high incident energy. This would change the total reaction cross sections and consequently the amplitudes of spectroscopic factors. Johnson and Soper extended the DWBA to include the effects of the breakup of the deuteron in the field of the target and of the transfer of the neutron into (or out of) the breakup continuum [Joh70]. The use of adiabatic approximation to the neutron, proton, and target three-body system is designated as Adiabatic Distorted-Wave Born Approximation (ADWA). In the Johnson-Soper (JS) adiabatic approximation, the effective nucleon-nucleus interaction is formulated as the sum of the nucleon optical-model potentials evaluated at half of the deuteron incident energy as shown in the following equation 2.5:

$$U_d(\vec{R}) = \frac{1}{\mathrm{D}_0}\int\{U_n\left(\vec{R}+\frac{1}{2}\vec{r}\right)+\ U_p\left(\vec{R}-\frac{1}{2}\vec{r}\right)\}\,V_{pn}(\vec{r}\,)\,\phi_0(\vec{r})\,d\vec{r} \qquad (2.5)$$

where U_p and U_d are the optical-model potentials for proton and deuteron respectively and V_{pn} is the interaction between proton and neutron, while ϕ_0 represents the internal wave function of deuteron. D_0 is strength of the Reid soft-core $^3S_1$-$^3D_1$ neutron-proton interaction.

2.1.2 Global optical model potential

The optical-model potential is the main model-dependent ingredient in the transfer reaction model. The local optical-model potential for nucleon-nucleus scattering can be written in the Woods-Saxon form [Aus70]:

$$U(r) = -V_r f(r, R_V, a_V) - iW_r f(r, R_W, a_W) + 4iW_s a_W \frac{d}{dr} f(r, R_W, a_W) + 2\,(V_{SO} + iW_{SO}) \left(\frac{1}{r}\frac{d}{dr} f(r, R_{SO}, a_{SO}) L \cdot \sigma\right) + V_c \qquad (2.6)$$

where

$$f(r, R, a) = \frac{1}{1+\exp\left[\frac{(r-R)}{a}\right]} \qquad V_c = \begin{cases} \dfrac{Z_a Z_b e^2}{r}, & r \geq R_c \\ \dfrac{Z_a Z_b e^2}{2R_c}\left(3 - \dfrac{r^2}{R_c^2}\right), & r < R_c \end{cases}$$

Here, *R* is the nuclear radius and *a* is the diffuseness; *V* and *W* represent the depths of the real and imaginary potential with the subscript *r*, *s*, *so* and *c* corresponding to volume term, surface term, spin-orbit and coulomb respectively. *L* is orbital angular momentum of relative motion of the scattered particle and σ is the spin operator. *Rc* is the radius of nucleon charge distribution, which is taken to be a constant density for r < *Rc*.

In the past, the optical model potential parameters for specific nucleus-nucleus reactions were obtained from fitting elastic scattering data for the relevant entrance and exit channels. However, such approach becomes difficult when radioactive beams are involved where beam time for elastic scattering is often not available or when a large range of beam energies and nuclei is needed in systematic studies. In addition, the optical potential parameters cannot be accurately determined from the data at a single incident energy. To be more accurate and to apply the analysis to a wide range of target-nucleus and bombarding energies, it is desirable to use global optical model potentials which is determined by fitting a large amount of data over a broad range of nuclei and energies, or a microscopic global optical potential which is derived from the relevant nuclear densities using effective Skyrme interactions. In the following section, we will briefly discuss two widely used optical-model potentials in transfer reactions.

Chapel-Hill 89 (CH89)

Chapel-Hill 89 (CH89) is a parameterization of the nucleon-nucleus optical model potential for nuclear mass range $40 \leq A \leq 209$ and nucleon laboratory energy range $10 \leq E \leq 65$ MeV [Var91]. It is obtained by fitting simultaneously a large database of nearly 300 proton and neutron differential cross sections and analyzing powers. CH89 parameterization is determined based on the current understanding of the basis of optical potential, such as folding model and nuclear matter approaches. Equations 2.7 -2.10 summarize the parameterization and features of CH89 optical model potential and Table 2.1 lists the parameters of CH89. Of many global optical model potentials, it has been shown that CH89 potential best describes the (*d,p*) experimental data [Liu05, Nun08]

$$R_{\mathrm{V}} = r_{\mathrm{V}}A^{\frac{1}{3}} + r_{\mathrm{V}}^{(0)} \quad , \qquad R_{\mathrm{W}} = r_{\mathrm{W}}A^{\frac{1}{3}} + r_{\mathrm{W}}^{(0)}$$

$$R_{SO} = r_{SO}A^{\frac{1}{3}} + r_{SO}^{(0)} \quad , \qquad R_{\mathrm{c}} = r_{\mathrm{c}}A^{\frac{1}{3}} + r_{\mathrm{c}}^{(0)} \qquad (2.7)$$

$$V(r) = V_0 \pm V_{\mathrm{t}}\left(\frac{N\text{-}Z}{A}\right) + (E - E_{\mathrm{c}})V_{\mathrm{c}} \qquad (2.8)$$

$$W_{\mathrm{V}}(r) = \frac{\mathrm{W_{V0}}}{1+\exp\left(\frac{\mathrm{W_{ve0}} - (E-E_C)}{\mathrm{W_{vew}}}\right)}$$

$$W_S(r) = \frac{\mathrm{W_{S0}} \pm \mathrm{W_{st}}\left(\frac{(\mathrm{N\text{-}Z})}{\mathrm{A}}\right)}{1+\exp\left(\frac{(E-E_C) - \mathrm{Wse0}}{\mathrm{W_{sew}}}\right)} \qquad (2.9)$$

$$E_{\mathrm{c}} = \frac{6\mathrm{Ze}^2}{5\mathrm{R_c}} \quad for\ proton; \quad E_{\mathrm{c}} = 0\ for\ neutron \qquad (2.10)$$

Table 2.1: Summary of parameters for CH89 global optical model potential

Parameters					
V_0	52.9 MeV	V_{so}	5.9 MeV.fm^2	W_{st}	18 MeV
V_t	13.1 MeV	r_{so}	1.34 fm	W_{se0}	36 MeV
V_e	-0.299 MeV	$r_{so}^{(0)}$	-1.2 fm	W_{sew}	37 MeV
r_v	1.250 fm	a_{so}	0.63 fm	r_w	1.33 fm
$r_v^{(0)}$	-0.225 fm	W_{vo}	7.8 MeV	$r_w^{(o)}$	-0.42 fm
a_v	0.690 fm	W_{veo}	35 MeV	a_w	0.69 fm
r_c	1.24 fm	W_{vew}	16 MeV		
$r_c^{(0)}$	0.12 fm	W_{s0}	10.0 MeV		

JLM Optical-model potential

To include microscopic description of the nuclear interior, a set of optical-model potential parameterization is derived from the nuclear matter effective nucleon-nucleon interaction of Jeukenne, Lejeune, and Mahaux (JLM) [Jeu77] based on the Brueckner-Hartree-Fock approximation and Reid's hard core interaction. This approach can be applied consistently for nuclei with mass numbers $12 \leq A \leq 208$ and for energies up to 160 MeV. Equation 2.11 gives the real and imaginary JLM potential respectively:

$$V_E(r) = \lambda_V \left(b\sqrt{\pi} \right)^{-3} \frac{V_E(r)}{\rho(r)} \int \rho(r') \exp\left(-\frac{|\vec{r}-\vec{r'}|}{b^2}\right) d^3r'$$

$$W_E(r) = \lambda_W \left(b\sqrt{\pi} \right)^{-3} \frac{W_E(r)}{\rho(r)} \int \rho(r') \exp\left(-\frac{|\vec{r}-\vec{r'}|}{b^2}\right) d^3r' \qquad (2.11)$$

The range of effective interaction b is set to be 1.2 fm. We adopt the conventional scale factors of λ_V = 1.0 and λ_W = 0.8 which are consistent with an analysis of data on several systems [Pet85]. V_E and W_E are the real and imaginary nucleon potential derived in the local density approximation (LDA), where the LDA potential with energy E in uniform nuclear matter with density ρ and asymmetry δ is expressed in Equation 2.12.

$$V_n(\rho, E) = V_0(\rho, E) + \delta V_1(\rho, E), \quad W_n(\rho, E) = W_0(\rho, E) + \delta W_1(\rho, E) \qquad (2.12)$$

where

$$\delta = \frac{\rho_n - \rho_p}{\rho_n + \rho_p}$$

The resulting energy- and density-dependent effective interactions are folded with the target one-body densities, using the mid-point local density prescription [Pet85].

These required densities are taken from Hartree Fock (HF) calculations based on a Skyrme parameterization that offers quantitative agreement with experimental nuclear size parameters. Specifically, we use the recent SkX parameter set [Bro98], determined from a large set of data on spherical nuclei, including nuclei far from stability. The parameter set accounts for the binding energy differences of mirror nuclei [Bro00], interaction cross sections [Bro01-2], and nuclear charge distributions [Ric03]. The aforementioned agreement of the systematics of the Skyrme SkX HF predictions with nuclear size parameters suggests that this theory will also give a good description of individual single-particle states. The computed neutron and proton HF densities were used individually in evaluating the isovector contribution to the JLM optical potentials [Bro99].

2.2 Methodology of extracting experiment spectroscopic factor

The purpose of this section is to explain the criteria that we used in the data evaluation and the quality control that we applied to the existing cross sections data in transfer reactions. Furthermore, we explain the procedure we used to extract a consistent set of spectroscopic factors from (*p*,*d*) and (*d*,*p*) transfer reactions. This section is organized as follows. We begin in sub-section 2.2.1 with a brief description of the input parameters used in ADWA three-body adiabatic reaction model. This is important because spectroscopic factors are usually extracted by dividing the measured differential cross sections by theoretical cross sections predicted by a reaction model. We then explain in sub-section 2.2.2 how the data have been compiled and the uncertainties introduced in the

process. We explain in sub-section 2.2.3 the procedure for extracting the SFs. Problems with consistencies between measurements and analysis with too low and too high incident energies are discussed in sub-sections 2.2.4 and 2.2.5 respectively. Sub-section 2.2.6 deals with the internal consistency of the approach. As the pickup (*p,d*) reaction is the inverse of the stripping (*d,p*) reaction, from detail balance, the ground state SFs obtained separately by the (*p,d*) and (*d,p*) reactions should be the same within experimental uncertainties. We use this fact to assess the consistency of our method and to assign uncertainties to the extracted spectroscopic factors.

2.2.1 Input parameters in reaction model

The transfer cross sections are calculated within the Johnson-Soper adiabatic approximation [Joh70], which approximates the full many-body system by a three-body system consisting of a neutron, a proton, and an inert core. The core would be the target in a (*d,p*) reaction or the final nucleus in a (*p,d*) reaction. The phenomenological proton- and neutron-optical model potentials (CH89) [Var91] are folded to construct the deuteron optical potential that is used in ADWA model. By using the folded potential instead of a phenomenological deuteron optical potential, one includes the main corrections to the transfer cross section from the breakup of the deuteron in the field of the target.

Even though the breakup effect is mainly important for energies above 15 MeV per nucleon, to be consistent, we constructed the deuteron potential using the Soper-Johnson approach at all incident energies. Similar results are obtained if DWBA is used at low energy. The potential of the transferred neutron to the inert core was chosen to be Woods-Saxon in shape, where we used the widely adopted values of the fixed radius parameter of 1.25 fm and diffuseness parameter of 0.65 fm [Liu04, Liu05]. The depths of

the central potential wells are adjusted to reproduce the experimental binding energies. Consistent with the findings of Ref. [Ver94], we find that the surface properties of the neutron bound state wave function are dominated by the central potential. Thus, we have neglected for simplicity the spin-orbit interaction in constructing the valence neutron wave function. (We have studied this effect. In the light nuclei, $4 \leq Z \leq 24$ studied here, the effect is of the order of 10% or less. Such effect may become important for heavier nuclei.) All calculations adopt the local energy approximation (LEA) for finite range effects [But64] using the zero-range strength (D_o^2=15006.25 MeV^2 fm^3) and range (β=0.7457 fm) parameters of the Reid soft-core $^3S_1$-$^3D_1$ neutron-proton interaction [Knu75]. Nonlocality corrections with range parameters of 0.85 fm and 0.54 fm are included in the proton and deuteron channels, respectively [Per62]. The same set of input parameters is used for all the reactions analyzed here. We label our SF values as SF(ADWA) in our figures, to distinguish them from other SF values obtained when different input parameters or potentials are used. The transfer reaction calculations were carried out using the University of Surrey version of the code TWOFNR [Iga] which respects the detailed balance between (*p,d*) and (*d,p*) reactions that connect the same states. The code TWOFNR is chosen mainly for convenience as it contains all the input options discussed below. With the same input parameters, we have compared the calculations from two other widely used reaction model codes, DWUCK5 and FRESCO, and find that they provide predictions that are basically the same as those provided by TWOFNR [Kee04, Del05, Liu05].

2.2.2 Compilation and digitization of angular distribution data

Nearly all the existing angular distributions we used have been digitized from the published figures [Lee07]. The few exceptions are some tabulated data found in the Nuclear Science References (NSR) database of the National Nuclear Data Center (NNDC) [NSR]. The sources of these data came from the Former Soviet Union or Japan whose journals are not widely available in the United States. These non-US and non-European data complement our search in the Physical Review, Physical Review Letters, Nuclear Physics and occasionally in Physics Letters and Journal of Physics G. While we have made an effort to find all the relevant experiments that published the absolute differential cross sections, we could have missed some reactions especially if the incident energy is below 10 MeV or above 70 MeV.

By checking some of the data carefully and sometimes repeating the digitization several times, we estimate the uncertainties introduced by the digitization process to be less than 0.5 deg in determining the angles and less than 10% in extracting the differential cross sections. For illustration, we use the data for the reaction ^{14}N(d,p)^{15}N at E_d=12 MeV [Sch67, Hef77]. This set of data was first published in tabulated form in ref. [Sch67]. The tabulated data are plotted as closed points in Figure 2.1. Later the authors in ref. [Hef77] plotted the data in a figure, which we digitized. We compare our digitized data (open points) with the tabulated data (closed points) in Figure 2.1. We see a difference of less than 10% between the two sets of data. Of course, the digitization errors also depend on the actual size of the graphs available in the original literature. As described later, generally, errors introduced by digitization are relatively small compared to the uncertainties in the absolute cross section measurements.

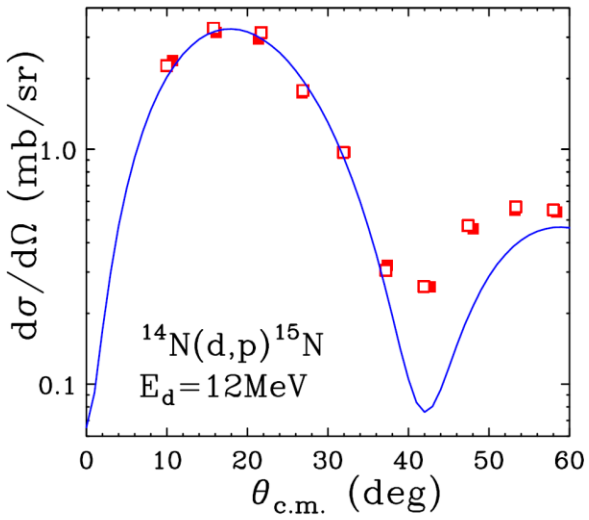

Figure 2.1: Comparison of tabulated data (closed points) [Sch67] and digitized data (open points) [Hef77] from the same measurement of the angular distributions of the protons obtained in the ^{14}N(*d*,*p*)^{15}N reaction at incident deuteron energy of 12 MeV. The curve is the predicted angular distributions from the code TWOFNR as described in the text, multiplied by 1.12 which is the spectroscopic factor.

2.2.3 Extraction of spectroscopic factors

The experimental SF value for transfer reaction is defined as the measured cross-section divided by the cross section calculated with a reaction model. For most of the nuclei we calculated, we use the ℓ values determined from the angular distributions and the $\mathbf{j}^{\pi}$ values of the valence neutron ground states found in the isotope tables [NNDC]. In general, the experimental angular distributions at larger angles are more sensitive to details of the optical potential, the effects of inelastic couplings and other higher order effects that are not well reproduced by most reaction models. Furthermore, discrepancies between the shapes from calculations and experiment are much worse at the cross section minimum, which could give these points an unduly large weight in a least squares minimization procedure. Thus, we follow the procedures used by many groups in the past

40 years that the spectroscopic factor is extracted by fitting the reaction model predictions to the angular distribution data at the first peak, with emphasis on the maximum. The accuracy in absolute cross section measurements near the peak is most important. When possible, we take the mean of as many points near the maximum as we can to extract the spectroscopic factors. We will use the angular distributions of $^{14}N(d,p)^{15}N$ shown in Figure 2.1 to illustrate the procedure we adopt to extract the spectroscopic factors.

In Figure 2.1, the first three data points with $\theta_{cm}<25°$ have been used to determine the ratios of the measured and calculated differential cross sections. The mean of these three ratios is adopted as the spectroscopic factor. For example, for the two sets of data plotted in Figure 2.1, the spectroscopic factors are 1.1 and 1.2 for tabulated data [Sch67] and digitized data [Hef77] respectively. The difference in the spectroscopic factors represents the uncertainties introduced by digitization. The theoretical angular distributions, obtained from TWOFNR have been multiplied by the spectroscopic factor, 1.1, and plotted as the solid curve in the figure.

In cases when a "first peak" is not obvious or that the angular distributions of the forward angles are nearly flat, e.g. in the reaction of $^{44}Ca(p,d)^{43}Ca$ at E_p=40 MeV [Mar72] as shown in Figure 2.2, we find that fitting the shoulder gives more consistent results. In general, the agreement of the measured shape of the angular distributions in the vicinity of the first peak or the shoulder to the shape predicted by the transfer model gives some indication as to the quality of the spectroscopic information that can be extracted by comparing the model to data. When there are more than one set of data that can be used

to determine a given spectroscopic factor, we use the number of measured data points from a given measurement that lie in the peak or shoulder region where data and theory are in good agreement to assign a relative weight for the SF extracted from that measurement. Various SF's extracted from different measurements are combined in a weighted average to compute the mean spectroscopic factors presented here.

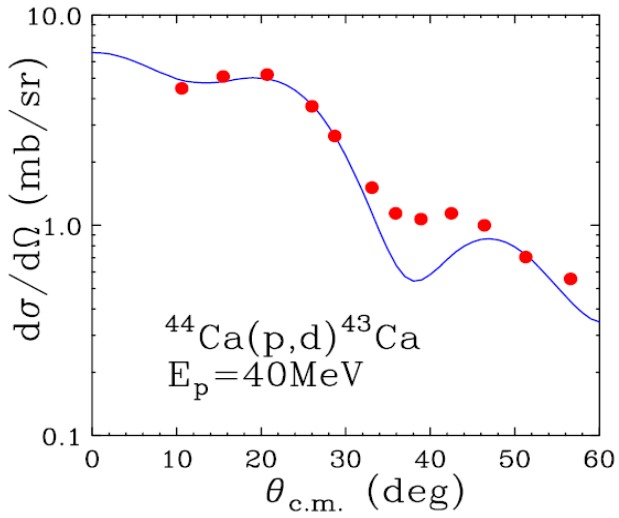

Figure 2.2: The angular distributions of the deuteron obtained in the ^{44}Ca(*p*,*d*)^{43}Ca reaction at incident proton energy of 40 MeV [Mar72]. The curve is the predicted angular distributions from the code TWOFNR as described in the text, multiplied by the spectroscopic factor.

2.2.4 Evaluation of the angular distribution measurements

Even though most published papers state the uncertainties of their cross section measurements to be 10-20%, the actual disagreements between experiments are often larger than the quoted uncertainties. An example is illustrated in the reactions ^{11}B(*d*,*p*)^{12}B reactions. From the literature, we find two measurements: one measurement at deuteron incident energy of 11.8 MeV [Liu01] and another measurement at 12 MeV [Sch67]. Since the incident deuteron energy is nearly the same, one would expect the angular

distributions from the two data sets plotted in Figure 2.3 to be the same within experimental error. Ref. [Sch67] (open circles) stated that the accuracy of the absolute cross section measurements is 15% while ref. [Liu01] (closed circles) quoted an error of 6%, which is smaller than the symbols in Figure 2.3. Not only do the cross sections differ sometimes by a factor of two, the shapes of the distributions (especially the first peak) are not even the same. In this case, the shape of the angular distributions in ref. [Liu01] agrees with the calculation (solid curve) better than that measured in ref. [Sch67]. Fortunately for this reaction, we are able to find another measurement in the NNDC database [Fic74] (open diamonds). Near the peak at forward angles, this latter angular distribution agrees with ref. [Liu01] and so we disregard the measurements of ref [Sch67]. Data in ref. [Liu01] were measured nearly 40 years later than data in ref. [Sch67] and one might be tempted to attribute the difference to the availability of better beam quality and detection systems for the measurements.

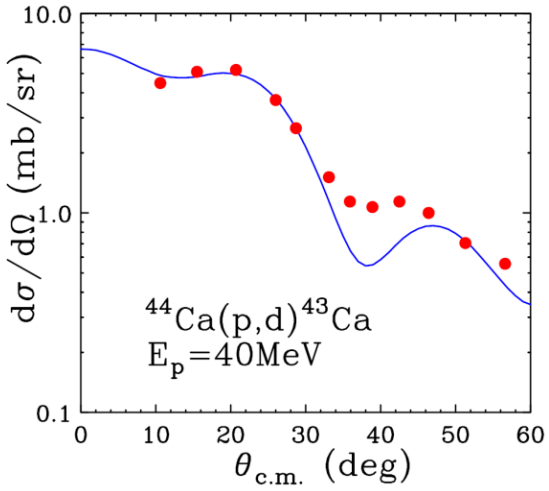

Figure 2.3: Comparisons of the angular distributions ^{11}B(d,p)^{12}B reactions. Open circles, closed circles, open diamonds represent data from refs. [Sch67], [Liu01] and [Fick74] respectively. The curve is the predicted angular distributions from the code TWOFNR normalized by the spectroscopic factor.

However, when another reaction, $^{12}C(d,p)^{13}C$ at E_d=11.8 MeV from ref. [Liu01] (closed circles) is compared to three other published angular distributions in Figure 2.4 at E_d=11.8 MeV (closed diamonds) [Sch64], 12 MeV (open circles) [Sch67], 12 MeV (open diamonds) [Lan88], the cross sections in the first peak measured in ref. [Liu01] is consistently low. No uncertainties in the measurements are given in ref. [Sch64] and ref. [Lang] but it is clear that data in ref. [Liu01] do not agree with the other measurements, especially in the most forward angle region. Thus we disregard the SF values derived from ref. [Liu01] in our compilation of $^{12}C(d,p)^{13}C$ reactions. The authors of ref [Liu01] cannot explain the discrepancies described here [Liu-priv]. In general, data taken by the same group with the same setup have similar systematic errors that lead to rejection of the entire data set. When there are independent measurements available for comparison, however, cross comparisons to other data can allow one to be more selective. The existence of confirming data, allowed us to keep $^{11}B(d,p)^{12}B$ data and discard the $^{12}C(d,p)^{13}C$ data even though both sets of data come from ref [Liu01].

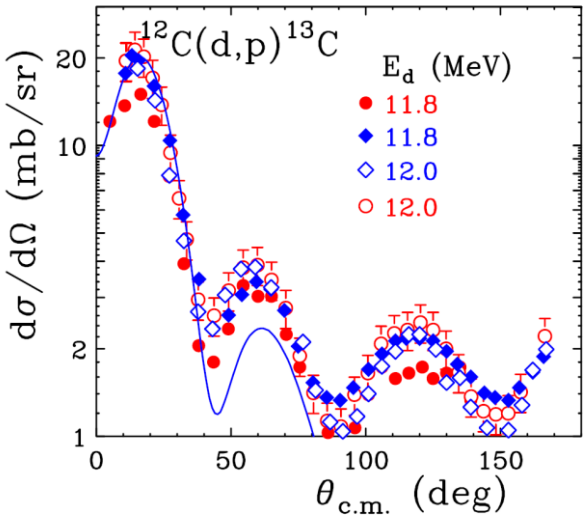

Figure 2.4: Comparisons of the angular distributions of the proton measured in the ^{12}C(*d*,*p*)^{13}C reactions in four different experiments. Open circles and closed circles, open and closed diamonds represent data from refs. [Sch67], [Liu01], [Lan88] and [Sch64] respectively. The curve is the predicted angular distributions from the code TWOFNR multiplied by the spectroscopic factor.

Cross comparisons of angular distributions sometimes help to establish common systematic problems when one set of measurements was performed by the same group with the same set up. An example is illustrated in the ^{40}Ca(*d*,*p*)^{41}Ca reactions in ref. [Lee64] where the ground state angular distributions of ^{41}Ca at E_d =7, 8, 9, 10, 11 and 12 MeV have been measured. Figure 2.5 shows the extracted spectroscopic factors (labeled as SF(ADWA)) as a function of incident deuteron energy for all the ^{40}Ca(d,p)^{41}Ca reactions. For clarity in presentation, no error bars are plotted. Except for the point at E_d=7 and 12 MeV, the extracted spectroscopic factors from ref. [Lee64] (open circles) are consistently larger than the spectroscopic factors extracted from other experiments that probed the same reaction at the same energy. Detailed comparisons of the angular distribution data show essentially the same effect, that the differential cross sections

measured in ref. [Lee64] are systematically higher than the other measurements [Sch64, Kat65, Hjo65, Nie66, And68, Fos69, Set70, Koc71, Bro74, Han75, Boy76, Alf78] measured by different groups. Clearly, there were problems in the determination of the absolute cross sections in ref. [Lee64]. As it is not possible to find the cause of this discrepancy after so many years, we disregard the spectroscopic factor values determined in ref. [Lee64] in our review of the data. The disagreements between data sets generally exceed the quoted uncertainties of the data. Indeed, we have found that the most important aspect of quality control of the data is to have as many independent measurements as possible. Comparisons of different measurements help to identify problematic measurements.

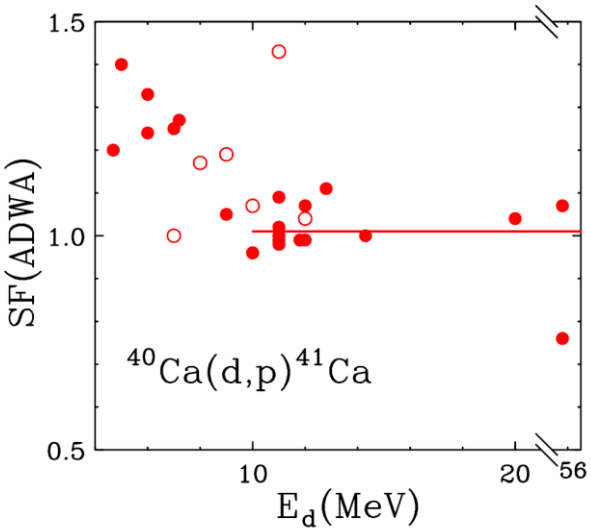

Figure 2.5: (Color online) Comparison of spectroscopic factors, SF(ADWA), obtained from Ref. [Lee64] (open circles) and from other measurements (closed circles). The increase of spectroscopic factors observed at E_d<10 MeV has been observed before [Liu05, Sch64] and has been attributed to the resonance structures in the elastic scattering of the deuterons [Ohl63]. The solid line is the mean SF(ADWA) between 10 and 56 MeV.

2.2.5 Transfer reactions at high and low energy

When Q-value, the momentum transfer or angular momentum transfer are not well-matched or when there are significant contributions from the compound nucleus, the shape of the experimental angular distributions may be poorly described by theory. We find better agreement for ground state transfers at incident energies of around 10-20 MeV and poorer agreement at very low or high (> 50 MeV) beam energies. Figure 2.6 shows the angular distributions of protons emitted from the ^{40}Ca(*d*,*p*)^{41}Ca (g.s) reaction from E_d=4.7 to 56 MeV. Only one angular distribution is shown at each incident energy. The agreement between data and prediction for the first peak improves with increasing energy. At very low incident energy, the shapes of the measurements and the calculated transfer cross sections do not agree. This phenomenon is also seen in other reactions. The spectroscopic factors as a function of incident energy are shown in Figure 2.5. The increase of spectroscopic factors at E_d<10 MeV has been observed before [Liu05, Sch64] and has been attributed to the resonance structures in the elastic scattering of the deuterons [Ohl63]. As explained in the last section, the open points based on the data from ref. [Lee64] are discarded. Between 10 to 56 MeV, we find that the mean spectroscopic factor, 1.01 ± 0.06 shown by the solid line in Figure 2.5, describes the data at all energies within experimental errors.

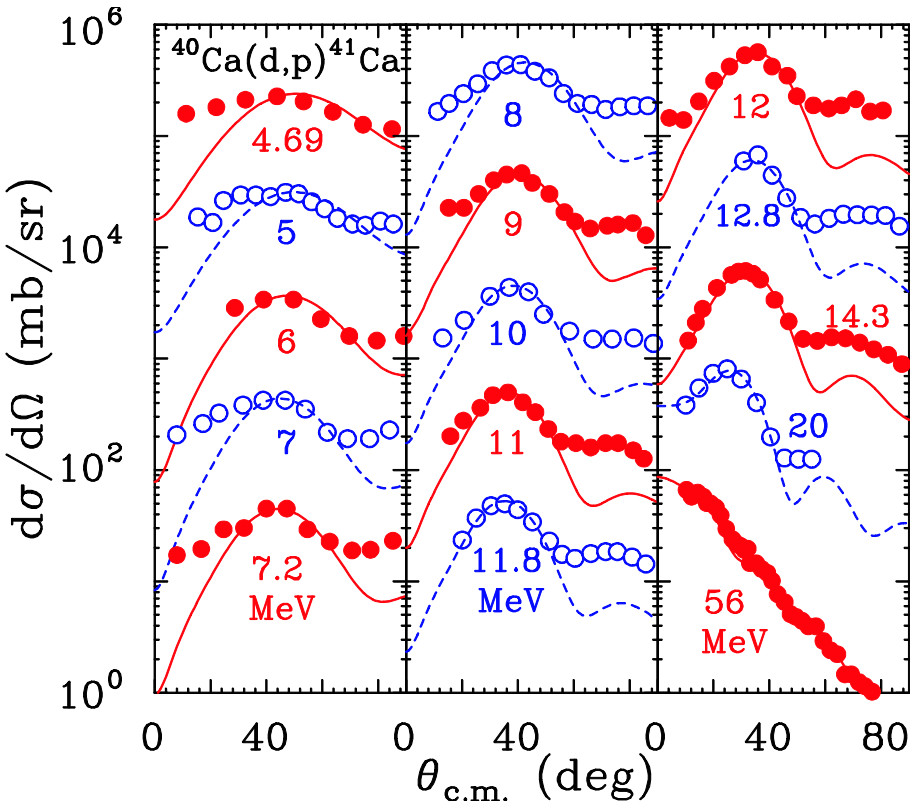

Figure 2.6: Angular distributions for ^{40}Ca(d,p)^{41}Ca reactions for beam energy from 4.69 to 56 MeV. Each distribution is displaced by factors of 10 from adjacent distributions. The overall normalization factor is 10 for the 7.2 MeV data. References are listed in ref.[Lee07].

In reactions which have large negative Q values such as ^{12}C(p,d)^{11}C (Q = –16.5 MeV), the center of mass energy available in the exit channel is very small even at ~20 MeV proton incident energy [Win01]. The validity of the calculated angular distribution is questionable at these energies and we discard these data. For other reactions measured at low incident energy (<10 MeV), the data could be dominated by compound nucleus emissions, or resonances in the low energy elastic scattering [Ohl63]. When possible, we exclude spectroscopic factors obtained with incident beam energy less than 10 MeV when computing the mean values of the spectroscopic factors.

Even though we exclude data with incident energy lower than 10 MeV from the calculation of the mean SF, these low energy data are still valuable. In cases where very few (sometimes only one) measurements with incident energy greater than 10 MeV are available, they provide checks for consistency of the measurements. In the ^{43}Ca(d,p)^{44}Ca reaction, only data at 8.5 MeV [Bje67] are available. Similarly, we only have data at 7.5 MeV for the ^{50}V(d,p)^{51}V reaction [deL67] and at 7.83 MeV for the ^{23}Na(d,p) ^{24}Na reaction [Dau63] . We adopt these results despite their low incident energies.

At high energies, momentum transfer and angular momentum transfer are mismatched so conditions may not be optimized to extract reliable spectroscopic factors. Furthermore, the global nucleon-nucleus potentials (CH89) [Var91] are fitted only to 65 MeV for protons and to 26 MeV for neutrons. Thus, we do not include data from reactions at incident energy greater than 65 MeV in this work. In examining data over a wide range of *d* or *p* incident energies, we find that the optimum beam energies for studying transfer reactions lie between 10-20 MeV.

2.2.6 Uncertainty assignment to the extracted spectroscopic factors

Since the ground-state transition of neutron pickup (*p*,*d*) and neutron stripping (*d*,*p*) reactions are inverse reactions, they should yield the same values for the spectroscopic factors. We used nuclei which have been studied reasonably well by both neutron pickup and stripping reactions to the ground state. The averaged SF values are listed in the second and fourth column of Table 2.2. The numbers of measurements contributing to the averages are listed next to the mean values in the third and fifth column.

There are strong correlations between the ground state neutron spectroscopic factors determined from the (*p*,*d*) and (*d*,*p*) reactions as shown in Figure 2.7. The solid line corresponds to perfect agreement. These are independent values determined using the procedure outlined above. The scatter of the data points about the solid line can be used to determine an overall uncertainty for such analyses. As explained in Section 2.3.4, the quoted experimental uncertainties are not always reliable. In the absence of a completely independent criterion that can be applied to each data set without comparison to others, we assume the uncertainty of each measurement to be the same, even though data from certain experiments may actually be more accurate than others. If we require the chi-square per degree of freedom of the scatter data shown in Figure 2.7 to be unity, we can extract a random uncertainty of 20% for a given measurement. The extracted uncertainty of 20% is consistent with comparisons with analysis on systems that have large number of measurements such as ^{12}C(*d*,*p*)^{13}C, ^{16}O(*p*,*d*)^{15}O, ^{16}O(*d*,*p*)^{17}O, ^{40}Ca(*d*,*p*)^{41}Ca and other reactions. In Table 2.2 and Figure 2.7, we have excluded measurements for ^{7}Li, ^{34}S and ^{10}Be nuclei due to large errors associated with either the (*p*,*d*) or (*d*,*p*) measurements. If we include these three measurements, the estimated uncertainty in a given measurement increases to 28%

Table 2.2: List of nuclei with spectroscopic factors obtained from both (*p*,*d*) and (*d*,*p*) reactions. N_{pd} and N_{dp} denote the number of (*p*,*d*) and (*d*,*p*) independent measurements included in the analysis.

B	*B(p,d)A*	N_{pd}	*A(d,p)B*	N_{dp}	B	*B(p,d)A*	N_{pd}	*A(d,p)B*	N_{dp}
^{11}Be	0.57	1	0.49	2	^{30}Si	0.87	1	0.79	2
^{11}B	1.29	1	1.55	3	^{42}Ca	2.12	2	1.82	3
^{13}C	0.81	4	0.73	12	^{43}Ca	0.63	1	0.63	2
^{14}C	1.50	3	1.82	2	^{44}Ca	3.93	3	5.14	1
^{15}N	1.65	2	1.39	4	^{48}Ti	0.11	3	0.14	1
^{17}O	0.81	3	0.99	10	^{49}Ti	0.26	2	0.23	1
^{18}O	1.60	2	1.80	1	^{50}Ti	5.50	2	7.12	2
^{21}Ne	0.03	1	0.04	2	^{51}V	1.10	2	1.58	1
^{26}Mg	2.80	3	2.01	1	^{53}Cr	0.37	1	0.39	8

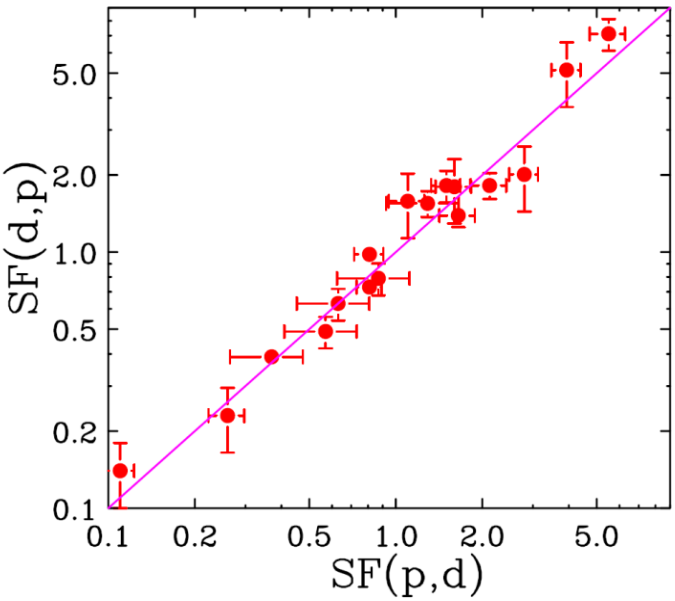

Figure 2.7: Comparisons of spectroscopic factors obtained from (*p*,*d*) and (*d*,*p*) reactions as listed in Table 2.2. The line indicates perfect agreement between the two values.

As mentioned in sub-section 2.2.3, the final SF values are obtained from the weighted average of independent measurements from both (*p*,*d*) and (*d*,*p*) reactions. In these weighted averages, the low energy (<10 MeV) data and the inconsistent data (nominally marked with asterisks) that differ significantly from other sets of data are excluded. For values determined from only one measurement without the consistency checks provided by other independent measurements, an associated uncertainty of 28% is assigned. For values determined by more than one measurement (N), we take into account the distribution of the SF's around the mean. Figure 2.8 illustrates this procedure. The open stars in Figure 2.8 represent the spectroscopic factors extracted from the good measurements of the calcium isotopes. However, the spread of the data are more than 20% for the ^{44}Ca and ^{48}Ca nuclei even though three "good" measurements are found for each of these nuclei. For these nuclei, it is more realistic to assign the uncertainty using the standard deviations of the mean of the data points. Each of the associated uncertainties is determined by adopting either the standard deviation of the mean or an uncertainty of $20\%/\sqrt{N}$, depending on which of the two uncertainties is larger. For comparison, the mean SF values with the associated uncertainties are plotted as the solid stars with error bars in Figure 2.8.

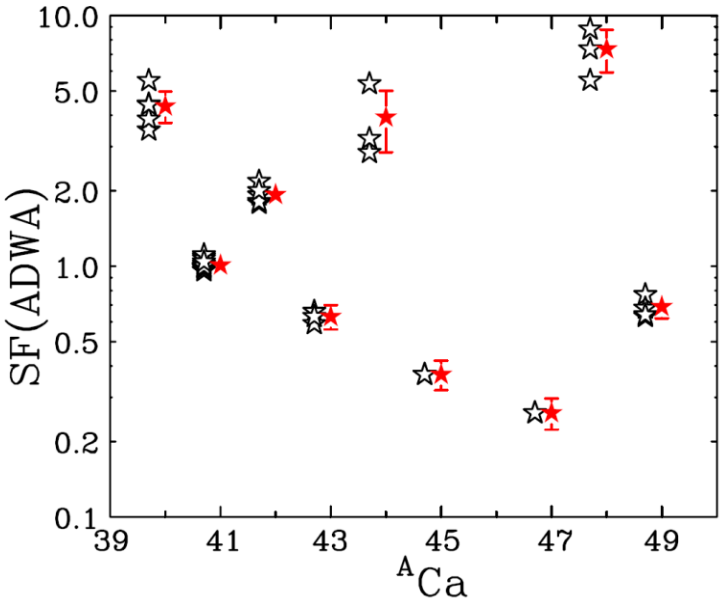

Figure 2.8: Spectroscopic factors obtained for the Ca isotopes. The open stars represent individual measurements. The accompanying solid stars are the weighted averaged values with the associated uncertainties determined from the standard deviations or $20\%/\sqrt{N}$, of the mean SF values whichever is larger.

2.3 Theoretical spectroscopic factor

Mathematically, spectroscopic factor is defined by a matrix element between the initial state in the entrance channel and the final state in the exit channels [Bro05]. For an B(*p*,*d*)A reaction, this matrix element evaluates the degree to which the wave function of the initial nucleus B can be described by the final nucleus A plus a neutron in a specific single particle orbit. The wave function for a specific state ψ_i^B in initial nucleus can be expanded in terms of a summation over the complete set of states ψ_f^A in final nucleus:

$$\psi_i^B = \sum_f \Phi_f^i(\vec{r})\psi_f^A \qquad (2.13)$$

The Φ_f^i is the overlap function between the wave function of one state in nucleus A (ψ_A) and another in B(ψ_B). The normalization of overlap function defines the theoretical spectroscopic factor between these states:

$$SF = \int \Phi_f^i(\vec{r})|^2 \, dr \;, \quad where \quad \Phi_f^i(\vec{r}) = < \psi_f^A \, | \psi_i^B > \qquad (2.14)$$

The simplest way to compute the wave function is to use independent particle model (IPM). IPM refers to the description of a nucleus in terms of particles in the orbits of a spherically symmetric potential. The particles in the last orbit are called valence nucleons. These nucleons are non-interactive except that maximum number of valence nucleons are paired up. Thus nuclei with even number of valence nucleons always have spin zero. Nucleons in the cores collectively produce the mean-field potential. This mean-field potential results in the well-known magic numbers (e.g. 2, 8, 20, 28 etc) for stable nuclei and the extreme single-particle values for the spectroscopic factors. This model works well for some nuclei, especially with valence nucleons near a closed shell.

In general, spectroscopic factors for nuclei with even number of valence neutrons generally exceed those of the neighboring nuclei with odd number of valence neutrons. This results from the pairing interaction, which couples pairs of neutrons to spin zero similar to the Cooper pairs in a superconductor. For nuclei in the vicinity of a closed shell, this trend can be well replicated by calculations that consider only pairing modifications to the independent particle model (IPM). Assuming maximal pairing (minimum Seniority), one can obtain a simple relationship between the spectroscopic factor and the number of valence nucleons *(n)* with total angular momentum *j* [Aus70] as

shown in Equation 2.15. The success of this Eq. 2.15 is illustrated by the ground state SF of Ca isotopes discussed in details in section 2.4.1.

$$SF = n \ \ , for\ n = even\ ; \qquad SF = 1 - \frac{\text{n-1}}{2j+1} \ , for\ n = odd \qquad (2.15)$$

In reality, however, most states are an admixture of the particle-hole configurations and therefore the residual interaction between nucleons is needed in the shell model calculation. The residual interaction introduces some long-range range correlations in the nuclear wave function beyond the mean field and can result in the fragmentation in the single-particle strength. Modern large-basis shell-models (LB-SM) were developed to take into account the shell-model configuration mixing and construct the wave function with different effective interactions in a specific Hilbert space. The effective interactions are usually obtained by fitting the two-body matrix elements and single-particle energies to the experimental energy levels, empirical nuclear masses, charge radii and low-lying excited state spectra for a wide range of nuclei within the region being studied [Bro01]. In our work, we used Oxbash [Bro04], the LB-SM code, to calculate the wave functions and theoretical spectroscopic factors.

2.4 Survey of spectroscopic factors (SF) using CH89 global optical model potential

About 640 neutron spectroscopic factors for ground-state and excited-state nuclei have been extracted by systematically analyzing more than 2500 measured (*d*,*p*) and (*p*,*d*) angular distributions. The systematic analysis as discussed in section 2.2 adopts global

optical-model potential CH89 and radius of transferred neutron orbital rms of r_o=1.25 fm. We compare the extracted spectroscopic factors to values predicted by large-basis shell-model (LB-SM). The survey of spectroscopic factors obtained over a wide range of nuclei provides important benchmarks and consistent analysis framework for neutron-transfer reaction studies. In addition, the spectroscopic factors provide an independent evaluation to the effective interactions used in shell models. In section 2.4.1, the extracted spectroscopic factor values are listed and compared to the LB-SM for ground-state and excited-state in *sd*- and *fp*- shell nuclei respectively. In section 2.4.2 and section 2.4.3, the extracted spectroscopic factors values will be compared to other compilations from Endt and ENDSF [End77, ENDSF].

2.4.1 Comparison with shell model predictions

2.4.1.1 Ground-state SF for Z=3-24 nuclei

The ground state neutron spectroscopic factors for 80 nuclei ranging in *Z* from 3 to 24 have been extracted by analyzing the past measurements of the angular distributions from (*d*,*p*) and (*p*,*d*) reactions [Tsa05, Lee07]. Table 2.3 lists the theoretical and experimental SF values determined for 80 nuclei, from ^{6}Li to ^{55}Cr, studied in this work.

The thin bars in Figure 2.9 show the predictions of Equation 2.15 as a function of the mass number A for the transfer of an $f_{7/2}$ neutron to or from Ca isotopes; the extracted neutron SF's are represented by star symbols. The excellent agreement reflects the fact that configuration mixing of $f_{7/2}$ neutrons outside the double magic ^{40}Ca core is well described by a pairing interaction, with little discernable contribution from core

polarization or higher lying orbits. Most nuclei display more significant configuration mixing than these Ca isotopes. Figure 2.10 compares experimentally extracted SF's for nuclei with predictions from the independent particle model plus pairing. Open symbols represent odd Z elements and the closed symbols represent even Z elements. The solid line indicates perfect agreement. Most extracted values are less than the predictions of the IPM-plus-maximal-pairing as represented by Equation 2.15. This is expected because the IPM neglects many important correlations between the nucleons in orbits near the Fermi energy as well as nucleon-core and short-range corrections. In the events that other correlations or interactions are negligible, the LB-SM predictions will be the same as the predictions from IPM.

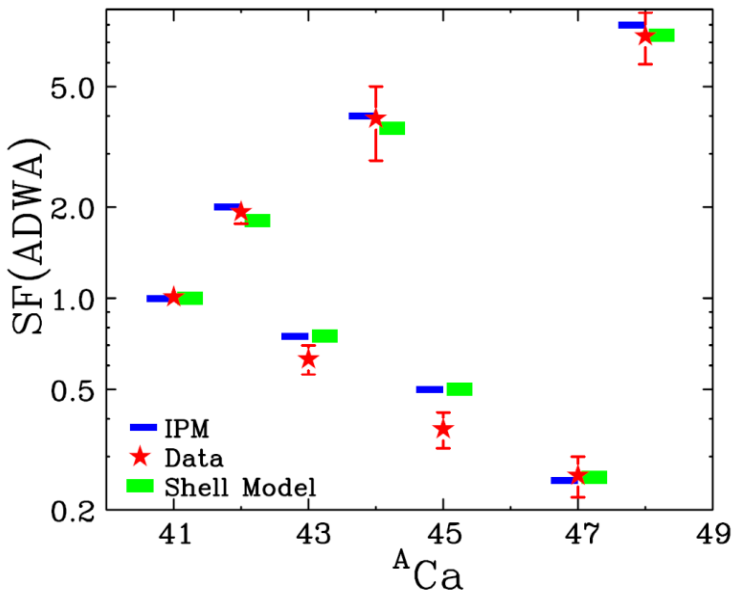

Figure 2.9: Ground state neutron spectroscopic factors for Calcium isotopes with valence neutrons in the $f_{7/2}$ orbit, star symbols represent SF values extracted from present analysis. Thin bars are IPM values and thick bars represent predictions from LB-SM using the program Oxbash.

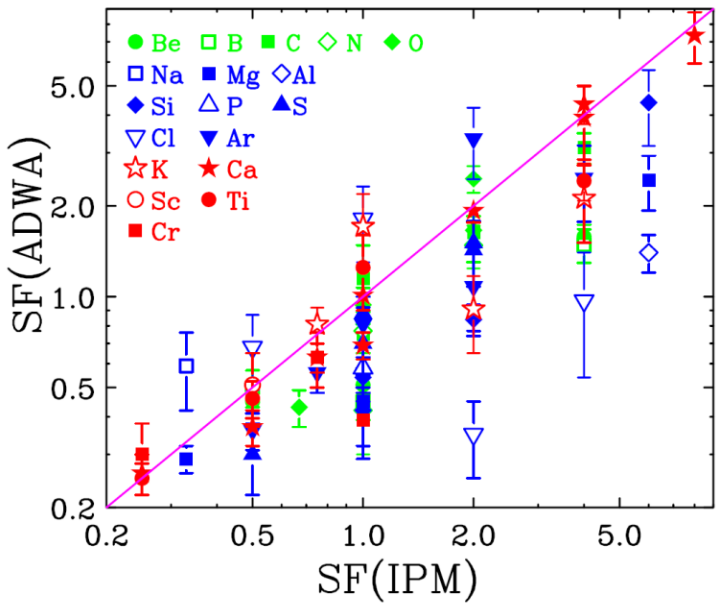

Figure 2.10: Comparison of experimental spectroscopic factors to predictions from the IPM. Open and closed symbols denote elements with odd and even Z respectively. The three different colors of green, blue and red represent Z=3-8, 9-18 and 19-22 isotopes respectively. The solid lines indicate perfect agreement.

If one diagonalizes the residual interaction within a LB-SM [Bro01], that involves the mixing of several different orbitals in the shell model basis that are close to the Fermi energy, one can obtain a better description of nuclei. Using Oxbash code with the PPN, SPSDPF, SDPN, SD, and FPPN model space and the corresponding CKPPN, WBP, WPN, W, and FPBPPN interactions [Bro01, Bro04] as input, the ground state neutron SF's for 74 nuclei have been calculated with uncertainties of about 10-20% [Bro01]. Their predicted values are listed in Table 2.3 and plotted in Figure 2.11. (In Figure 2.11, we exclude the deformed ^{24}Mg, Li, F and Ne isotopes, some of which have small calculated or measured SF values, which, in general, tend not to be accurate.) In contrast to the IPM-plus-pairing calculations, the agreement between data and LB-SM predictions are within 20% for most cases, as indicated by the two dashed lines. This shows that the

correlations between nucleons in orbits near the Fermi energy included in the LB-SM calculation are the most important one to consider. For the $^{41-48}$Ca isotopes, there is close agreement between LB-SM predictions and IPM values as shown in Figures 2.9.

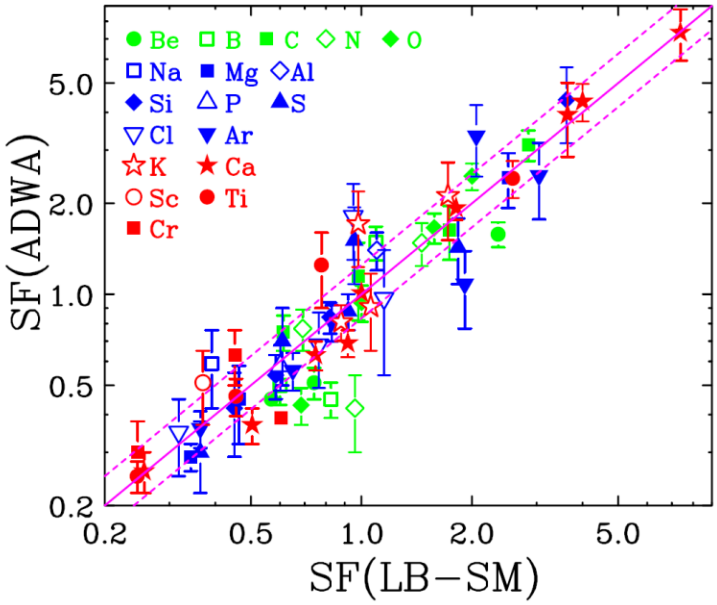

Figure 2.11: Comparison of experimental spectroscopic factors to predictions from the LB-SM. Open and closed symbols denote elements with odd and even *Z* respectively. The three different colors of green, blue and red represent *Z*=3-8, 9-18 and 19-22 isotopes respectively. The solid lines indicate perfect agreement. For reference, the two dashed lines indicate ±20% of the solid line.

Due to the absorption of flux into other channels in the nuclear interior, the adiabatic three-body model samples the neutron bound state wave function mainly at the nuclear surface. Transfer reactions constrain the exterior but not the interior contributions to the overlap integral that defines SF. In this analysis, we assume a smooth variation of the potential radius ($R=r_o A^{1/3}$) for the bound neutron global potential. Consistent with findings in [Ver94], we find the surface properties of the neutron bound-state wave

function to be dominated by the central potential; for simplicity, we have neglected the spin-orbit interaction in constructing the neutron wave function. The good overall agreement between calculated and measured SF's indicates that these assumptions are reasonable, and that the relative magnitudes of SF's from nucleus to nucleus appear to be well described. However, the absolute values of the surface contributions to the SF are influenced by these geometrical assumptions.

2.4.1.2 Excited-state SF for Z=3-28 nuclei

In astrophysics calculations, states involving resonances near the nucleon thresholds are also relevant [Des00]. For instance, the astrophysical rate calculations of the captures or emissions of single-nucleons in stellar burning processes often involve short-lived nuclear states with small spectroscopic factors which are used to determine the decay widths of resonance states [Sch05]. With current experimental technique, it is difficult or even impossible to measure all the spectroscopic factors which are necessary inputs to such astrophysical network calculations, particularly those for the short-lived nuclear states. In these cases, shell-model calculations provide the principal means to estimate these spectroscopic factors.

In general the shell model describes the properties of ground state nuclei very well, but the success of the shell model is less certain in describing such excited states [Sch05]. It is therefore important to address the accuracy of such predictions using different Hilbert spaces [Sch05]. Such an assessment can be obtained by comparing the calculated spectroscopic factors to those extracted using well-calibrated experimental probes, such as (*p*,*d*) and (*d*,*p*) transfer reactions. We therefore adopt the analysis

procedure described in section 2.21 to extract the neutron spectroscopic factors of the excited states of the following sd shell nuclei: ^{17}O, ^{18}O, ^{21}Ne, ^{24}Na, ^{25}Mg, ^{26}Mg, ^{27}Mg, ^{29}Si, ^{30}Si, ^{31}Si, ^{33}S, ^{35}S. We also extend our analysis to ^{41,43,45,47,49}Ca, ^{47,49,51}Ti and ^{51,53,55}Cr isotopes as well as ^{57,59,61,62,63,65}Ni isotopes with neutrons in the pf shell. Comparisons have been performed by matching between the theoretical and experimental levels based on the exact agreement of the quantum numbers (l,j) and spin-parity J^{π} of the transferred neutron and the approximate agreement of the energy of the states. In general, the agreement between energy levels calculated with LB-SM and the data is within 300 keV. Comparison of experimental and theoretical spectroscopic factors provides an independent method to evaluate the interactions used in shell-model calculations, most of which have been obtained from fitting the binding energy and excitation energies of a range of nuclei.

2.4.1.2.1 *sd*-shell nuclei

In ref. [Bro06], two new interactions, USDA and USDB, have been obtained to describe sd shell nuclei with an inert ^{16}O core. In extracting the USDA and USDB interactions, constraints based on the binding energy and energy levels were used and the rms deviation of the predicted energy levels ranges from 130-170 keV. To further test the validity of these interactions, we compare the experimental and calculated spectroscopic factors, which were not used to determine the parameters of the USDA or USDB interactions. This comparison includes all (d,p) transfer reaction data on these nuclei for which spectroscopic factors can be calculated in the corresponding Hilbert spaces in large-basis shell-model (LB-SM). In this section, we show a quantitative overall

evaluation of the success of LB-SM calculations in describing the SFs. There are only a handful of states where the agreement between the experimentally extracted and predicted SFs is unusually poor. These states are identified and discussed. The experimental and predicted SF values are listed in Table 2.4.

Figure 2.12 shows the comparisons of the experimental SFs to shell-model predictions. The average SF values obtained with USDA and USDB (x co-ordinates) are plotted vs. the experimental extracted SF values obtained in this study labeled as SF(ADWA) (y co-ordinates). The horizontal error bars indicate the range of the USDA and USDB results. For most of the cases, the two values are nearly identical. The solid diagonal line indicates perfect agreement between theoretical predictions and experimental data. Nearly all the data cluster around the solid line. For excited states SF, the measured angular distributions are often of poorer quality than those for the ground state. Even though we adopted the deduced experimental uncertainties of 20-30% in the figure as discussed in section 2.2.6, the larger scatter of the excited state data could imply larger experimental uncertainties closer to 40%. For reference, the dashed lines in all the figures indicate 40% deviation from the solid line. There are three states (3.908 MeV ($5/2^+$) state in ^{25}Mg, 7.692 MeV ($3/2^+$) and 8.290 MeV ($5/2^+$) states in ^{29}Si), with very small calculated spectroscopic factors (<0.005), outside the range of the established systematics. Small calculated SFs originate from large cancellations of contributions from different components of the wave functions, which are hard to control even in the best shell-model calculation. Indeed, the calculated values using USDA and USDB interactions differ from each other by more than a factor of two and under-predict the experimental values by more than a factor 10. Clearly, these cases would be important to

examine further, both experimentally and theoretically as the capability of predicting very small (<0.005) spectroscopic factors of sd shell nuclei is important for astrophysical applications.

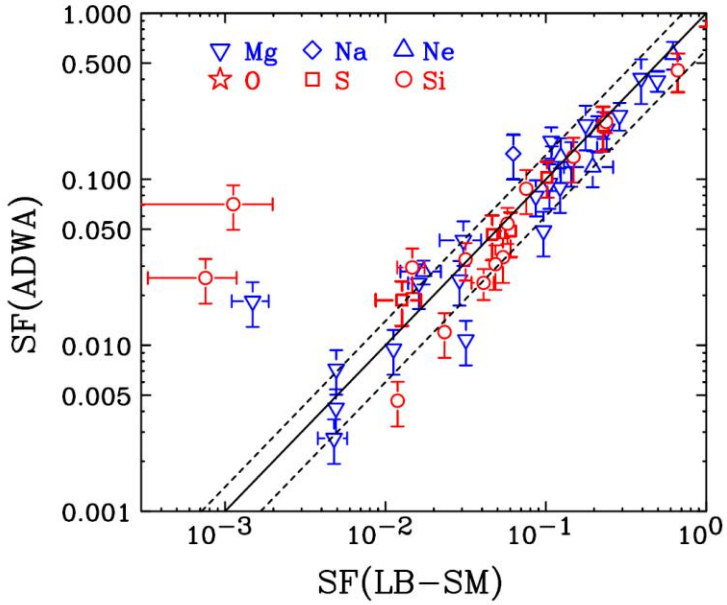

Figure 2.12: Comparison of experimental excited states spectroscopic factors, SF(ADWA), to predictions from large-basis shell-model calculations, SF(LBSM), using the USDA and USDB interactions. The ends of the horizontal error bars indicate the range of values predicted by USDA and USDB interactions. Symbols indicate the averaged values. The solid line represents perfect agreement between data and theory. The dashed lines correspond to ±40% deviations (expected experimental uncertainties) from the solid line.

2.4.1.2.2 Ca,Ti and Cr isotopes

Beyond the sd shell nuclei, regions of interest will be around the N=20, 28 and Z=20, 28 magic shell closures. The ground states of Ca isotopes are good single-particle states with doubly magic cores. Spectroscopic factor predictions by both the Independent Particle Model and by the fp shell LB-SM are nearly the same and agree with the experimental

values to within 20% as shown in Figure.2.13. Figure 2.13 compares excited states neutron spectroscopic factors for ^{41,43,45,47,49}Ca, ^{47,49,51}Ti and ^{51,53,55} Cr isotopes. Most of the values lie within the experimental uncertainties of 40% indicated by the deviations of the dashed lines from the solid line. On the other hand, the calculated and measured SFs near the boundaries of the *fp* shell-model space can disagree by factors of hundreds. The largest discrepancies when using the modern GXPF1A interaction [Hon04, Hon05] occur for the 2.462 MeV ($p_{3/2}$) and 6.870 MeV ($f_{5/2}$) states in ^{41}Ca, the 2.944 MeV ($p_{3/2}$) state in ^{43}Ca and the 4.312 MeV ($p_{1/2}$) and 4.468 MeV ($p_{1/2}$) states in ^{45}Ca, most of which have theoretical predicted spectroscopic factors near unity. Due to proximity of these nuclei to the sd shell, their excited state wave functions have strong contributions from particle-hole excitations that have hole in the sd shell. These lie outside the *fp* model space [Hon02]. It is rather difficult at the present time to include hole excitations of the sd shell core due to the huge model space that would require reliable effective interactions for the larger $sd \otimes fp$ shell Hilbert space. In contrast, the excited states of mid-shell nuclei, such as Ti and Cr, where the contribution of the hole excitations of the sd shell core is relatively smaller, do not have this problem and are consequently better described by the shell model. The experimental and predicted SF values are listed in Table 2.5.

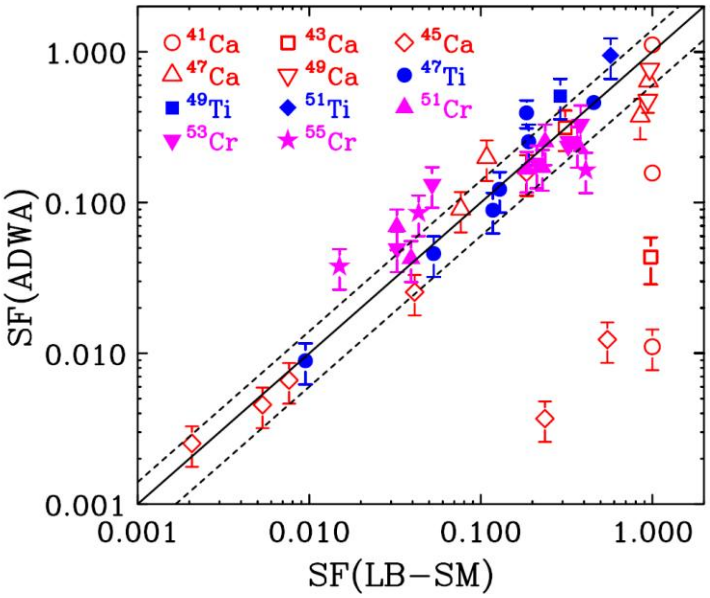

Figure 2.13: Comparison of experimental spectroscopic factors, SF(ADWA), to predictions from large-basis shell-model for the Ca, Ti and Cr isotopes, SF(LB-SM). Complete basis with the interaction GXPF1A is used in the theoretical calculations. The solid line indicates perfect agreement between data and predictions. Dashed lines represent ±40% deviations from the solid line.

2.4.1.2.3 Ni isotopes

The shell structure of the unstable doubly magic nucleus ^{56}Ni (N=Z=28) has attracted much attention recently [Yur04, Yur05, Ber09, Min06, Kra94]. In most shell model calculations, the N=28 core in ^{48}Ca is assumed to be a well-established closed shell. However, Relativistic Hartree+Bogoliubov calculations predict a strong suppression of the N=28 shell gap for neutron rich nuclei [Lal99]. While experimental investigations of the 2^+ energies of ^{36,38,40}Si provide evidence for the weakening of the N=28 shell gap in nuclei with large neutron excess [Cam06], the evidence is inconclusive for the case of ^{47}Ar [Gau06, Sig07]. Recent measurements of the nuclear magnetic moment of the

ground state of ^{57}Cu, which could be viewed as a valence proton outside a closed ^{56}Ni core, suggests significant breaking of the $f_{7/2}$ shell [Min06]. To further explore the property of the single particle states outside ^{56}Ni, we extracted the neutron spectroscopic factors for ^{57}Ni to ^{65}Ni isotopes and the values are listed in Table 2.6. The extracted spectroscopic factors are important bench marks in evaluating different *pf*-shell model interactions that are used to predict the structure of Ni or Cu nuclei, particularly the ^{78}Ni which is a major waiting point in the path of the r-process [Kra93]. Isotopes around ^{56}Ni are of special importance for the stellar evolution and electron capture in supernovae.

Shell model calculations for Ni isotopes have been available since 1960's. In the early calculations, such as ref. [Aue67], ^{56}Ni is assumed to be an inert core and the influence of core excitation was taken into account in the effective residual interaction between the valence nucleons in the pf-shell. With advances in computational capability, many new effective interactions, which are the key elements for successful predictions, have been proposed. The GXPF1A interaction, a modified version of GXPF1 with five matrix elements, involving mostly the $p_{1/2}$ orbitals, has been obtained by adjusting the parameters used in the interaction to the experimental data [Hon02]. Another interaction KB3 [Pov01, Cau05] has also been used to predict properties in the pf shell nuclei. Both of these calculations require full pf model space with ^{40}Ca as inert core. Recently, a new T=1 effective interaction for the $f_{5/2}$, $p_{3/2}$, $p_{1/2}$, $g_{9/2}$ model space has been obtained for the ^{56}Ni-^{78}Ni region by fitting the experimental data of Ni isotopes from A=57 to A=78 and N=50 isotones for ^{89}Cu to ^{100}Sn [Lis04]. This interaction provides an improved

Hamiltonian for Z=28 with a large model space and new Hamiltonian for N=50. It has been mainly used to describe heavier Ni isotopes using a ^{56}Ni core. Following the convention established in ref [Ver07], this new interaction is called JJ4PNA in the present work.

To demonstrate the sensitivity of the spectroscopic factors to interactions used in the shell model calculations. We first obtained the ground state neutron spectroscopic factors with the Auerbach interactions [Aue67] and JJ4PNA interactions with ^{56}Ni inert core [Lis04] using Oxbash code [Bro04]. For calculations with GXPF1A and KB3 interactions with ^{40}Ca inert core, we use the m-scheme code Antoine [Cau99]. The latter calculations are CPU intensive. The comparison of the ground-state spectroscopic factors between experiments and calculations are shown in Figure 2.14 The solid lines are the least square fits of the linear correlations between data and predictions. The slopes of the lines are labeled inside each panel. The predicted spectroscopic factors using the KB3, JJ4PNA, and Auerbach interactions are about 25% larger than the experimental values. The results using the full pf model space and the GXPF1A interaction, shown in the upper left panel of Figure 2.14, give better agreement with the data as indicated by the slope (0.93±0.06) of the solid line in the upper left panel. This is consistent with the observation that with the improved modification in the monopole and pairing matrix elements of the Hamiltonian, the GXPF1A interaction is better than KB3 for the lighter isotopes around ^{56}Ni [Hon05, Hor06]. This overall agreement with the results from GXPF1A interaction is consistent with the trends established in nuclei with Z=3-24 as shown in section 2.4.1.1.

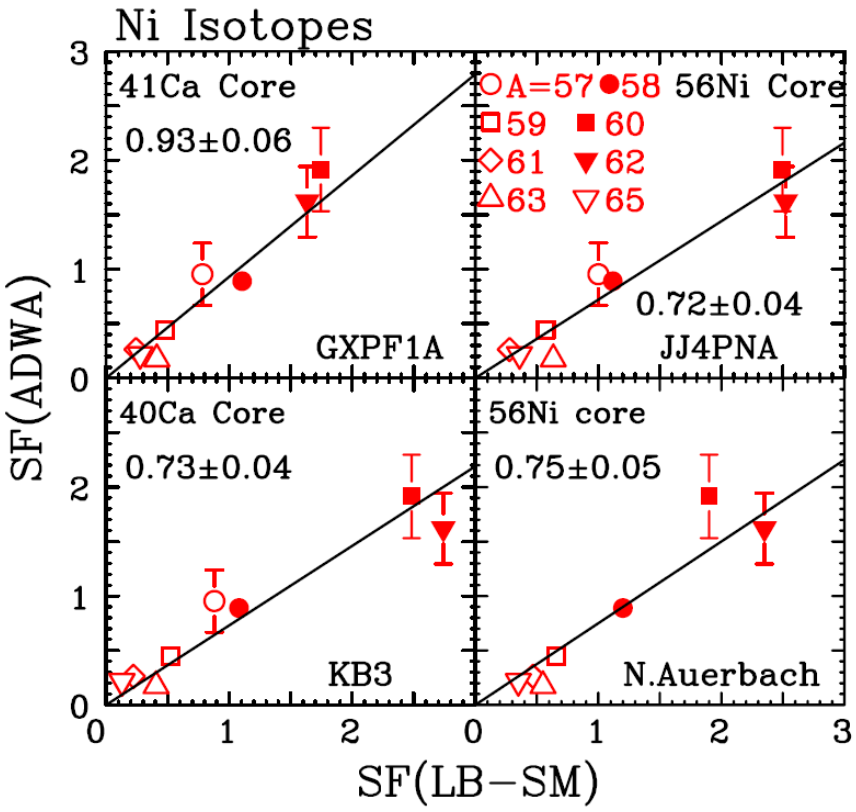

Figure 2.14: Left panels: Comparison of the ground-state experimental SF(ADWA) values and the shell model calculations using GXPF1A (top) and KB3 (bottom) interactions in full in *gfp* model space . Right panels: Same, but with the shell model calculations using JJ4PNA (top) and N. Auerbach (bottom) based on ^{56}Ni inert core. The solid lines are the linear fits with y-intercept fixed at zero. The slopes of the lines are listed in the individual panels.

Figure 2.15 shows comparisons of predictions using the GXPF1A interaction (left panel) and the XT interaction (right panel) to experimental values of the excited states in Ni isotopes. The current analysis yields spectroscopic factors that cluster around the large-basis shell-model predictions. Due to difficulties in identifying states at higher excitation energy, only SF values for a few states less than 3 MeV are obtained from calculations using the GXPF1A interaction. More states from calculations using the XT interaction are compared to data as shown in the right panel. The data and the predictions

agree to within a factor of two. The scatter in the calculated values is large compared to experimental uncertainties, which are estimated to be around 40% as indicated by the dashed lines above and below the solid line. For small calculated SF values of less than 0.01, two of the data points (the 4.709 MeV, $9/2^+$ state in ^{59}Ni and the 2.124 MeV, $1/2^-$ state in ^{61}Ni) deviate from the systematics in the right panel. Unfortunately, there are not enough data to draw a firm conclusion on the reliability of small calculated SF values from calculations with the XT interaction in the Ni isotopes. Calculations for Ni isotopes with GXPF1A in complete *fp* model basis were performed by M. Horoi.

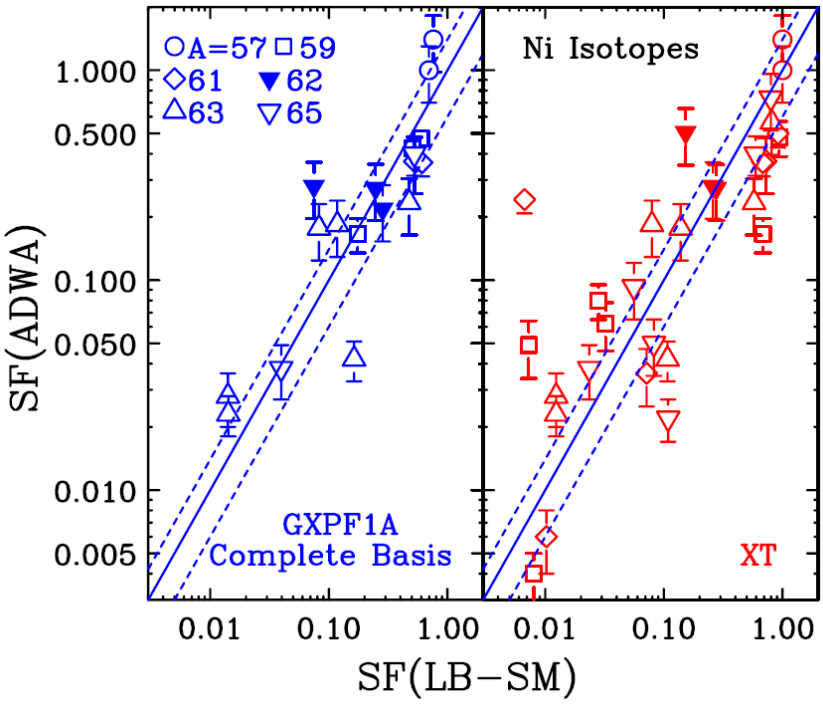

Figure 2.15: Comparison of the experimental SF values, SF(ADWA) and the shell-model calculations with the GXPF1A interaction in the pf model space (left panel) and the XT interaction in gfp model space (right panel). The solid line indicates perfect agreement between data and predictions. Dashed lines represent ±40% deviations from the solid line.

The predictions from the JJ4PNA interaction with ^{56}Ni core [Lis04], using Oxbash code [Bro04], as well as predictions from the GXPF1A interaction with ^{40}Ca core using the Antoine code [Cau99] are listed in Table 2.7. All the states in *fp*-shell have the same parity assignments ("-" for odd and "+" for even nuclei). In both calculations, the number of states, which have corresponding matched states in the shell model calculations, decreases with energy of the levels. For these reasons, a large number of experimental states have no counterparts in the shell model predictions and Table 2.7 lists 43 levels as compared to 177 experimental levels listed in Table 2.6.

More insights regarding the residual interactions may be obtained by combining the spectroscopic factors with energy level information. Each panel in Figure 2.16 compares the experimental energy levels and SF values to corresponding values obtained from shell model calculations for one isotope using the GXPF1A and JJ4PNA interaction. The lengths of the horizontal bars represent the values of the spectroscopic factors. As described earlier, very few states above 2 MeV have been obtained in the full pf model space using GXPF1A interaction. Figure 2.16 only show states with energy levels up to 2 MeV of ^{57,59,61,62,63,65}Ni nuclei. In the upper left panel of Figure 2.16, only three states have been measured for ^{57}Ni. The description of the data by both calculations is quite reasonable. In ^{61}Ni, the ordering of the states is not reproduced by calculations using either one of the two interactions. In general, shell model calculations tend to predict larger spectroscopic factors for the low-lying states, thus assigning larger single particle characteristics to these states. Due to the limitation of the model space, no $g_{9/2}$

states (dashed lines in ^{63}Ni and ^{65}Ni nuclei) are predicted by calculations using the GXPF1A interactions

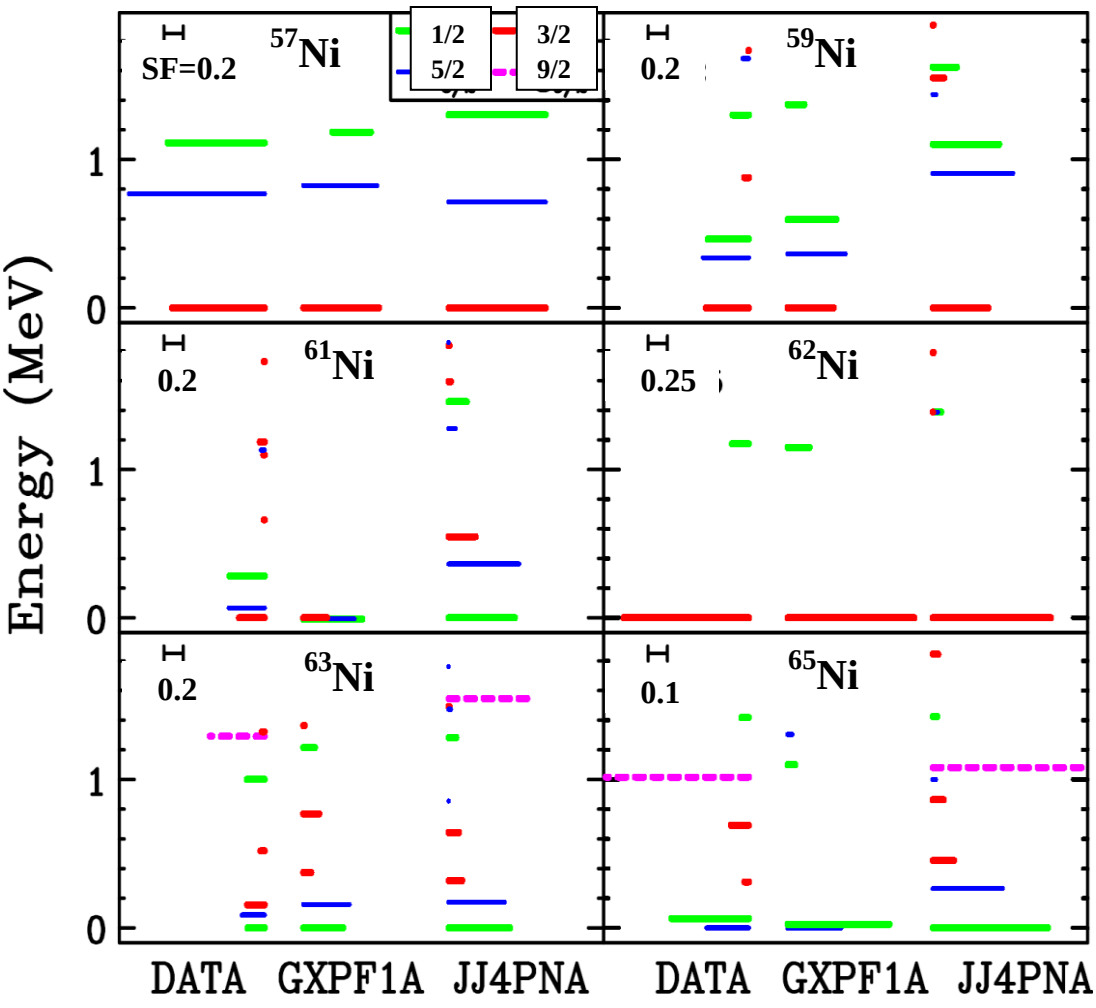

Fig. 2.16: Left panels: Plot of energy levels below 2 MeV for ^{57,61,63}Ni nuclei with the length of the horizontal bars representing the values of the spectroscopic factors. Right panels: Same as left panels, but for ^{59,62,65}Ni nuclei. The scale of the SF factor is given in the upper left corner of each panel.

2.4.2 Comparison with Endt's "best values"

In 1977, Endt compiled a list of the "best" spectroscopic factor values for A=21-44 isotopes. Most of them are sd-shell nuclei [End77]. For the neutron spectroscopic factors, Endt compiled the published spectroscopic factors from (d,t), (p,d), (^3He,α) and

(*d*,*p*) reactions. An uncertainty of 25% is assigned to the values. (When only the (*p*,*d*) and (*d*,*p*) reactions are studied, Endt assigned 50% uncertainties.) Endt's best values for ground-state SFs are listed in Table 2.3. Figure 2.17 compares the ground-state spectroscopic factors determined by Endt and the ground-state SF(ADWA) for Z=3-24. There are strong correlations between the two procedures even though the values scatter around the dashed line, which indicates perfect agreement. From the consistency check with (*p*,*d*) and (*d*,*p*) reactions, we expect that our values should have smaller random uncertainties because a systematic approach is used to extract the SF values directly from the measured angular distributions while Endt's compilation depended on the analysis by different authors and relied on the communication with the authors concerning the normalizations of the spectroscopic factors. We also have the advantage that many more measurements are included in our work than those that were available for Endt's compilations. The comparison of excited-state SFs between Endt's values with 25% error bars and SF(ADWA) for sd-shell nuclei is plotted in Figure 2.18. Endt's excited-state SFs appear to be larger than the SF(ADWA). More than a factor of 10 difference between Endt's values and some small SF(ADWA) less than 0.1 are found Endt's values for excited-state SFs are listed in Table 2.4.

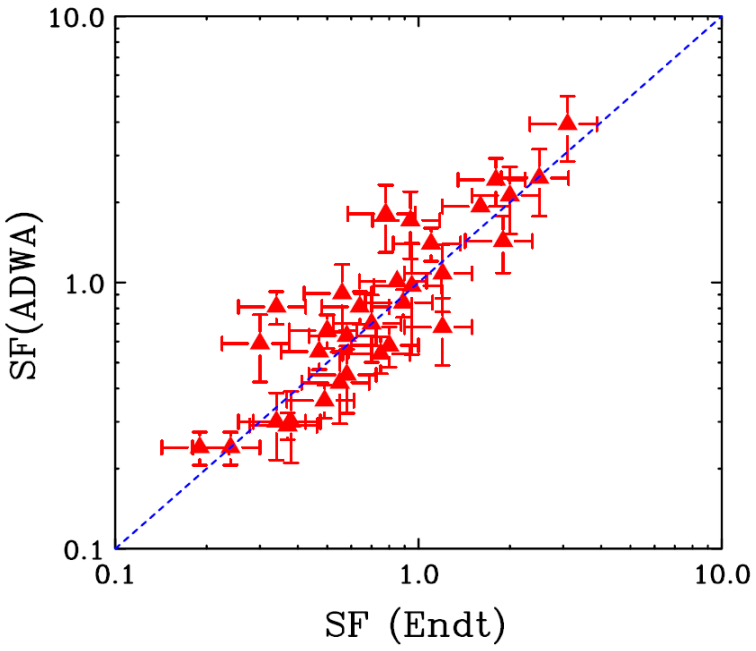

Figure 2.17: Comparisons of the ground-state spectroscopic factors obtained from this work SF(ADWA) and the compiled values of Endt [End77]. All the values are listed in Table 2.3. The line indicates perfect agreement between our values and Endt's compilation.

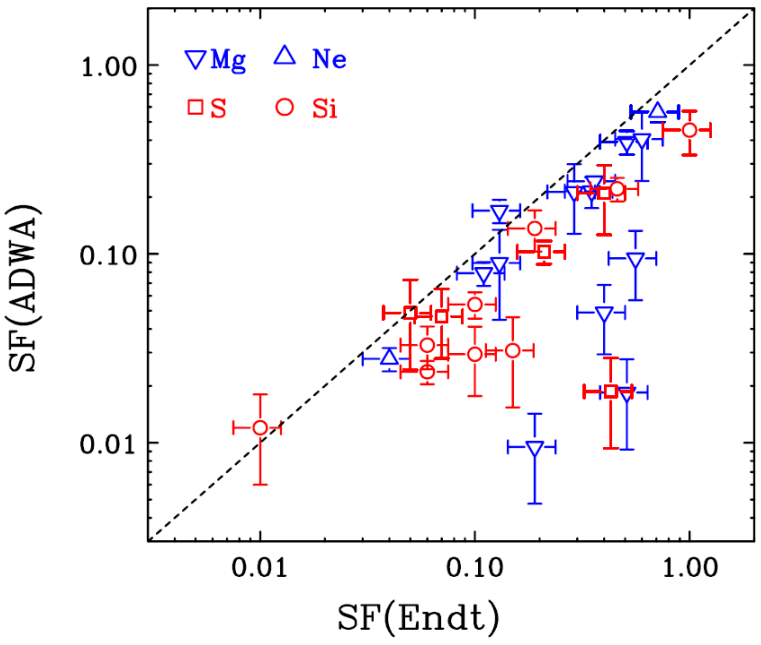

Figure 2.18: Comparisons of the excited-state spectroscopic factors obtained from this work SF(ADWA) and the compiled values of Endt [End77]. The line indicates perfect agreement between our values and Endt's compilation. All the values are listed in Table 2.4.

2.4.3 Comparison with ENDSF

From the published angular distributions, which are of reasonable quality, we extracted 177 spectroscopic factors, SF(ADWA), for the Ni isotopes as discussed in sub-section 2.2.4.2.3 [Lee09]. These values are listed in Table 2.6. When available, spectroscopic factors from the Evaluated Nuclear Structure Data File (ENSDF) compiled by the National Nuclear Data Center (NNDC) [ENDSF] are also listed in Table 2.6 in the last column. Unlike Endt's best values which have been evaluated by Endt, SF(ENSDF) values are taken directly from the published values, which came from different experiments and might be analyzed differently using different optical potentials and different reaction models. As a result, these SF values may not be consistent with each other or with the results from the present work. Figure. 2.19 compares the spectroscopic factors obtained in this work, SF(ADWA), (y-ordinate) to those listed in ENDSF (x-abscissa). The solid line indicates perfect agreement. Most of the ENDSF values are about 30% larger than the values obtained in the present work. (The spectroscopic factors for the data set ^{61}Ni(d,p)^{62}Ni are not included in the comparison because of the discrepancies between the ENSDF and the values published in ref [ENDSF]. The second set of ENDSF values obtained from reference [Ful63] for the same reaction does not have published angular distributions in the paper.

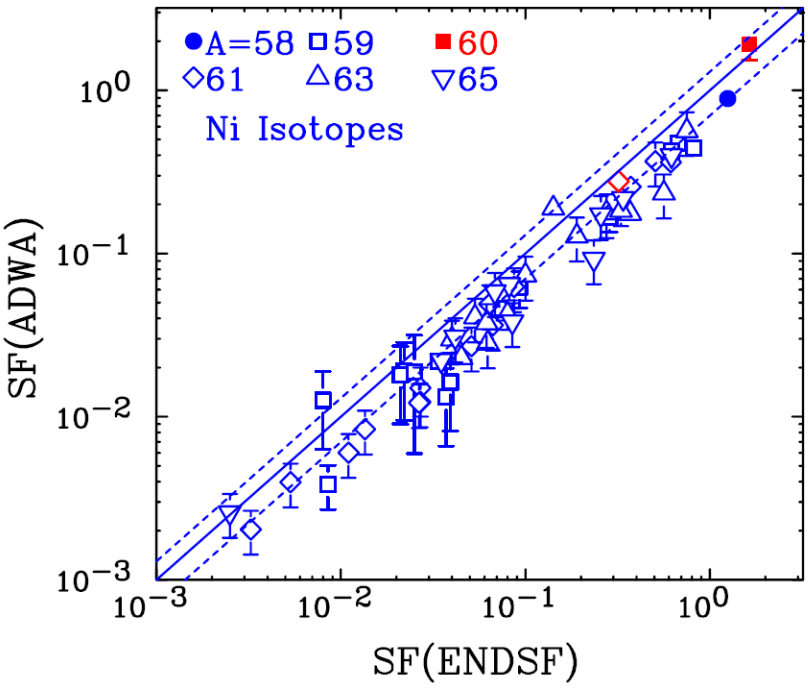

Figure 2.19: Comparison of the extracted SF(ADWA) values in the present work and the compiled values in ENDSF [ENDSF]. The solid line indicates perfect agreement and dashed lines represent ±30% of solid line.

2.5 Reduced SF values with JLM optical model potential

A recent analysis of (*e, e'p*) reactions suggests that proton SF values deduced from nuclei near closed shells, including ^{40}Ca, are suppressed by about 30–40% compared to the independent particle model (IPM) expectations [Kra01]. This suppression has been attributed, in different proportions, to short- and medium-range (tensor) nucleon-nucleon correlation effects and to longer range correlations arising from couplings, by nucleons near the Fermi surface, to collective degrees of freedom.

Historically, conventional distorted wave Born approximation (DWBA) transfer reaction analysis has shown little need for such a systematic suppression of single-

particle strength [End03, Tsa05]. Marked differences in proton SFs extracted from the (*e, e'p*) and (*d,*^{3}*He*) proton transfer reaction analyses were reconciled by a reanalysis of the (*d,*^{3}*He*) data [Kra01], requiring significant changes to the (DWBA) (*d,*^{3}*He*) calculations used there. These included fine-tuning of the root mean squared (rms) radii of the active proton single-particle orbitals to be consistent with the (*e, e'p*) data analysis. The optical model potentials for deuteron and ^{3}He were obtained from the elastic scattering measurements [Kra01, Ban85].

In this section we assess related effects in (*d,p*) and (*p,d*) ground-state neutron transfer reactions by constraining the geometry of the nucleon optical interactions with the target and the transferred neutron orbital rms radii using modern Hartree-Fock (HF) calculations [Bro98]. In this way we not only reduce long-standing parameter ambiguities but also introduce into the transfer reaction description the systematic behavior manifested by the HF calculations across extended mass regions [Bro00, Bro01-2, Ric03]. This agreement between the systematics of the HF predictions and a range of nuclear size parameters suggests that the theory should also provide a good description of the spatial extent of individual single-particle states.

We thus propose the following consistent three-body analysis with HF theoretical input for ground-state-to-ground-state neutron transfer reactions. The analysis would be the same as the framework we discussed in sub-section 2.2.1, except different global optical model potential and transferred neutron orbital rms radii are used. The key inputs of the approach are that we calculate the transfer reaction amplitudes using the Johnson-Soper adiabatic approximation [Joh70] and adopt the JLM nuclear matter effective nucleon-nucleon interaction [Jeu77] rather than CH89 phenomenological nucleon-target

interactions [Var91]. The remaining critical ingredient is the geometry of the potential used to generate the neutron overlap function. Basically, we fix the diffuseness parameter at a_0 = 0.65 fm, to which the calculations are only weakly sensitive. We then adjust the radius parameter r_0 for each reaction to reproduce the rms radius of the relevant transferred neutron orbital, as given by the HF calculation. More precisely, r_0 is adjusted so that the mean squared radius of the transferred neutron orbital is $\langle r^2 \rangle = [A/(A-1)]\langle r^2 \rangle_{HF}$, where $\langle r^2 \rangle_{HF}$ is the HF calculation value. This adjustment is carried out using the HF separation energy. The small mass correction factor corrects the fixed potential center assumption used in the HF approach. For the binding potential choices, the depths of the central potential wells are adjusted to reproduce the experimental separation energies to ensure the correct asymptotic form of the overlap functions. A spin-orbit potential of strength 6 MeV, with the same (central) geometry parameters, r_0 and a_0, was included.

Before we examine a broader range of targets, we first focus on available data for the $^{40-45,47-49}$Ca isotopes. Since ^{40}Ca is doubly magic, with closed proton and neutron *sd* shells, the additional neutrons in $^{41-48}$Ca fill the $f_{7/2}$ orbit. These valence neutron wave functions in the Ca isotopes are expected to have good single-particle property. Indeed, the predicted SF values from large-basis shell-model (LB-SM) calculations, which include configuration mixing, and the IPM, which neglects such effects, are essentially equal in the calcium isotopes. Figure 2.20 shows the ratios of the extracted SFs to these SF(IPM) as a function of mass number *A*. The solid stars in Figure 2.20 represent the ratios SF(JLM+HF)/ SF(IPM) for the calcium isotopes. These SF(JLM+HF) are the new

results of our constrained analysis, using the HF-inspired neutron binding potential geometries and the JLM nucleon optical potentials obtained using the HF densities of the targets. We observe an overall reduction in the SF(JLM+HF) compared to the IPM values of about 25%–30%. The additional data point for A = 40 (open circle) is the proton SF value, 0.645(50), as deduced from the (e,e'p) analysis of Ref. [Kra01]. Within the assigned experimental uncertainties, the neutron SF(JLM+HF) and the proton SF(e, e'p) for ^{40}Ca agree. For comparison, we also plot the SF values from the conventional adiabatic three-body model reaction analysis using the CH89 global potential and the standard binding potential geometry of r_0=1.25 fm. The open stars in Figure 2.20 show the corresponding SF ratios, SF(ADWA)/SF(IPM). The ratios for these latter calculations are close to unity within experimental uncertainties, although three odd-A isotopes, ^{43}Ca, ^{45}Ca, and ^{49}Ca, are somewhat suppressed. The suppression for ^{49}Ca may be traced to a sharp increase in the rms radius of the $2p_{3/2}$ orbit in ^{49}Ca (4.59 fm), compared to that of the $1f_{7/2}$ orbit (3.99 fm) in neighboring ^{48}Ca, when using the standard geometry. However, this explanation cannot address the reduction in the SFs for the ^{43}Ca and ^{45}Ca nuclei. The deduced SF(JLM+HF) are consistently reduced compared to the SF(CH89). The reduction of the SF(JLM+HF) values comes from both the changes of optical potential and the use of more realistic (larger) neutron bound-state wave functions. On average, the use of the JLM potential folded with nucleon densities calculated with Skyrme SkX HF instead of the CH89 global potential results in reduction of the SF values by 15%. Similar effects were observed in ref. [Liu05]. The rms radii of the neutron bound-state wave functions based on the Skyrme SkX HF predictions are also, on

average, about 2% larger than the rms radii of 1.25 fm. This results in further reduction of the SF values by about 15% [Lee06]. The observed suppression is thus a manifestation of both effects. As was stated earlier, we believe that these changes, constrained by the same (HF) theoretical systematics, will better determine the all-important overlap of the distorted waves and bound-state wave functions at the nuclear surface.

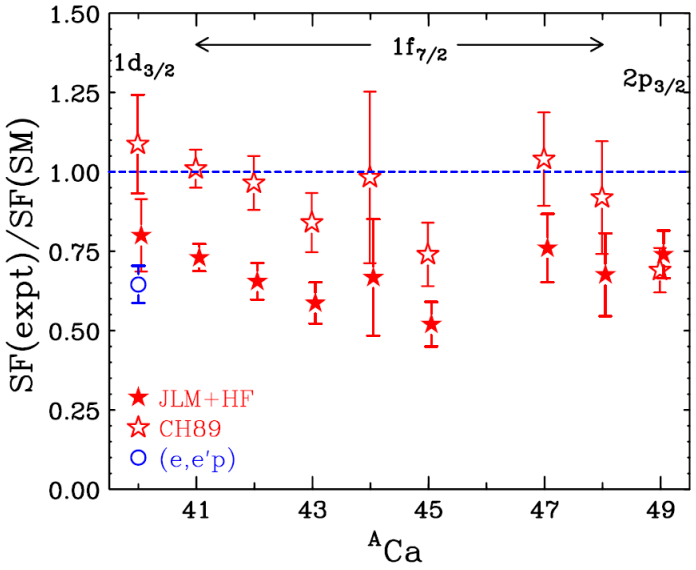

Figure 2.20: Ratios of the experimentally deduced spectroscopic factors to those of the independent particle shell-model SF(IPM) for the calcium isotopic chain. The open symbols, from SF(CH89), result from the use of conventional, three-body adiabatic model calculations using the CH89 global nucleon optical potentials and a fixed neutron bound-state geometry of 1.25 fm. The solid symbols, from SF(JLM+HF), are the results of constrained three body model calculations, where both the nucleon optical potentials (the JLM microscopic optical model) and the neutron bound-state potential geometry are determined by the Skyrme (SkX) HF calculations of Ref. [Bro98].

The Ca isotope SF(CH89) values are included in the large-scale survey of 80 nuclei, studied via (*p*,*d*) and (*d*,*p*) transfer reactions discussed in sub-section 2.4.1.1. In the survey, it was shown that within experimental and theoretical uncertainties, most extracted SF(CH89) values, like those for the Ca isotopes, agreed with the predictions of

the LB-SM. To examine whether or not the reductions in the deduced SF(JLM+HF) are limited to the calcium isotopes, we have applied the same HF-constrained analysis to a selection of the 80 nuclei. As the HF is less appropriate for the description of single-particle configurations of very light systems, we limit the analysis to $A > 11$. Additionally, beyond the calcium isotopes, the IPM does not take proper account of configuration mixing effects, so we now compare the extracted SF(JLM+HF) to large-basis shell-model SF(LB-SM) predictions, which are calculated with the code OXBASH [Bro04]. These ratios are listed in Table 2.8 and shown in Figure 2.21 as a function of the difference between the neutron and proton separation energies (ΔS). The physics implication of using ΔS is discussed in Section 2.8. For clarity, only those points with an overall uncertainty of less than 25% are included. Data with uncertainties much larger than 20% (the random error assigned to each measurement) have quality-control problems in the evaluation. In such cases, there is either no second measurement to corroborate the validity of a data set or the standard deviations of the measurements used to extract the SF values are larger than 25%. For the (statistically most significant) cases presented, we note once again an overall SF(JLM+HF) reduction of order 30% compared to the SF(CH89), but with significant residual fluctuations between the values for different nuclei.

In principle, like other optical potentials based on the microscopic folding model, JLM approach should be more appropriate than the global optical potential such as CH89 to extract structural information, since such formulation of the optical potential is more fundamental and possesses no free parameters. More importantly, the JLM microscopic model adopts the nuclear density and an effective nucleon-nucleon interaction. However,

we found that JLM parameterizations display discontinuity in the calculated cross sections and give energy dependence in the SF determinations for some reactions in the energy region of ~10-50 MeV. Bauge et al located the discontinuity at 10 MeV in the imaginary part of JLM parameterizations, which consequently yields a discontinuity of the volume integral [Bau96]. Using the refitted JLM parameterizations from Bauge et al., some significant discontinuities in the cross section calculations can be removed, however, we still obtain instabilities in the energy dependence which is not completely understood. Due to these limitations and the difficulties in calculating the nuclear densities for nuclei at excited states, we have not extended similar transfer reaction studies using JLM parameterization to extract excited-state SFs.

2.6 Asymmetry dependence of reduction factors for stable nuclei in transfer reactions

Figure 2.21 plots the reduction factor, which is the ratio of experimental SF to LB-SM predictions, as a function of the difference between the neutron and proton separation energies ΔS ($\Delta S = Sn - Sp$ for neutron SF and $\Delta S = Sp - Sn$ for proton SF), where ΔS characterizes the asymmetry dependence of relative shifts for neutron and proton Fermi surfaces. For the nuclei investigated using transfer reaction based on the systematic approach discussed above, there is no evident asymmetry dependence of the observed reduction factors on ΔS. Limiting the observations to the calcium isotopes (the solid stars in Figure 2.20), which span neutron-proton separation energy differences from –11.3 MeV (^{49}Ca) to 7.3 MeV (^{40}Ca), one draws the same conclusion. The open circles in Figure 2.21 are the corresponding ratios of the proton ground state SF for ^{7}Li, ^{12}C, ^{16}O,

^{30}Si, ^{31}P, ^{40}Ca, ^{48}Ca, ^{51}V, ^{90}Zr, and ^{208}Pb (as listed in Table 2.8), studied with the (*e*, *e*'*p*) reaction [Kra01, Wes92]. Similarly, the solid triangles show the ratios of the deduced SF to SF(LB-SM) values from both exclusive and inclusive studies of intermediate-energy nucleon knockout reactions. Neutron (proton) knockout values are shown as inverted (upright) triangles (and listed in Table 2.8). These include, at the extremes of the $|S_n - S_p|$ scale, ^{15}C [Ter04], ^{22}O [Gad04-1], ^{34}Ar [Gad04-2], and ^{32}Ar [Gad04-1], whereas the values for ^{8}B, ^{9}C [End03], ^{46}Ar [Gad05], ^{12}C, and ^{16}O [Bro02] overlap the ΔS values of both the transfer and the (*e*, *e*'*p*) analyses. In the case of the inclusive knockout reaction analysis of Ref. [Bro02], effective neutron and proton removal energies, obtained by weighing the physical separation energies to each final state by the corresponding cross-sections, were used. The suppression with respect to the SF(LB-SM) is similar for the three different reactions within the ΔS region in which they overlap. A dependence of the suppression on ΔS is indicated by the nucleon-knockout data that extend the data set into regions of significant neutron and proton asymmetry. However, SFs from past transfer data focus on stable nuclei and the large systematic uncertainties from different experiments reduce the sensitivity in determining the dependence. Thus, to confirm this behavior with a transfer reaction probe, measurements over a larger range of asymmetry corresponding to a larger ΔS are needed.

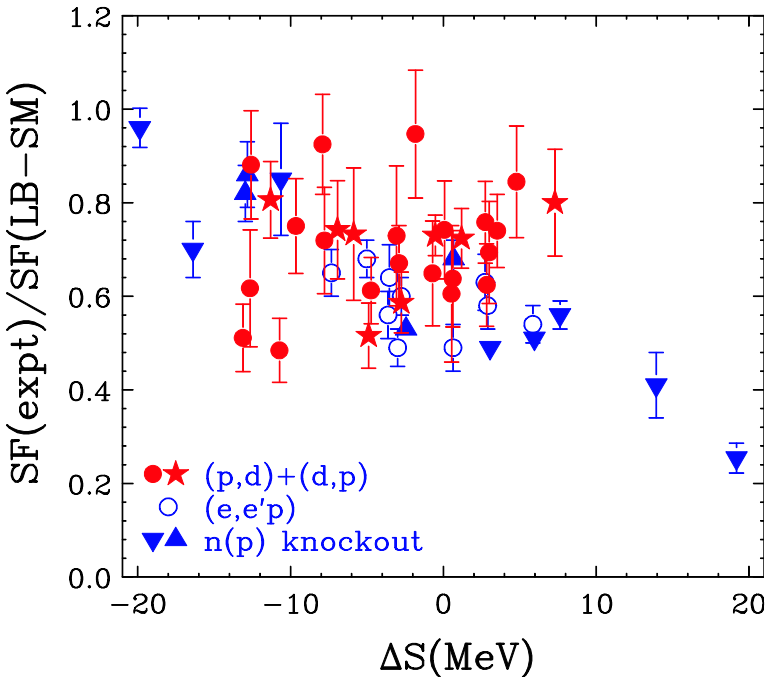

Figure 2.21: Ratios of experimentally deduced SF to those of the large-basis shell-model calculations SF(LB-SM) for nuclei with A = 12–49 as a function of the difference of neutron and proton separation energies, ΔS (see text). The solid circles and stars are the present results from transfer reactions. The solid stars represent the Ca isotopes, as in Fig. 1. The open circles are ground-state proton SF from (*e, e'p*) analysis and the triangles are the results from proton knockout reactions (with inverted triangles for neutron knockout). The data points are listed in Table 2.8 and are referenced in the text.

2.7 Applications of the established systematics in spectroscopic factors

As shown in Section 2.4, we have evaluated the accuracy for different interactions and established the systematics of SFs in different shell regions. The established systematics suggests the theoretical SFs calculated in large-basis shell-model using good interactions agree to the experimental SF deduced using CH89 approach in ADWA model to within 20-30%. The definition of experimental SF is the ratio of the experimental to calculated differential cross sections. Based on the systematics, we can predict reliable experimental cross sections using the predicted SF value and calculated cross sections in CH89 analysis. Such cross-section estimation is needed when designing (*p*,*d*) and (*d*,*p*) transfer reaction experiments.

The established systematics can be also used in confirming the spin assignment. In *sd*-shell nuclei with USDA/USDB interactions in LB-SM, for instance, we have used the established systematics between the experimental and theoretical spectroscopic factors to assign the spins of three selected states in ^{27}Mg that have no definitive spin assignments from measurements. The spins for these states listed in Table 2.9 can either be $3/2^+$ or $5/2^+$ (second column) according to NUDAT [NUDAT]. Since the measured angular distributions are sensitive to the angular momentum *l* but not very sensitive to the spin *J*, the extracted SF values (third column) are similar for different values of *J*. However, the shell-model spectroscopic factors (sixth column) for the $3/2^+$ and $5/2^+$ states within 100 keV of the 5.627 MeV state differ by more than a factor of 25. The systematics of Figure 2.13 indicates that the spins of the 5.627 MeV, 3.491 MeV and 4.150 MeV states are consistent with a $J=3/2^+$, $J=3/2^+$ and $J=5/2^+$, respectively.

Table 2.3: List of isotopes with the extracted spectroscopic factors, SF(ADWA) and other information such as the mass number (*A*), charge number (*Z*) and neutron number (*N*) for the nuclei. j^{π}, T and S_n are the spin and parity, isospin and neutron separation energy of the nuclei. For completeness, we list the root mean square radii of the neutron wave functions. Endt compiled values are also listed when available. The model space and interactions used in Oxbash [Bro04] are listed together with the predicted SF values labeled as LBSM.

B	A	Z	N	j^{π}	T	S_n	rms	Endt	SF (ADWA)	LBSM	Model Space	Interaction
^{6}Li	6	3	3	$1/2^-$	0	5.66	2.91		1.12 ± 0.32	0.68	PPN	CKPPN
^{7}Li	7	3	4	$1/2^-$	1/2	7.25	2.81		1.85 ± 0.37	0.63	PPN	CKPPN
^{8}Li	8	3	5	$1/2^-$	1	2.03	3.66		0.62 ± 0.18	1.09	PPN	CKPPN
^{9}Li	9	3	6	$1/2^-$	3/2	4.06	3.23		0.98 ± 0.28	0.81	PPN	CKPPN
^{9}Be	9	4	5	$3/2^-$	1/2	1.67	3.86		0.45 ± 0.03	0.57	PPN	CKPPN
^{10}Be	10	4	6	$3/2^-$	1	6.81	2.96		1.58 ± 0.15	2.36	PPN	CKPPN
^{11}Be	11	4	7	$1/2^+$	3/2	0.50	7.11		0.51 ± 0.06	0.74	SPSDPF	WBP
^{10}B	10	5	5	$3/2^-$	0	8.44	2.85		0.50 ± 0.07	0.60	PPN	CKPPN
^{11}B	11	5	6	$3/2^-$	1/2	11.45	2.73		1.48 ± 0.19	1.09	PPN	CKPPN
^{12}B	12	5	7	$1/2^-$	1	3.37	3.46		0.45 ± 0.06	0.83	PPN	CKPPN
^{12}C	12	6	6	$3/2^-$	0	18.72	2.53		3.12 ± 0.36	2.85	PPN	CKPPN
^{13}C	13	6	7	$1/2^-$	1/2	4.95	3.26		0.75 ± 0.10	0.61	PPN	CKPPN
^{14}C	14	6	8	$1/2^-$	1	8.18	3.00		1.63 ± 0.33	1.73	PPN	CKPPN
^{15}C	15	6	9	$1/2^+$	3/2	1.22	5.51		1.12 ± 0.32	0.98	SPSDPF	WBP
^{14}N	14	7	7	$1/2^-$	0	10.55	2.87		0.77 ± 0.12	0.69	PPN	CKPPN
^{15}N	15	7	8	$1/2^-$	1/2	10.83	2.89		1.48 ± 0.24	1.46	PPN	CKPPN
^{16}N	16	7	9	$3/2^+$	1	2.49	4.26		0.42 ± 0.12	0.96	SPSDPF	WBP
^{16}O	16	8	8	$1/2^-$	0	15.66	2.74		2.46 ± 0.26	2.00	PPN	CKPPN
^{17}O	17	8	9	$5/2^+$	1/2	4.14	3.48		0.94 ± 0.13	1.00	SD	USD
^{18}O	18	8	10	$5/2^+$	1	8.04	3.24		1.66 ± 0.19	1.58	SD	USD
^{19}O	19	8	11	$5/2^+$	3/2	3.95	3.57		0.43 ± 0.06	0.69	SD	USD
^{19}F	19	9	10	$1/2^+$	1/2	10.43	2.66		1.60 ± 0.23	0.56	SD	USD
^{20}F	20	9	11	$3/2^+$	1	6.60	3.39		~0.01	0.02	SD	USD
^{21}Ne	21	10	11	$3/2^+$	1/2	6.76	3.41	0.01	0.03 ± 0.01	0.03	SD	USD
^{22}Ne	22	10	12	$3/2^+$	1	10.36	3.27	0.19	0.24 ± 0.03	0.13	SD	USD
^{23}Ne	23	10	13	$5/2^+$	3/2	5.20	3.58	0.24	0.24 ± 0.03	0.32	SD	USD
^{24}Na	24	11	13	$1/2^+$	1	8.87	3.49	0.30	0.59 ± 0.17	0.39	SD	USD
^{24}Mg	24	12	12	$3/2^+$	0	16.53	3.13		0.41 ± 0.06	0.41	SD	USD
^{25}Mg	25	12	13	$5/2^+$	1/2	7.33	3.50	0.37	0.29 ± 0.03	0.34	SD	USD
^{26}Mg	26	12	14	$5/2^+$	1	11.09	3.35	1.80	2.43 ± 0.50	2.51	SD	USD

Table 2.3 (cont'd)

B	A	Z	N	j^{π}	T	S_n	rms	Endt	SF (ADWA)	LBSM	Model Space	Interaction
^{27}Mg	27	12	15	$1/2^+$	3/2	6.44	3.90	0.58	0.45 ± 0.13	0.46	SD	USD
^{27}Al	27	13	14	$5/2^+$	1/2	13.06	3.31	1.10	1.40 ± 0.20	1.10	SD	USD
^{28}Al	28	13	15	$1/2^+$	1	7.73	3.78	0.50	0.66 ± 0.10	0.60	SD	USD
^{28}Si	28	14	14	$5/2^+$	0	17.18	3.22		4.40 ± 1.24	3.62	SD	USD
^{29}Si	29	14	15	$1/2^+$	1/2	8.47	3.73	0.55	0.42 ± 0.13	0.45	SD	USD
^{30}Si	30	14	16	$1/2^+$	1	10.61	2.87	0.89	0.84 ± 0.10	0.82	SD	USD
^{31}Si	31	14	17	$3/2^+$	3/2	6.59	3.70	0.75	0.54 ± 0.07	0.58	SD	USD
^{32}P	32	15	17	$1/2^+$	1	7.94	3.64	0.80	0.58 ± 0.10	0.60	SD	USD
^{32}S	32	16	16	$1/2^+$	0	15.04	3.40		1.51 ± 0.43	0.96	SD	USD
^{33}S	33	16	17	$3/2^+$	1/2	8.64	3.63	0.70	0.70 ± 0.20	0.61	SD	USD
^{34}S	34	16	18	$3/2^+$	1	11.42	3.53	1.90	1.43 ± 0.35	1.83	SD	USD
^{35}S	35	16	19	$3/2^+$	3/2	6.99	3.77	0.38	0.30 ± 0.09	0.36	SD	USD
^{37}S	37	16	21	$7/2^-$	5/2	4.30	4.02		0.88 ± 0.12	0.92	SDPF	SDPFNOW
^{35}Cl	35	17	18	$3/2^+$	1/2	12.64	3.51		0.35 ± 0.10	0.32	SD	USD
^{36}Cl	36	17	19	$1/2^+$	1	8.58	3.70	1.20	0.68 ± 0.19	0.77	SD	USD
^{37}Cl	37	17	20	$1/2^+$	3/2	10.31	3.64	0.95	0.97 ± 0.43	1.15	SD	USD
^{38}Cl	38	17	21	$1/2^-$	2	6.11	3.94	0.78	1.81 ± 0.51	0.95	SDPF	SDPFNOW
^{36}Ar	36	18	18	$3/2^+$	0	15.26	3.45		3.34 ± 0.89	2.06	SD	USD
^{37}Ar	37	18	19	$3/2^+$	1/2	8.79	3.71	0.49	0.36 ± 0.05	0.36	SD	USD
^{38}Ar	38	18	20	$3/2^+$	1	11.84	3.60	2.50	2.47 ± 0.70	3.04	SD	USD
^{39}Ar	39	18	21	$7/2^-$	3/2	6.60	3.94	0.64	0.81 ± 0.11	0.83	SDPF	SDPFNOW
^{40}Ar	40	18	22	$7/2^-$	2	9.87	3.83	1.20	1.08 ± 0.31	1.91	SDPF	SDPFNOW
^{41}Ar	41	18	23	$7/2^-$	5/2	6.10	4.01	0.47	0.55 ± 0.08	0.65	SDPF	SDPFNOW
^{39}K	39	19	20	$3/2^+$	1/2	13.08	3.58	2.00	2.12 ± 0.60	1.72	SD	USD
^{40}K	40	19	21	$5/2^-$	1	7.80	3.90	0.94	1.71 ± 0.48	0.98	SDPF	SDPFNOW
^{41}K	41	19	22	$5/2^-$	3/2	10.10	3.84	0.56	0.91 ± 0.26	1.06	SDPF	SDPFNOW
^{42}K	42	19	23	$1/2^-$	2	7.53	3.96	0.34	0.81 ± 0.11	0.88	SDPF	SDPFNOW
^{40}Ca	40	20	20	$3/2^+$	0	15.64	3.81		4.35 ± 0.62	4.00	SD	USD
^{41}Ca	41	20	21	$7/2^-$	1/2	8.36	3.90	0.85	1.01 ± 0.06	1.00	FPPN	FPBPPN
^{42}Ca	42	20	22	$7/2^-$	1	11.48	3.82	1.60	1.93 ± 0.17	1.81	FPPN	FPBPPN
^{43}Ca	43	20	23	$7/2^-$	3/2	7.93	3.97	0.58	0.63 ± 0.07	0.75	FPPN	FPBPPN
^{44}Ca	44	20	24	$7/2^-$	2	11.13	3.87	3.10	3.93 ± 1.08	3.64	FPPN	FPBPPN
^{45}Ca	45	20	25	$7/2^-$	5/2	7.41	4.03		0.37 ± 0.05	0.50	FPPN	FPBPPN
^{47}Ca	47	20	27	$7/2^-$	7/2	7.28	4.08		0.26 ± 0.04	0.26	FPPN	FPBPPN
^{48}Ca	48	20	28	$7/2^-$	4	9.95	3.99		7.35 ± 1.42	7.38	FPPN	FPBPPN
^{49}Ca	49	20	29	$3/2^-$	9/2	5.15	4.59		0.69 ± 0.07	0.92	FPPN	FPBPPN

Table 2.3 (cont'd)

B	A	Z	N	j^{π}	T	S_n	rms	Endt	SF (ADWA)	LBSM	Model Space	Interaction
^{45}Sc	45	21	24	$3/2^-$	3/2	11.32	3.89	0.34	0.30 ± 0.08	0.35	FPPN	FPBPPN
^{46}Sc	46	21	25	$1/2^-$	2	8.76	4.00		0.51 ± 0.14	0.37	FPPN	FPBPPN
^{46}Ti	46	22	24	$7/2^-$	1	13.19	3.85		2.42 ± 0.34	2.58	FPPN	FPBPPN
^{47}Ti	47	22	25	$5/2^-$	3/2	8.88	4.01		0.03 ± 0.01			
^{48}Ti	48	22	26	$5/2^-$	2	11.63	3.94		0.11 ± 0.01			
^{49}Ti	49	22	27	$7/2^-$	5/2	8.14	4.08		0.25 ± 0.03			
^{50}Ti	50	22	28	$7/2^-$	3	10.94	4.00		6.36 ± 1.10			
^{51}Ti	51	22	29	$3/2^-$	7/2	6.37	4.46		1.25 ± 0.35			
^{51}V	51	23	28	$5/2^-$	5/2	11.05	4.01		1.28 ± 0.32			
^{50}Cr	50	24	26	$5/2^-$	1	13.00	3.94		0.11 ± 0.02			
^{51}Cr	51	24	27	$7/2^-$	3/2	9.26	4.08		0.30 ± 0.08			
^{52}Cr	52	24	28	$7/2^-$	2	12.04	4.00		6.24 ± 0.88			
^{53}Cr	53	24	29	$3/2^-$	5/2	7.94	4.34		0.39 ± 0.03			
^{54}Cr	54	24	30	$3/2^-$	3	9.72	4.22		0.71 ± 0.20			
^{55}Cr	55	24	31	$3/2^-$	7 /2	6.24	4.53		0.63 ± 0.13			

Table 2.4. List of neutron excited-state spectroscopic factors for the *sd*-shell nuclei. We adopt the energy levels compiled in the data base NUDAT by the National Nuclear Data Center [NNDC]. SF(ADWA) is the deduced experimental SF value with the uncertainty from the present work. SF(USDA) and SF(USDB) are the large-basis shell-model calculations using USDA and USDB interactions in SD shell respectively. <SF(LB-SM)> is the average of the SF(USDA) and SF(USDB). Endt compiled values are also listed when available.

Nucleus	Ex	l	j		SF (ADWA)	Error	SF(USDA)	SF(USDB)	<SF> (LB-SM	Endt
^{17}O	0.871	0	1/2	+	1.020	±0.194	1.000	1.000	1.000	
^{21}Ne	0.351	2	5/2	+	0.564	±0.107	0.624	0.616	0.620	0.71
	3.736	2	5/2	+	0.028	±0.005	0.022	0.012	0.017	0.04
	4.526	2	5/2	+	0.136	±0.041	0.117	0.130	0.124	
	5.550	2	3/2	+	0.118	±0.029	0.130	0.262	0.196	
	6.608	2	3/2	+	0.192	±0.047	0.219	0.199	0.209	
^{24}Na	2.563	2	5/2	+	0.142	±0.043	0.061	0.064	0.063	
^{25}Mg	0.585	0	1/2	+	0.392	±0.055	0.507	0.483	0.495	0.51
	0.975	2	3/2	+	0.215	±0.040	0.232	0.224	0.228	0.35
	1.965	2	5/2	+	0.079	±0.019	0.084	0.089	0.086	0.11

Table 2.4 (con'd)

Nucleus	Ex	l	j		SF (ADWA)	Error	SF(USDA)	SF(USDB)	<SF> (LB-SM)	Endt
	2.563	0	1/2	+	0.169	±0.036	0.102	0.114	0.108	0.13
	2.801	2	3/2	+	0.242	±0.046	0.290	0.285	0.288	0.36
	3.908	2	5/2	+	0.018	±0.006	0.002	0.001	0.001	0.51
	4.359	2	3/2	+	0.009	±0.003	0.010	0.012	0.011	0.19
	5.475	0	1/2	+	0.121	±0.036	0.104	0.114	0.109	
^{26}Mg	3.589	2	5/2	+	0.201	±0.049	0.232	0.247	0.239	
	4.972	2	5/2	+	0.043	±0.013	0.039	0.022	0.031	
^{27}Mg	0.985	2	3/2	+	0.405	±0.122	0.396	0.389	0.392	0.60
	1.699	2	5/2	+	0.089	±0.027	0.122	0.123	0.123	0.13
	3.476	0	1/2	+	0.213	±0.064	0.163	0.191	0.177	0.29
	3.491	2	3/2	+	0.049	±0.015	0.085	0.108	0.097	0.40
	3.787	2	3/2	+	0.095	±0.028	0.118	0.093	0.105	0.56
	4.150	2	5/2	+	0.025	±0.007	0.027	0.031	0.029	
	5.029	0	1/2	+	0.024	±0.007	0.018	0.014	0.016	
	5.172	2	5/2	+	0.003	±0.001	0.004	0.006	0.005	
	5.172	2	3/2	+	0.004	±0.001	0.004	0.005	0.005	
	5.627	2	3/2	+	0.129	±0.039	0.141	0.147	0.144	
	5.764	2	3/2	+	0.011	±0.003	0.033	0.030	0.032	
	5.764	2	5/2	+	0.007	±0.002	0.005	0.000	0.005	
^{29}Si	1.273	2	3/2	+	0.453	±0.119	0.679	0.651	0.665	1.00
	2.028	2	5/2	+	0.136	±0.041	0.142	0.155	0.148	0.19
	3.067	2	5/2	+	0.054	±0.013	0.057	0.058	0.058	0.10
	4.840	0	1/2	+	0.024	±0.005	0.034	0.047	0.041	0.06
	5.949	2	3/2	+	0.029	±0.009	0.012	0.018	0.015	0.10
	7.692	2	3/2	+	0.025	±0.008	0.000	0.001	0.001	
	8.290	2	5/2	+	0.071	±0.021	0.000	0.002	0.001	
^{30}Si	5.232	2	5/2	+	0.012	±0.004	0.022	0.025	0.023	0.01
^{31}Si	0.752	0	1/2	+	0.221	±0.031	0.224	0.251	0.237	0.46
	2.317	2	3/2	+	0.033	±0.008	0.028	0.035	0.032	0.06
	2.788	2	5/2	+	0.034	±0.010	0.050	0.058	0.054	
	4.259	2	3/2	+	0.031	±0.009	0.048	0.049	0.049	0.15
	4.720	0	1/2	+	0.088	±0.026	0.073	0.078	0.075	
	6.252	2	3/2	+	0.005	±0.001	0.011	0.013	0.012	
^{33}S	0.841	0	1/2	+	0.210	±0.063	0.221	0.233	0.227	0.40
	2.313	2	3/2	+	0.047	±0.014	0.043	0.050	0.046	0.07
	2.868	2	5/2	+	0.049	±0.015	0.052	0.069	0.060	0.05
^{35}S	1.573	2	1/2	+	0.103	±0.025	0.101	0.102	0.102	0.21
	2.717	2	5/2	+	0.019	±0.006	0.009	0.017	0.013	0.43

Table 2.5. List of neutron excited-state spectroscopic factors for the Ca, Ti and Cr isotopes. We adopt the energy levels compiled in the data base NUDAT by the National Nuclear Data Center [NNDC]. SF(ADWA) is the deduced experimental SF value with the uncertainty from the present work. SF(LB-SM) is the large-basis shell-model calculations using GXPF1A in *pf*-shell.

Nucleus	Ex	l	j	π	SF(ADWA)	Error	SF(LB-SM)
^{41}Ca	2.462	1	3/2	-	0.157	±0.014	1.000
	4.753	1	1/2	-	1.111	±0.157	1.000
	6.870	3	5/2	-	0.011	±0.004	1.000
^{43}Ca	2.938	1	3/2	-	0.044	±0.015	0.976
	4.239	1	1/2	-	0.314	±0.125	0.310
^{45}Ca	3.442	1	1/2	-	0.159	±0.079	0.185
	4.312	1	1/2	-	0.004	±0.001	0.237
	4.468	1	1/2	-	0.012	±0.005	0.547
	4.885	3	5/2	-	0.007	±0.003	0.008
	5.373	1	3/2	-	0.003	±0.001	0.002
	5.440	1	3/2	-	0.005	±0.002	0.005
	5.764	3	5/2	-	0.025	±0.010	0.041
^{47}Ca	2.014	1	3/2	-	0.640	±0.090	0.949
	2.875	1	1/2	-	0.199	±0.079	0.108
	4.058	1	1/2	-	0.374	±0.150	0.850
	4.785	3	5/2	-	0.090	±0.045	0.076
^{49}Ca	2.023	1	1/2	-	0.766	±0.108	0.966
	3.991	3	5/2	-	0.478	±0.085	0.942
^{47}Ti	1.550	1	3/2	-	0.393	±0.083	0.185
	1.794	1	1/2	-	0.122	±0.049	0.129
	2.163	3	5/2	-	0.009	±0.004	0.010
	2.548	1	3/2	-	0.046	±0.018	0.053
	2.600	3	7/2	-	0.253	±0.101	0.190
	2.839	3	5/2	-	0.089	±0.036	0.118
^{49}Ti	1.380	1	3/2	-	0.510	±0.204	0.291
^{51}Ti	1.167	1	1/2	-	0.945	±0.378	0.571
^{51}Cr	0.749	1	3/2	-	0.243	±0.097	0.365
	0.777	1	1/2	-	0.253	±0.101	0.237
	1.353	3	5/2	-	0.171	±0.068	0.228
	1.557	3	7/2	-	0.069	±0.028	0.032
	3.056	1	1/2	-	0.043	±0.017	0.039
	4.040	1	1/2	-	0.166	±0.067	0.185

Table 2.5 (cont'd)

Nucleus	Ex	l	j	π	SF(ADWA)	Error	SF(LB-SM)
^{53}Cr	0.564	1	1/2	-	0.330	±0.110	0.382
	1.006	3	5/2	-	0.237	±0.031	0.324
	1.290	3	7/2	-	0.049	±0.025	0.033
	2.321	1	3/2	-	0.182	±0.057	0.212
	2.723	1	1/2	-	0.132	±0.053	0.052
	3.617	1	1/2	-	0.254	±0.036	0.326
^{55}Cr	0.518	3	5/2	-	0.164	±0.066	0.409
	1.215	3	5/2	-	0.038	±0.019	0.015
	2.008	3	5/2	-	0.086	±0.034	0.043

Table 2.6. List of neutron spectroscopic factors for the Ni isotopes. We adopt the energy levels compiled in the data base NUDAT by the National Nuclear Data Center [NNDC]. SF(ADWA) are SF values from the present work and SF(ENDSF) values are obtained from ENDSF data base [ENDSF]. Spin value, J, enclosed in "( )" represents state with uncertain J value and the symbol "*" represents doublet state. State with undetermined parity (π) is labeled "*N*".

Nucleus	Ex (MeV)	l	J	π	SF(ADWA)	Error	SF(ENDSF)
^{57}Ni	0.000	1	3/2	-	0.954	±0.286	
	0.769	3	5/2	-	1.400	±0.420	
	1.113	1	1/2	-	1.000	±0.300	
^{58}Ni	0.000	1	0	+	0.890	±0.087	1.250
^{59}Ni	0.000	1	3/2	-	0.444	±0.045	0.816
	0.339	3	5/2	-	0.472	±0.059	0.677
	0.465	1	1/2	-	0.424	±0.060	0.620
	0.878	1	3/2	-	0.046	±0.006	0.072
	1.301	1	1/2	-	0.166	±0.031	0.286
	1.680	3	5/2	-	0.062	±0.016	0.093
	1.735	1	3/2	-	0.004	±0.001	0.009
	1.948	3	7/2	-	0.013	±0.007	0.037
	2.415	1	3/2	-	0.013	±0.006	0.008
	2.627	3	7/2	-	0.016	±0.008	0.039
	2.640	1	(1/2)	-	0.022	±0.007	
	2.640	1	(3/2)	-	0.011	±0.003	
	2.681	3	(5/2)	-	0.019	±0.010	0.022
	3.026	1	1/2	-	0.023	±0.007	
	3.026	1	1/2*	-	0.009	±0.002	
	3.026	3	(5/2*)	N	0.016	±0.003	
	3.061	4	9/2	+	0.479	±0.096	

Table 2.6 (con't)

Nucleus	Ex (MeV)	l	J	π	SF(ADWA)	Error	SF(ENDSF)
	3.429	0	(1/2)	N	0.010	±0.003	
	3.452	1	3/2	-	0.022	±0.003	0.034
	3.546	2	(5/2)	N	0.019	±0.006	
	3.652	3	(5/2)	N	0.018	±0.009	0.021
	3.858	1	3/2	-	0.019	±0.013	0.025
	4.036	1	(3/2)	-	0.031	±0.016	0.012
	4.506	2	5/2	+	0.175	±0.053	0.234
	4.542	2	5/2	-	0.161	±0.023	
	4.709	4	9/2	+	0.049	±0.024	0.098
	4.822	2	(5/2)	N	0.040	±0.020	
	4.939	1	(1/2)	N	0.054	±0.027	
	5.069	1	1/2	-	0.009	±0.003	0.017
	5.149	0	1/2	+	0.065	±0.019	0.093
	5.213	2	5/2	+	0.018	±0.005	0.026
	5.258	2	(5/2)	N	0.017	±0.009	
	5.429	4	(9/2)	+	0.080	±0.015	
	5.458	2	(5/2)	+	0.151	±0.075	
	5.528	0	1/2	+	0.120	±0.060	
	5.569	0	(1/2)	+	0.021	±0.006	0.024
	5.692	0	1/2	+	0.077	±0.023	0.126
	5.894	2	(5/2)	+	0.014	±0.004	
	6.142	1	1/2	-	0.027	±0.005	
	6.142	1	3/2	-	0.014	±0.003	
	6.206	2	(5/2)	+	0.023	±0.011	0.011
	6.284	2	(5/2)	N	0.053	±0.026	
	6.380	0	1/2	+	0.039	±0.012	0.078
	6.648	2	3/2	+	0.036	±0.011	
	6.648	2	5/2	+	0.024	±0.007	
	7.073	0	1/2*	+	0.027	±0.008	0.029
	7.073	2	5/2*	+	0.007	±0.002	0.012
	7.204	0	1/2*	+	0.017	±0.005	0.019
	7.204	2	5/2*	+	0.005	±0.001	0.012
	7.302	3	7/2	-	0.011	±0.003	0.017
	7.353	2	5/2	+	0.040	±0.020	0.007
	7.604	2	3/2	+	0.004	±0.001	
	7.604	2	5/2	+	0.013	±0.004	
^{60}Ni	0.000	1	0	+	1.915	±0.383	1.640
^{61}Ni	0.000	1	3/2	-	0.263	±0.026	0.346
	0.067	3	5/2	-	0.368	±0.110	0.507
	0.283	1	1/2	-	0.363	±0.051	0.615
	0.656	1	1/2	-	0.015	±0.005	0.027
	1.100	1	3/2	-	0.012	±0.004	0.027

Table 2.6 (con't)

Nucleus	Ex (MeV)	l	J	π	SF(ADWA)	Error	SF(ENDSF)
	1.132	3	5/2	-	0.036	±0.011	0.067
	1.185	1	3/2	-	0.049	±0.015	0.064
	1.729	1	3/2	-	0.006	±0.002	0.011
	2.122	4	9/2	+	0.499	±0.071	
	2.124	1	1/2	-	0.242	±0.034	
	2.640	1	1/2	-	0.028	±0.009	
	2.640	1	3/2	-	0.014	±0.004	
	2.697	2	5/2	+	0.062	±0.019	0.087
	2.765	1	3/2	-	0.008	±0.003	0.014
	2.863	1	1/2	-	0.010	±0.003	
	2.863	1	3/2	-	0.005	±0.002	
	3.062	0	1/2	+	0.023	±0.007	
	3.273	1	(3/2)	-	0.002	±0.001	0.003
	3.382	1	1/2	-	0.007	±0.002	
	3.382	1	3/2	-	0.003	±0.001	
	3.506	2	3/2	+	0.158	±0.047	
	3.506	2	5/2	+	0.105	±0.031	
	3.686	1	1/2	-	0.018	±0.005	
	3.686	1	3/2	-	0.009	±0.003	
	4.568	2	(3/2)	+	0.006	±0.002	
	4.568	2	(5/2)	+	0.004	±0.001	
	4.600	2	5/2	-	0.004	±0.001	0.005
	5.112	1	1/2	-	0.035	±0.010	
	5.112	1	3/2	-	0.018	±0.005	
	5.185	0	1/2	+	0.027	±0.008	0.051
	5.309	0	1/2	+	0.012	±0.004	0.027
	5.723	2	(3/2)	N	0.055	±0.016	
	5.723	2	(5/2)	N	0.036	±0.011	
	5.987	0	1/2	+	0.021	±0.006	
	6.016	2	(3/2)	+	0.006	±0.002	
	6.016	2	(5/2)	+	0.004	±0.001	
	6.346	2	3/2	+	0.019	±0.006	
	6.346	2	5/2	+	0.013	±0.004	
	6.371	2	3/2	+	0.008	±0.002	
	6.371	2	5/2	+	0.006	±0.002	
	6.609	2	3/2	+	0.005	±0.002	
	6.609	2	5/2	+	0.004	±0.001	
^{62}Ni	0.000	1	0	+	1.619	±0.324	
	1.173	1	2	+	0.218	±0.065	
	2.049	1	0	+	0.280	±0.084	
	2.336	3	4	+	0.274	±0.082	
	2.891	1	0	+	0.505	±0.152	
	3.059	3	2	+	0.233	±0.070	
	3.158	1	2	+	0.052	±0.016	

Table 2.6 (con't)

Nucleus	Ex (MeV)	l	J	π	SF(ADWA)	Error	SF(ENDSF)
	3.262	3	(2)	+	1.119	±0.336	
	3.370	1	1	+	0.295	±0.089	
	3.370	1	2	+	0.177	±0.053	
	3.519	1	2	+	0.248	±0.074	
	3.757	4	3	-	0.361	±0.108	
	3.849	1	0	+	1.028	±0.309	
	3.849	1	1	+	0.343	±0.103	
	3.849	1	2	+	0.206	±0.062	
	4.393	3	(2)	N	0.144	±0.043	
	4.503	4	(3)	-	0.264	±0.079	
	4.720	4	(3)	-	0.791	±0.237	
	4.863	4	5	-	1.079	±0.324	
	4.863	4	6	-	0.913	±0.274	
	5.331	2	(3)	-	0.163	±0.049	
	5.545	4	3	-	0.653	±0.196	
	5.545	4	4	-	0.508	±0.152	
	5.545	4	5	-	0.416	±0.125	
	5.545	4	6	-	0.352	±0.106	
	5.628	2	3	-	0.024	±0.007	
	6.103	2	1	-	0.451	±0.135	
	6.103	2	2	-	0.270	±0.081	
	6.103	2	3	-	0.193	±0.058	
	6.103	2	4	-	0.150	±0.045	
	6.540	2	1	-	0.350	±0.105	
	6.540	2	2	-	0.210	±0.063	
^{63}Ni	0.000	1	1/2	-	0.176	±0.025	0.370
	0.087	3	5/2	-	0.234	±0.070	0.563
	0.156	1	3/2	-	0.177	±0.053	0.275
	0.518	1	3/2	-	0.042	±0.008	0.080
	1.001	1	1/2	-	0.184	±0.037	0.330
	1.292	4	(9/2)	+	0.565	±0.169	0.750
	1.324	1	3/2	-	0.028	±0.008	0.063
	2.297	2	5/2	+	0.189	±0.027	0.142
	2.697	1	1/2	-	0.023	±0.003	0.045
	2.953	0	1/2	+	0.128	±0.038	0.190
	3.104	2	3/2	+	0.016	±0.005	
	3.104	2	5/2	+	0.011	±0.003	
	3.283	2	(5/2)	N	0.041	±0.012	0.053
	3.292	2	5/2	+	0.037	±0.011	
	3.740	2	(3/2)	N	0.030	±0.009	0.040
	3.951	2	5/2	+	0.074	±0.022	0.100
	4.387	2	5/2	+	0.038	±0.011	0.062
	4.622	2	3/2	+	0.053	±0.016	
	4.622	2	5/2	+	0.036	±0.005	

Table 2.6 (con't)

Nucleus	Ex (MeV)	l	J	π	SF(ADWA)	Error	SF(ENDSF)
	5.060	2	(3/2)	+	0.009	±0.003	
	5.060	2	(5/2)	+	0.006	±0.002	
^{65}Ni	0.000	3	5/2	-	0.218	±0.031	0.338
	0.063	1	1/2	-	0.399	±0.056	0.620
	0.310	1	3/2	-	0.022	±0.003	0.035
	0.693	1	3/2	-	0.093	±0.028	0.235
	1.017	4	9/2	+	0.738	±0.221	0.085
	1.418	1	1/2	-	0.038	±0.011	0.257
	1.920	2	5/2	+	0.173	±0.052	
	2.163	1	(1/2)	N	0.031	±0.009	
	2.325	3	(5/2*)	N	0.030	±0.009	
	2.325	4	(9/2*)	N	0.050	±0.015	
	2.336	3	(5/2)	N	0.085	±0.025	
	2.336	3	(7/2)	N	0.063	±0.019	0.003
	2.712	2	3/2	+	0.003	±0.001	
	3.044	1	(1/2)	N	0.022	±0.007	
	3.044	1	(3/2)	N	0.011	±0.003	
	3.411	2	(3/2)	+	0.130	±0.039	
	3.411	2	(5/2)	+	0.087	±0.026	
	3.463	2	(3/2)	N	0.008	±0.002	
	3.463	2	(5/2)	N	0.005	±0.002	0.082
	3.563	2	5/2	+	0.065	±0.013	0.042
	3.743	2	5/2	+	0.031	±0.009	0.068
	3.907	2	5/2	+	0.058	±0.018	
	4.391	2	3/2	+	0.057	±0.017	
	4.391	2	5/2	+	0.038	±0.011	

Table 2.7: Comparison of experimental and large-basis shell-model energy levels and spectroscopic factors for Ni isotopes.

				Ex (MeV)			SF			
Nucleus	**l**	**J**	**P**	**NUDAT**	**GXPF1A**	**JJ4PNA**	**ADWA**	**Error**	**GXPF1A**	**JJ4PNA**
^{57}Ni	1	3/2	-	0	0	0	0.954	±0.286	0.783	1.000
	3	5/2	-	0.769	0.825	0.714	1.400	±0.42	0.76	1.000
	1	1/2	-	1.113	1.184	1.302	1.000	±0.3	0.698	1.000
^{58}Ni	1	0	+	0	0	0	0.890	±0.087	1.105	1.118
^{59}Ni	1	3/2	-	0	0	0	0.444	±0.045	0.477	0.574
	3	5/2	-	0.339	0.364		0.472	±0.059	0.597	
	1	1/2	-	0.465	0.595		0.424	±0.06	0.504	
	1	1/2	-	1.301	1.371	1.103	0.166	±0.031	0.175	0.685
	3	5/2	-	1.68		1.439	0.062	±0.016		0.032
	1	3/2	-	1.735		1.906	0.004	±0.001		0.008
	4	9/2	+	3.061		3.454	0.479	±0.096		0.938
	4	9/2	+	4.709		4.540	0.049	±0.024		0.007
	4	9/2	+	5.429		5.418	0.080	±0.015		0.028
^{60}Ni	1	0	+	0	0	0	1.915	±0.383	1.746	2.496
^{61}Ni	1	3/2	-	0	0	0.547	0.263	±0.026	0.244	0.278
	3	5/2	-	0.067	-0.006	0.364	0.368	±0.11	0.527	0.727
	1	1/2	-	0.283	-0.008	0	0.363	±0.051	0.609	0.683
	1	1/2	-	0.656		1.457	0.015	±0.005		0.188
	3	5/2	-	1.132		1.277	0.036	±0.011		0.072
	1	3/2	-	1.729		1.835	0.006	±0.002		0.010
	4	9/2	+	2.122		2.516	0.499	±0.071		0.917
	1	1/2	-	2.124		2.280	0.242	±0.034		0.007
	1	3/2	-	3.686		3.669	0.009	±0.003		0.001
^{62}Ni	1	0	+	0	0	0	1.619	±0.324	1.635	2.522
	1	2	+	1.173	1.148		0.218	±0.065	0.284	
	1	0	+	2.049	2.188	2.263	0.280	±0.084	0.075	0.259
	3	4	+	2.336	2.256	2.317	0.274	±0.082	0.247	0.275
	1	0	+	2.891		2.740	0.505	±0.152		0.153
^{63}Ni	1	1/2	-	0	0	0	0.176	±0.025	0.412	0.634
	3	5/2	-	0.087	0.158	0.171	0.234	±0.07	0.476	0.576
	1	3/2	-	0.156	0.373	0.319	0.177	±0.053	0.083	0.138
	1	3/2	-	0.518	0.77	0.643	0.042	±0.008	0.163	0.107
	1	1/2	-	1.001	1.216	1.282	0.184	±0.037	0.118	0.079
	4	9/2	+	1.292		1.546	0.565	±0.169		0.811
	1	3/2	-	1.324	1.363	1.491	0.028	±0.008	0.014	0.012
	1	1/2	-	2.697	2.79		0.023	±0.003	0.014	

Table 2.7 (cont'd)

				Ex (MeV)	SF					
Nucleus	**l**	**J**	**P**	**NUDAT**	**GXPF1A**	**JJ4PNA**	**ADWA**	**Error**	**GXPF1A**	**JJ4PNA**
	1	1/2	-	0.063	0.025	0	0.399	±0.056	0.526	0.594
	1	3/2	-	0.310		0.453	0.022	±0.003		0.109
	1	3/2	-	0.693		0.864	0.093	±0.028		0.056
	4	9/2	+	1.017		1.082	0.738	±0.221		0.797
	1	1/2	-	1.418	1.100	1.425	0.038	±0.011	0.040	0.024
	4	9/2	+	2.325		2.474	0.05	±0.015		0.083

Table 2.8. List of isotopes plotted in Fig. 2.21. J^{π} is the angular momentum and parity of the transferred nucleon. For the (*p*,*d*), (*d*,*p*) [Tsa05, Lee07], and (*e*,*e*'*p*) [Kra01,Wes92] reactions, only ground-state SFs are extracted. The theoretical SF values are obtained from the LB-SM code OXBASH [Bro02,Lee07,Bro04]. For the neutron and proton knockout reactions [Ter04,Gad04-1,Gad04-2,Gad05mEbd03], the deduced quantities are the cross-section reduction factors *Rs* , which are equivalent to SF(expt)/SF(LB-SM).

(p,d), (d,p)	**J**	**Sn-Sp**	**SF(expt)**	**SF(LB-SM)**	**SF(expt)/SF(LB-SM)**
^{12}**B**	1/2-	-10.72	0.4 ± 0.06	0.83	0.48 ± 0.07
^{12}**C**	3/2-	2.75	2.16 ± 0.25	2.85	0.76 ± 0.09
^{13}**C**	1/2-	-12.58	0.54 ± 0.07	0.61	0.88 ± 0.12
^{14}**C**	1/2-	-12.65	1.07 ± 0.22	1.73	0.62 ± 0.12
^{14}**N**	1/2-	3.00	0.48 ± 0.08	0.69	0.69 ± 0.11
^{15}**N**	1/2-	0.62	0.93 ± 0.15	1.46	0.64 ± 0.1
^{16}**O**	1/2-	3.53	1.48 ± 0.16	2.00	0.74 ± 0.08
^{17}**O**	5/2+	-9.64	0.75 ± 0.1	1.00	0.75 ± 0.1
^{18}**O**	5/2+	-7.9	1.46 ± 0.17	1.58	0.92 ± 0.11
^{19}**O**	5/2+	-13.12	0.35 ± 0.05	0.69	0.51 ± 0.07
^{25}**Mg**	5/2+	-4.73	0.21 ± 0.02	0.34	0.61 ± 0.07
^{26}**Mg**	5/2+	-3.06	1.83 ± 0.38	2.51	0.73 ± 0.15
^{27}**Al**	5/2+	4.79	0.93 ± 0.13	1.10	0.84 ± 0.12
^{28}**Al**	1/2+	-1.82	0.57 ± 0.08	0.60	0.95 ± 0.14
^{30}**Si**	1/2+	-2.9	0.55 ± 0.07	0.82	0.67 ± 0.08
^{31}**Si**	3/2+	-7.78	0.42 ± 0.07	0.58	0.72 ± 0.11
^{32}**P**	1/2+	-0.71	0.39 ± 0.07	0.60	0.65 ± 0.11
^{34}**S**	3/2+	0.54	1.11 ± 0.27	1.83	0.61 ± 0.15
^{37}**Ar**	3/2+	0.08	0.27 ± 0.04	0.36	0.74 ± 0.1
^{40}**Ca**	3/2+	7.31	3.2 ± 0.46	4.00	0.80 ± 0.11
^{41}**Ca**	7/2-	-0.53	0.73 ± 0.04	1.00	0.73 ± 0.04
^{42}**Ca**	7/2-	1.2	1.31 ± 0.12	1.81	0.72 ± 0.06

Table 2.8 (cont'd)

(p,d), (d,p)	J	Sn-Sp	SF(expt)	SF(LB-SM)	SF(expt)/SF(LB-SM)
^{43}Ca	7/2-	-2.75	0.44 ± 0.05	0.75	0.59 ± 0.07
^{45}Ca	7/2-	-4.88	0.26 ± 0.04	0.50	0.52 ± 0.07
^{47}Ca	7/2-	-6.93	0.19 ± 0.03	0.26	0.74 ± 0.1
^{48}Ca	7/2-	-5.86	5.41 ± 1.05	7.38	0.73 ± 0.14
^{49}Ca	3/2-	-11.3	0.74 ± 0.08	0.92	0.81 ± 0.08
^{46}Ti	7/2-	2.85	1.61 ± 0.23	2.58	0.62 ± 0.09
(e,e'p)	**J**	**Sp-Sn**	**SF(expt)**	**SF(LB-SM)**	**SF(expt)/SF(LB-SM)**
^{7}Li	3/2-	2.73	0.42 ± 0.04	0.67	0.63 ± 0.06
^{12}C	3/2-	-2.75	1.72 ± 0.11	2.85	0.60 ± 0.04
^{16}O	1/2-	-3.53	1.27 ± 0.13	2.00	0.64 ± 0.07
^{30}Si	5/2+	2.9	2.21 ± 0.2	3.8	0.58 ± 0.05
^{31}P	0+	-5.01	0.4 ± 0.03	0.58	0.68 ± 0.04
^{40}Ca	3/2+	-7.3	2.58 ± 0.19	4.00	0.65 ± 0.05
48Ca	1/2+	5.86	1.07 ± 0.07	1.98	0.54 ± 0.04
^{51}V	7/2-	-2.99	0.37 ± 0.03	0.75	0.49 ± 0.04
^{90}Zr	1/2-	-3.62	0.72 ± 0.07	1.28	0.56 ± 0.05
^{208}Pb	1/2+	0.63	0.98 ± 0.09	2.00	0.49 ± 0.05
n-knockout	**J**	**Sn-Sp**	**SF(expt)**	**SF(LB-SM)**	**SF(expt)/SF(LB-SM)**
^{12}C	incl	3.07			0.49 ± 0.02
^{15}C	1/2+	-19.86		0.98	0.96 ± 0.04
^{16}O	incl	7.64			0.56 ± 0.03
^{22}O	5/2+	-16.39		5.22	0.7 ± 0.06
^{32}Ar	5/2+	19.2		4.12	0.25 ± 0.03
^{34}Ar	incl	13.94			0.41 ± 0.07
^{46}Ar	7/2-	-10.03		5.41	0.85 ± 0.12
p-knockout	**J**	**Sp-Sn**	**SF(expt)**	**SF(LB-SM)**	**SF(expt)/SF(LB-SM)**
^{8}B	incl	-12.82			0.86 ± 0.07
^{9}C	3/2-	-12.96		0.94	0.82 ± 0.06
^{12}C	incl	-2.43			0.53 ± 0.02
^{16}O	incl	0.68			0.68 ± 0.04

Table 2.9: Spin assignments of three excited states, 3.491, 4.150 and 5.627 MeV of ^{27}Mg. The NUDAT [NNDC] values listed in column 2 are not confirmed by experiments. The shell-model information is listed in Column 4, 5 and 6. Our recommended spin values are listed in the last column.

E* (MeV)	***J*** **(NUDAT)**	**SF(ADWA)**	**E(LB-SM)**	***J*** **(LB-SM)**	**SF (LB-SM)**	**SF(ADWA)/SF(LB-SM)**	***J*** **(this work)**
3.49	(3/2+)	0.049 ± 0.015	**3.562**	3/2+	0.097 ± 0.012	0.51±0.17	**3/2+**
	(5/2+)	0.032 ± 0.010					
4.15	(3/2+)	0.038 ± 0.011					
	(5/2+)	0.025 ± 0.007	**4.097**	5/2+	0.029 ± 0.002	0.86±0.25	**5/2+**
5.627	(3/2+)	0.129 ± 0.039	**5.561**	3/2+	0.144 ± 0.003	0.89±0.27	**3/2+**
	(5/2+)	0.085 ± 0.026	**5.690**	5/2+	0.0054 ± 0.0004	16±4.8	

Chapter 3

Experimental Setup and Detectors

To understand the nature of neutron correlations in the regions of asymmetric nuclei, spectroscopic factor measurements using (*p*,*d*) neutron transfer reactions have been performed using proton-rich ^{34}Ar and neutron-rich ^{46}Ar beams in inverse kinematics. The experiments of $p(^{34}\mathrm{Ar},d)^{33}\mathrm{Ar}$ and $p(^{46}\mathrm{Ar},d)^{45}\mathrm{Ar}$ with beam energy of about 33 MeV/nucleon were performed at the National Superconducting Cyclotron Laboratory at Michigan State University. In this chapter, the method of measurement and experimental design are discussed. It is followed by the description of the detectors. In addition, the method and results of position measurement for the experimental setup are presented. The electronic and data acquisition system for the present experiments are also included.

3.1 Experimental design

3.1.1 Method of measurement

The goal of the present experiment is to determine the neutron spectroscopic factors of ^{34}Ar and ^{46}Ar using (*p*,*d*) single-nucleon transfer reactions in inverse kinematics. The differential cross sections of emitted deuterons are the experimental observables. We used the high resolution silicon array, HiRA [Wal07], to measure the energies and angles of the emitted deuterons. To ensure the particles observed were actually the deuterons of interest, forward going recoil residues were detected in coincidence in the S800 mass

spectrometer [Yur99, Baz03]. With these kinematically complete measurements, the coincident deuteron energies and angles could be used to identify the states populated in the final nuclei.

Studies of unstable p-rich ^{34}Ar and n-rich ^{46}Ar measurements were carried out in inverse kinematics by impinging the radioactive ^{34}Ar and ^{46}Ar beams on polyethylene $(CH_2)_n$ targets. Since ^{36}Ar(*p*,*d*) reaction has been studied before in normal kinematics[Koz68], the ^{36}Ar induced reaction was used as the calibration beam for our detectors. Due to the considerable size of the secondary beam spot, two multi-channel plate detection systems (MCP) [Sha00-1, Sha00-2] with thin Carbon foils were employed to track the positions of the incoming beams and correct the deuteron angles for the beam positions on the target [Rog10-2]. Figure 3.1 summarizes the designed experimental setup. The HiRA array with 16 telescopes was placed at 35 cm from $(CH_2)_n$ reaction target. The design of this configuration is explained in Section 3.1.3. Two MCP foils were positioned individually at 10 cm and 60 cm upstream of the reaction target. To avoid blocking the beam with the MCP detectors, the foils are orientated at an angle of 60° relative to the beam line. The MCP also monitored the absolute beam intensities throughout the experiment for overall normalization of deuteron cross sections. The HiRA, MCP and reaction targets were accommodated in the S800 scattering chamber in front of the S800 spectrometer as shown in Figure 3.2.

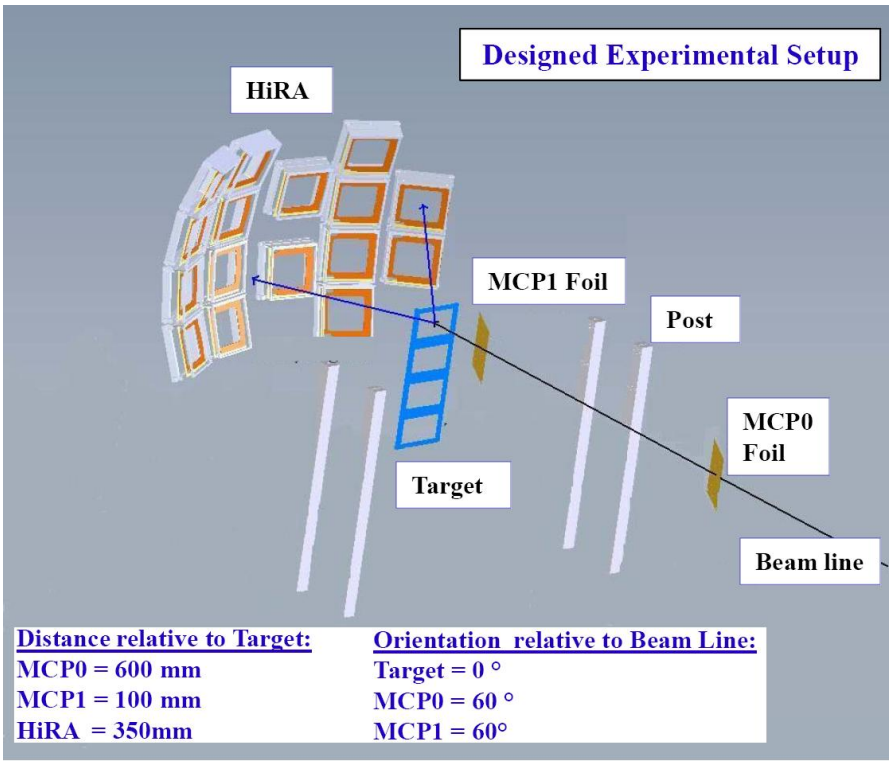

Figure 3.1: Simplified schematic diagram of the designed experimental setup inside the S800 chamber. The 4 posts were not placed inside the chamber during experiment. They were used only in the LBAS measurement as discussed in Section 3.5.

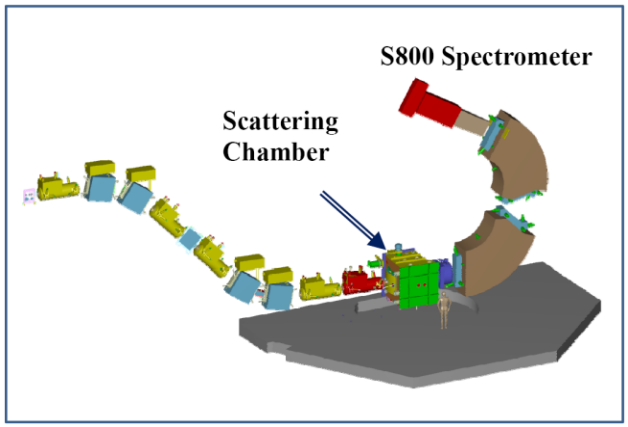

Figure 3.2: 3-D rendering of the S800 spectrometer aligned with the scattering chamber and analysis beam line.

Precise reconstruction of the reaction dynamics requires accurate knowledge of the beam trajectory and alignment of detectors with respect to the reaction target. Sub-millimeter position measurement without mechanically touching the experimental setup (especially for the fragile MCP Carbon foils and reaction targets) is essential. The working principle and performance of the position measurements using a laser-based alignment system (LBAS) are discussed in Sections 3.5 and 3.6.

3.1.2 Radioactive beams and reaction targets

Our survey of (*p,d*) and (*d,p*) transfer reactions suggests that incident energies ranging from 10 to 20 MeV per nucleon permit accurate comparison of theoretical and experimental angular distributions, as discussed in Section 2.2.5. The radioactive beam is produced at 120 MeV/nucleon or higher, and its intensity generally decreases as the beam energy is decreased by degrading with absorbers in the A1900 fragment separator. Therefore there is a compromise between the intensity of the radioactive beam and the optimum choice of bombarding energy. With all the optimal and practical issues considered, we chose the energy of 33 MeV/nucleon for the ^{34}Ar and ^{46}Ar secondary beams in the present measurements.

It is desirable to check whether the beam energy satisfies the angular momentum matching condition presented in Equation 3.1, even though it is not a necessary condition [Joh89].

$$L \approx Q \cdot R = |\boldsymbol{K}_{in} - \boldsymbol{K}_{out}| \cdot R \qquad (3.1)$$

where L is the momentum of the transferred nucleon, $\boldsymbol{K}_{in}$ and $\boldsymbol{K}_{out}$ are the wave number in the entrance and exit channel respectively and $R= r_o A^{1/3}$.

If such condition is well-matched, the transferred angular momentum is given by the condition to $Q \cdot R-1 \leq L \leq Q \cdot R+1$. In such cases, the nucleon-transfer probability to that particular state will be relatively large and dependent on the accurately calculated parts of the DWBA integrals. As a result, the simple one-step DWBA description to the data is more valid [Sch09]. Figure 3.3 shows the momentum matching calculations for valence neutron in the $p(^{34}\mathrm{Ar},d)^{33}\mathrm{Ar}$ and $p(^{46}\mathrm{Ar},d)^{45}\mathrm{Ar}$ reactions. A beam energy of 33 MeV/nucleon gives $Q \cdot R$ of 0.1 and 1.5 for $p(^{34}\mathrm{Ar},d)^{33}\mathrm{Ar}$ and $p(^{46}\mathrm{Ar},d)^{45}\mathrm{Ar}$ reactions respectively. The neutron transition to the ground-state of ^{33}Ar is $2s_{1/2}$; while to the ground- and first-excited states of ^{45}Ar are $1f_{7/2}$ and $2p_{3/2}$. Even though the l-transfer to the ground-state of ^{45}Ar is slightly outside this criterion, the 33 MeV/nucleon beam energy is not unreasonable for the reactions being studied.

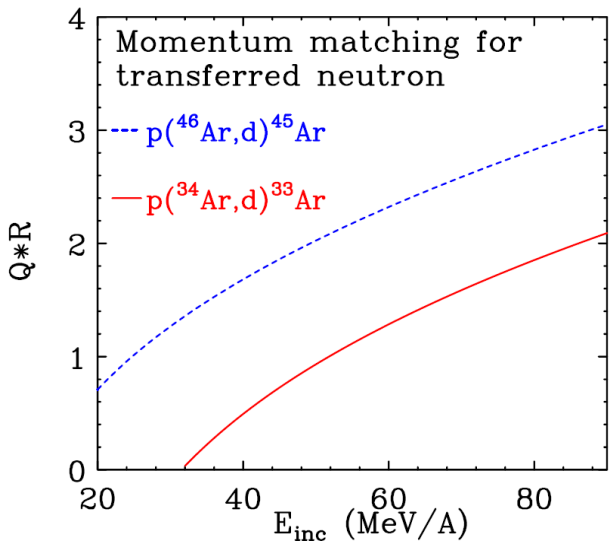

Figure 3.3: Momentum matching for neutron for the *l*=0 ground-state transition of *p*(^{34}Ar,*d*) ^{33}Ar and *l*=3 ground-state transition of *p*(^{46}Ar,d) ^{45}Ar reactions.

The primary beams ^{36}Ar and ^{48}Ca were produced by the Coupled-Cyclotron Facility (CCF) [NSCL94, Mor94, She02] which consists of two superconducting cyclotrons, the K500 and the K1200. Using the in-flight projectile fragmentation technique, secondary beams of ^{34}Ar and ^{46}Ar at 33 MeV/nucleon were produced by fragmentation of 150 MeV/nucleon ^{36}Ar primary beam on a 1480 mg/cm^2 ^{9}Be production target and 140 MeV/nucleon ^{48}Ca beam on a 1763 mg/cm^2 ^{9}Be production target respectively. After fragmentation, the radioactive beams were separated by the A1900 large-acceptance fragment separator [Mor03]. A schematic of A1900 fragment separator is shown in Figure 3.4. A 375 mg/cm^2 thick achromatic aluminum wedge degrader and momentum slits at the dispersive image of the separator were employed to purify the beams. The secondary ^{34}Ar and ^{46}Ar beams were identified unambiguously by the time

of flight from cyclotron to the A1900 focal plane, using the radio-frequency (RF) of cyclotron and a scintillator at the extended focal plane of the A1900. In addition, ^{36}Ar primary beam was degraded to 33 MeV/nucleon for calibration purposes. $(CH_2)_n$ targets with thickness of 7.10 mg/cm^2 for the $p(^{34,36}\text{Ar},d)$ reactions and 2.29 mg/cm^2 for the $p(^{46}\text{Ar},d)$ reaction were chosen, which compromise between maximizing the cross-section yields and minimizing the energy loss and the angular and energy straggling of deuterons in the target.

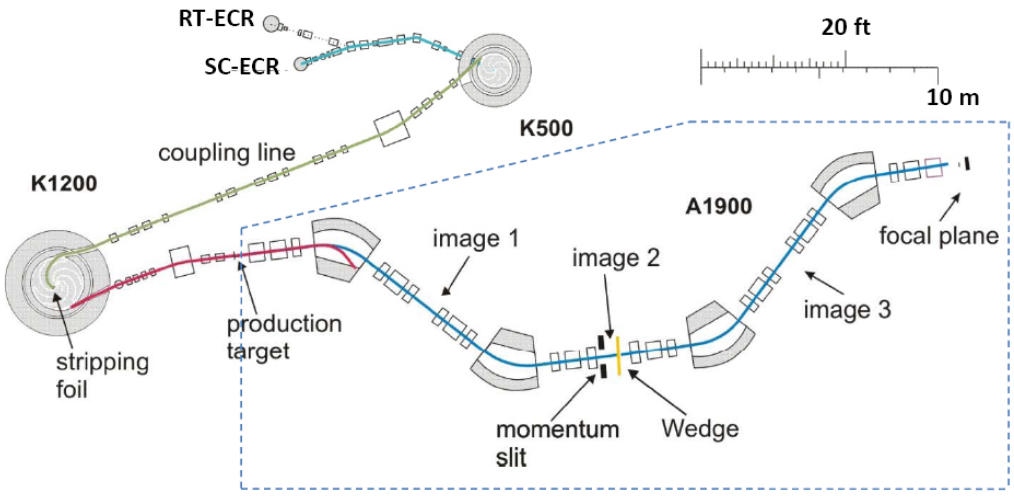

Figure 3.4: Schematic of the Coupled Cyclotron Facility at the NSCL. The K500 and K1200 are connected by the coupling line. The 1900 fragment separator is enclosed in the dashed-line area.

3.1.3 Geometry of HiRA detector Array

In this experiment, HiRA detects the deuteron particles emitted from the $p(^{34,36,46}\text{Ar},d)$ reactions. Deuteron angular distributions in the center-of-mass frame calculated using TWOFNR code for the ground-state transfers for the three different reaction systems are

displayed in the left panels of Figure 3.5. The right panels show the corresponding angular distributions in laboratory frame. In inverse kinematics, all deuterons are emitted to the forward angles and any single angle in laboratory corresponds to two different deuteron energies and COM angles. This can be understood by the velocity diagram displayed in Figure 3.6, where V_0^{COM} is the velocity of the center of mass in the laboratory frame; V_d^{lab} and V_d^{COM} are the deuteron velocity in the laboratory and center of mass frame. The corresponding laboratory and center-of-mass angles are θ_{lab} and θ_{COM} respectively. The circle represents the velocity of the deuteron in the center-of-mass frame. The relations between the deuteron emitting angles in the center of mass and laboratory frame for all three reactions are presented in Figure 3.7.

Figure 3.8 shows a photograph of the HiRA detector array and the downstream MCP. A total of 16 HiRA telescopes were arranged in five towers positioned at 35cm from the reaction target and subtended polar angles of $4° \leq \theta_{lab} \leq 45°$. The gap at angles less than 4° allows the beam and heavy reaction fragments go to the S800 spectrometer. Due to the forward focusing of the deuteron particles, this setup covers most of the important solid angle in the center-of-mass frame for all three reactions. The geometrical efficiency of the HiRA array setup, calculated based on Monte-Carlo principle, is shown in Figure 3.9, where 30-40% coverage is achieved in general. In addition to a large geometry efficiency in the angular regions covering the first peak, the design of the HiRA configuration also optimizes the energy and angular resolutions. At 35 cm setup, the pixelation of the HiRA telescope allow angle determination to a precision of ± 0.16°.

The HiRA coverage is plotted in the Cartesian and Spherical coordinate systems as shown in Figure 3.10. The beam direction is defined as the z axis and vertical direction is defined as the x axis. The polar angle θ defines the angle of the particle direction with respect to the beam axis and the azimuthal angle ϕ defines the angle between the particle projection on the x-y plane and y axis. For reference, each telescope is assigned a number as labeled in Figure 3.10.

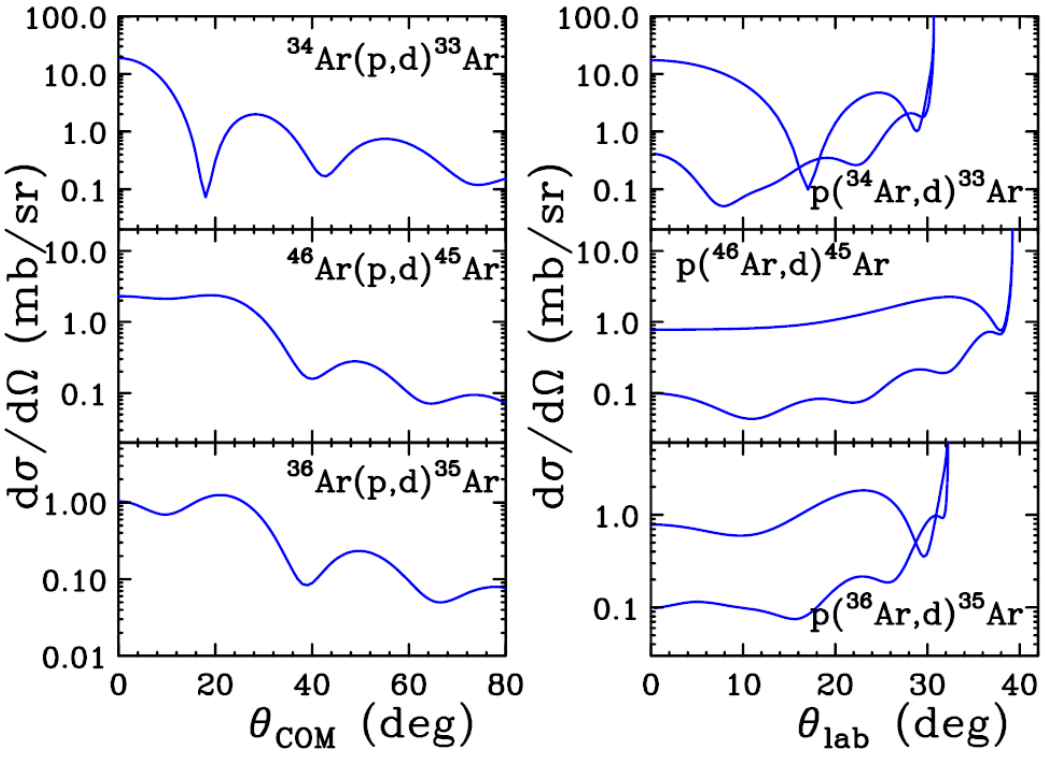

Figure 3.5: The calculated deuteron angular distributions of $p(^{34,36,46}\mathrm{Ar},d)$ for ground-state transitions in center-of-mass frame (left panels) and in laboratory frame (right panels) at beam energy of 33 MeV/nucleon.

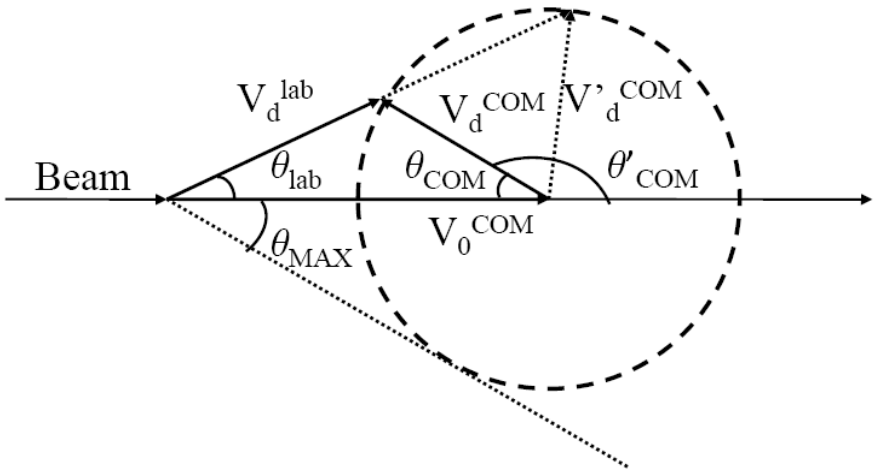

Figure 3.6: Velocity diagrams for (*p*,*d*) reaction in inverse kinematics.

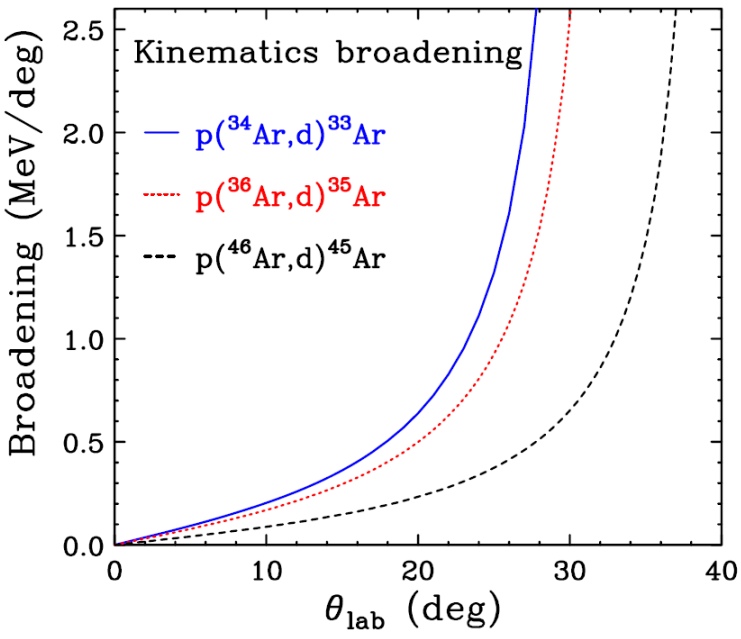

Figure 3.7: The deuteron emitted angles in center of mass angle versus the emitted angle in laboratory frame for *p*(^{34,36,46}Ar,*d*) of ground-state transitions at beam energy of 33 MeV/nucleon.

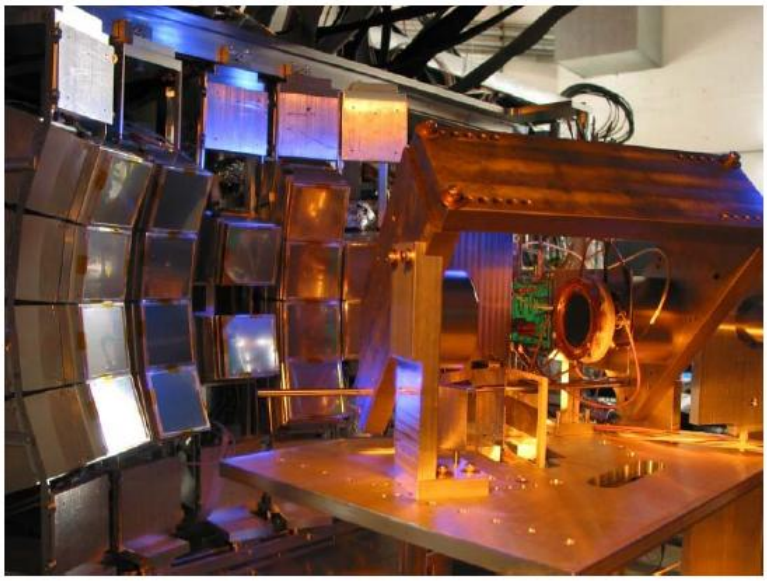

Figure 3.8: Photograph of the HiRA detector array and the downstream MCP.

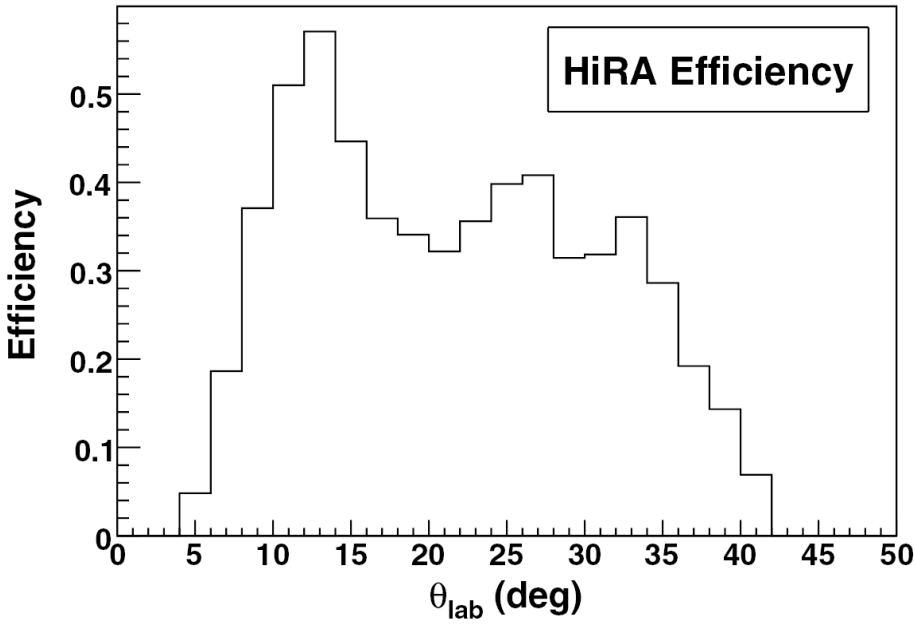

Figure 3.9: Efficiency of HiRA setup in 2-degree bin where 16 telescopes were placed at 35 cm from the reaction target.

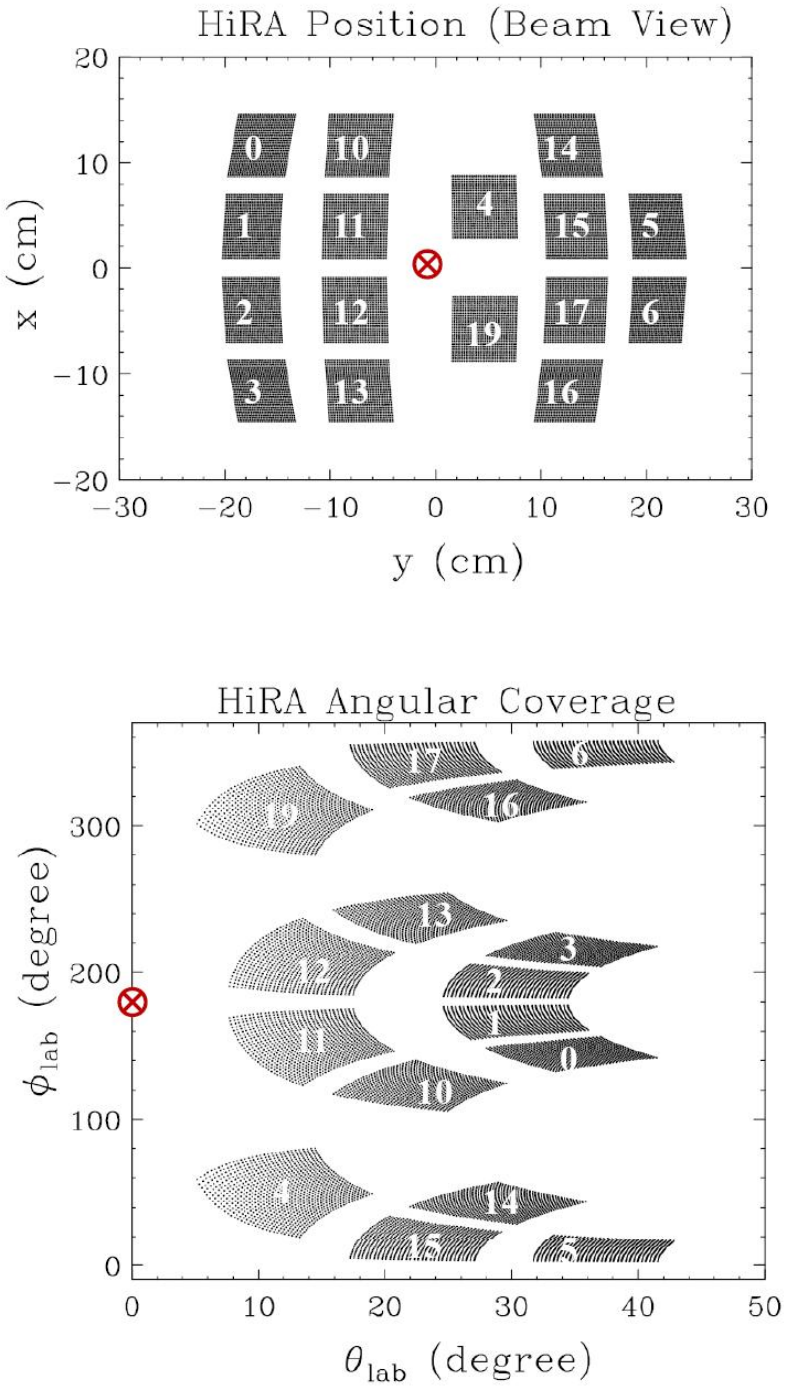

Figure 3.10: The HiRA configuration from mechanical design in the Cartesian coordinate systems (top) and Spherical coordinate systems (bottom) with a number assigned for each telescope. The beam position is indicated as a red cross.

3.1.4 Total energy and kinematics measurement

In the present (*p,d*) measurements, deuteron energies were recorded from all the silicon detectors, with the total energy in the telescopes calculated from the sum of the DE, E and CsI energies. The calculated kinematic curves for deuterons corresponding to ground-state transitions in different reactions are plotted in Figure 3.11. The deuteron punch-through energy of the silicon detectors is about 21.5 MeV. If deuterons are emitted at the forward angles, they would have energy less than 21.5 MeV and therefore stop in silicon E detectors. Particle identifications (PID) can be constructed by using DE and E. The CsI crystals covering the forward angles are mainly used to veto energetic particles that punch through the silicon detector and reduce the background in the DE-E PID spectra. In the lower right panel in Figure 3.11, the red/blue shaded part in the detector array represents the region where deuterons from the (*p,d*) reactions stop in the thick silicon detectors for ^{34}Ar (red) and ^{46}Ar (blue and red) reactions. Deuterons emitted at larger angles have energies larger than 21.5 MeV and stop in the CsI crystals. E-CsI spectra can be used for PID. No DE was mounted to telescope 5 and 6 which allow monitors of alpha calibration for E detectors thoughout the whole experiment.

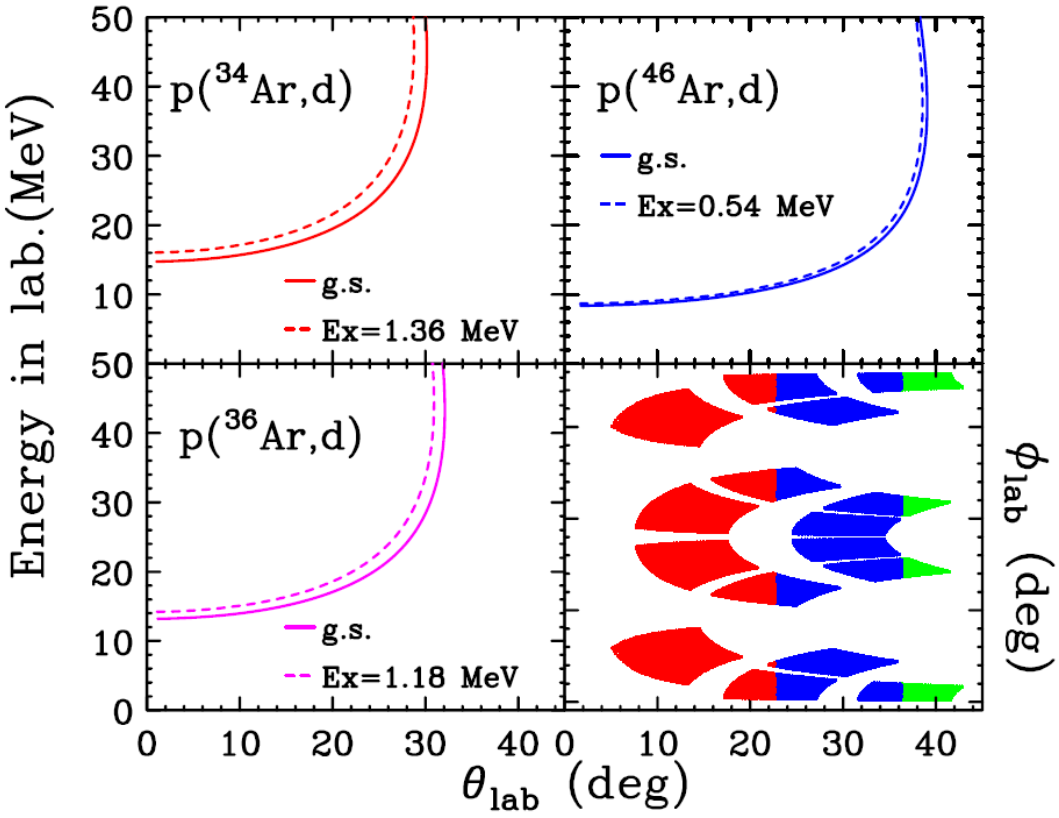

Figure 3.11: (Top panels and bottom left panel) Kinematic curves of deuterons from $p(^{34,36,46}\mathrm{Ar},d)$ reactions at beam energy of 33 MeV/nucleon. (Bottom Left) HiRA configuration in the spherical coordinate system with the shaded part representing the region where deuterons stop in the thick silicon detectors for ^{34}Ar (red) and ^{46}Ar (red and blue) reactions

3.2 HiRA Detector Array

The High Resolution Array (HiRA) is a state-of-the-art detection array capable of detecting charged particles produced in nuclear reactions. It allows precise measurement of energy, charges and masses of various charged particle species with high angular resolution. Currently, HiRA consists of twenty identical detector telescopes. Depending on the experimental requirements, HiRA can be configured into different geometries with

the flexibility in using different number of detectors as demonstrated in photographs of actual experimental set ups in Figure 3.12. Each HiRA telescope contains 2 layers of position-segmented silicon detectors backed by four separate CsI(Tl) crystals mounted in quadrants. An expanded view of a single telescope is shown in Figure 3.13. Of critical importance in HiRA is the ability to identify the mass and element number of various particles to an excellent degree of resolution. For particle identification, HiRA relies on the technique of ΔE vs E identification where the energy loss ΔE is roughly proportional to AZ^2/E. A plot of ΔE vs E uniquely identifies A and Z of the charged particle that stop in the detectors. Further details of the HiRA detectors can be found in Ref.[Wal07].

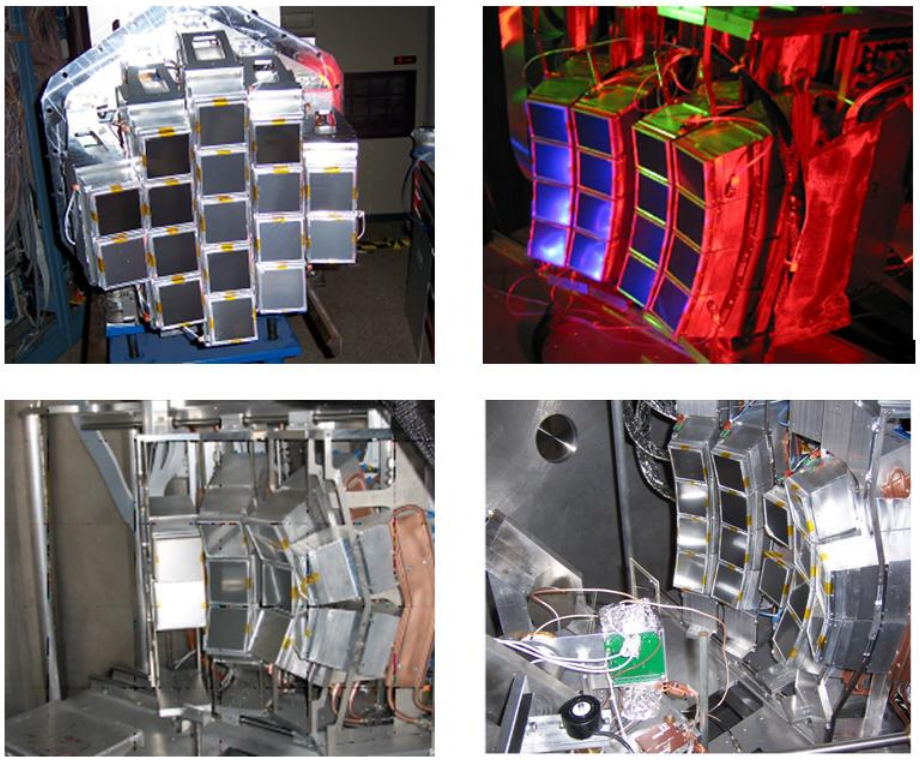

Figure 3.12: Photographs of different HiRA setup used in four experiments, where the bottom-right shows the configuration used in the present measurement.

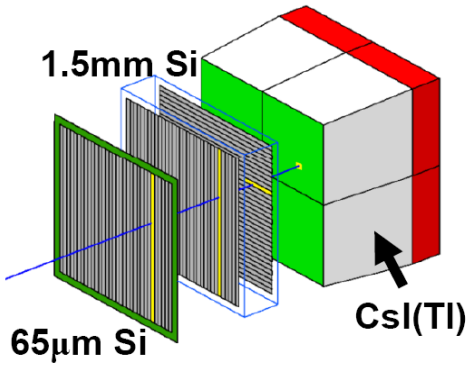

Figure 3.13: Schematic of a single HiRA telescope containing two layers of silicon detectors with thickness of 65 um and 1.5mm backed up by a cluster of four CsI crystals.

3.2.1 Silicon strip detectors and CsI(Tl) detectors

Silicon detectors have been widely used in nuclear experiments because of their excellent energy resolution and linear energy response over a large dynamic range for charged particles. As displayed in Figure 3.13, a HiRA telescope consists of a single-sided thin (65 *u*m) and double-sided (1500 *u*m) silicon detectors. Each has active surface area of 6.25 cm x 6.25 cm segmented into 32 position-sensitive strips with pitch of 1.95 mm. The 32x32=1024-pixel constructed by the front-vertical and back-horizontal strips in the double-sided E silicon detector allows excellent angular measurement of the detected particles. If the array is set up at 35cm from the reaction target, the angular resolution achieved is ± 0.16°. There is a gap of 25 *u*m between the active strips. Its effect is included in the efficiency determination of HiRA.

The thin detector is denoted as “DE” as it is used to measure the energy loss by the particle passing through the thin detector. The thick detector is denoted as “E” with

the front and back sides labeled as “EF” and “EB” respectively. To allow the close-packed design of the array, flexible polyimide cables with small printed circuit boards connected to the 34-pin Amp female header are used to read the signals from the detectors. Figure 3.14 and 3.15 show photographs of the front side of a single-sided and a double-sided Si strip-detector respectively.

Figure 3.14: HiRA single-sided silicon strip-detector in a circular plastic container.

Figure 3.15: HiRA double-sided silicon strip-detector in a circular plastic container.

Scintillators fabricated from thallium doped CsI (Cesium-Iodide) crystals have been extensively used for detecting charged particles because they are cost effective and easily machined into different shapes. In addition, CsI crystals have reasonable energy resolutions and light output uniformity. Each HiRA telescope contains four CsI(Tl) scintillation crystals arranged in quadrants behind the silicon detectors. The trapezoidal crystals are 3.5 x 3.5 cm^2 on the front and 3.9 x 3.9 cm^2 in the rear. For compact packing, the sides between adjacent crystals are cut straight back while the sides next to the frame are cut at an angle of 5.3°. With a thickness of 4 cm, all CsI(Tl) crystals can stop proton, deuteron and alpha with energy up to 115.8 MeV, 154.8 MeV and 462.3 MeV respectively. A light guide is attached to the back of each CsI. Glued on the back of the light guide is a photodiode with active area of 1.8 x 1.8 cm^2 which is painted with reflective white paint BC600 to prevent light leak and cross-talks. Figure 3.16 displays the side and front view of a CsI crystal, light guide and photo-diode assembly. Each crystal is individually wrapped in cellulose nitrate membrane filter paper to maximize the light collection efficiency. To ensure optical isolation and maximize light reflection, the front surface of the crystal array and the sides between crystals are covered with 1.9 *u*m thick aluminized Mylar foil.

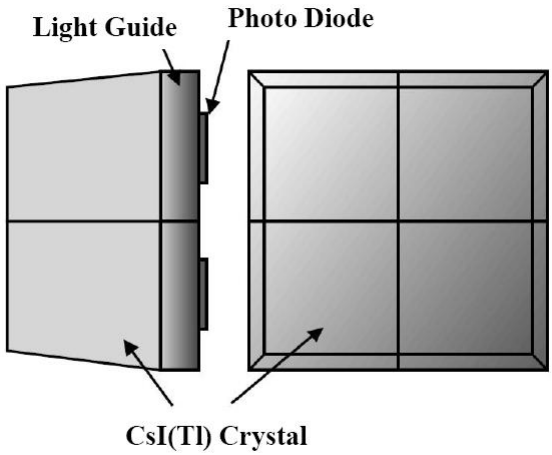

Figure 3.16: Side and front view of a CsI crystal, light guide and photo-diode assembly.

3.2.1.2 Readout Electronics -- Application Specific Integrated Circuit (ASIC)

The HiRA array with 20 telescopes of DE and E consists of 1920 individual silicon strips. Application Specific Integrated Circuits (ASIC) were developed for signal processing to greatly reduce the cost and space to implement the readout electronics [Wal07].

The HiRA ASIC contains charge sensitive amplifiers, pseudo constant fraction discriminators, shaping amplifiers, time to analog convertors and a sample and hold circuit along with the digital logic necessary for communication and multiplexing the signals out. Figure 3.17 shows the block diagram of the HiRA ASIC. Each ASIC chip processes signals for 16 individual channels. Since HiRA silicon detectors have 32 strips on each surface, two ASIC chips with other high density electronics mounted on a chipboard are used for each surface. Input and output signals of several chipboards are

merged by a circuit board called the “motherboard”. Each motherboard can accept 15 chipboards. Since three are used for each telescope, this allows up to 5 detectors connected within one motherboard. Photographs of a motherboard and chipboard are shown in Figure 3.18. Details of the HiRA electronics can be found in ref [Eng07].

In this experiment, 16 telescopes were used. All the chipboards for EF and EB were inserted to four motherboards placed inside the scattering chamber with each motherboard supporting readout for four telescopes. The chipboards for DE were processed by another two motherboards placed outside the chamber. DE signals were pre-amplified externally because of higher noise due to low capacitance of the thin Si detectors.

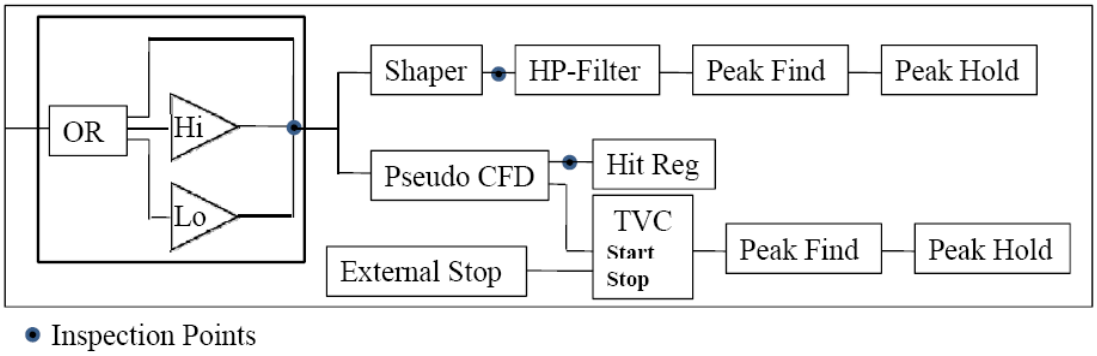

Figure 3.17: Block diagram of the HiRA ASIC.

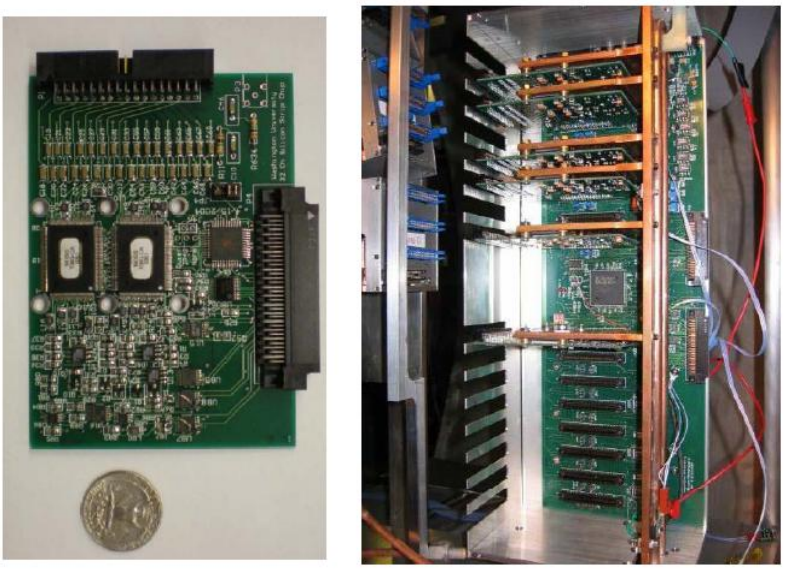

Figure 3.18: (Left) Photograph of a chipboard with two ASIC's attached. A U.S. quarter is used for size reference. (Right) Photograph of a motherboard with 6 chipboards inserted.

3.3 S800 Spectrometer

The S800 Spectrograph is a high resolution and high acceptance spectrometer [Yur99, Baz03]. It covers a solid angle of 20 msr and momentum acceptance of 5%. The setup is composed of two parts: the analysis line and the spectrograph itself. Figure 3.19 shows the schematic of S800 spectrometer. The analysis line can be operated in two optics modes: focus mode and dispersion matching mode. In this experiment, focus mode was used where the secondary beam is focused on the reaction target and dispersed on the S800 focal plane. This mode allows large momentum acceptance of approximately $\pm$ 2%, but it limits the momentum resolution at the focal plane of the spectrograph to about 1 part in 1000. For best resolution, tracking of the incident beam is necessary to recover momentum resolution of the reaction products. Behind the S800 scattering chamber are

two superconducting dipoles for selecting the reaction fragments of interest by setting the corresponding magnetic rigidity. The selected fragments will reach the focal plane detector array which measures their positions, energies and timing. Three quantities obtained in the S800, including magnetic rigidity time-of-flight and energy loss, suffice to identify the residues of the reactions.

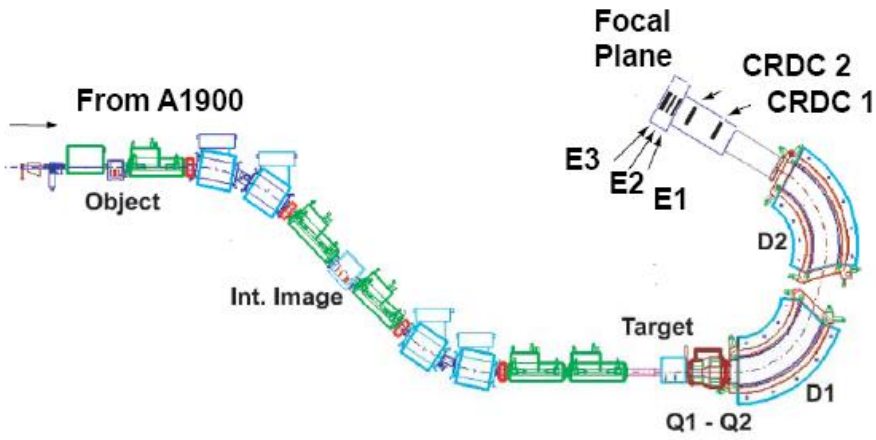

Figure 3.19: Schematic of S800 spectrometer.

The focal plane detector array of the S800 spectrograph consists of two Cathode Readout Drift Chambers (CRDC) followed by an ion chamber and a stack of three plastic scintillators [Yur99, Baz03]. The schematic of the focal plane detector system is shown in Figure 3.20. Two CRDCs are gas-filled high-voltage single-wire drift detectors with active areas of 30 cm x 59 cm separated by approximately one meter. Figure 3.21 shows the schematic of CRDC detector. Particles traveling though the detectors ionize the gas. The electrons drift to the anode wire by the constant vertical electric field in the detectors

and the drift time of the electrons gives the vertical position information (non-dispersive). A total of 224 cathode pads with pitch of 2.54 mm located in the front and back of the anode wires collect the positive image charges induced by the anode currents. The horizontal position (dispersive) is obtained from the centroid of the Gaussian fit to the charge distribution. The dispersive and non-dispersive angles can be calculated from a pair of associated position measurements in the CRDC detectors. The segmented ionization chamber (IC) following the CRDCs is used for energy loss measurement. Additional energy loss and total energy measurement as well as timing and trigger information are provided by the three plastic scintillators labeled as E1, E2 and E3 with thickness of 5, 10 and 20 cm respectively. Signals collected by the photomultiplier tubes on both top and bottom ends of the scintillator were used.

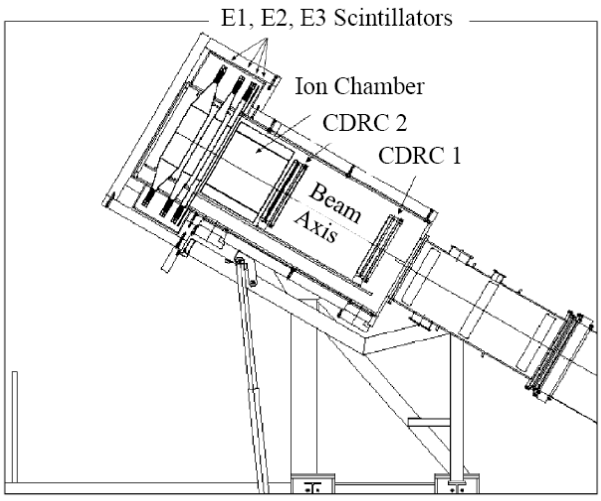

Figure 3.20: The schematic of the focal plane detector system in S800.

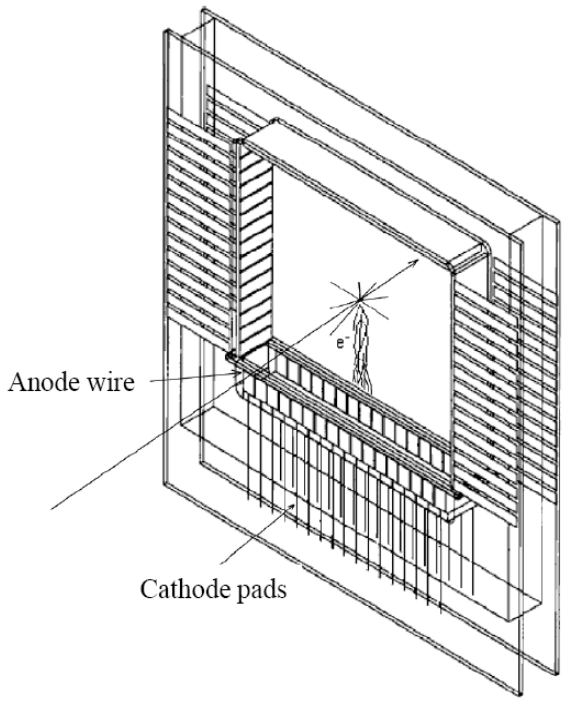

Figure 3.21: Schematic of CRDC detector.

3.4 Micro Channel Plate detectors

In order to resolve the energy states of the residuals at high resolution level, accurate determination of deuteron emission angle is required. Therefore beam tracking that determines the beam positions to 1-1.5 mm, much smaller than the beam spot size which is of the order of 10 mm (FWHM) and the beam incident angles on the reaction target is necessary. Micro Channel Plate detector (MCP) is employed for beam tracking in this experiment. The micro-channel plate is a compact electron multiplier array made with many tiny glass tubes closely packed together. The plate itself has an active diameter of 40 mm and thickness of 0.46 mm. The diameter of each tube is about 10 *u*m and the center to center distance between adjacent tubes is about 12 *u*m. Figure 3.22

shows the schematic design of a Micro Channel Plate. The working principle involves the amplification and detection of the secondary electron emission from the reaction of the beam on the MCP foil. An electron strikes the inner surface which is coated with material having a low work function for electron emission. The impact then starts a cascade of electrons that propagates through the tube as shown in Figure 3.23. An avalanche of electrons will eventually be generated and emerges on the other end of the tube. In our MCP detection system, there are two micro-channel plates in which the second plate with angled channels oriented in the opposite angle as shown in Figure 3.23 to significantly enhance the secondary electron emissions and amplify the signals. The secondary electrons emitted from the MCP are collected by a thin anode resistive layer placed behind the second micro-channel plate. The position of the electrons on the anode is determined from the signal amplitude of the four corners of the anode resistive layer [Sha00-1, Sha00-2].

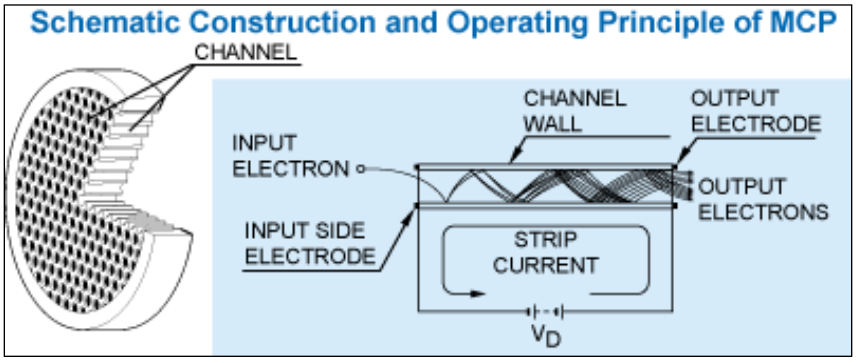

Figure 3.22: Schematic design of a micro-channel plate (adopted from [Wal05]).

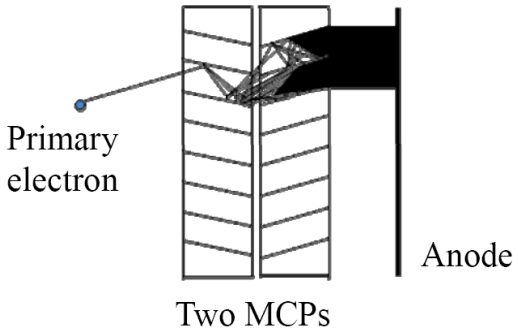

Figure 3.23: The detection system with two micro-channel plates and the view of chevron style MCPs (adopted from [Wal05])..

The schematic setup of MCP detection system is shown in Figure 3.24. Secondary electrons are produced when a beam ion strikes the foil. The electrons are accelerated by an electric field generated by applying 1000 V bias between the foil and front surface of the MCP. The strong voltage also ensures the drift time of electrons is sufficiently short for excellent timing resolution. The overall fast timing response allows the MCP to function at beam rates of up to $1x10^6$ pps. To ensure good spatial resolution, a strong magnetic field created by two permanent magnets (14 kG on the surface), manufactured by Magnet Sales & Manufacturing Inc, part number: 35NERR192, confined the electrons to narrow helical orbit while traveling towards the MCP. In our MCP detection system, the magnetic field measured at the MCP and the MCP target foil positions are 5000 G and 3000 G respectively.

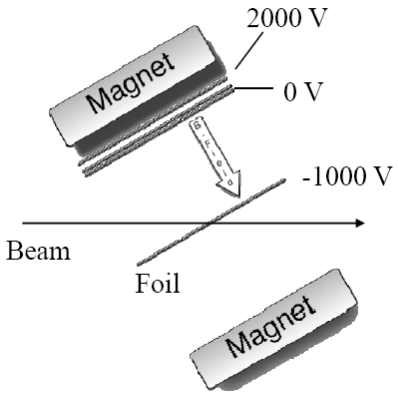

Figure 3.24: The schematic setup of MCP detection system with MCP, two permanent magnets, foil and anode layer (adopted from [Wal05])..

In the experiment, two MCP detection systems were used and placed at 50 cm apart, with MCP0 and MCP1 denote the upstream and downstream MCPs respectively. The reaction target was located at 10 cm downstream of the MCP1 as displayed in Figure 3.2. From the position information of the beam given by MCP0 and MCP1, beam positions and angles on the reaction target can be deduced accurately. The Ar beams used in this experiment have masses of 34, 36 and 46 with charges of 18+, their trajectories are influenced by the strong magnet fields in the MCP setup. When assuming the beam come horizontally, the angle being deflected under the B-field can be simply estimated using $\delta\theta = B \cdot d / B\rho$, where B is the magnetic B-field at MCP foil (~3000G), d is the beam traveling distance in B-field (~ 8cm) and $B\rho$ is the magnetic rigidity of the beam. The estimated deflection angles are therefore 0.66°, 0.71°, 0.56° for ^{34}Ar, ^{36}Ar and ^{46}Ar respectively. The fields in the two MCP are in the opposite direction, so the beam angle is not changed. Instead, if there is a net effect as a vertical displacement of the beam, this

basically means that the displaced dispersive angle calculated by the MCP is off by δθ. This needs to be taken in to account in the calibration. As explained later that we are unable to use the MCP for actual beam checking, details for the optimal operation of the MCP is described in the ^{56}Ni(*p*,*d*) experiment NSCL Expt 06035 [Expt06035] which was performed after the runs with Ar isotope beams.

3.5 Position Measurements with Laser Based Alignment System (LBAS)

Direct transfer reactions carried out in inverse kinematics using short-lived heavy beams bombarding light targets, suffer from strong kinematic broadening. For example, the kinematic broadening (dE/dθ) of *p*(^{46}Ar,*d*) at 33 MeV/nucleon in this experiment is up to 2 MeV per degree for θ_{lab} >36°. To resolve the energy states of the residual nuclei at high resolution level, it is critical to accurately reconstruct the reaction dynamics where sub-millimeter determination in positions of beam tracking systems for beam particles and array of highly segmented detectors for reaction fragments is needed. Such accuracy is desired as the actual position of the detectors and the designed position can deviate by more than 1 mm due to torque and the weight of the detectors even with the best care in assembling the designed mechanical mounts of the detectors.

Such measurement should be done without touching the detectors to avoid altering the configuration setup and damaging the fragile components (such as the detectors, reaction target and MCP foils). The device should be portable and small enough to operate in the S800 scattering chamber. Based on these requirements, we used

a high precision alignment tool, the Laser Based Alignment System (LBAS), to perform the measurement [Rog10-1].

3.5.1 The Laser Based Alignment System (LBAS)

The LBAS is composed of 2 basic devices as shown in Figure 3.25: Acuity laser [Acuity] and two OWIS rotary stages [OWIS]. The acuity laser (Schmitt Measuring Systems, Inc, USA; Model no: Acuity AR600) is contained in a box of 90 mm long, 26 mm wide and 154 mm tall. Laser beam is projected from the housing and is reflected from the target surface to the laser collection system. The laser collection system contains lens for focusing the image of the spot on a CCD digital camera. The laser sensor employs triangulation measurement principles to determine distance with high sensitivity to very low amounts of reflected light. LBAS measures distance in the range of 25.4 to 40.6 cm with resolution of 45.6 *u*m.

The sensor housing box is mounted on two rotary stages with OWIS stepping motors [OWIS] and controllers (Wheedco, Model no: IMJ-105D-1-D). The LBAS stepping motors are controlled by two digital signal processing based motion controllers independently. Two Rotary stages provide angular motion to the laser sensor for the capability of measuring 360 degrees for both theta and phi with resolution better than 0.006 degrees. The overall position measurement can achieve resolution of 52.8-61.9 *u*m. A Java language based program was developed to control the laser, scan with specified step sizes and output the distance, theta and phi in spherical coordinates to a file. Detailed descriptions of LBAS components and operation can be found in ref. [Rog10-1].

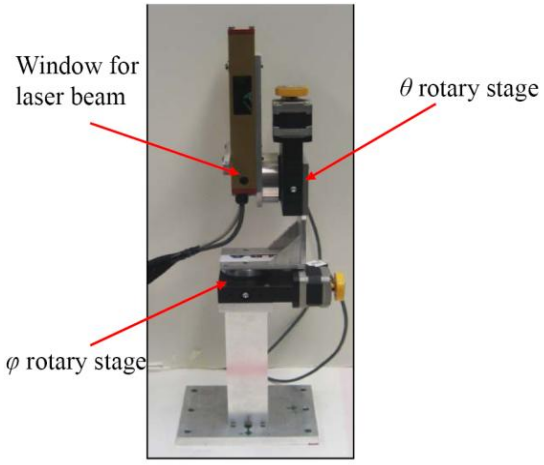

Figure 3.25: Photograph of Laser Based Alignment System (LBAS) with an Acuity laser accommodated inside a box and two OWIS rotary stages.

To determine the position of an edge, laser beam is used to scan along the surface planes and across the edge in between. The abrupt change in the trend of scanned points locates the edge point. Figure 3.26 presents the measured angles in θ-direction verse distances (ρ) obtained in a typical laser scan across a hole on a plate where φ-rotation stage remains stationary. The scanned object is displayed in the right panel of Figure 3.26. A circular hole of 2 mm diameter is located at the center of the rectangular plate, which is used as target mask as described in Section 3.6.2. The hole was covered by a plastic foil on the back side of the plate, which allows laser-light reflection in the hole opening. The red dotted line indicates the path of the laser scan.

The slight fluctuation of scanned points can be attributed to the surface imperfection and roughness of the object; while the outlining data points can be attributed to the variation of the laser beam transportation and deflection. The data with larger distance corresponds to the measurements in the hole region and reflect the plate

thickness of 1.56 mm by design. The abrupt change in the scanned points locates two edge positions of the hole as indicated in the right panel of Figure 3.26. The separation between two edges of about 1.78 mm suggests the laser does not travel through the center of the hole. With another laser scan in the horizontal direction, a total of 4 edge positions of the hole are obtained and the hole center can be interpolated. The measured data points need to be corrected for the offsets due to a non-superposition of the rotation axis of motor stage and the laser source as described in Section 3.5.

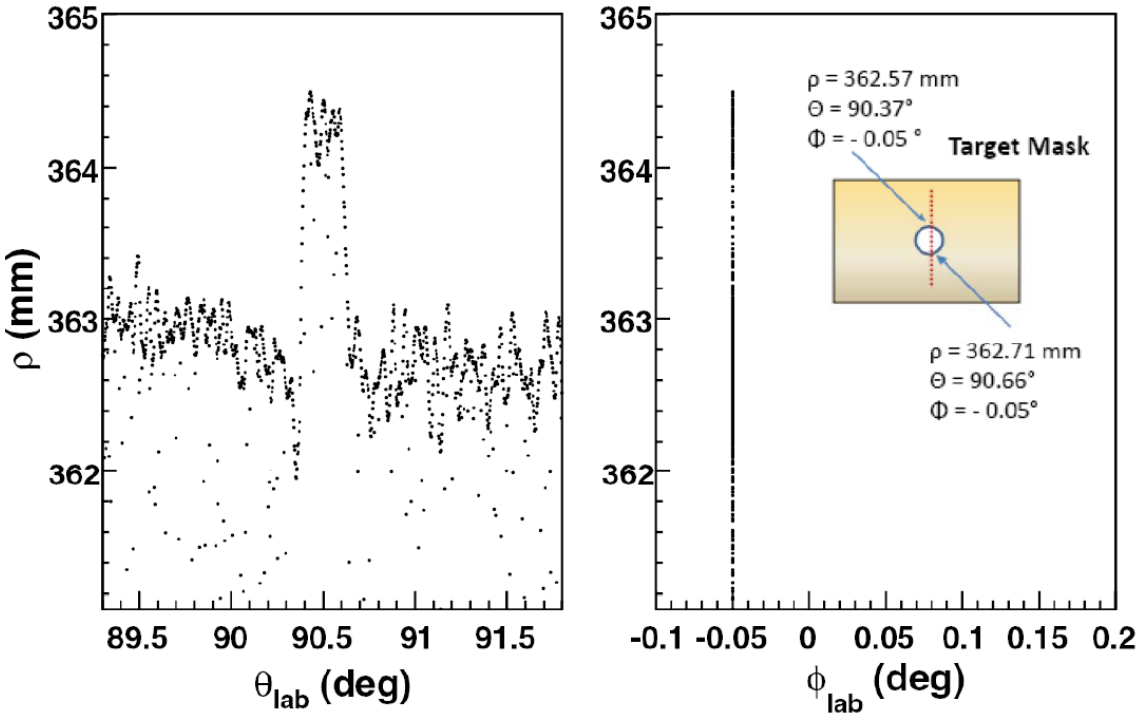

Figure 3.26: Data of angles in θ-direction verse distances (ρ) obtained in a laser scan across a hole on a plate where φ-rotation stage remains stationary. The scanned object with values of measured positions of two edges is shown.

3.5.2 Setup of position measurement

To measure the exact position of the HiRA Array, targets and the two MCP foils, we have to cover an overall distance of 95 cm. Considering the size of the LBAS and the limitation in its measurement range, we had to measure the HiRA array and the target separately with LBAS mounted at different positions. In addition, since it is important to know the positions of the MCP foils relative to the target center, measurements of the MCP0 and MCP1 masks were also performed. The schematic setup of position measurement is shown in Figure 3.27. Along the beam lime, the laser was first placed at position 0 between two MCPs systems (see figure) to measure the reaction target and MCP0 mask. To measure the MCP1 mask, the laser was then moved to the position 1, between the HiRA array and the MCP1 detection system. Finally, the MCP1 detection system and the reaction target ladder were removed, and the laser was moved to position 2 in front of the HiRA array to measure each telescope. A photograph of the setup with laser being placed at position 0 is shown in Figure 3.28.

In order to transform the positions of the HiRA telescopes, target center and MCP masks measured by laser at different locations into one absolute coordinate system, we need to know the laser positions (position 1, 2 and 3) relative to each others. Reference objects were used for such purpose. The positions of the reference objects are shown as grey squares in Figure 3.27. Because of its working principles, LBAS works reasonably in determining the sharp edges. The reference object was therefore designed and machined to be a 1.9 x 1.9 cm^2 square reference post, 35 cm high. Two posts are shown in Figure 3.29. By scanning the edges of the reference posts at different laser

positions, the same corners of the post with respect to different laser positions could be determined and used to match all three laser coordinate systems.

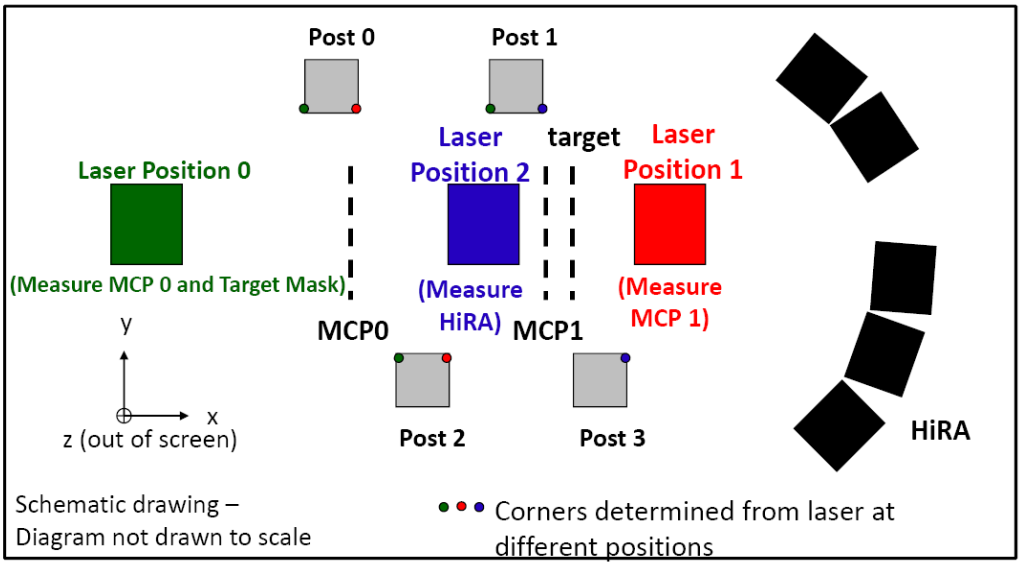

Figure 3.27: Schematic setup of position measurement. The dashed lines indicate the positions of target and foils of MCP0 and MCP1 detection systems. The drawing is not drawn to scale.

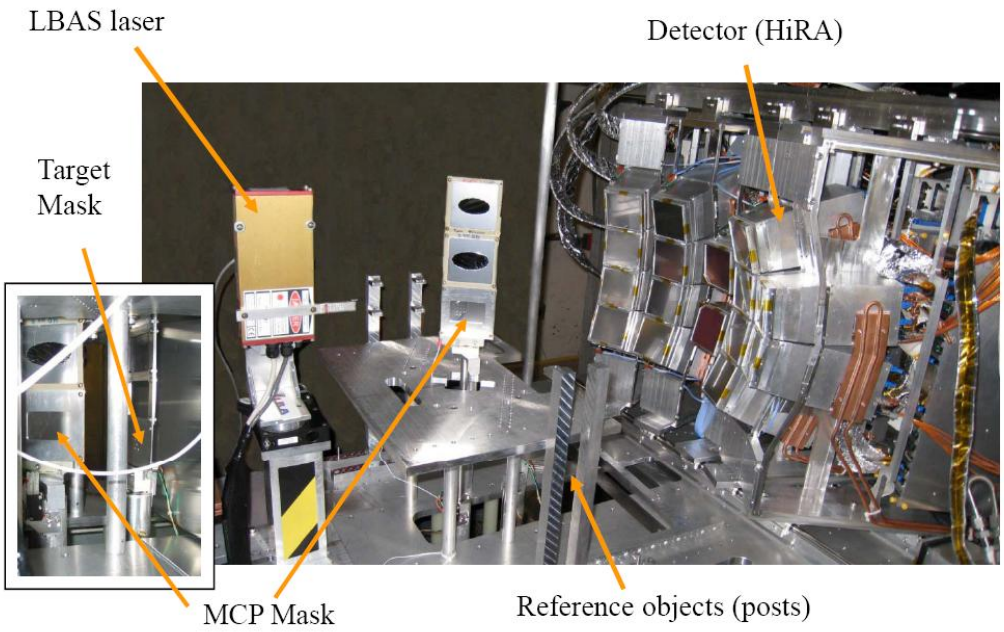

Figure 3.28: Photograph of setup with laser being placed at position 0.

Figure 3.29: A photograph of reference posts used for transforming different laser positions.

To do beam tracking using the S800 inverse mapping, it is important to know the position of our setup (LBAS coordinates) relative to the entire laboratory (global coordinates) and relate our setup to the magnetic elements of the S800 spectrometer. A high-precision laser tracker has been used to measure the locations of various monuments installed around the laboratory and the fiducials on the beamline magnets and defines the location and orientation of the beamline system in the laboratory [San06]. In this experiment, the laser tracker measured the position of the center of balls sitting on reference points along the HiRA alignment posts with respect to the global coordinate system. The corners of the HiRA alignment posts can be deduced from the measured ball positions according to the known dimensions of the posts. By transforming the corners measured in LBAS coordinate to those obtained by laser tracker in the NSCL global coordinate system, we can match our experimental setup to the beamline, all the way back to the K1200 cyclotron. Figure 3.30 shows the layout of the beamline in the

laboratory. Our experiment was performed in S3 vault. The distance between the origin of the NSCL global coordinate system and S3 vault is about 76 meters.

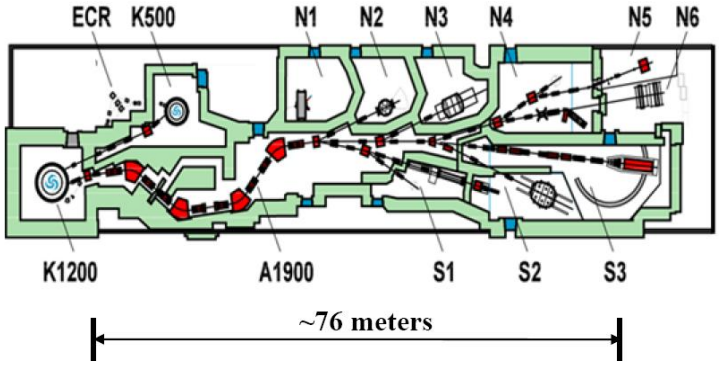

Figure 3.30: Layout of the beamline in the laboratory. The S800 spectrograph is located inside S3 vault.

3.5.3 Offset correction for LBAS

The most significant problem of the LBAS is the non-superposition of the rotation axis of motor stage and the laser source. Ideally, the coordinate axes that define the laser box and OWIS motor stages would be perfectly aligned under rotations. However, due to the inherent mechanical design of how the laser box is rotated, all 3 body axes of the laser source is displaced during rotations as demonstrated in Figure 3.31. The offsets in rotation axes have to be corrected for accurate position measurements.

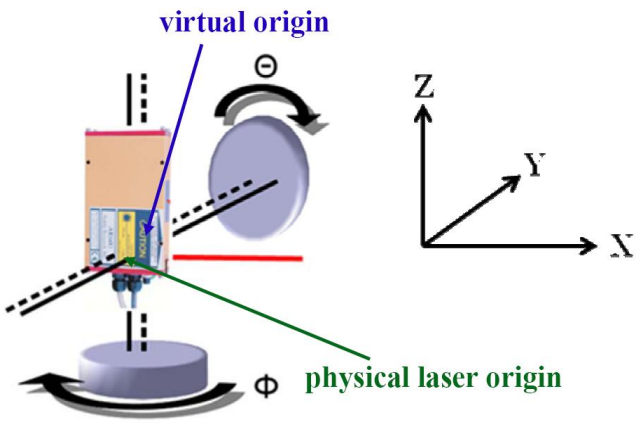

Figure 3.31: Schematics of laser Based Alignment System (LBAS) where the intersection of two dash lines and blue line defines the virtual origin, while the intersection of two solid lines and blue line defines the physical laser origin.

Figure 3.31 defines the axes for θ-rotation perpendicular to that for the φ-rotation and the offsets which need to be determined. There exists a unique plane which is normal to the φ-rotation axis and containing the θ-rotation axis. The intersection of this plane with the φ-rotation axis defines the origin which is shown as the intersection of two dash lines and blue line in Figure 3.31. If the rotation is perfect, this origin remains stationary. Because the laser is not located in this origin, actual laser position after rotations is changed. Thus we would name the origin before rotation as "virtual origin" and after rotation as "physical laser origin" as labeled in Figure 3.31. The offset correction in the axes can be considered as two components: Laser offset correction and theta-stage offset correction. The former one is the correction with respect to the theta-stage rotation axis for aligning laser box with theta-stage axis. The latter one corresponds to the correction with respect to the phi-stage rotation axis for aligning the theta-stage assembly with the

phi-stage. As a result, the offset correction can be written analytically in the following Equation 3.4:

$$\begin{pmatrix} x' \\ y' \\ z' \end{pmatrix} = \begin{pmatrix} \rho sin\theta cos\varphi \\ \rho sin\theta sin\varphi \\ \rho cos\theta \end{pmatrix} + \begin{pmatrix} cos\varphi & sin\varphi & 0 \\ -sin\varphi & cos\varphi & 0 \\ 0 & 0 & 1 \end{pmatrix} \begin{pmatrix} \cos(\theta - 90°) & 0 & -sin(\theta - 90°) \\ 0 & 1 & 0 \\ sin(\theta - 90°) & 0 & cos(\theta - 90°) \end{pmatrix} \begin{pmatrix} \Delta x \\ 0 \\ \Delta z \end{pmatrix} + \begin{pmatrix} cos\varphi & sin\varphi & 0 \\ -sin\varphi & cos\varphi & 0 \\ 0 & 0 & 1 \end{pmatrix} \begin{pmatrix} \Delta x_{\varphi} \\ \Delta y_{\varphi} \\ 0 \end{pmatrix} \quad (3.4)$$

The sum in the RHS of Equation 3.4 consists of three parts: The first part is the vector point from the physical laser origin to the measured object. The second part is the theta-stage offset correction, denoted by the vector (Δx, 0, Δz), which aligns the physical laser origin to θ axis. The third part is the phi-stage offset correction, denoted by the vector (Δx_{φ}, Δy_{φ} ,0), which aligns the θ axis to the φ axis. The second and third terms of the sum together give the vector pointing from the virtual origin to the physical laser origin.

In the Cartesian coordinate system, the direction of $\varphi = 0^{o}$ and $\theta = 90^{o}$ defines the *x* direction. The φ axis (i.e. $\theta = 0^{o}$) defines the *z* axis. *y* direction is defined by the **z** × **x**. The coordinate system is hence right-handed. The convention used in LBAS is that **x** is the beam direction, **z** direction is vertical-up, and **y** is defined by **z** × **x**. It is important to note that the LABS convention is different from the one used in standard laboratory convention where z is the beam direction for instance. The reason of using the current

convention in LBAS is because it closely coincides with the basic movement and orientation of LBAS.

Displacements of all components (Δx, Δz, Δx_{φ}, Δy_{φ}) were measured on the granite surface plate with tall vertical caliper and steel calibration plates. It is found that the largest correction is the 7.5431 mm displacement of the laser box with respect to the theta-rotation stage (Δz). The other corrections are relatively smaller with Δx=-0.1300 mm, Δx_{φ}=-0.1400mm and Δy_{φ}=-0.4198mm.

3.6 LABS Position measurements

After extracting all the edge points from the laser scanning corrected for laser offsets as discussed in section 3.5, we analyzed the data and determined the position of objects in a quantitative and systematic approach. The whole method relies on the least square plane fitting constrained by dimensions of the objects. There are three types of objects measured: reference posts, HiRA telescopes and masks for both reaction target and MCP foils. With the systematic and general analytical method, 0.3 millimeters (which corresponds to 0.05°) precision, well below the intrinsic position resolution of the detectors, is achieved in present experiment. Such accuracy is sufficient for the transfer experiment. In the following sections, data analysis and results on the LBAS measurement for the entire experimental system will be discussed in detail.

3.6.1 Transformations of laser coordinate systems

Due to the limitations of the laser measurement ranges, laser scanning data for the whole system in the scattering chamber were acquired in three different positions as shown in Figure 3.27. Transformations among different laser positions are determined by scanning the reference posts (gray squares) as shown in Figure 3.27. For each reference post, LBAS measured five edges with three scans made on each edge as demonstrated in Figure 3.32. Three planes can be consequently constructed by least-square plane fitting which requires the planes to be orthogonal. The intersection of the 3 planes defines the corner position of the post. Lasers at different locations measured different corners within one post which can be matched using the known mechanical dimension of the post. Transformation between the positions of the same corners with respect to different lasers could be performed by Equation 3.5:

$$\mathbf{x}_a = \mathbf{R}(\theta)\mathbf{x}_b + \mathbf{d} \qquad (3.5)$$

where $\mathbf{x}_a$ and $\mathbf{x}_b$ are the same point in space relative to different laser positions. $\mathbf{R}=\mathbf{R_x}(\theta_x)\mathbf{R_y}(\theta_y)\mathbf{R_z}(\theta_z)$ is the rotation matrix which is characterized by 3 angles θ_x, θ_y and θ_z; and $\mathbf{d}$ is the translation vector characterized by 3 vector components d_x, d_y and d_z. There are altogether six parameters that need to be determined.

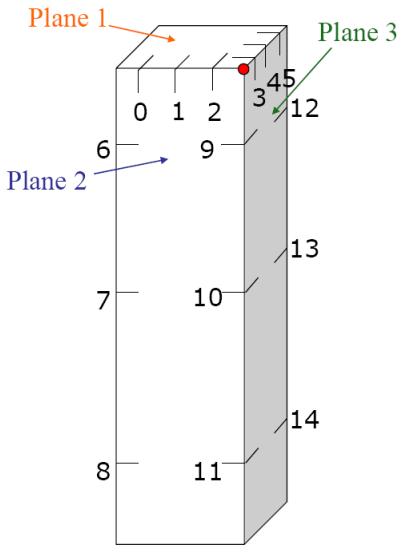

Figure 3.32: Schematic diagram to present the strategy of laser scanning on the post.

We selected the co-ordinates of laser position 2 as the LBAS reference where HiRA telescopes were measured. For the transformation from laser position 0 to laser position 2, we found that the rotation (θ_x, θ_y, θ_z)=(-0.16°, -0.30°, 0°) and the translation (d_x, d_y, d_z) = (-401.59mm, 0.58mm, -1.17mm). The -1.17 mm difference in z direction between laser 0 and laser 2 reflects the non-flatness of the aluminum table where the HiRA and MCP detection systems are placed. The transformation from laser 1 to laser 2 could not be determined from fitting due to insufficient data points taken with LBAS. Therefore, we only calculated the translation vector by subtracting two laser measurements on the same point which gives (d_x, d_y, d_z)=(123.15mm, -0.84mm, 0.15mm).

Regarding the transformation of the LABS to the NSCL global coordinates system [San06], we employed the same algorithm as Equation 3.5. Balls placed on the

stand mounted on the sides of the posts were measured by the laser tracker and the centers of the balls were consequently deduced in global coordinates system. The mount is mechanically attached to the post by dowel pins and screws and can be moved to different heights as shown in Figure 3.29. Using the dimension of the post, we could determine the ball center from the deduced corner positions in LABS coordinate system. We transformed the global coordinates to laser 2 position and found the rotation (θ_x, θ_y, θ_z)=(0.01°, -0.06°, 5.47°) and the translation (d_x, d_y, d_z)=(-75191.7mm, -14193.2mm, 5512.7mm). It is known that the S800 beam line is at an angle of 5.46° relative to the cyclotron beam axis in the global coordinates system, the θ_z value of 5.47° in our deduced transformation matrix shows good agreement. This verifies proper alignment of the detectors in the chamber and the S800 magnets and indicates accurate position determinations with LBAS.

3.6.2 Reaction target position

A large target with dimensions of 4.1 cm x 5.7 cm was used in this experiment to accommodate the large beam spot (~2 cm in diameter for ^{46}Ar beams). To determine the position of the target center, a mask with 5 well-defined holes as shown in Figure 3.33 occupied one of the target positions. During the experiment, the target mask was remotely inserted by the target drive to the position where the center hole is located at the center of the target. Figure 3.33 shows the target ladder with a beam scintillator viewer placed on the top following by four $(CH_2)_n$ reaction targets of different thickness, a highly uniform thickness of carbon target and target mask. Two laser scans were

performed on each hole on the mask giving a total of 20 edge points as shown in Figure 3.33. We obtained the first-order estimate of the centers by averaging the scanned edge points of each hole. Determination of center positions was done by requiring that all the centers lie on the plane forming a 1 cm x 1 cm square. The center of the central hole corrected for the target mask thickness represents the reaction target center.

The results indicate the target mask is titled by 0.7 degree with respect to the beam axis. We have problems in determining the radius of the hole precisely because the holes appeared to be elliptical instead of circular in the analysis. It could be contributed by the long distance from the laser to the target mask which is about ~36 cm apart (the optimal measurement range of LBAS is 25.4 - 40.6 cm) and the asymmetric shape of the finite-size laser beam spot.

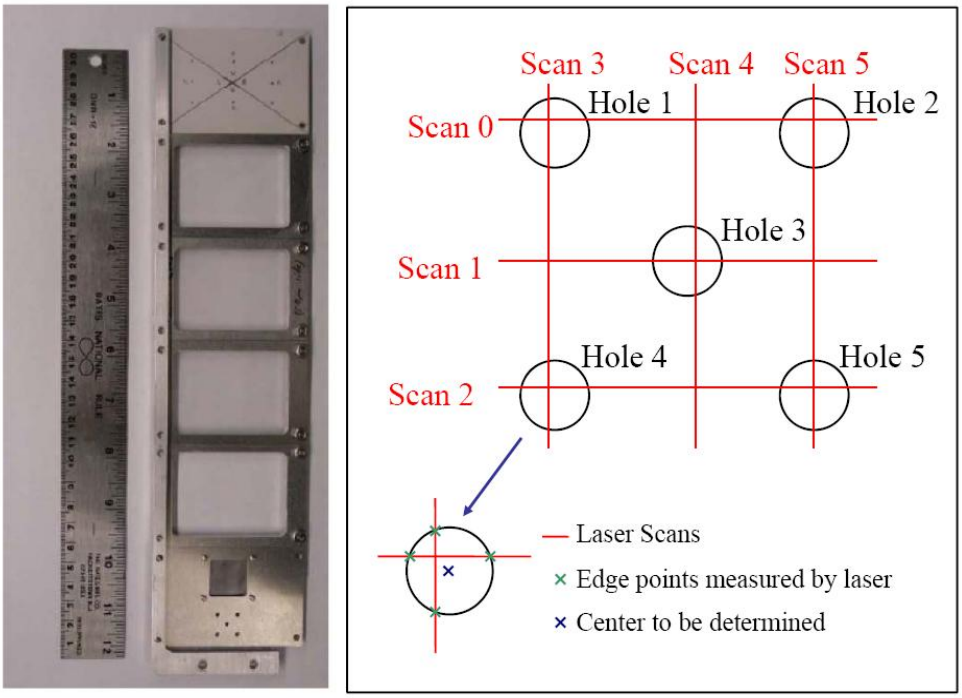

Figure 3.33: (left) Target ladder with a beam scintillator viewer placed on the top following by four $(CH_2)_n$ reaction targets of different thickness, a highly uniform carbon target (appeared as a black square and target mask. (Right) Schematic diagram of the strategy of laser scanning on the target mask.

3.6.3 HiRA pixel position

A layer of 265 *u*g/cm^2 aluminized mylar foil is attached to the frame that covers the window of each HiRA telescope. This foil is used to provide a dark environment to the Si detectors and protect them from electrons produced in nuclear collisions. More importantly, the Al layer on the mylar in contact with the frame provides a faraday cage to the telescope. For each HiRA telescope, the frame was measured with three scans performed on each side. Four corner positions of the frame were determined by fitting the plane with the constraints of 4 corners forming a square lying on the same plane. Since

the distance between the frame and the silicon detectors is known, the positions of the pixels were then deduced from the 4 corners of the frame with information of the strip dimension. The center of reaction target is defined as the origin in our reaction system.

Figure 3.34 and 3.35 compare the positions between the LBAS measurement and mechanical design. Most of them are in good agreement, while some of the pixels deviate up to 0.9°. Table 3.1 summarizes the distance from the center of each telescope (Si face) to the target. Our LBAS measurements give 35.97 ± 0.12 cm while the design is 35.76 cm. It is also shown in Table 3.1 that the normal of some telescopes did not point to the target center. The maximum deviation, the angle between of normal of telescope face and the line joining the center of telescope to center of target, is 2.58° (telescope 5). These systematic and consistent discrepancies reflect the distortion in the mounting structure.

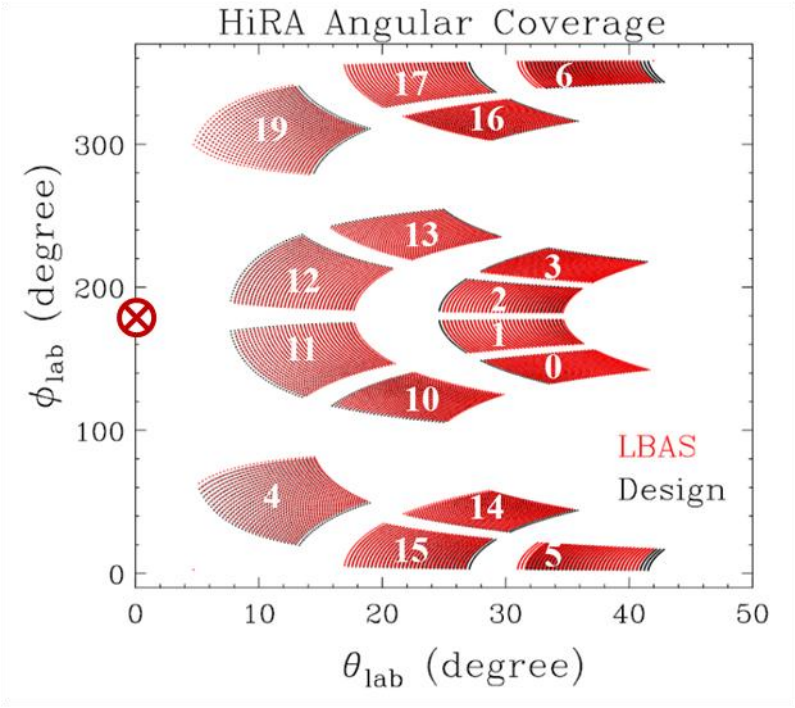

Figure 3.34: Comparison between the telescope angles on theta and phi in laboratory frame obtained from the LBAS measurements and mechanical design.

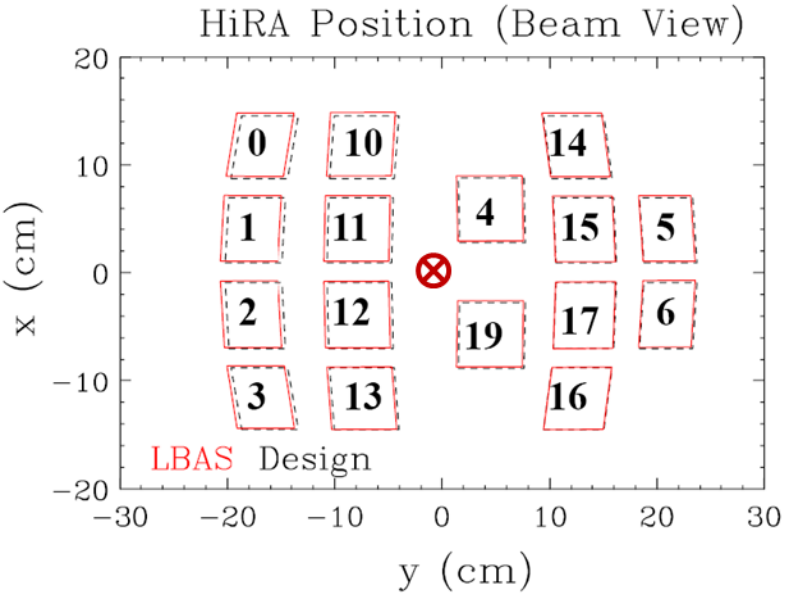

Figure 3.35: Comparison between the telescope positions obtained from the LBAS measurements and mechanical design.

Tower	Telescope	Titled angle (deg)	distance (mm)
0	0	1.03	360.73
0	1	1.44	360.52
0	2	1.39	360.16
0	3	1.43	359.02
3-I	4	0.24	360.57
3-I	19	0.42	359.37
3-O	5	2.58	360.43
3-O	6	2.10	359.57
1	10	1.17	360.30
1	11	1.43	359.53
1	12	1.30	359.29
1	13	1.34	358.52
2	14	2.09	359.87
2	15	1.92	359.11
2	16	1.76	358.63
2	17	1.75	358.86
		Average	359.66
		Design	357.63

Table 3.1: Summary of the distances of the telescope center and target center, and the angles between the normal of the telescope (Si face) and the normal of reaction target.

3.6.4 MCP foil position

To obtain the information about the MCP foil positions, laser scanning on the MCP mask was performed. A MCP mask for position calibration is show in Figure 3.36. A brass MCP mask with an array of holes was inserted to the foil position for each MCP detection system. The holes are 5 mm apart. The smaller holes have a diameter of 0.75 mm while an “L” pattern, used for orientation of the mask pattern, is composed of six larger holes, each with a diameter of 1.5 mm.

Figure 3.37 displays the configuration of six large holes on each MCP mask. Following the same strategy used in the target mask measurement, four edge points were obtained for each hole and used to constrain fitting to determine the centers of holes. The results show that the angle between MCP foil and the beam is 58.46° for MCP0 and 59.79° for MCP1. It should be 60° by design. The centers of the MCP0 and MCP1 foil deviate from the target center by approximately 1.5 mm and 0.7 mm in vertical and 0.91 mm and 0.54 mm in horizontal direction respectively. To achieve the best angular and energy resolution at large laboratory angles, these offsets are taken into account in the analysis.

It is interesting to find that the radii of the holes in the MCP mask are better determined compared to the target mask. This may be attributed to the fact that the measuring distance for MCP mask better fulfilled the measurement range of LBAS (Laser was put at about 24-26 cm from the MCP masks in present measurement) and the MCP mask is thinner (0.13 mm) than the target mask (1.57 mm) which allows better determination of the positions of edges around the hole.

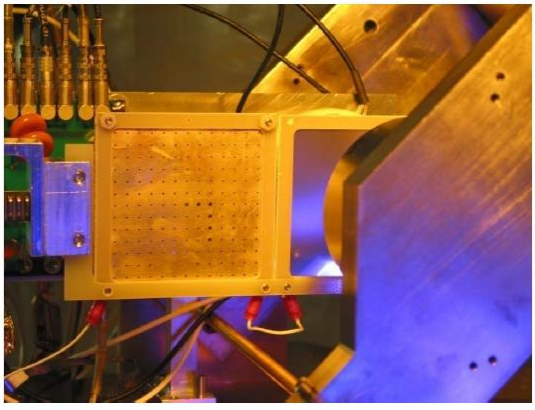

Figure 3.36: A photograph of a MCP mask for position calibration.

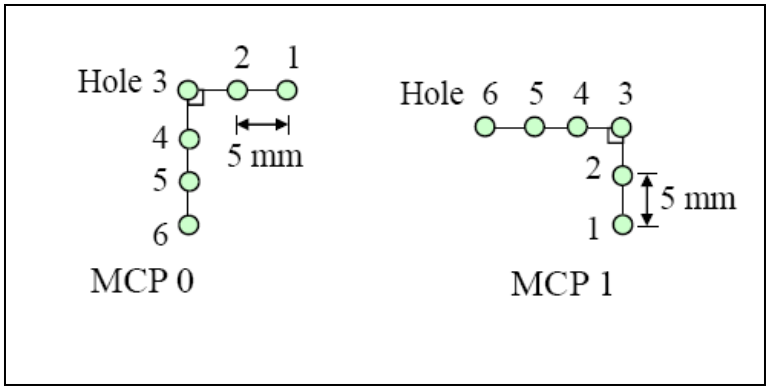

Figure 3.37: The configuration of six large holes in the MCP mask.

3.7 Electronic and Data acquisition system

Figure 3.38 (a-c) are the schematic diagrams of the electronic circuit of this experiment. The data acquisition system can be divided into three parts, the S800 (Fig. 3.38a), the HiRA (Fig. 3.38b) and the MCP's (Fig. 3.38c). The kinematically complete measurements were achieved using the high resolution silicon array (HiRA), to detect the deuterons in coincidence with the recoil residues detected in the S800 mass spectrometer. Therefore, the "AND" signal from HiRA and S800 serves as the main trigger in the S800 trigger box. The MCP signals came as slave signals which were recorded for the coincidence events or downscaled MCP events.

Concerning the S800, the signals from the up and down PMT's of the first scintillator E1 are amplified and split. One of them is read by its own fast encoding ADC (FERA), and another is sent to a constant fraction discriminator (CFD) module to provide a logic pulse. The outputs of the CFDs are logically AND-ed to give the S800 premaster signal. The S800 premaster signal is used as the start for the drift time in the CRDCs,

while the CFD output of the anode wires in the CRDC detector is used as the stop for the flight time information taken relative to the RF pulses of the cyclotron. The Time to Analog Converter (TAC) output is digitized by the analog-to-digital converter (ADC). Each cathode pad (a total of 224 in each CRDC) is read by the STAR Front End Electronic (FEE) system. The STAR FEE read is enabled by the S800 premaster and stopped by the anode pulse. Signals such as E1 timing or XFP timing are digitized by the S800 TDC (Phillips 7186H). The input mapping of the S800 TDC is listed in Ref.[S800]. In addition, the S800 premaster timing signal is delayed and sent to the MCP time-to-digital convertor (TDC) (CAEN V775).

In the HiRA data electronics system, the signal from DE, EF or EB is sent to the amplifier, the pseudo-constant fraction discriminator CFD) and the shaper implemented in the ASIC. If the signal passes through the CFD, then the time, energy and event address are sent to the HiRA motherboard buffer. In addition, the CFD time signal is sent to a logical OR to trigger the XLM universal logic module via the ECL-NIM module. The “OR” signals from different motherboards are fanned out and logically OR-ed to give the HiRA premaster signal. The HiRA premaster is then AND-ed with the S800 signal to give coincidence premaster signal. In addition, the OR-ed signal from all towers for E detectors is delayed and sent to the MCP TDC.

The control of the readout and storing of address from each motherboard along with the Flash analog-to-digital converter (FADC) clock are handled by an XLM. Once the XLM is triggered, the event address information is sent directly to the XLM and the corresponding time and energy information are sent to the FADC. A clock signal issued

by XLM is input to FADC to initiate FADC to digitize the time and energy signals and store them in its internal buffer. When the requested data is no longer acknowledged by the motherboard, a logic "complete" signal is sent out by XLM and used as the start for the trigger latch. On the other hand, the master is then logically AND-ed with the NOT *BUSY* signal from the computer and coincidence premaster. The master signal serves as the start signal to the computer and stop signal for the NIM Latch.

The NIM output signals from three latch modules are AND-ed to preserve the slowest signal and give the HiRA singles trigger signal which is sent to the S800 trigger box. The HiRA singles (labeled as "Secondary" in the S800 trigger box) was selected when HiRA was used for data taking such as alpha source data runs.

The signal from CsI, amplified by the preamplifier board located within the telescope, is sent to the external CAMAC Pico System shaper modules. Output from the variable gain shaping amplifiers is routed to the ADC (CAEN V785). The gating and readout of the peak sensing ADC is triggered by the master signal. The ADC module is operated in zero compression mode ensuring that only those channels with signal heights above the thresholds are read in the individual ADC channels. There are four other CsI crystals used for monitoring the reaction rates. The OR signals from the crystals is further OR-ed with the MCP OR signal to provide another trigger labeled as "External 1" in the S800 trigger box.

In the MCP detection system, signal of each corner is amplified by the fast amplifiers (ORTEC 820). The signal is split and digitized by the charge-to-digital converter (QDCs) (CAEN V792N) with and without further being amplified (High and

low gain). The timing signal from the MCP is sent to the fast amplifiers (ORTEC VT120) and constant-fraction discriminator, then the logic signal is split into two. One will be delayed and eventually be digitized by TDC. Another signal is OR-ed with the same timing signal from another MCP. The OR signal is downscaled by the rate divider and further split into two. One is delayed and serves as the common stop to the TDC. Another is delayed and OR-ed with the master trigger to generate the gate signals for the QDCs. The latter one is also OR-ed with the OR signal from four CsI monitor crystals and used as one of the trigger conditions (External 1).

The data acquisition was performed by running the standard NSCL data acquisition system NSCLDAQ [Daq] in the Linux operating system. The data were collected and distributed by the SpectroDaq server. In addition to writing the data on disks, the NSCLDAQ allows user to run online analysis using NSCL SpecTcl software [Spectcl].

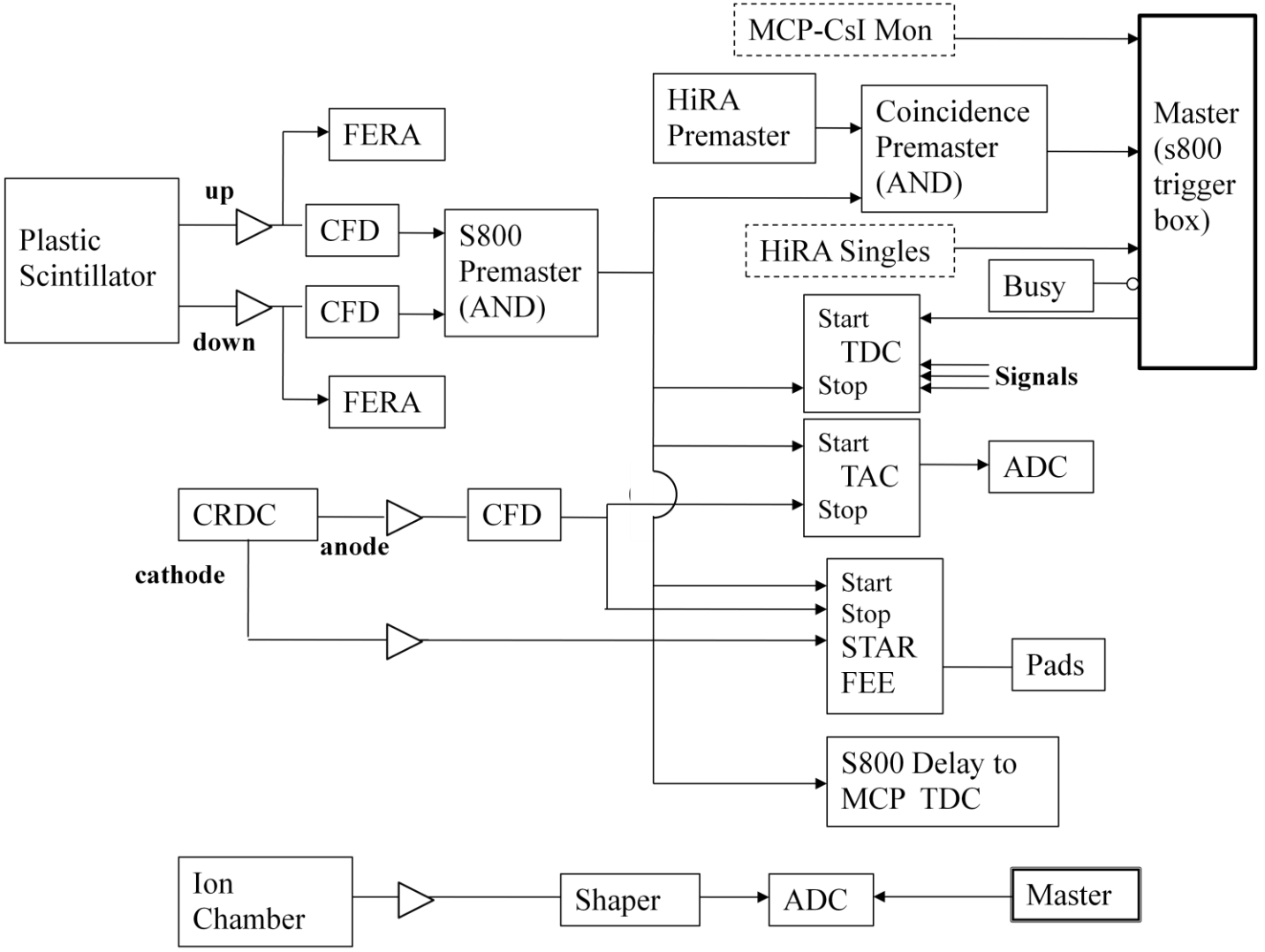

Figure 3.38a: Schematic of data acquisition system (S800).

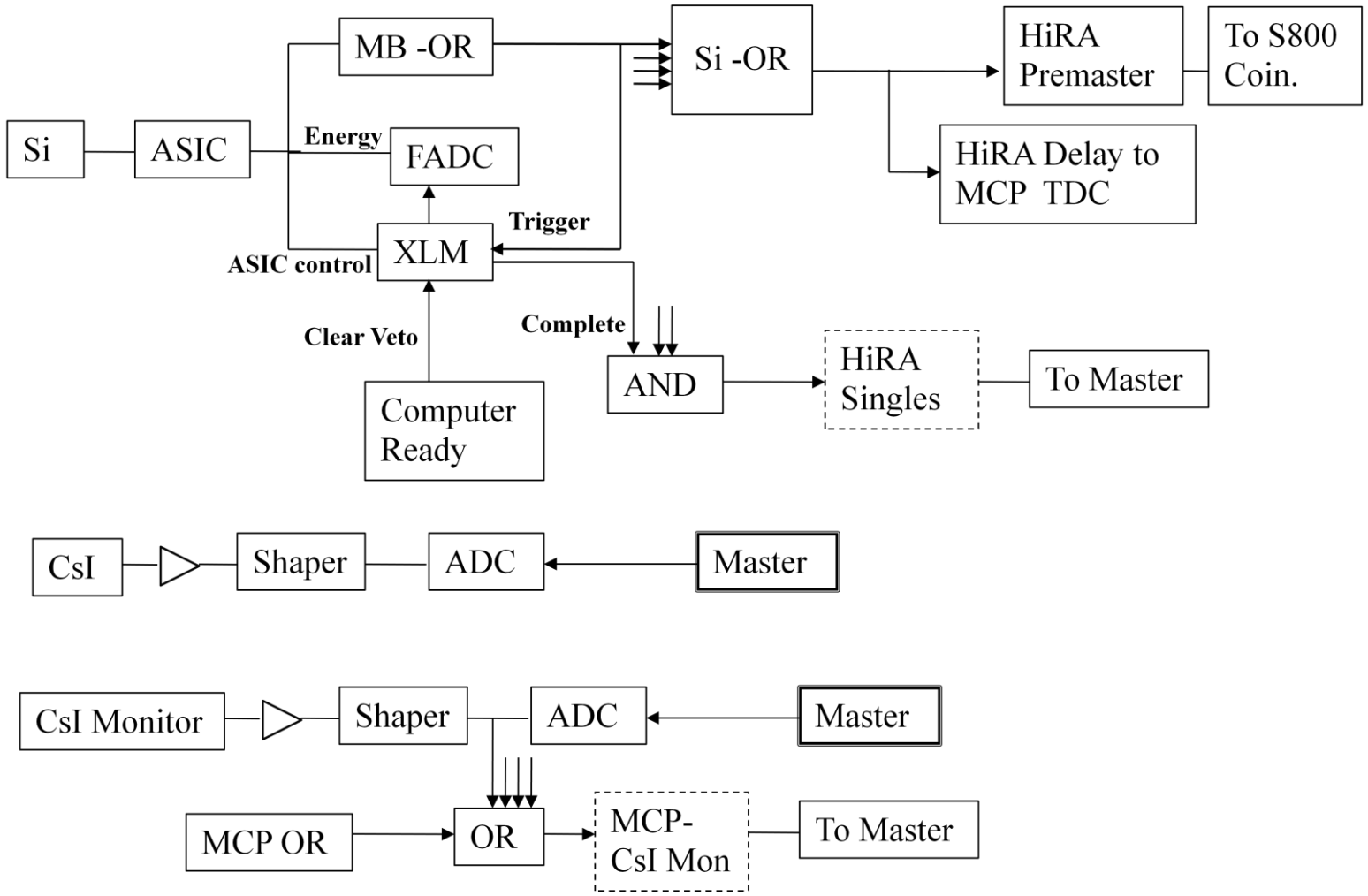

Figure 3.38b: Schematic of data acquisition system (HiRA).

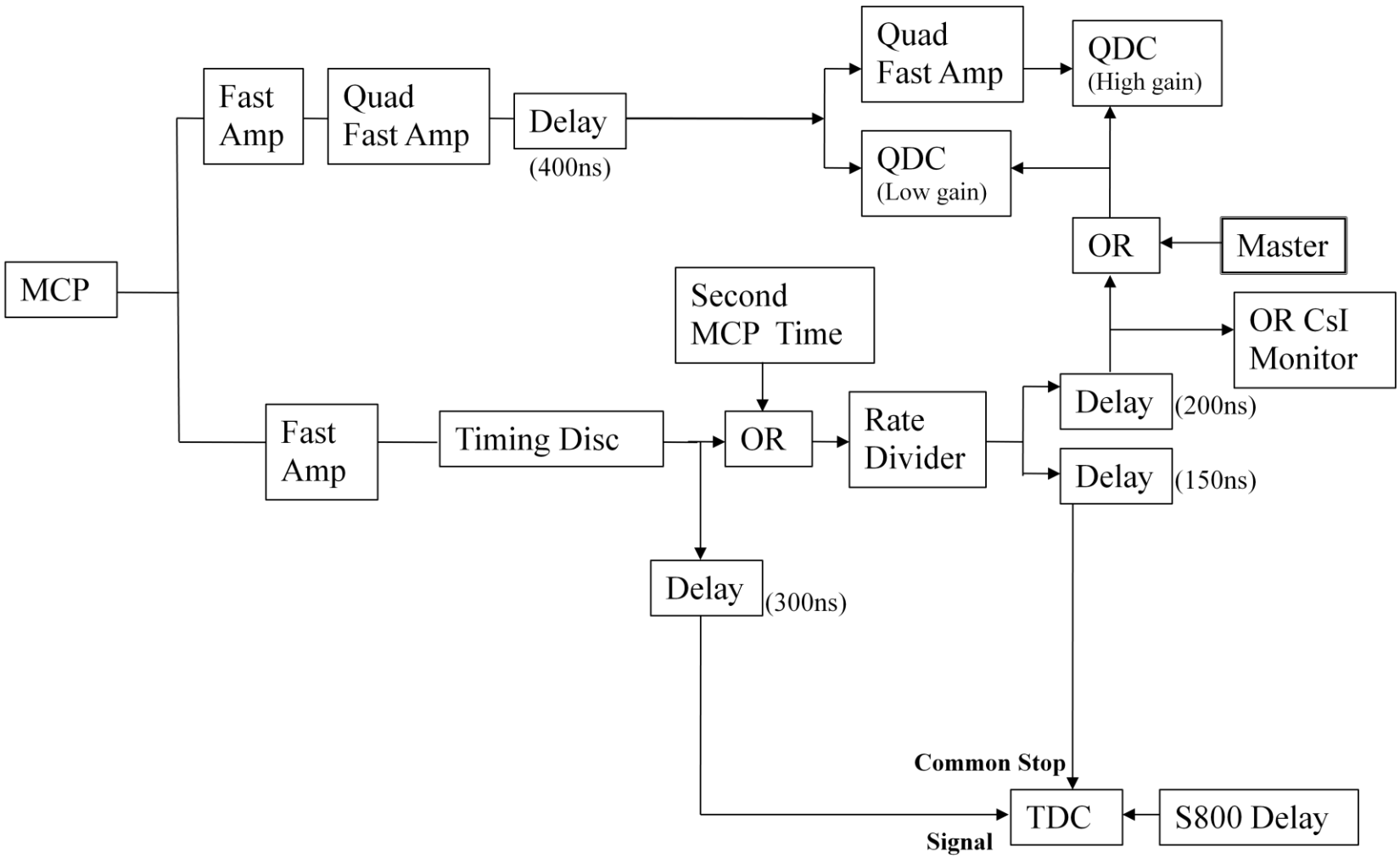

Figure 3.38c: Schematic of data acquisition system (MCP).

Chapter 4

Data Processing and Analysis

4.1 Overview of the analysis

Figure 4.1 shows the flow chart of the data analysis for converting the raw data into the final physics results. In general, the analysis splits into three streams comprising HiRA, S800 and MCP. The raw data stored in the event files are decoded and sorted into three different ROOT [ROOT] files, each containing the data relevant to its own pathway. This strategy reduces the sizes of data files and time needed in the analysis of each device. The analysis data from each device is combined to provide the final measurements.

In HiRA analysis, we first analyzed data of precision pulser and corrected the readout order problems in the chip electronics. Then the energy calibrations for silicon and CsI detectors were performed. The HiRA analysis incorporates the pixelation procedure which associates specific EF and EB strips hit by the same particle, and further links the identified particle in the EF-EB pixel to its corresponding DE strip and CsI crystal. Eventually, the HiRA particle identification (PID) gates were constructed. On the other hand, the S800 analysis aims at constructing identification gates of both beam particles and reaction residues. Identification of the residues requires CRDC position determination and the trajectory corrections to the time-of-flight and energy in the S800 focal plane. Regarding MCP analysis, the main objective is to construct beam trajectory

and correct deuteron scattering angles using the actual beam positions on the reaction target.

By merging the calibrated data files generated in each analysis pathway, deuterons produced from the reactions of interest with the scattering angles corrected for beam positions could be identified using HiRA, MCP and S800 gates. The corresponding reaction Q-value was calculated on an event-by-event basis. Finally, the full set of information consisting of the kinematic energies and emission angles for the deuterons of interest, Q-values as well as the counts of deuterons within defined angular bins was recorded in the final physics ROOT file. In the subsequent sections of this chapter, the analysis and associated problems will be discussed in detail. In order to obtain the reaction cross sections, background from random coincidence should be subtracted. In addition, normalization is needed to determine the cross sections in absolute magnitudes. The detection efficiency would have to be calculated and corrected due to the limited coverage of HiRA array. The analysis results and the extraction of cross sections will be discussed in Chapter 5.

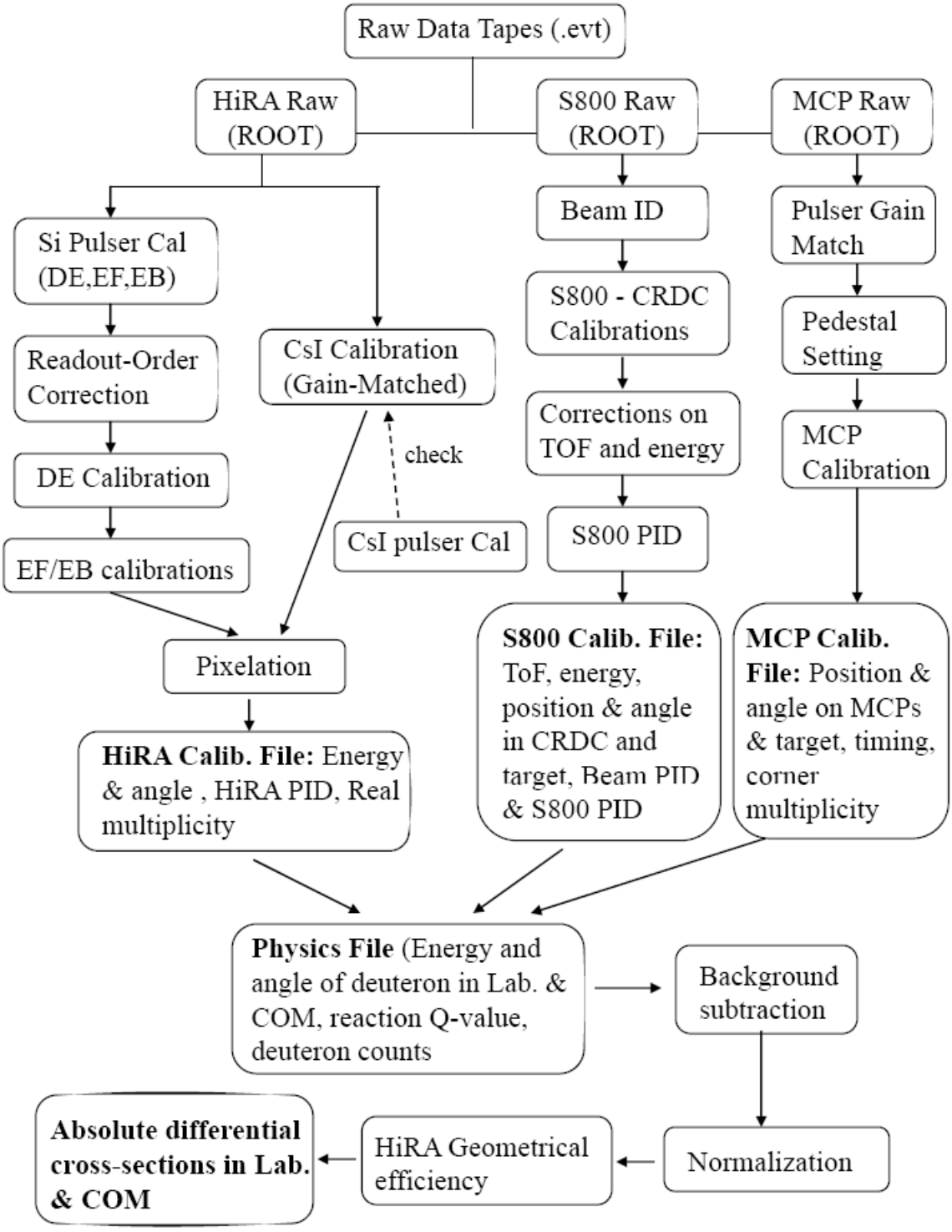

Figure 4.1: Flow chart of the data analysis

4.2 High Resolution Array (HiRA)

The high resolution array (HiRA) was employed to measure the energies and positions of the emitted deuterons in this experiment. Each HiRA telescope contains silicon strip detectors and CsI crystals. This section focuses on the calibration procedures which include the corrections on readout order, actual silicon detector thickness and total calibrated energies. The thickness uniformity and dead-layer thickness of silicon detectors are examined. The difficulties in CsI calibrations are discussed. For proper particle identification, pixelation method which utilizes the position information to associate energies measured in DE, E and CsI for a single particle is also presented.

4.2.1 Silicon energy calibrations

4.2.1.1 Readout Order Problems

This method to correct the readout order is mainly based on the findings of V. Henzl in the data analysis of NSCL Expt03045 [Expt03045]. The main defect of the current ASIC electronics is the readout order problems on the chipboards and motherboards. It is discovered that the raw channel number read out from the chipboard (CB) and motherboard (MB) is significantly shifted by various amounts depending on the readout order. The response also depends on the particular channel in the chipboard and its position within the motherboard. No universal corrections can be applied because the shifts would vary for different settings of the gains and dynamic ranges etc.

The problem is illustrated by the double peak structures that were observed in the pulser ramp on the EF strips with the precision IU pulser [IU]. IU pulser is an automated

pulsing system which is stable to within ~0.1 %. It injects a precise voltage into the test input of each channel of the silicon detector electronics while the detectors were still attached. The pulser ramp (a series of signals with a constant increment of pulsed voltage) was carried out for all strips individually. Figure 4.2 shows the spectrum of IU pulser ramp in one electronic channel. The double peak structures, which are clearly identified around channel 3100 and 4200, were found to be the consequence of cross-talk induced on the neighboring detector strips. Figure 4.3 shows the cross-talk problem on the neighboring strips when pulsing only tele10 EF strip 10 by the IU pulser from channel 4000 to 16000.

The top two panels of Figure 4.3 show that cross-talk was induced on strips 9 and 11 respectively when the pulse on strip 10 was sufficiently high. And the bottom panel shows the correlation of two cross-talk signals on strip 9 and 11 when their common neighbor (strip 10) was fired. Such cross-talk induced by high energy pulses is also observed in the experimental data. The cross-talk induction depends on the energy of the mother pulse and threshold on the corresponding electronic channel of the recipient strip. In addition, by performing the IU pulser ramp with and without detector attached, the cross-talk signals are shown to come from the detector itself, not on the cables, chipboards or IU pulser.

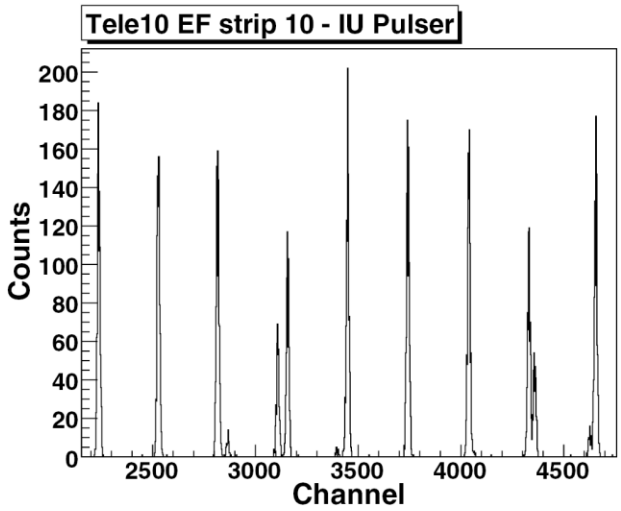

Figure 4.2: Spectrum of IU pulser ramp in one electronic channel.

Such cross-talk causes a serious problem in our readout electronic system. On the chipboard, chip 0 is the first chip readout. With the ASIC chip mapping file used in this experiment, the chip with odd channels is always read prior to the chip with even channels for EF and the order is reversed for EB. If the main signal on the even strip is too small to induce cross-talk, then it will be read first. But if it is large, cross-talks can be induced up to 2 strips left and right from the pulsed strip, resulting in the pulsed strip being read as the second to the forth in the readout sequences. On the motherboard, the chipboards are readout from the bottom slot to the top. Since the chipboard for EB is conventionally inserted in a lower slot than the corresponding EF, EB is read first and therefore read-order correction affects EF most. If the signal is big enough to induce severe cross-talk in the adjacent strips on the EB side, readout correction for EF pulsed strip needs to be determined up to significantly high order.

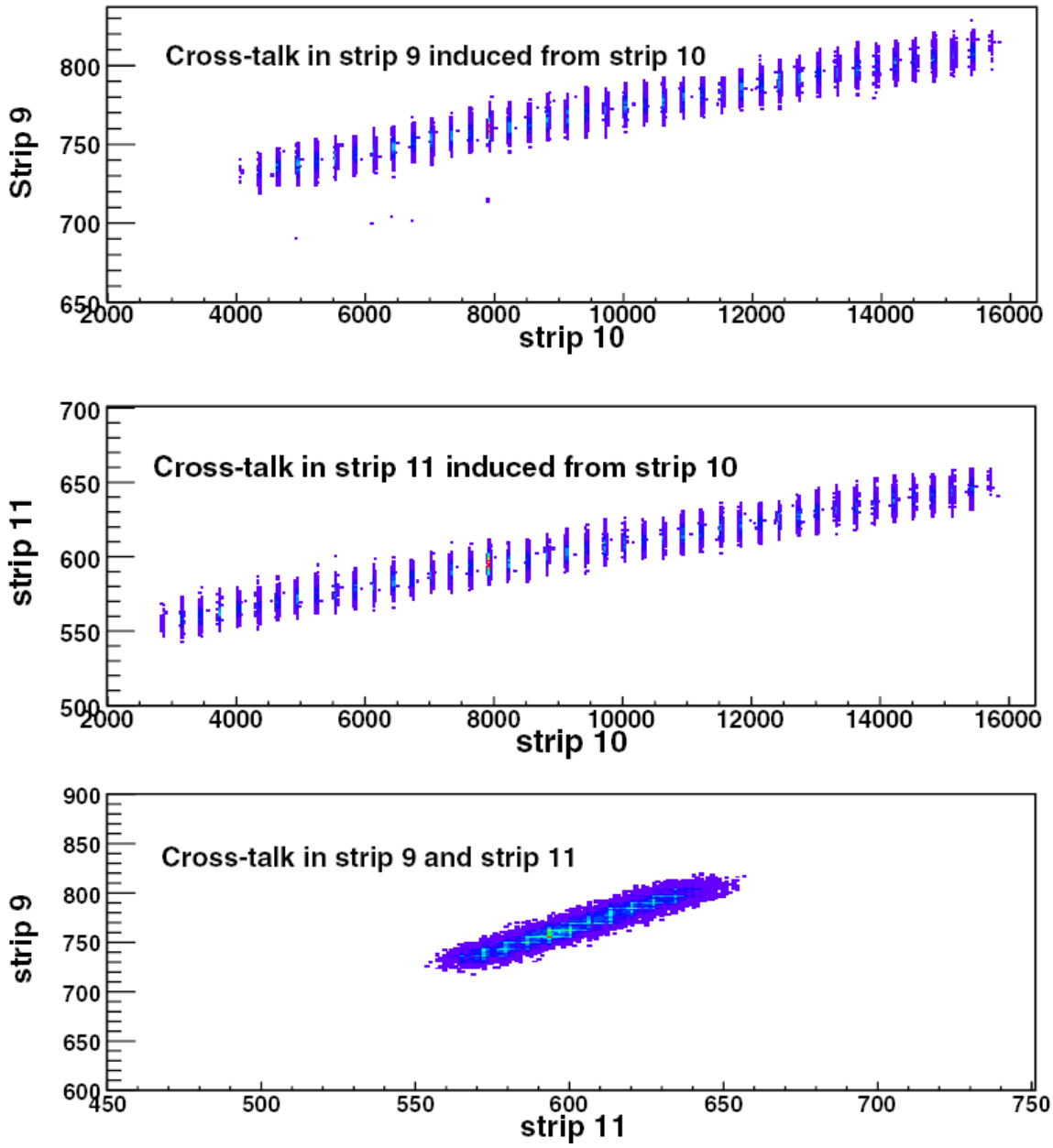

Figure 4.3: Cross-talk problem on the neighboring strips (strip 9 and 11) when only one strin (strip) is pulsed by IU pulser.

^{228}Th source calibration data are used to examine the effect of readout order problem on energy resolution. The decay of ^{228}Th is characterized by eight well-known alpha energies and the alpha peaks are separated by at least 100keV. The diagram of the ^{228}Th decay chain is displayed in Figure 4.4. There are five strong alpha peaks with energies of 8.787, 6.778, 6.288, 5.685 and 5.423 MeV. Figure 4.5 is a spectrum of alpha particles emitted from the decay of ^{228}Th. Without any readout-order corrections, there are severe peak shifts in raw channel for one EF strip read out directly from the electronics. Figure 4.6 shows the same alpha spectrum after readout order corrections are applied. It is apparent that readout order correction is critical and essential for correct calibration and energy resolution of silicon E detector.

For DE detectors with preamps outside the chamber, it is found from the alpha source data that the statistics in the second (or higher) readout sequence is significantly lower than that of the first order. While low statistics is not sufficient to determine the readout corrections for DE, it indeed suggests that the readout order issue in DE can be neglected.

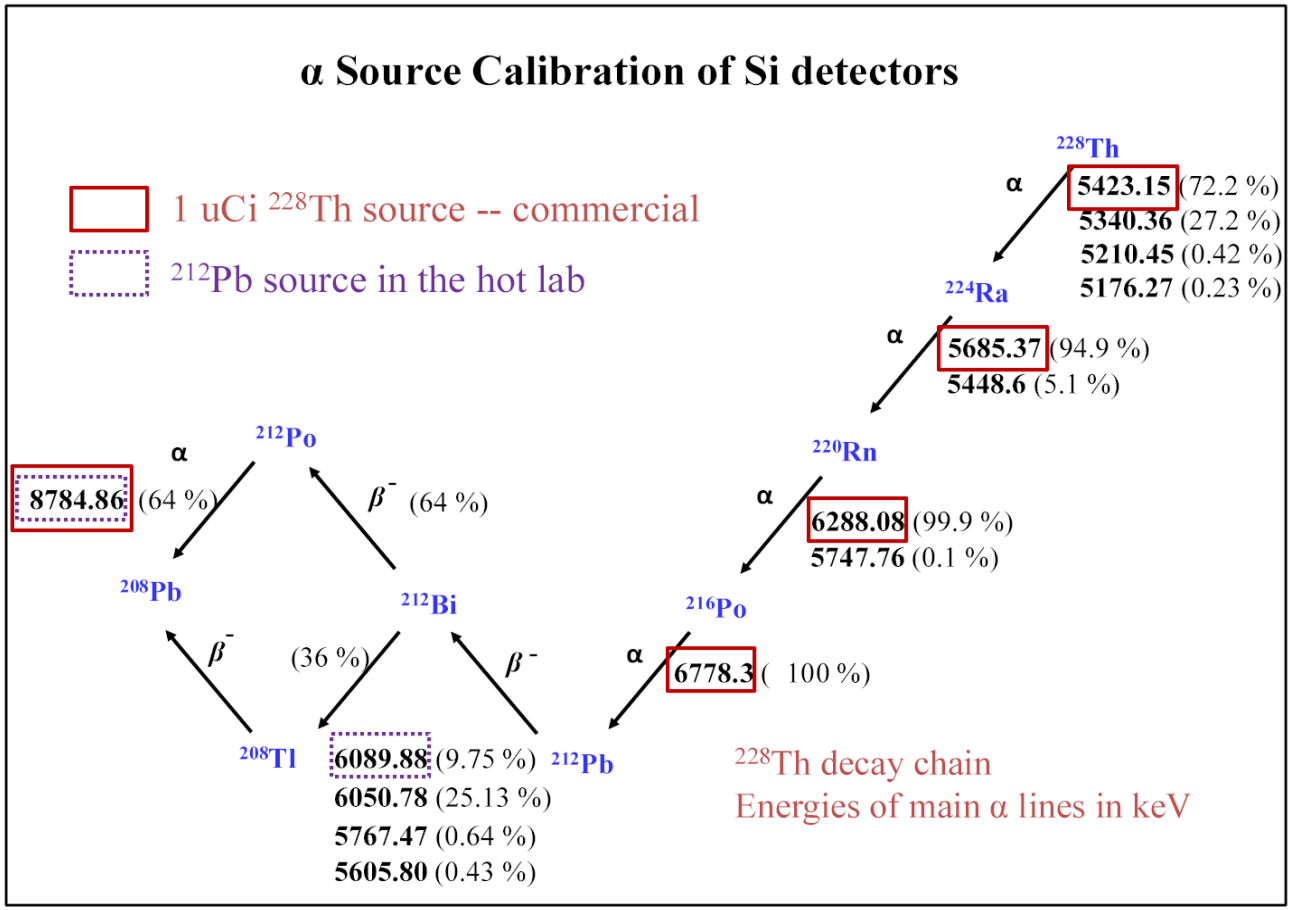

Figure 4.4: Diagram of the decay chain of ^{228}Th.

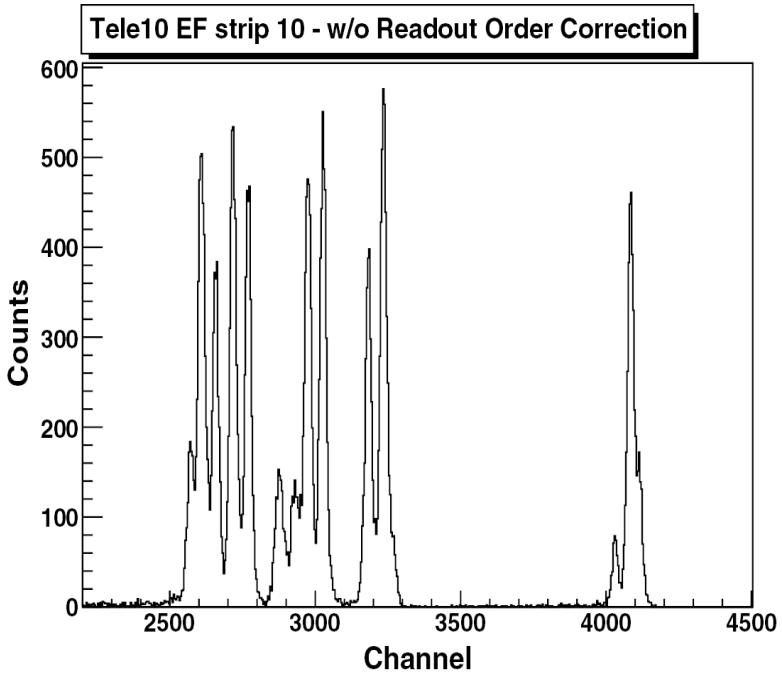

Figure 4.5: Alpha spectrum in raw channel of one EF strip without readout order correction.

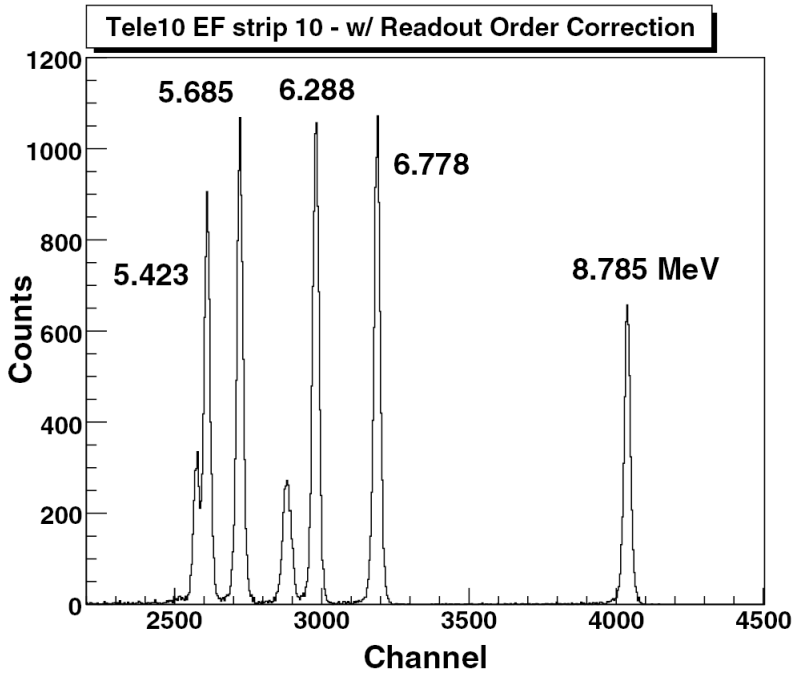

Figure 4.6: Alpha spectrum in raw channel of one EF strip after readout order correction applied on both motherboard and chipboard readout

4.2.1.2 Readout Order Corrections

As shown in Section 4.2.1.1, it is crucial to determine the readout order corrections and incorporate the corrections before carrying out any energy calibrations and data analysis in silicon detectors. To determine the correction values, the readout order of each signal within the motherboard (MB) and chipboard (CB) were identified when unpacking the data from an event file using two parameters. One of them is a 32-bit array which is used to represent channels being fired in a CB with the corresponding bits flipped to 1 from 0. Another parameter counts the number of channels read in a tower. From these two parameters, we can deduce the readout sequences of a hit in its corresponding MB and CB, which are labeled as ”OrdTow” and “OrdDet” respectively in the analysis code.

Since the MB and CB readout order problems do not seem to interfere with one another, the readout order corrections for the motherboards and chipboards could be distinguished and determined independently. Procedures used for readout order correction as described in the following are established by V. Henlz [Hen08]. To investigate the MB readout correction alone, we can look at ^{228}Th alpha spectrum for each strip gated on the first event of each CB (OrdDet=1) with different order on MB (OrdTow=1,2 and so on). Figure 4.7 shows the alpha spectrum with OrdTow=1 and 2 gated on OrdDet=1. There are small shifts in the peaks between OrdTow=1 and 2. The shift in the channel number for a particular MB readout order relative to the first readout order gives the MB readout correction for that particular readout sequence. Since there is no evidence that the readout order correction on the motherboard is energy dependent, the correction for each strip is the average of shifts in four alpha peaks with energies of 5,69,

6.29, 6.78 and 8.78 MeV at the particular MB readout sequence. The MB readout corrections in unit of channel averaged within each telescope are listed in Table 4.1. It should be noticed that the average values in the table present the general idea about readout order effect for each telescope. The readout corrections are slightly different among the strips within a telescope and each strip is corrected individually with its own correction values. The non-integral shift in channel is due to the randomization in the analysis corrected for data digitization.

For the CB readout correction, we first applied the MB readout order corrections to the IU pulser data and then determined the peak shifts in IU pulser ramp for individual strip gated on different readout order on each CB (OrdDet=1,2 and so on). The spectrum of IU pulser ramp for one strip gated on different OrdDet is shown in Figure 4.8. Peak shifts could be found by comparing the channels of the same peak with different OrdDet. Figure 4.9 shows a zoom-in of Figure 4.8 between channel 13200 to 15500 where the same peaks with different OrdDet coexist. This enables determination of the second and third order correction in CB. Depending on the response of each channel, the third and fourth order corrections could be determined. IU pulser ramp was performed for the chips on EF only, because we used energy from EF for analysis due to its better energy resolution than EB. Table 4.2 lists the averaged CB readout corrections in unit of channel for EF within each telescope. Again, the averaged corrections only serve as a summary of overall effect. Slightly different correction values were applied to each strip individually within a telescope.

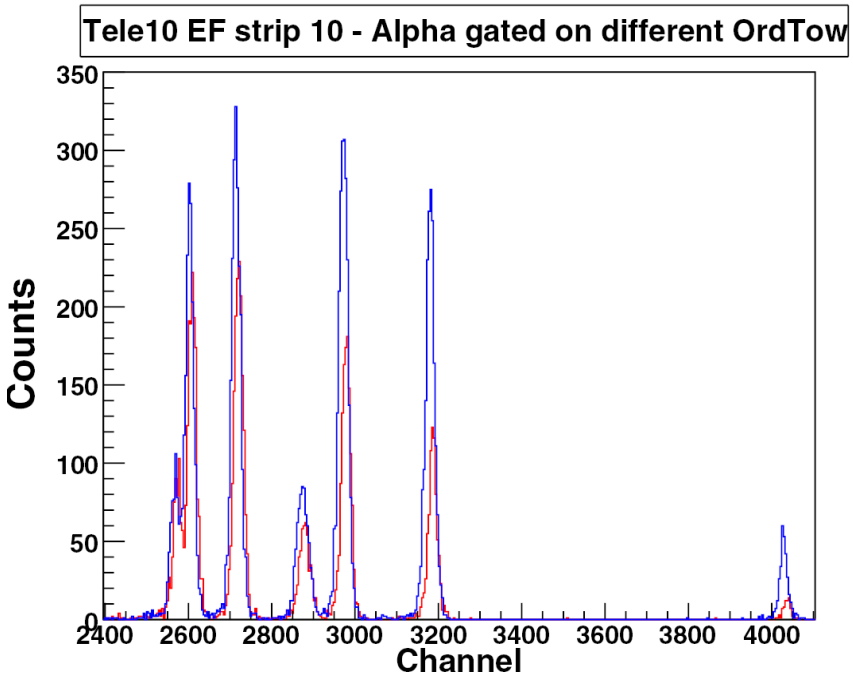

Figure 4.7: Spectrum of alpha source gated on OrdDet=1 with OrdTow=1 (red) and OrdTow=2 (blue) respectively.

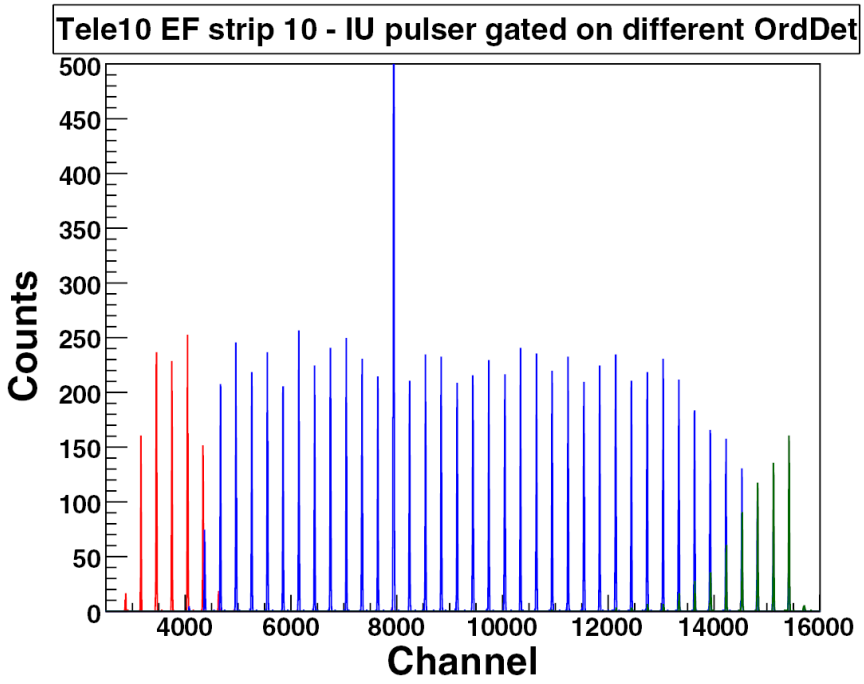

Figure 4.8: Spectrum of IU pulser ramp gated on different OrdDet corrected with readout order of motherboard. The OrdDet=1,2,3 are highlighted in red, blue and green respectively.

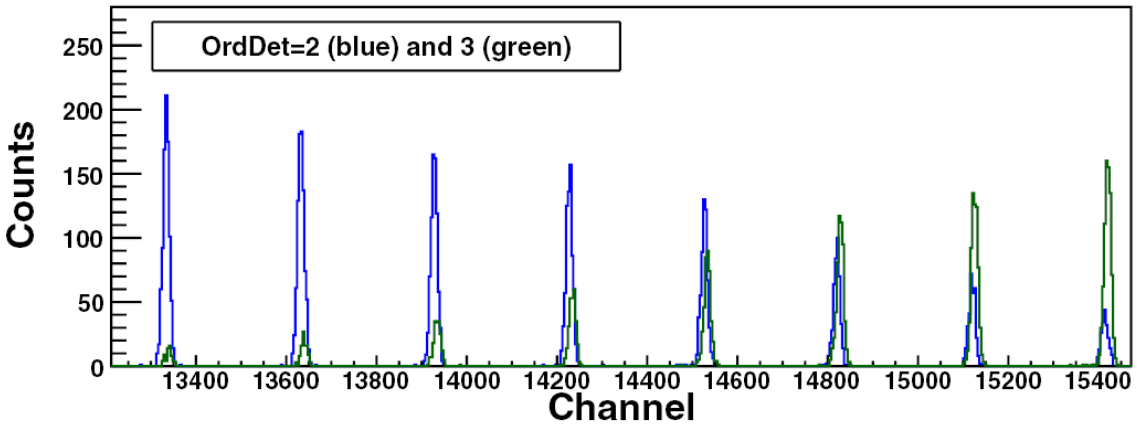

Figure 4.9: Zoom-in of Figure 4.8 on the regions where the same peaks with different OrdDet appear in the spectrum.

Averaged readout order correction for MB on EF											
Tower0			Tower1			Tower2			Tower3		
Tele	1st	2nd	Tele	1st	2nd	Tele	1st	2nd	Tele	1st	2nd
0	-6.72	-12.33	10	-6.97	-10.51	14	-0.09	2.01	4	-7.86	-10.53
1	-4.07	-5.98	11	-7.54	-12.96	15	-0.27	1.85	5	-6.72	-8.32
2	-4.59	-7.90	12	-6.89	-10.45	17	0.64	2.17	6	-7.06	-10.68
3	-5.68	-9.39	13	-7.19	-11.08	16	-4.00	-5.42	19	-7.39	-11.87
Averaged readout order correction for MB on EB											
Tower0			Tower1			Tower2			Tower3		
Tele	1st	2nd	Tele	1st	2nd	Tele	1st	2nd	Tele	1st	2nd
0	18.14	29.51	10	37.60	65.47	14	32.48	61.32	4	14.61	25.27
1	33.91	54.71	11	30.56	46.70	15	26.20	42.97	5	15.59	25.95
2	35.82	54.50	12	32.92	60.86	17	33.90	62.95	6	16.73	26.33
3	31.59	45.86	13	37.06	68.59	16	31.11	55.74	19	17.55	27.09

Table 4.1 Averaged corrections for the first two readout order on the motherboard for EF and EB within each telescope.

Averaged readout order correction for CB on EF									
Tower0					Tower1				
Tele	1st	2nd	3rd		Tele	1st	2nd	3rd	
0	56.03	90.49	98.71		10	55.32	85.80	94.43	
1	82.88	94.74			11	56.92	89.78	96.53	
2	52.94	89.32			12	54.50	87.67	103.18	
3	54.36	85.88			13	60.17	100.37	115.52	
Tower2					Tower3				
Tele	1st	2nd	3rd	4th	Tele	1st	2nd	3rd	4th
14	50.72	82.09	109.06		4	49.79	77.14	84.02	
15	52.53	84.01	114.05		5	53.97	86.23	102.78	
17	34.87	57.60	80.71	94.12	6	44.67	70.03	86.12	95.14
16	34.39	54.67	76.42		19	52.03	83.74	93.96	

Table 4.2 Averaged corrections for the readout order on the motherboard for EF within each telescope.

4.2.1.3 Energy Calibration

After readout order corrections, energy calibrations for DE and E silicon detectors can be carried out using alpha particles emitted from ^{228}Th source. The source was put in the target position. The ^{228}Th alpha decay peaks of each strip are shown in Figure 4.6. We use the five strongest alpha peaks which correspond to energies of 8.787, 6.778, 6.288, 5.685 and 5.423 MeV and establish a linear function to convert the channel readout from each strip into particle energy in unit of MeV. The energy resolution is typically represented by the FWHM of the 6.778 MeV peak. More accurate calibrations can be achieved if the dead-layer, mylar foil covering each telescope and the window of the alpha source are taken into account. The mylar foil and the Au window of the ^{228}Th source in this experiment are 265 *u*g/cm^2 and 50 *u*g/cm^2 thick respectively. Determination of dead-layer thickness is discussed in Section 4.2.1.5.

In this experiment, DE was placed in front of E silicon detector and alpha particles could not penetrate the DE. To calibrate E detectors, the HiRA telescopes had to be disassembled from the array in order to dismount the DEs and then assembled back to the system. To check if there is any change in the E calibrations due to the handling of silicon detectors, pin source was used to calibrate E detector without removing DEs in each telescope. A pin source is a 0.5" dowel pin activated by electroplating the tip with daughter nuclei from ^{228Th}. The pin was attached to the frame and inserted in the slot between DE and E detector for each telescope as shown in Figure 4.10. ^{212}Pb is the primary deposition on the pin which emits strong alpha particles at 8.785 MeV, 6.050

MeV and 6.090 MeV as presented in Figure 4.4. The pin source is not covered and sharp alpha energy spectrum can be obtained as shown in Figure 4.11.

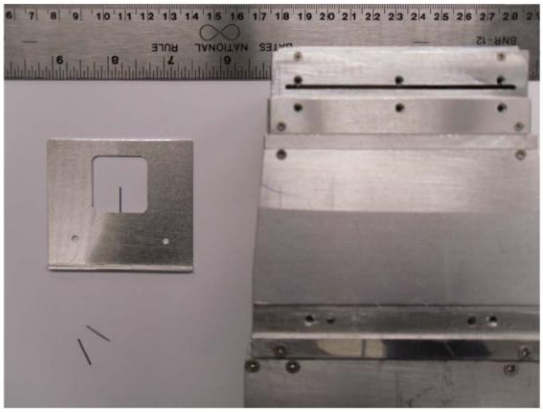

Figure 4.10: Photograph of the frame with a pin source attached. A slot between the DE and E detectors in the front part of HiRA telescope shown on the right is designed for the frame to be inserted. Extra pins are shown on the bottom left. A ruler is displayed for size reference.

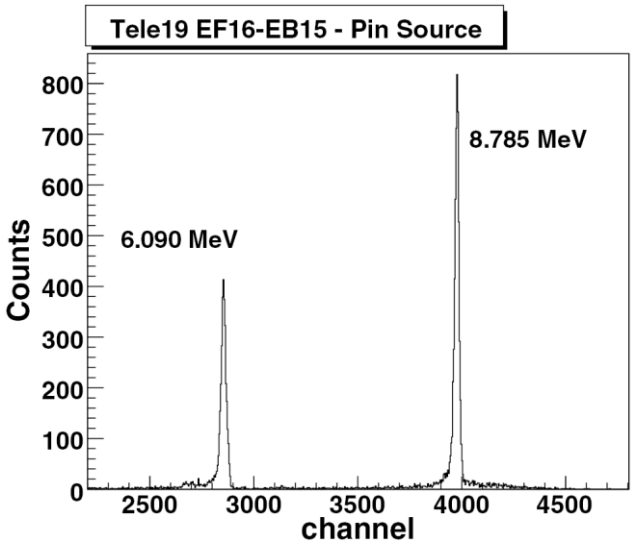

Figure 4.11: Pin source spectrum in raw channel of one pixel (EF16-EB15 in tele19) with MB and CB readout sequences problem corrected.

In general, all DE and EF achieve good energy resolutions of 45-55keV and 60-75 keV respectively. Regarding strips on EB, about 80% of them have resolutions of 60-85 keV while the rest is about 90-120 keV. Therefore energies in EF strips were used to represent the energy deposited in E silicon detectors in the analysis. Since the energy of alpha particles used in the calibration ranges only from 5.42 to 8.79 MeV while the dynamic ranges of DE and EF were set up to be about 13 and 38 MeV, respectively, in this experiment, IU and BNC precision linear pulse systems were used to pulse each strip to check the linearity of energy response over the ADC range. Overall, all strips have good linearity suggesting the calibrations obtained from alpha source spectra can be applied for the full ADC ranges.

To check if there is any gain shift in silicon detectors during the experiment, we chose three groups of alpha source data taken at different periods of time. We first used the alpha runs at the end of the experiment to obtain calibration parameters for silicon detectors and applied the same parameters to calibrate the alpha runs performed at the beginning and in the middle of the experiment. The average energy shift of the alpha peaks indicates the stability of the silicon detector. It is found that the performance of DE was very stable over the entire experiment. We examined the stability of E detectors using telescope 5 and 6 since these are the two telescopes without DE. There is no shift observed in the alpha runs in the middle of the experiment compared to those taken at the end. However about 70-85 keV energy shifts are found in EF at the beginning of the experiment, while the shifts in EB are relatively smaller. It is not conclusive that the calibration parameters for E detectors obtained from the alpha data taken five days before the first beam (^{36}Ar) came in even though the detectors were not changed during that

period of time are applicable. Also, the performance of telescopes 5 and 6 could not represent all the E detectors in the system. Nevertheless, since absolute energy calibration is not required in this experiment, such problems would be corrected when calculating the total energy of detected particles as discussed in section 4.2.5.

It is reported from the manufacture that the thickness of silicon detector is known to 10% accuracy. The energy calibrations in silicon detectors can be used to determine thickness of DEs. In the data run, we use ^{4}He particles which stopped and deposited 6 MeV in E detector and found the corresponding energy deposited in DE. Using LISE++ code, we can deduce DE thickness from the ^{4}He energy deposit in DE with the dead-layer thickness taken into account. The reasons of using EF energy at 6 MeV are because the DE-E energy relation is steep in this region which allows better energy determination. Furthermore, the corresponding DE energy would be approximately at 5.5-6.5 MeV depending on the actual DE thickness resulting in both energies in DE and E lie in the calibration regions. Table 4.3 compares the thickness from the manufacturer and our analysis. In general, the agreement is good and the deviations from the manufactuer's values are at most about 12%.

Tele	Manu.(um)	Deduced (mm)	% difference
0	63	62	-1.59
1	65	58	-10.77
2	62	62	0.00
3	66	62	-6.06
4	62	63	1.61
10	66	63	-4.55
11	66	62	-6.06
12	65	62	-4.62
13	66	58	-12.12
14	62	62	0.00
15	61	62	1.64
16	64	63	-1.56
17	63	62	-1.59
19	63	63	0.00

Table 4.3 Thickness of DE detectors given from manufacture and deduced from experimental data.

4.2.1.4 Uniformity of Silicon thickness

Non-uniformity of silicon detector thickness would result in position-dependent variation in the energy loss of particle across the silicon surface and poor energy resolution of the detector. Therefore, the effect of non-uniformity of silicon thickness needs to be investigated and incorporated in the calibrations if necessary. To study the non-uniformity of silicon, we used the alpha particles which punched through the thin silicon (65 *u*m) but stopped in the thick silicon detectors. We further gated these alpha particles on two regions of DE energy around 5.4 and 7.4 MeV with the corresponding E energy around 35 to 40 MeV and 25 to 30 MeV respectively. Then we used the E energy of each event and calculate the corresponding DE energy based on the DE thickness provided by the manufacture. The ratio of the measured to the calculated DE energy for the alpha data

gated on DE energy of around 5.4 and 7.4 MeV for one DE detector was studied in another HiRA experiment -- NSCL Expt03045 [Expt03045]. Energy loss of a particle passing through the silicon detector is proportional to the detector thickness. The difference between the calculated DE energy to the measured DE energy for those alpha particles on event-by-event basis reflects the non-uniformity of silicon thickness. It is found that the effect of thickness variation on DE energy is less than 2%, which corresponds to less than 5% variation in thickness. This DE detector (HiRA part number: 2266-4) shows the most significant variation compared to the other DE detectors. Since the E detector is more than 20 times thicker than the DE silicon detector, the effect of non-uniformity on E detector is negligible. No correction for the non-uniformity of thickness of E detector was applied in the data analysis.

4.2.1.5 Determination of Dead-layer thickness

Dead-layer is the metallic electrodes and non-depleted region on the surface of the silicon detector. Energy loss of the particles in these regions could not be measured. The thickness of the dead-layer has to be considered for an accurate energy calibration. To determine the dead-layer thickness of E detector, we use the calibration data of E detectors with the pin source as described in Section 4.2.1.3. Schematically, the pin source was located 2.72 mm away from the front of the E detector as shown in Figure 4.12. The energy loss of the detector can be described by Equation 4.1, where E is the measured energy deposited in the silicon detector, E' is the total energy of alpha particle emitted from the source, DL is the dead-layer thickness, θ is the oblique angle of alpha

particle, and *dE/dx* is the stopping power of alpha. The stopping power of alpha particle in silicon at certain energy can be found in the ref. [Sky67].

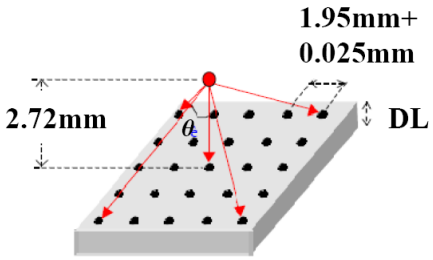

Figure 4.12: Geometry of pin source calibration.

$$E = E' - \frac{dE}{dx}\frac{DL}{Cos\theta} \qquad (4.1)$$

The pin source is capable of hitting all pixels on the E detector. Due to the close proximity to the silicon surface, the alpha particles that strike the pixels near the edge of the surface have much larger oblique angles compared to those near the center. We assume the pin is a point source. Since the thickness of dead-layer that the particle passing through depends on the oblique angle, the dead-layer near the edge will sufficiently shift the energy of the alpha particle. The dead-layer thickness could be determined by varying the DL thickness until the difference between the measured energy from data and calculated energy from Equation 4.1 is minimum. Our result indicates the averaged thickness of the dead-layer for E detector is 1.0 ± 0.5 um silicon equivalent. In the analysis, we assumed the same averaged dead-layer thickness for both DE and E detectors.

4.2.2 CsI Energy calibration

The light output of CsI(Tl) crystals are mass and charge dependent and non-linear. It also depends on the Tl doping of the CsI crystal. Therefore, calibration has to be performed for each CsI individually. Two-dimensional spectrum of calibrated EF energy vs. raw signal from CsI is generated to calibrate each CsI as shown in Figure 4.13. For a fixed ADC channel in CsI, the corresponding energy in the Si detector could be found in each identified isotope. Using the energy loss from calculations using LISE++ [LISE], we can obtain a set of points with their individual energies deposited in Si and the corresponding CsI, and eventually establish a 5^{th} order polynomial function between energy in Si detector and CsI crystal for each particle species. Since the light output is roughly proportional to the energy deposited in the CsI, a linear relation between the ADC channel and the particle energy could be determined as demonstrated in Figure 4.13. In this experiment, we used deuterons for CsI calibrations because it is the particles of interest.

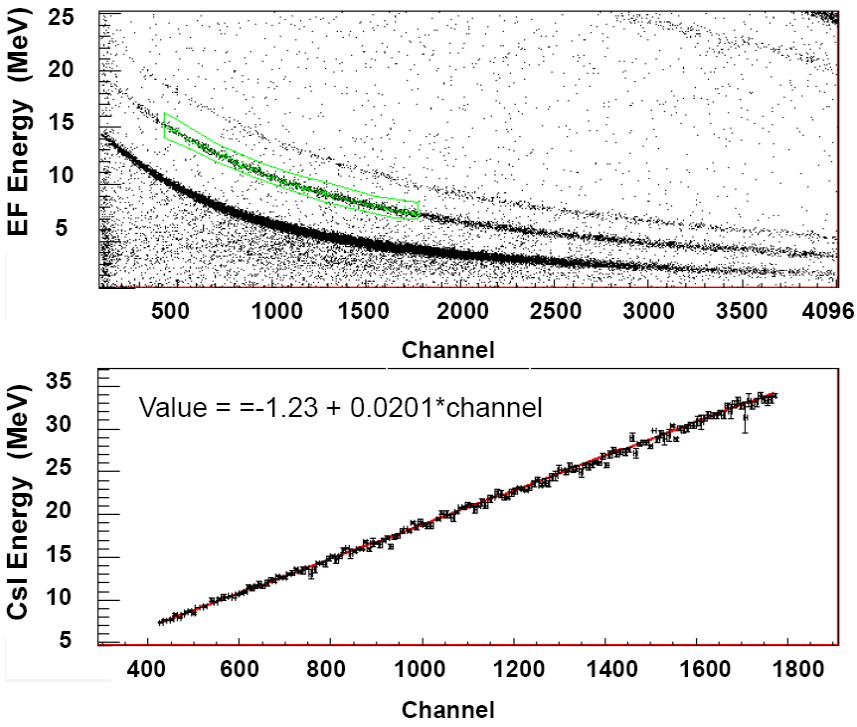

Figure 4.13: (Top panel) 2D spectrum of EF in MeV vs. CsI in channel. (Bottom Panel) Linear fit between the ADC channel and the particle energy in CsI.

The BNC pulser with linearity specifications was also used to extract absolute zero offset based on the linear response of CsI crystal. The zero offset of each CsI crystal was converted into energy using the calibration parameters. The offsets are compared to the offsets obtained from BNC pulsers. Figure 4.14 shows the corresponding energy of zero offset in units of MeV, where each crystal ID represents one CsI crystal with a total of 63. One CsI was not working in the experiment. If the zero offset given by the pulser is correct, the deviation in calibrated energy of zero offset from 0 MeV indicates that there may be about 0.5 MeV inaccuracies in the CsI calibration. In principle, the zero offset and CsI punch-through points are sufficient to constraint the calibrations parameters

assuming linear response of the light output from CsI(Tl) crystals. Unfortunately, there are no punch-through points in this experiment because of the setting of CsI dynamics range and the low energy of the incoming beam.

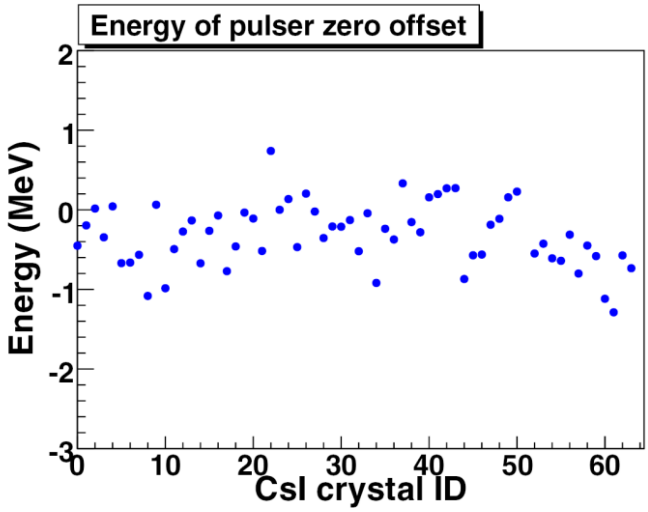

Figure 4.14: The zero offset of each CsI crystal converted into energy using the calibration parameters from Si-CsI energy relations, where each crystal ID represents one CsI crystal with a total of 63.

Using ΔE-E relation for calibration would require knowing the exact thickness of E detectors. There is 10% uncertainty in the thickness given from the manufacture. However, the thickness of some E detectors have been determined using the deuteron elastic data on Au target in another HiRA experiment – NSCL Expt02023 [Rog09]. In the elastic data, the energies of the deuteron peaks were known from the beam magnetic rigidity Bρ. Based on the calibrated energy from the CsI, the energy deposited in the E detectors could be determined and used to deduce the E thickness using LISE++. Table 4.4 lists the thickness of E detectors from the manufacture and our results. It is found in

general that the E detector is about 45 *u*m thinner than the thickness given by the manufacture.

From Expt 02023 -- elastic scattering				
Telescope	**Manu. (um)**	**Deduced (um)**	**Difference (um)**	**% difference**
0	1496	1442.09	53.91	-3.74
1	1503	1452.71	50.29	-3.46
2	1490	1453.91	36.10	-2.48
3	1488	1411.99	76.01	-5.38
4	1489	1444.93	44.07	-3.05
5	1499	1447.25	51.75	-3.58
6	1471	1435.47	35.53	-2.48
10	1511	1462.66	48.34	-3.31
11	1491	1457.57	33.43	-2.29
12	1452	1410.90	41.11	-2.91
13*	1473	1430.64	42.36	-2.96
14*	1533	1490.64	42.36	-2.84
15*	1506	1463.64	42.36	-2.89
16	1513	1475.43	37.57	-2.55
17	1496	1333.35	162.65	-12.20
19	1541	1512.16	28.84	-1.91
		Avg.	**51.98**	
		Best Avg.	**42.36**	
*Deduce from best avg.				

Table 4.4 Thickness of E detectors given from manufacture and deduced from experimental data of NSCL Expt 02023 [Rog09]. The telescope index with "*" means the specific telescope was not used in Expt 02023, and the thickness was deduced from the average value.

The deduced E thickness could be used to establish an accurate ΔE-E relation for each individual telescope. For each deuteron produced from the reactions of interests, we calculated the corresponding CsI energy based on its energy deposited in E detectors using LISE++ code and used the calculated CsI energy for further data analysis. There are three E detectors (telescope 13, 14 and 15) employed in this experiment which were not being used in the previous experiment with elastic scattering data in NSCL Expt

02023 [Rog09]. Since the results from the elastic scattering data indicate a systematical difference of about 42 *u*m on average between the data-deduced and manufacture value, we assume those three detectors follow the same trend.

4.2.3 Pixelation technique

The highly-segmented 32-strip double-sided silicon detector allows the construction of 1024-pixels within one telescope, giving precise position determination of the detected charge-particles. To fully utilize this advantage, associating the proper EF and EB strips hit by the specific particle is important and necessary. Such identification is clear if only one single particle hits the telescope during one event. For the multiple-hit case, however, there can be ambiguities in assigning the position of each particle. In addition, particles hitting the inter-strip may result in charge signal splitting between two neighboring strips. Cross-talk and noise issues also need to be considered. Therefore, the following procedure [Hen08] is used to properly assign particles to their respective pixels in all different combinations of situations.

When more than one strip on EF or EB are fired within a telescope in one event, we first examine two adjacent channels of each registered strip and disgard the signal with energy smaller than the threshold defined as 1.25+1% of the energy of the registered channel. Such small signals are regarded as noise or cross-talk. After that, the remaining signals in the particular telescope are sorted according to their signal amplitudes (calibrated energies) in descending order for EF and EB separately. On each face, hits in separated and non-neighboring strips are considered as “singlet”; while hits in neighboring strips are labeled as “doublet” unless it is found to be accidental neighboring

single hit. If hits are identified as “singlet” on both sides, then we can pair them up according to their energies. When the energy difference between a “singlet” on one side and the sum of two “doublet” signals on another side is smaller than 1+5% of the energy of singlet energy, then we combine the “doublet” hits together and pair it to the corresponding singlet. When two singlet signals are on one side and one singlet is on another side, we consider it to be described in one of the following circumstances. The double-hit situation is when two particles in separate strips on one side hit only one strip on another side. Another corresponds to the hit on one of the strips giving no output signals due to either the problem of electronics or strips with broken wire bonds. These situations can be identified and proper matching can be done according to the signal energies. Same principles are applied for the more complicated situation, for instance two doublets and three singlet signals. After the pairing process, the discrepancy in calibrated energy between EF and EB for almost all particles is less than +/- 0.5 MeV as shown in Figure 4.15. This is one of the constraints used in the data analysis. In addition to the particle position and energy, the real multiplicity in each telescope can also be determined after the pixelation procedure.

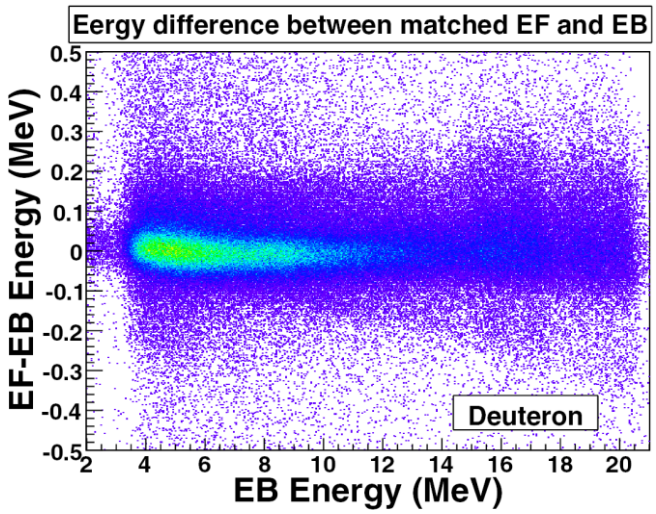

Figure 4.15: Energy difference between a pair of matched EF and EB strip versus energy in the corresponding EB strip.

To obtain the correct total energy of the particle, DE and CsI also need to be associated properly to the EF-EB pair for specific particle. Since DE strips are parallel to EF strips and the separation between DE and EF is only 0.8 cm, we assumed the particle on the EF strip has passed through the specific DE strip with allowance of +/- 1 strip off. It is validated by GEANT4 simulations [geant4] which show that more than 99% of particles can be described by this assumption. 86% of them hit exactly the same corresponding DE and EF strips. Therefore, we pair up the signal which has the largest amplitude within three adjacent DE strips to the hit in the corresponding EF strip. For CsI, if more than one charged particles punch through two layers of silicon detectors and stop in the same CsI crystal, signals induced by multiple particles superimposed in CsI could not be separated. In principle, such events do not give correct particle ID and would be disregarded in the analysis. Furthermore, to ensure that the particles in EF-EB

would hit the corresponding CsI quadrant, we discard the middle strips (strip 15 & 16) in both EF and EB as they cover the gaps between four separated CsI crystals.

When particles hit bad strips on DE, EF and EB in a telescope, the reconstruction fails because the position and energy information could not be retrieved. All the bad strips are taken into account in the geometric efficiency of HiRA array as discussed in Section 5.4.

4.2.4 Particle Identification of HiRA

After associating energies measured in DE, E and CsI to a single particle, proper particle identification (PID) can be performed. HiRA relies on the technique of ΔE vs. E for particle identification. The principle of this can be approximated by Bethe-Bloch energy loss formula:

$$\Delta E \approx \frac{k A Z^2}{E}\, dx \qquad (4.2)$$

where dx is the detector thickness, k is proportionality, A is the mass of the particle and Z is the atomic number of the particle. From the formula, energy loss ΔE is proportional to AZ^2/E. A plot of ΔE vs E could be used to uniquely identify the A and Z of the charged particle. For particles stopping in the E detectors, particle identification can be achieved by using DE vs. EF as shown in Figure 4.16. For particles having higher energies that penetrate the E detector and deposit energies in CsI, a plot of EF vs. CsI as displayed in Figure 4.17 is used for PID. The punch-through energies of deuteron in E detector and CsI crystal are about 22 MeV and 155 MeV respectively. In either case, one can clearly

see a family of bands corresponding to p, d, t of hydrogen isotopes as well as bands of ^{3}He and ^{4}He of helium isotopes in the PID plots.

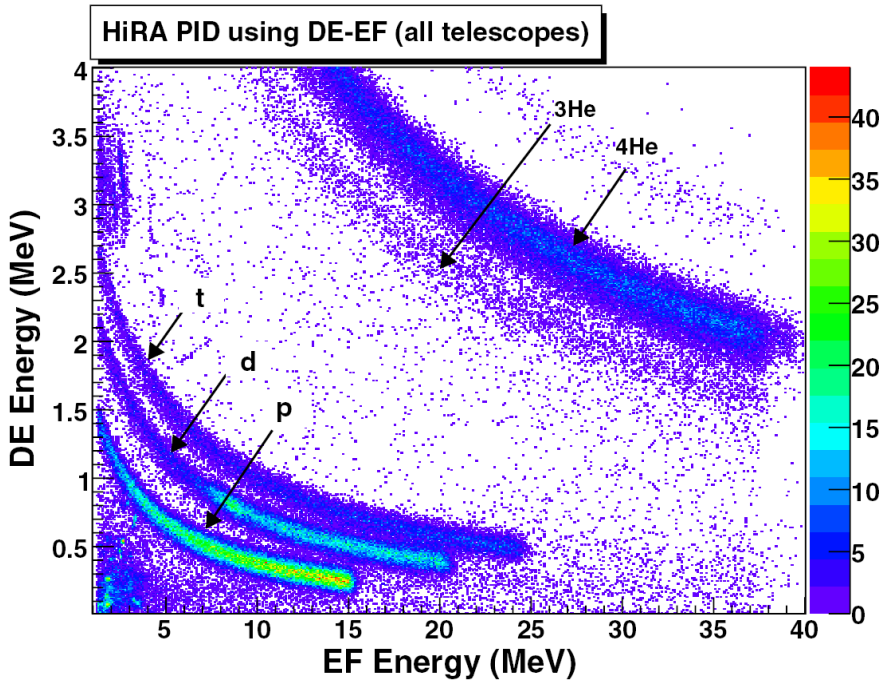

Figure 4.16: PID spectrum of EF vs. DE energy in unit of MeV.

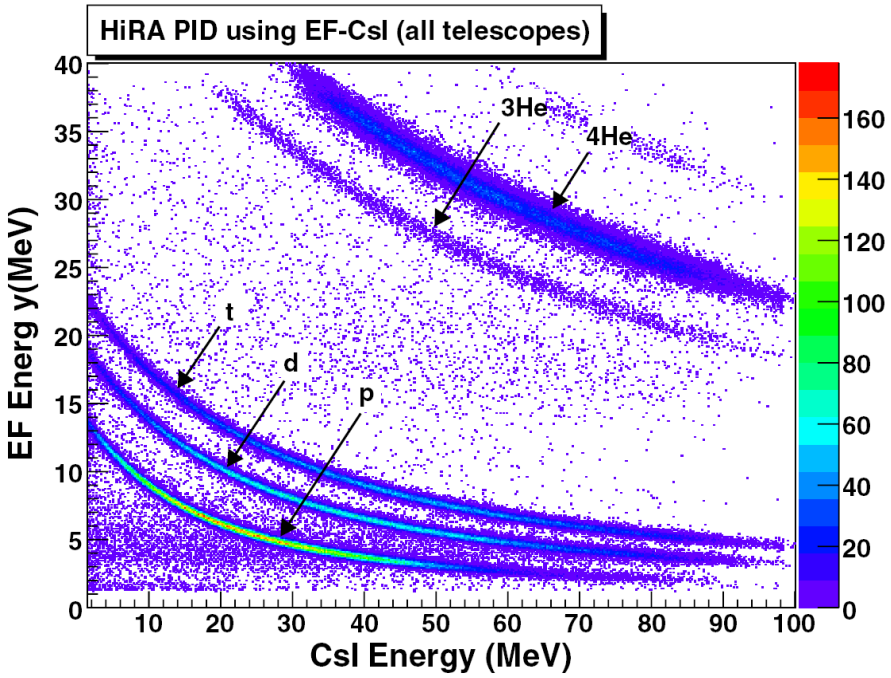

Figure 4.17: PID spectrum of CsI vs. EF energy in unit of MeV.

4.2.5 Deuteron total energy

After applying the PID gates from HiRA, beam and S800, deuterons produced from the reactions of interests could be identified. The total energy of deuteron is the sum of energy in both silicon detectors and CsI detector as well as the energy loss in the target, Mylar foil and dead-layer. The energy loss tables for deuteron in different materials were generated using LISE Excel [LISE] for each individual telescope based on the thickness of DE and E detectors.

As discussed in section 4.2.2, the CsI energy was calculated from the corresponding energies in E detectors. Uncertainties in the deduced silicon thickness and the silicon calibrations would therefore result in the inaccuracies in the total energy of deuteron and the reaction Q-value calculations. To improve the final energy of deuteron

and the energy matching between different telescopes, we gated on the deuterons in the reactions of ground-state transitions and extracted the total energy of deuteron at three different laboratory angles within one telescope. The total energy is corrected by linear fitting to the corresponding calculated kinematics values. The left panel of Figure 4.18 demonstrates the linear relation for Telescope 10 with reaction of p(^{34}Ar,d) of ground-state transition.

In general, kinematic broadening increases dramatically at the large angles. To check the final deuteron total energy corrected by the kinematics in laboratory frame, the deuteron energy in the center-of-mass is extracted and compared to the calculations. The right panel of Figure 4.18 plots the deuteron center-of-mass total energy from p(^{34}Ar,d) reaction for telescope 10 which was located at angle of about 23° in the region of large kinematics broadening. The center-of-mass deuteron energy in this telescope is 15.50 MeV which is consistent with the calculation of 15.53 MeV.

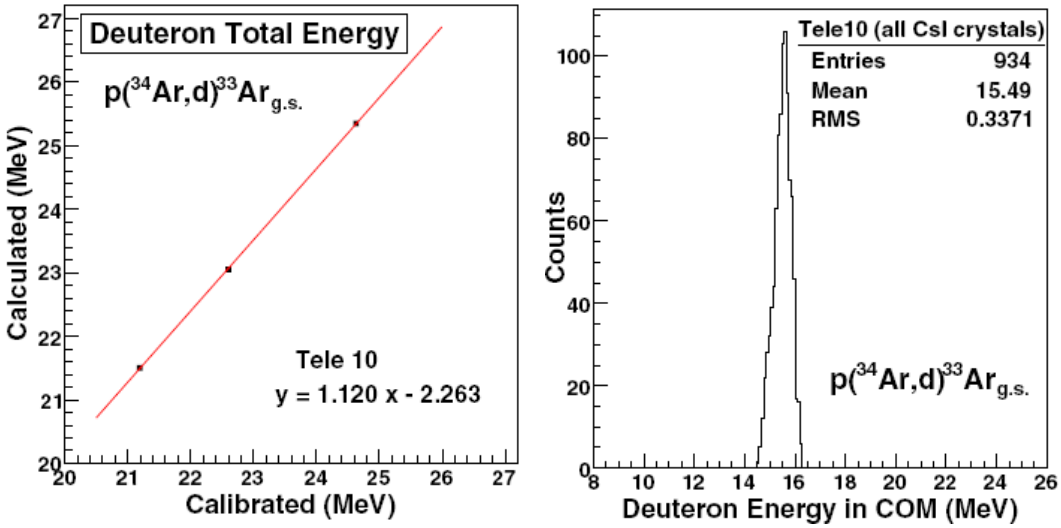

Figure 4.18: (Left) Linear fits of the calculated and calibrated total energy in laboratory frame for telescope 10 in p(^{34}Ar,d) reaction of ground-state transition. (Right) Total energy of deuteron in Tele10 in the center-of-mass frame.

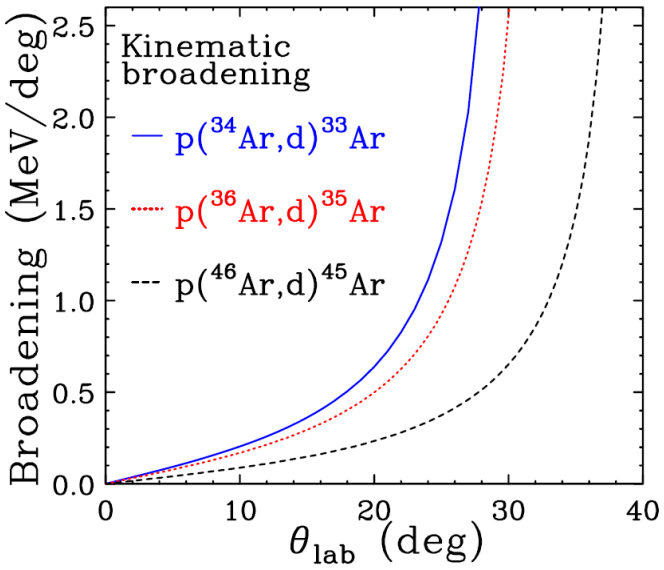

Figure 4.19: The calculated kinematic broadening of p(^{34,36,46}Ar,d) for ground-state transitions in laboratory frame.

4.3 S800 Spectrometer

In this experiment, the time-of-flight and energy loss were measured by the S800 spectrometer to identify various beams and fragments. To achieve the best separations between different species in the particle identification, time-of-flight for the fragment of interest was corrected by its trajectory using the position and angle detected in the S800 CRDC detectors on an event-by-event basis. In addition, the actual average beam energy for precise kinematics analysis can be determined from the dispersive position of the unreacted beam in the S800 focal plane. This section presents all the methods and results in details.

4.3.1 Beam particle identification

Ar isotope beams of ^{34,36,46}Ar were used in this experiment. The E1 scintillator signal in S800 spectrometer provided the event trigger in data acquisition and the time-of-flight (ToF) start. Two different time signals are measured with respect to the S800 E1 trigger. One is the start time from the A1900 extended focal plane (XFP) which is a plastic scintillator with thickness of 100 mm and an area of 150 x 100 mm^2 placed at the end of the A1900 fragment separator. Another start time is the radio frequency (RF) pulse from the cyclotron. Incoming beams are identified by plotting the TOF-RF verse TOF-XFP. Figure 4.20 – 4.22 display the beam PID of ^{36}Ar, ^{34}Ar and ^{46}Ar respectively. Several bunches of beams appear in the spectra. They are the RF bunches due to the multi-turn extractions in the K1200 cyclotron. They were combined in the analysis using the known radio frequency. Incident beams can be identified unambiguously using the ToF

technique. It is found that the secondary ^{34}Ar beam is approximately 94% pure with main contamination of ^{33}Cl. ^{46}Ar beam is nearly 100% pure.

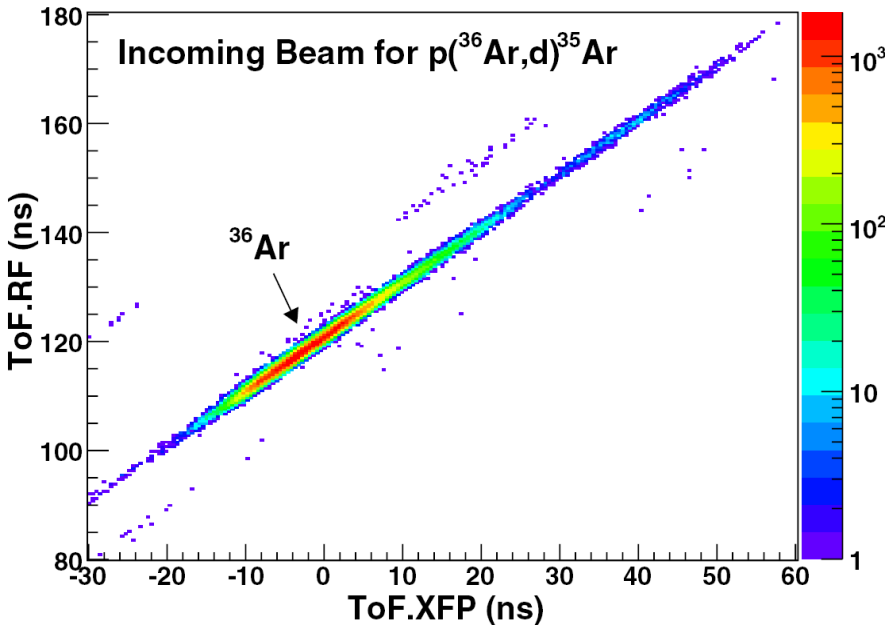

Figure 4.20: The beam PID spectrum for p(^{36}Ar,d) reaction.

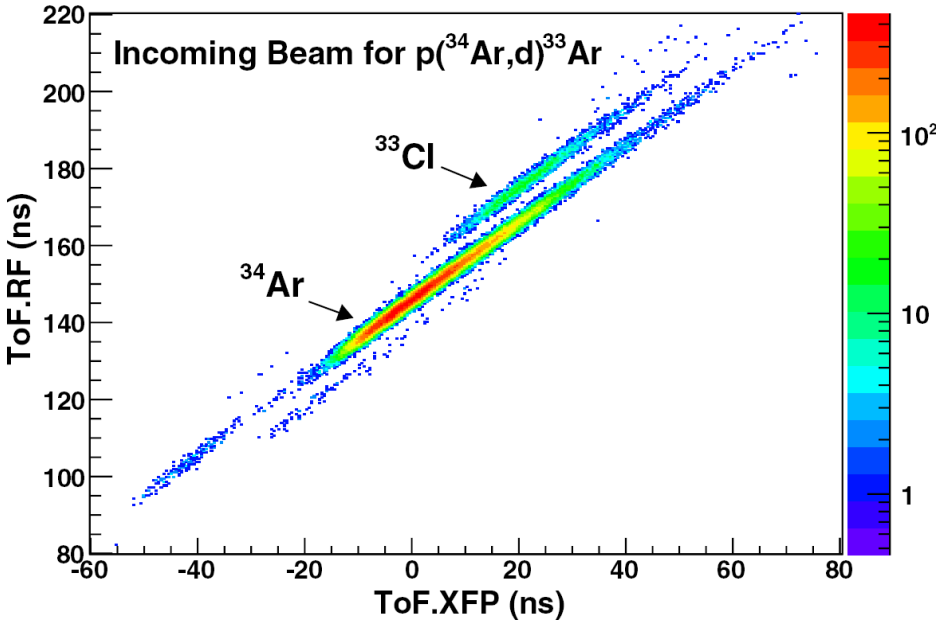

Figure 4.21: The beam PID spectrum for p(^{34}Ar,d) reaction.

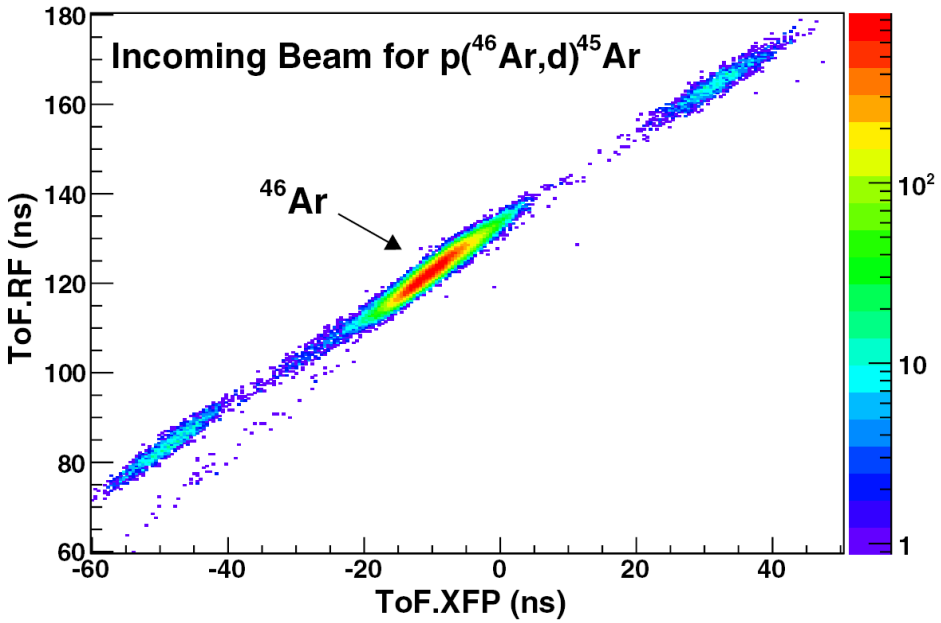

Figure 4.22: The beam PID spectrum for p(^{46}Ar,d) reaction.

4.3.2 CRDC position calibration

CRDC mask calibrations have to be performed to relate the channel numbers and true physical distance for the position-sensitive CRDC. A mask with well-determined pattern of slits and holes are inserted remotely in front of each CRDC. The pattern of the mask used in the position calibration is displayed in Figure 4.23. First order polynomial fitting is used for the calibration which is accurate enough for our experiment. Figure 4.24 plots the two-dimensional position spectra of CRDC1 and CRDC2. The centroids of the image of well-defined holes were extracted and compared to the pattern of the mask. In the non-dispersive direction (y-direction), first-order polynomial fitting is used to relate the raw channel to the distance in mm. On the other hand, only the offset value needs to be determined in the dispersive direction (x-direction) because the slope of the first-order polynomial is fixed by the geometry of the cathode pads which are separated by 2.54 mm/pad and 224 pads are evenly spaced across the detector. There is a beam axis hole on the mask which provides the optical center of the detector. Table 4.5 summaries the results of CRDC calibrations for ^{34}Ar and ^{46}Ar reactions. Unfortunately the position calibration data for ^{36}Ar were not saved onto the disk during the experiment, we assumed the pressure in the gas system was stable so that the non-dispersive position calibration from ^{34}Ar is applicable to the ^{36}Ar reactions. Mask data run on regular basis would be useful to monitor the stability over the entire experiment.

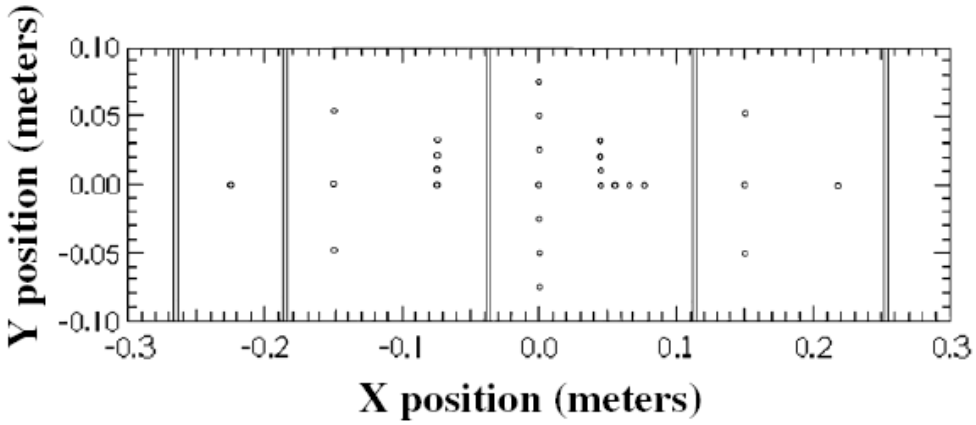

Figure 4.23: Pattern of the mask used in the CRDC2 position calibration, when the mask is inverted for CRDC1.

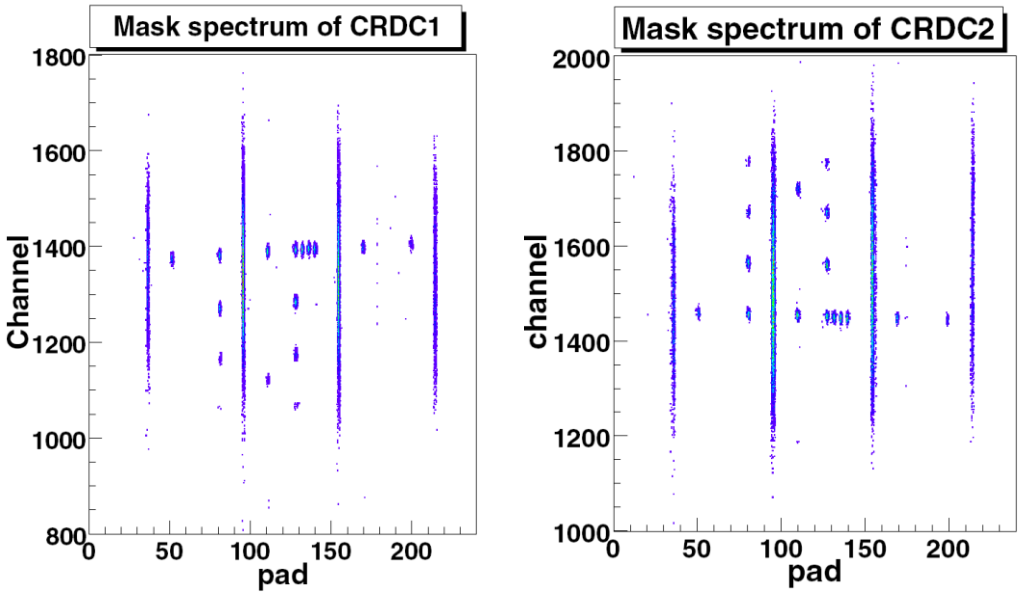

Figure 4.24: Two-dimensional position spectra of CRDC1 (left) and CRDC2 (right). The pattern in CRDC1 is upside down compared to that in CRDC2.

		^{34}Ar	^{46}Ar
CRDC1	Y slope [mm/TAC ch]	-0.0913	-0.0988
	Y offset [mm]	127.4091	125.6478
	X offset [mm]	-281.432	-283.21
CRDC2	Y slope [mm/TAC ch]	0.09140	0.09969
	Y offset [mm]	-132.828	-132.023
	X offset [mm]	-279.4	-280.924

Table 4.5: Summary of S800 CRDC calibrations.

4.3.3 S800 Particle Identification

Particle identification in S800 spectrometer was achieved by using the Δ*E*-ToF technique. Figure 4.25 shows the S800 PID spectrum of $p(^{36}\mathrm{Ar},d)^{35}\mathrm{Ar}$ reaction. Energy deposited in the ion chamber ΔE is roughly proportional to the square of nuclear charge (Z^2) according to Equation. 4.2, the Bethe-Bloch formula [Bethe]. Time of flight (ToF) refers to the time between the radio frequency (RF) pulse and S800 E1 time signal. Because of the magnetic rigidity Bρ in the spectrometer, the ToF can be expressed as a function of the *A*/Z ratio as shown in Equation 4.3. As a result, isotopes of particular element form the tilted bands; while fragments with a constant neutron excess *N*-*Z* form vertical bands. The straight-vertical band corresponding to the nuclei with *N*=*Z* and the neighboring one corresponding to the *N*-*Z*=1 or *N*-*Z*= -1.

$$ToF = \frac{L}{c\beta} = \frac{L\gamma u}{B\rho}\frac{A}{Z}; \qquad B\rho = \beta\gamma uc\frac{A}{Z} \qquad (4.3)$$

where $\gamma = \frac{1}{\sqrt{1-\beta^2}}$ is the relativistic factor and *u* is the atomic mass unit.

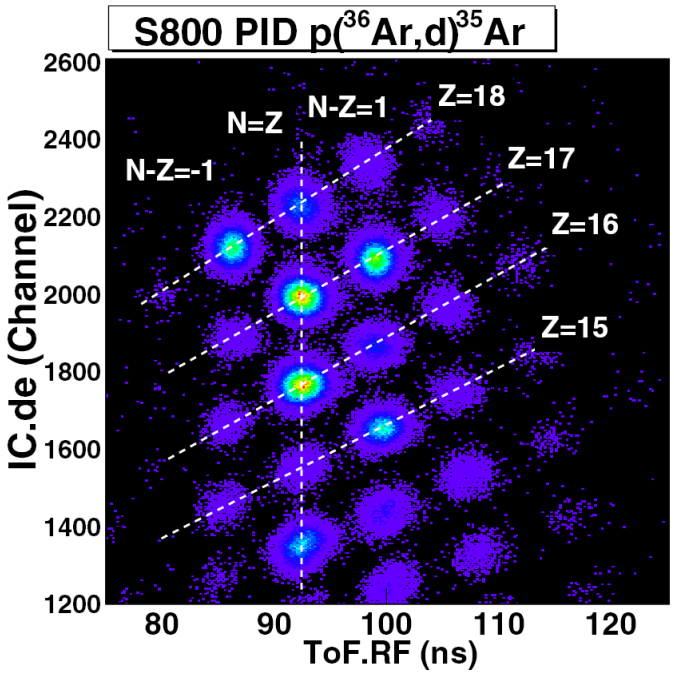

Figure 4.25: S800 PID spectrum for $p(^{36}\mathrm{Ar},d)$ reaction where the fragment $^{35}\mathrm{Ar}$ is circled.

The large momentum acceptance of the S800 spectrograph leads to a relatively large spread in the ToF, which adversely affects the PID resolution. In particular for the secondary beam when the beam spot size is relatively large (diameter ~20 mm for $^{34}\mathrm{Ar}$ beam), the fragments of interests detected in the focal plane have broad position and angular distributions in the dispersive direction, resulting in bad S800 PID as shown in the left spectrum of Figure 4.26. The timing resolution can be improved by correcting the ToF for the trajectory dependence. In addition, the trajectory correction is necessary to achieve good energy loss resolution, because the energy loss in the ion chamber depends on the travelling distance of the particle. After the trajectory correction in both ToF and energy loss, a well-resolved PID can be obtained as shown in the right panel in Figure 4.26.

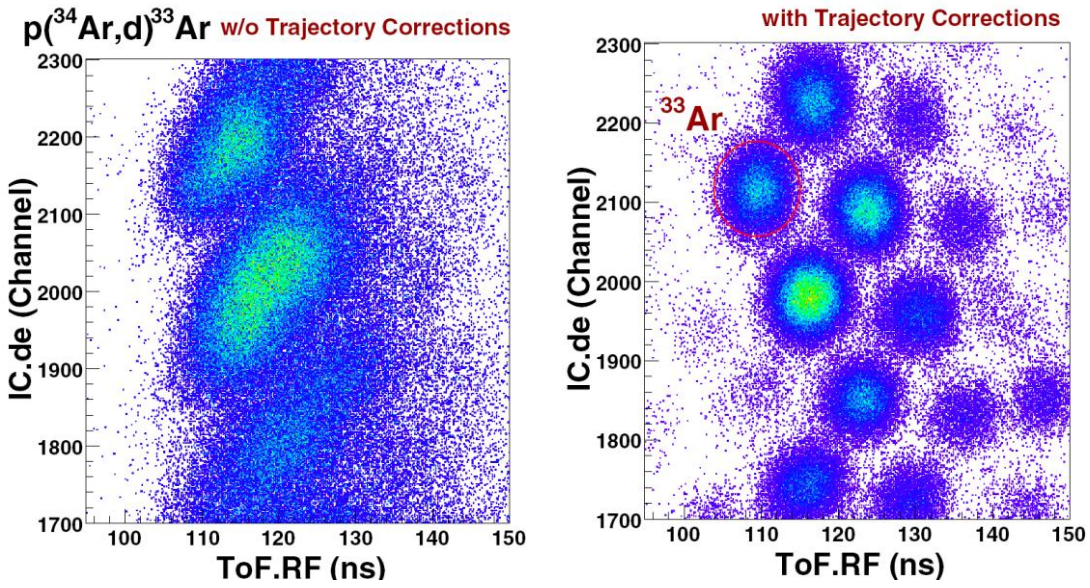

Figure 4.26: (Left) S800 PID spectrum of p(^{34}Ar,d)^{33}Ar without trajectory corrections in ToF and energy loss in the ion chamber. (Right) Same as left panel, but with trajectory corrections where the fragment ^{33}Ar is circled.

The trajectory dependences of ToF and energy loss are expressed explicitly in Equations 4.4 and 4.5. As seen in Equation 4.4, part of the ToF resolution is correlated with the angle in the dispersive direction of the S800 focal plane (S800.AFP), because particles with larger incident angles into the CRDCs compared to the central path would have deviated from the central trajectories. This means that those particles take longer time to travel from the reaction target to the focal plane. Therefore, parameter a_1 is needed to minimize the angle-dependence. Since AFP is calculated from the particle positions on two CRDCs, trajectory corrections can be improved by removing the dependence on the x and y components of CRDC (CRDC.x and CRDC.y). On the other hand, the energy loss in the ion chamber is positively correlated to the travelling distance

of particles, which can be deduced from position information of CRDC. Trajectory correction to the energy loss is made based on Equation 4.5.

$$ToF.RF(Corr.) = ToF.RF(orig.) - E1.time + a_1 \cdot S800.AFP + a_2 \cdot CRDC1.x + a_3 \cdot CRDC2.x \quad (4.1) + a_4 \cdot CRDC1.y + a_5 \cdot CRDC2.x \qquad (4.4)$$

$$IC.de(Corr.) = IC.de(orig.) + b_1 \cdot CRDC1.x + b_2 \cdot CRDC2.x + b_3 \cdot CRDC1.y + b_4 \cdot CRDC2.y \qquad (4.5)$$

The procedure of determining the trajectory correction parameters (a_i *and* b_i) is demonstrated below using $p(^{34}\mathrm{Ar},d)^{33}\mathrm{Ar}$ as an example. To achieve good resolution in S800 PID for the region of interest, we gated on the fragment from the reaction being studied and adjusted the parameters a_i until the angle and position dependences are minimized as displayed in Figures 4.27-4.29. Since AFP and X-Y corrections are correlated, several iterations between them are needed. The left panel of Figure 4.27 shows the ToF-RF of ^{33}Ar fragment corrected for the trajectory (ToF.RF(Corr.)) gated on ^{34}Ar beam versus the dispersive angle (AFP) in S800 focal plane; while points in the right panel denote the corresponding centroids of ToF-RF. The red line is the linear fit of the data points. The horizontal straight line indicates the disappearance of angle-correlation. Figure 4.28 shows the spectra of position dependence for ^{33}Ar gated on ^{34}Ar beam in each CRDC after corrections are applied. The respective centroids are extracted and plotted in Figure 4.29. Same procedure was used to adjust the correction parameters

(b_i) until we could remove the trajectory dependence on energy loss in ion chamber as demonstrated in Figure 4.30 and 4.31. The corrections parameters (a_i *and* b_i) were then applied based on Equations 4.4 and 4.5 for S800 detected particles on the event-by-event basis. The right spectrum of Figure 4.26 is the S800 PID of $p(^{34}\mathrm{Ar},d)$ ^{33}Ar reactions compensated for the correlation with the trajectory for fragments of interest.

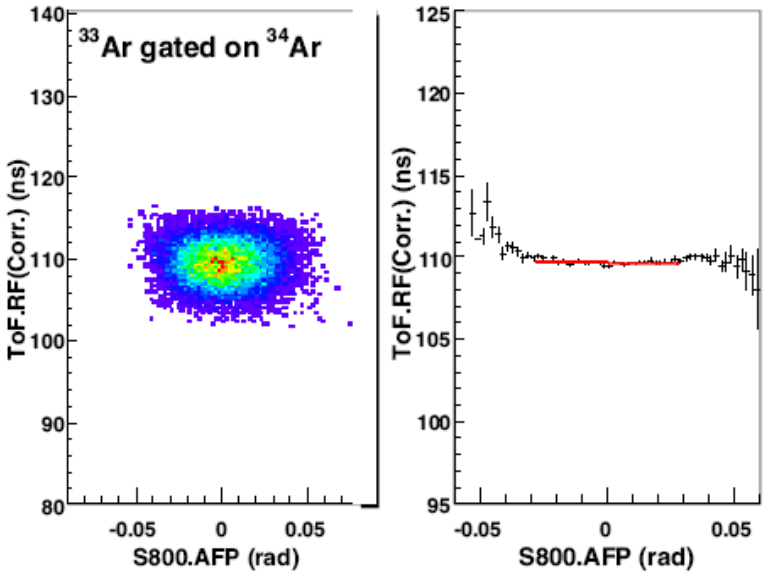

Figure 4.27: (Left) Spectrum of the corrected ToF-RF signal of ^{33}Ar fragment gated on ^{34}Ar beam versus the dispersive angle in S800 focal plane after the trajectory corrections are applied. (Right) Centroids of the corrected ToF-RF shown in the left panel in the bin of AFP. The red line is the linear fit of the data points

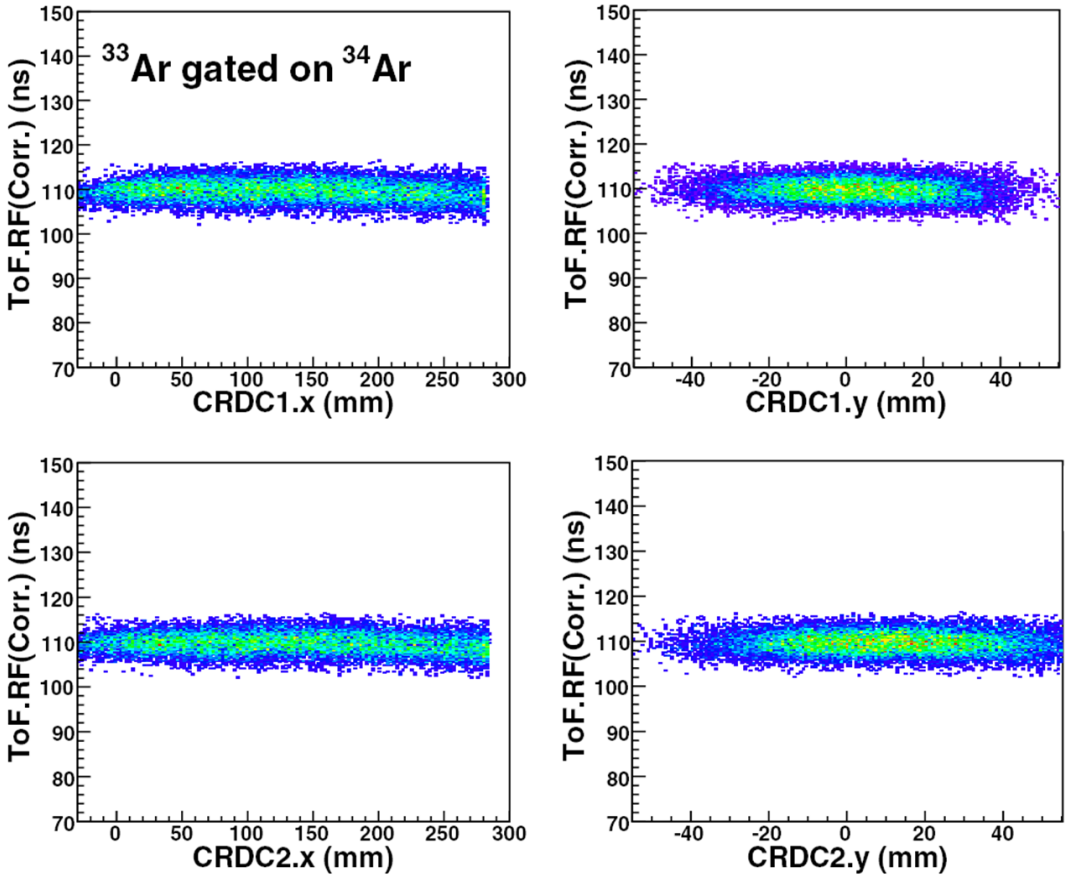

Figure 4.28: Spectra of the position dependence of the corrected time-of-flight ToF.RF for ^{33}Ar gated on ^{34}Ar beam for CRDC1.x (upper left), CRDC1.y (upper right), CRDC2.x (bottom left), CRDC2.y (bottom right) after the trajectory corrections are applied.

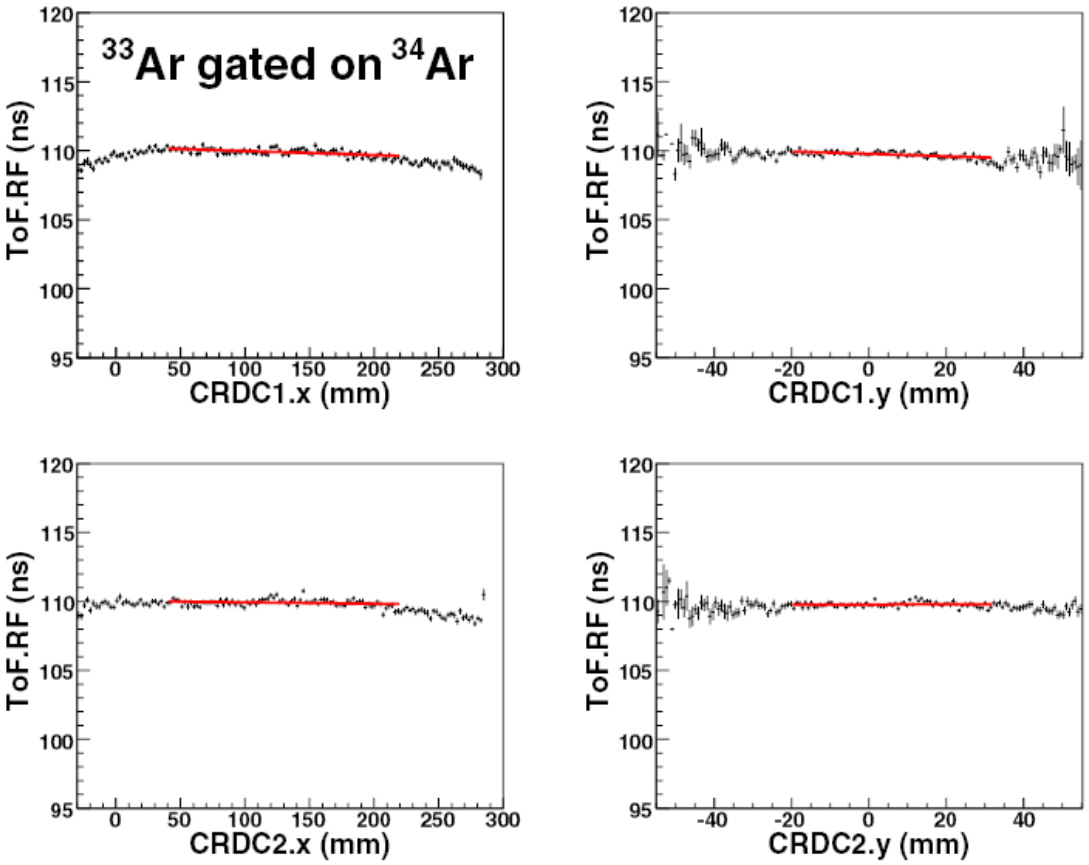

Figure 4.29: The centroids of the corrected ToF.RF in the bin of CRDC positions from corresponding spectrum shown in Figure 4.28. The red line is the linear fit of data points.

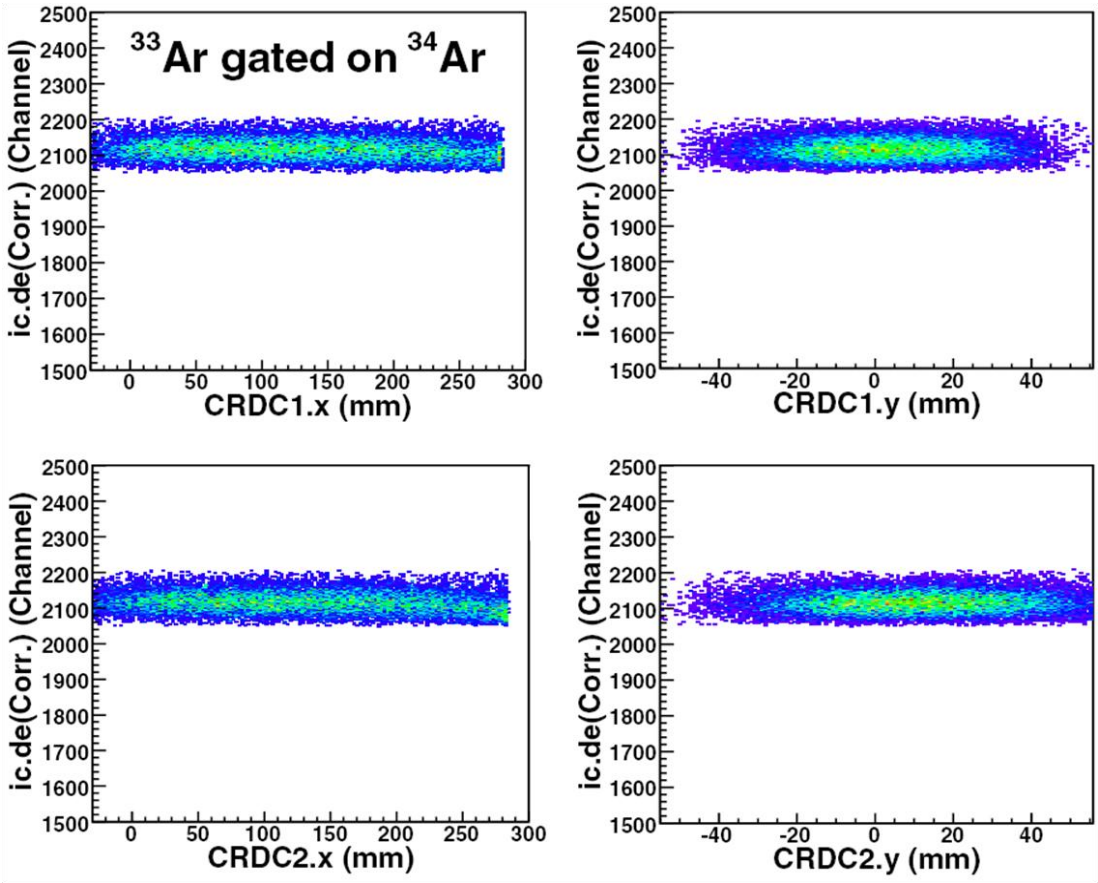

Figure 4.30: Spectra of the position dependence of the corrected energy loss in S800 Ion Chamber ic.de for ^{33}Ar gated on ^{34}Ar beam for CRDC1.x (upper left), CRDC1.y (upper right), CRDC2.x (bottom left), CRDC2.y (bottom right) after the trajectory corrections are applied.

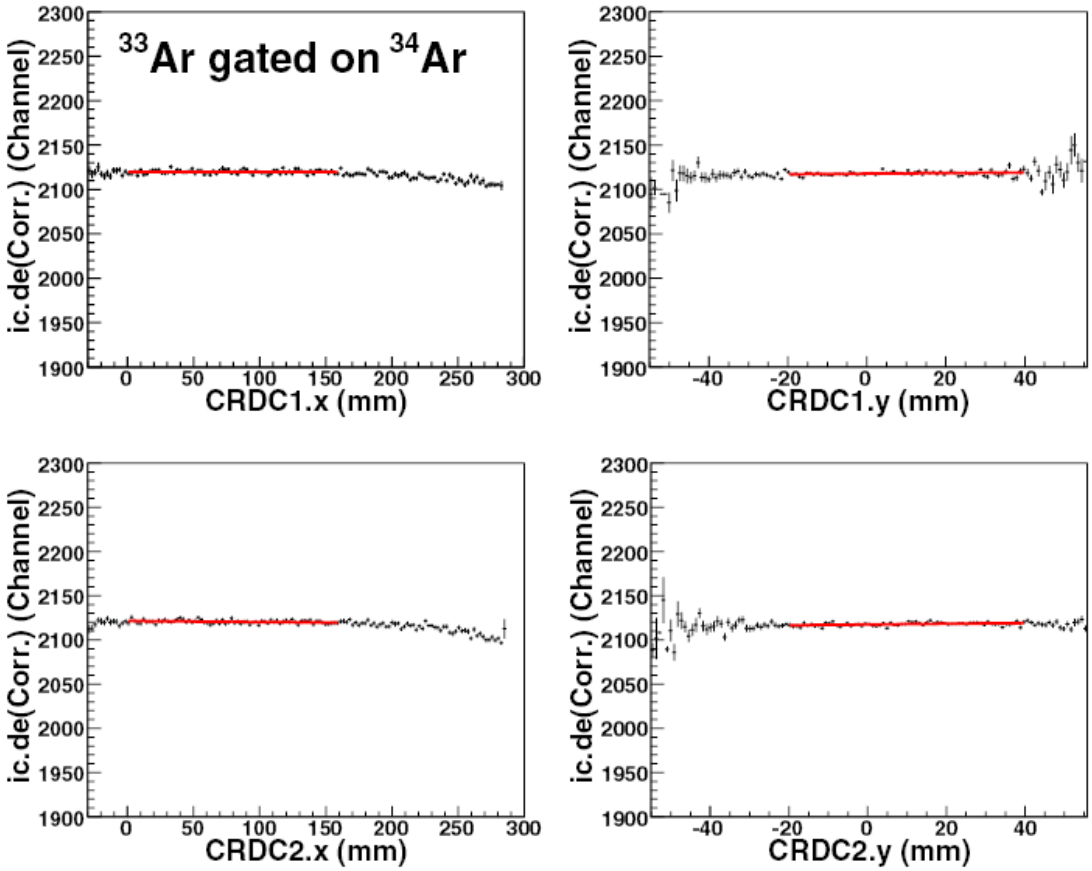

Figure 4.31: The centroids of the corrected ic.de in the bin of CRDC positions from corresponding spectrum shown in Figure 4.30. The red line is the linear fit of data points.

Figures 4.32 show the trajectory corrected S800 PID spectrum gated on emitted deuterons and incoming beams for $p(^{34}\mathrm{Ar},d)$ and $p(^{46}\mathrm{Ar},d)$ reactions. The reaction residues produced from each transfer reaction could be identified unambiguously as circled in the spectra and the corresponding S800 residue-gates could be generated for further analysis. For $p(^{46}\mathrm{Ar},d)\ ^{45}\mathrm{Ar}$, the centroid of $^{45}\mathrm{Ar}$ gate in the PID spectrum had to be shifted by 27 channels in IC.dE starting from the middle of the experiment. The shift corresponds to approximately additional 0.11 MeV/nucleon energy loss. Since the

magnetic setting remained the same over the entire experiment, it is suspected that the shift in energy might be attributed to the change in gas pressure of the ion chamber

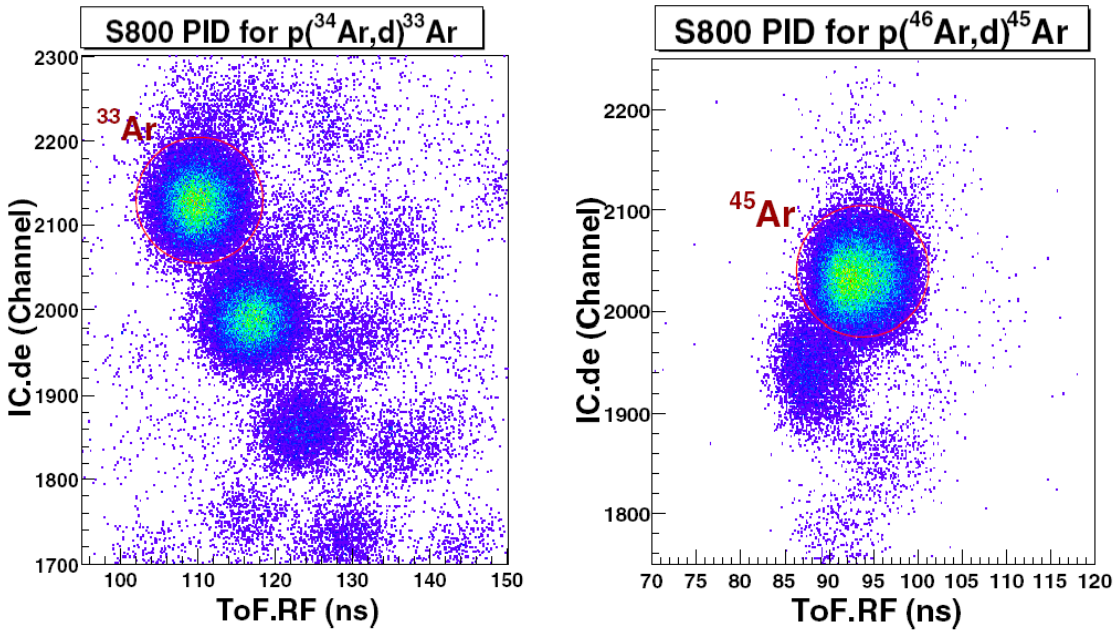

Figure 4.32: (Left) S800 PID spectrum for $p(^{34}\mathrm{Ar},d)$ reaction where the fragment ^{33}Ar is circled. (Right) Same, S800 PID spectrum for $p(^{46}\mathrm{Ar},d)$ reaction where the fragment ^{45}Ar is circled

4.3.4 Beam and reaction residue energy

From past experiments, the beam energy given by the A1900 magnetic setting have been found to be different from the real beam energy by about one percent. To determine the real energy of the beam, we allowed the beam to travel directly to the S800 focal plane without passing through the reaction target. In the unreacted beam runs, the magnetic rigidity of S800 was set according to the A1900 magnetic setting for the incoming beam. If the real beam energy is the same as expected from the A1900 Bρ setting, the incoming

beam would be focused in the middle of the dispersive axis (x-axis) of the S800 focal plane. The radius of S800 is 2.8028 meters and the momentum dispersion is 95.6 mm/%. Therefore the 95.6 mm deviation from center for the beam dispersive position on S800 focal plane would imply 1% momentum dispersive and consequently 1% difference in Bρ value compared to the setting. Figure 4.33 plots the dispersive position (FP.x) of the incoming beams (^{36}Ar, ^{34}Ar and ^{46}Ar) with the centriods of beam obtained from Gaussian-fit. The real beam energy can be determined accordingly from the position deviations. Table 4.6 summaries the beam energy from A1900 and the beam energy determined from unreacted runs.

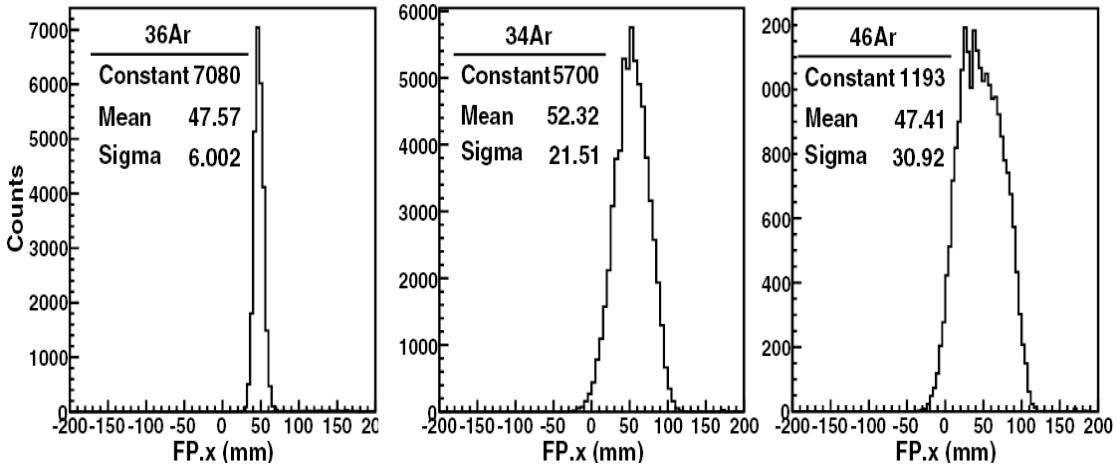

Figure 4.33: The dispersive position (FP.x) of the incoming beams of ^{36}Ar, ^{34}Ar and ^{46}Ar. The centriods of beam are obtained using Gaussian-fit and shown in the spectra.

Beam	A1900/ S800Brho [Tm]	Energy expected [MeV/nucleon]	FP.x [mm]	Real Brho of Beam [Tm]	Real beam energy [MeV/nucleon]	% diff. in energy
^{36}Ar	1.6691	33.07	47.57	1.6608	32.75	-0.98
^{34}Ar	1.5741	32.96	52.32	1.5654	32.6	-1.1
^{46}Ar	2.1308	33.00	47.41	2.1202	32.68	-0.98

Table 4.6: Summary of the beam energy determined from the Brho ofA1900 and S800.

In Figure 4.34, the calculated residue energies of ^{35}Ar, ^{33}Ar and ^{45}Ar at ground state are plotted versus laboratory scattering angles. The emitted angles span from 0 to 1.75° and selected Bρ setting ensures the desired fragments are measured in the S800 without being blocked by the beam blocker. To estimate the energy resolution given by the S800 spectrometer, we studied $p(^{34}\text{Ar}, d)^{33}$Ar ground-state transition and plotted the resulting ^{33}Ar fragments with scattering angle between 0.17°-0.23° as displayed in Figure 4.35. This range of the residue angles correspond to the deuteron emitted angles of 6°-8°. The reason of choosing the angular range of 0.17°-0.23° is because there is no angle-dependence in the residue energy as seen in the calculations. By performing Gaussian fitting to the peak in Figure 4.35, the energy of ^{33}Ar corrected for the energy loss in the target was found to be 32.04 MeV/nucleon with resolution of 490 keV/nucleon FWHM. The measured energy is consistent to the calculations of 32.06 MeV/nucleon, however the energy resolution is not better than 1.5%.

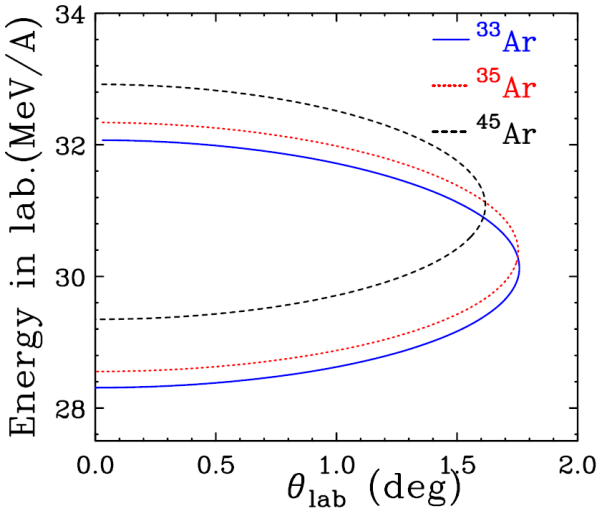

Figure 4.34: The calculated energy of reaction residues of ^{35}Ar, ^{33}Ar and ^{45}Ar at ground state in laboratory frame.

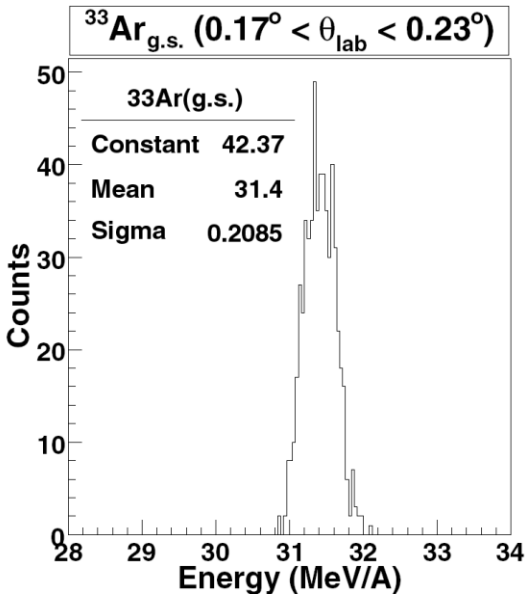

Figure 4.35: The energy spectrum of ^{33}Ar produced from reaction of p(^{34}Ar ,d)^{33}Ar ground-state transition gated on scattering angle between 0.17°-0.23°. Energy is corrected for the energy loss in the target.

4.3.5 Trajectory reconstruction

Inverse map was employed to reconstruct the particle trajectories so that the scattering angles of the particles on the reaction target could be deduced analytically from measured dispersive and non-dispersive angles in the CRDC on an event-by-event basis. The Inverse map was calculated using the ion optics code COSY Infinity with correction of optical aberrations to the fifth order according to the magnet and Bρ settings in the spectrometer [Baz03]. In addition, the reconstruction procedure assumes perfect alignment of magnetic elements. The distance between the reaction target and pivot point of the S800 optics is also required for the calculation of the map. In this experiment, the reaction target was placed at 59.4 cm upstream of the pivot point. The beam trajectories deduced from the MCP detection systems were combined with the deuteron angles from

HiRA to calculate the scattering angles of recoil residues, which can be compared to the scattering angles reconstructed from the positions in CRDC. However, the MCP performance in present experiment was not satisfactory as discussed in Section 4.4. Detailed analysis of the MCPs and the comparisons between the angles obtained from MCP and S800 can be found Ref. [Expt06035]. Expt06035 [Expt06035] to study the spectroscopic factors from p(^{56}Ni,d) reaction, was carried out with the same experimental set up right after this experiment.

4.4 Micro Channel Plate detectors

In this section, the performance of MCP and associated problems are discussed. Due to the considerable size of the beam spot and the actual beam trajectory, corrections for the beam positions and angles on reaction target is necessary in order to achieve good angular resolutions. Ideally, we could use the position information given by MCP0 and MCP1 to deduce the position and angle of beam trajectory on the target.

We first ran the experiment with the stable beam ^{36}Ar. It is found that substantial amounts of position signals in the central region of the resistive anode plate in the MCP detector are too weak to be registered by all four corners of the anode plate. In MCP detection system, signal amplitude is proportional to the amount of secondary electrons produced along the photo-multiplier tube. The significant decrease of signal amplitude indicates severe deterioration of the central part of the micro-channel plates. Since the central region suffers from the highest count rates, we speculate that the excessive

exposure from the secondary electrons induced from the focused beam damages the inside of the channel walls. Such observation raises concern about the practical lifetime of MCP-PMT under high counting rates. The problems are partly solved by splitting the corner signals into two groups and amplified one of them before sending the signals to the charge-to-digital convertor (QDC) for digitization. Unfortunately, the high-gain system was implemented only for MPC1 in the reactions using ^{34}Ar and ^{46}Ar beams due to the limitation of time and insufficient electronic modules. Figure 4.36 shows the corn multiplicity of MCP0 and MCP1. Corner multiplicity indicates how many corners receive signal above the preset threshold for an event. Position could not be determined for an event when multiplicity is less than 4. Without operating in high-gain mode for MCP0, it is obvious that the number of events with multiplicity 3 is comparable to those with multiplicity 4, resulting in significant loss of position information for a lot of events.

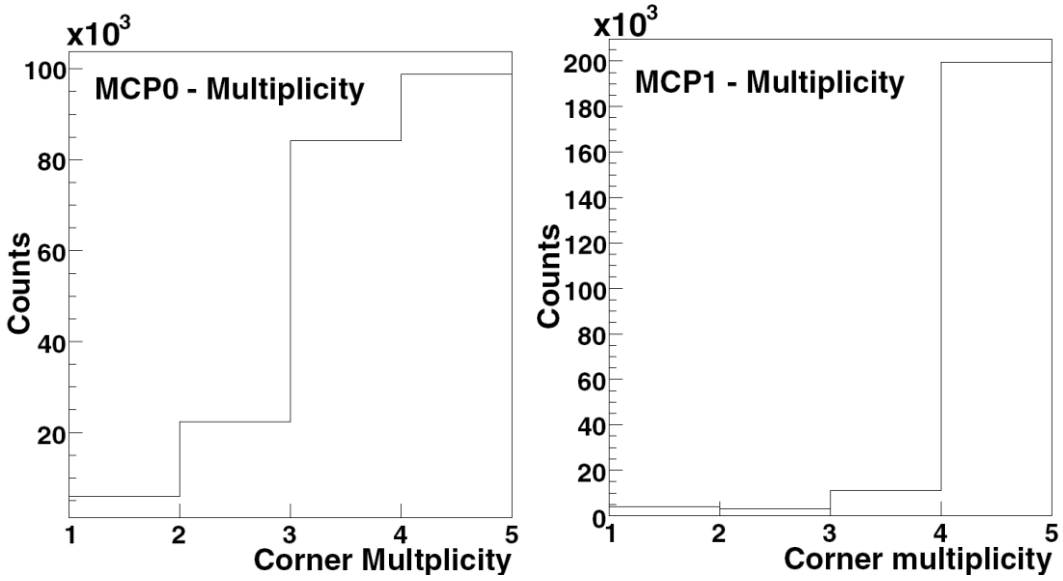

Figure 4.36: Multiplicity of MCP0 and MCP1.

To avoid losing significant amount of useful data, we assumed zero-degree beam angle and the position of beam particle on MCP1 to be the same as that on the reaction target which is only 10 cm downstream of MCP1. However, no improvement in the angular resolutions is observed. This can be attributed to neglecting the effects from the beam angles and the actual beam position of the reaction target, as well as the unsatisfactory position calibrations in MCP1. A mask as discussed in Section 3.6.4 was used for MCP position calibration. For MCP1, the mask coverage is relatively limited due to the relatively small beam spot size. Analysis of the defoused beam which has much larger beam spot was tried with no success due to the unsatisfactory beam intensity. In addition, there was efficiency drop of the MCP1 performance for ^{46}Ar during the experiment. The MCP1 corner amplifications only give 91% and 94% multiplicity-4 signal for ^{34}Ar and ^{46}Ar respectively. Multiplicity equal to 4 is required to determine the position. With the unsatisfactory performance of the MCP we decided not to include the MCP data in the present analysis. Nevertheless, whether to include the MCP data or not does not change the conclusions from the experimental results. The MCP performance was improved significantly for another transfer reaction experiment [Expt06035] which allows precise determination of the beam angles, beam position and emitting deuteron angles resulting in improved position and energy resolution.

Chapter 5

Experimental results

After proper energy and position calibrations for all detectors, important physical observables including reaction kinematics, Q-values and differential cross sections were extracted. This chapter presents the experimental results for $p(^{34,36,46}\mathrm{Ar},d)\ ^{33,35,45}\mathrm{Ar}$ reactions and describes the method for absolute normalization and its associated uncertainties. In addition, structural information such as the orbital angular momentum and spectroscopic factor of the populated states, deduced by comparing the experimental differential cross sections to the reaction model calculations, is also presented. Theoretical spectroscopic factors from shell model predictions are discussed. The extracted asymmetry dependence of the reduction factors in transfer reactions is compared to the measurements from knockout reactions. The result is also compared to trends obtained from the results from dispersive optical-model analysis on Ca isotopes.

5.1 Reaction kinematics

The kinematics (energy and angles) of deuterons from $p(^{34}\mathrm{Ar},d)^{33}\mathrm{Ar}$, $p(^{36}\mathrm{Ar},d)^{35}\mathrm{Ar}$ and $p(^{46}\mathrm{Ar},d)^{45}\mathrm{Ar}$ reactions were obtained by gating on deuterons, beams and recoil residues. Figures 5.1-5.3 present the deuteron kinematics (energy vs. angle) for different reaction systems in laboratory frame. In each spectrum, the bands correspond to deuteron in coincidence with various states of reaction residues and the curves are the calculated kinematics according to the excitation energies compiled in the NNDC database

[NNDC]. The energy levels of ^{33}Ar, ^{35}Ar and ^{45}Ar below 6 MeV, with spin and parity assignments if available, are listed in Table 5.1. Those highly populated states with corresponding kinematics calculations shown in Figures 5.1-5.3 are highlighted in bold. It is apparent from the kinematics spectra that the agreement between the data and calculations is satisfactory and the ground-state kinematics bands for ^{36}Ar and ^{34}Ar are well-separated from the excited states. Such agreement allows clear identification of the strongly populated states.

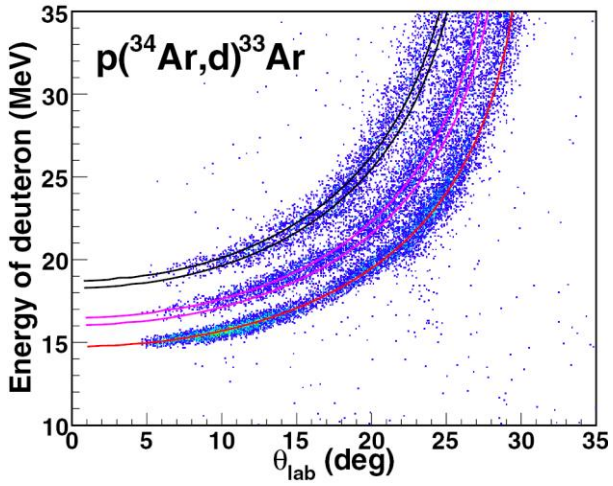

Figure 5.1: Deuteron kinematics for $p(^{34}\text{Ar},d)^{33}\text{Ar}$ in laboratory frame.

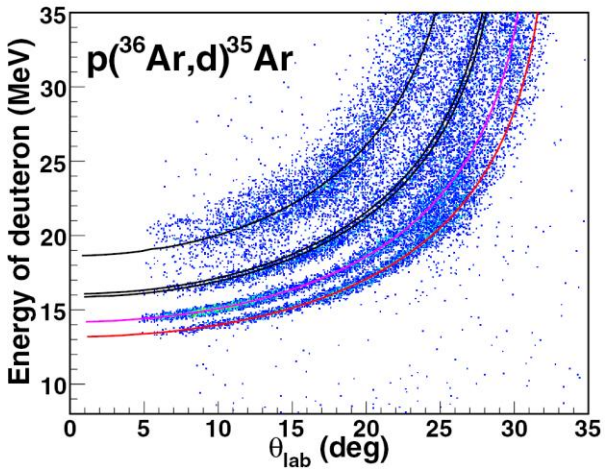

Figure 5.2: Deuteron kinematics for $p(^{36}\text{Ar},d)^{35}\text{Ar}$ in laboratory frame.

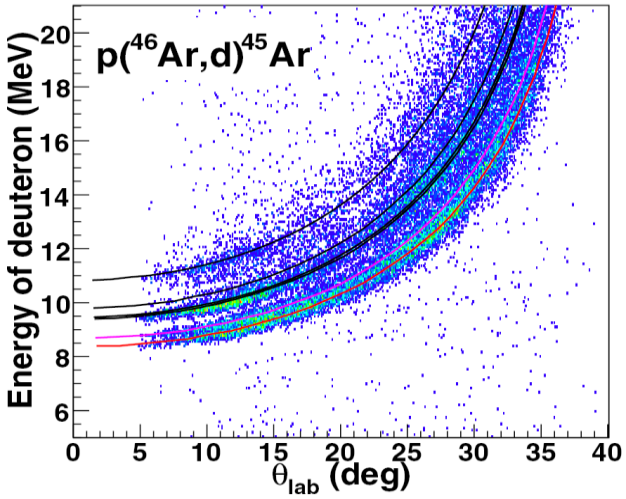

Figure 5.3: Deuteron kinematics for $p(^{46}\mathrm{Ar},d)^{45}\mathrm{Ar}$ in laboratory frame.

Table 5.1: Energy levels (< 6 MeV), spin and parity assignments for each reaction [NNDC] where the energy levels with corresponding kinematics plotted in Figure 5.1-5.3 are presented in bold.

^{33}Ar		**^{35}Ar**		**^{45}Ar**	
level (keV)	J^{π}	level (keV)	J^{π}	level (keV)	J^{π}
0	1/2+	**0**	3/2+	**0**	5/2-, 7/2-
1359	(3/2+)	**1184.0**	1/2+	**542.1**	1/2-, 3/2-
1798	(5/2+)	1750.6	(3/2, 5/2)+	1339.9	
2439 ?	(3/2+)	2600.8		1416.1	1/2-, 3/2-
3154	(3/2+)	2637.9	(3/2, 5/2)+	1660 ?	
3361	(5/2+)	**2982.81**	(3/2, 5/2)+	**1734.7**	
3456	(7/2+)	**3193**	(5/2, 7/2)-	**1770.3**	
3819	(5/2+)	3884	1/2+	**1876**	1/2-, 3/2-
		4012	(1/2, 3/2)-	**1911**	
		4065.1	(1/2, 3/2, 5/2)+	**2420**	
		4110		2510	1/2-, 3/2-
		4142	(1/2, 3/2)-	2757.0 ?	
		4350		3230	
		4528.2	(1/2, 3/2, 5/2)+	3294.8	
		4725.8	1/2+	3718	
		4785.8	(1/2, 3/2, 5/2)+	**3949.7**	
		5048		4280	
		5116	(3/2, 5/2)+	4326.1	
		5205		4800	
		5387		5773	
		5484	(3/2, 5/2)+		
		5572	3/2+		
		5591	(3/2, 5/2)+		
		5911			

5.2 Q-value calculations

For best resolution, the reaction Q-value calculation is mainly based on the excitation energy of residue determined from the measured kinetic energy and angle of the emitted deuteron. From conservation of energy and momentum of the binary reaction of $A+p \rightarrow B+d$, we can express the kinematic energy of deuteron in center-of-mass (COM) frame with relativistic approach:

$$t_{\mathrm{d}}^{\mathrm{COM}} = \frac{(E_{\mathrm{COM}} - m_{\mathrm{d}})^2 - (m_{\mathrm{B}}^*)^2}{2E_{\mathrm{COM}}} \qquad (5.1)$$

where m_d is the rest mass of deuteron; m_B* is the rest mass of residue plus the excitation energy; E_{COM} is the center-of-mass energy which can be calculated from the beam energy and the rest mass of the beam particle and proton.

By Lorentz transformation of Four-Vector momentum $P_d = (E_d, \overrightarrow{P_d})$, the kinetic energy of emitted deuteron in COM frame (t_d^{COM}) can be determined from its measured kinetic energy and angle in the laboratory frame. Here the beam angle is assumed to be sufficiently small and is not considered in the calculations.

After determining m_B* using Equation 5.1, the reaction Q-value of p(A,d)B* is obtained on an event-by-event basis:

$$Q = m_{\mathrm{A}} + m_{\mathrm{a}} - m_{\mathrm{d}} - m_{\mathrm{B}}^* \qquad (5.2)$$

where m_A, m_p, m_d are the rest mass of the beam particle, proton and deuteron respectively; m_B* is the rest mass of the residue plus its excitation energy.

Figures 5.4-5.6 show the reaction Q-value spectra for $p(^{34}\mathrm{Ar},d)^{33}\mathrm{Ar}$, $p(^{36}\mathrm{Ar},d)^{35}\mathrm{Ar}$ and $p(^{46}\mathrm{Ar},d)^{45}\mathrm{Ar}$ respectively. For the ^{34}Ar Q-value spectrum (Figure 5.4), the peak corresponding to the ground-state transition is well-distinguished with FWHM of approximately 500 keV; while the peak at the second lowest excitation is comprised of the first two low-lying states (1.358 and 1.798 MeV). In the Q-value spectrum of ^{36}Ar (Figure 5.5), the ground-state and the first excited state (1.184 MeV) are clearly identified, where the FWHM of the ground-state peak is 470 keV. Since the resolution of CsI crystals is much worse than the resolution of the Si detectors, the Q-value spectra presented here exclude events of deuterons punching though the thick Si detector. Therefore, the laboratory angular coverage in the Q-value spectrum for ^{34}Ar and ^{36}Ar is up to 23° and 26° respectively. In addition to excluding deuterons punching through silicon detectors, the ^{46}Ar Q-value spectrum shown in Figure 5.6 covers laboratory angles only up to 19°. Since the beam positions and angles on reaction target are not well-determined from MCP data as discussed in Section 5.3, the ground-state and first excited state (0.542 MeV) at larger angles could not be clearly resolved. The FWHM of the ground-state peak of $p(^{46}\mathrm{Ar},d)^{45}\mathrm{Ar}$ is about 416 keV. The excitation energies of a number of low-lying states were also determined as indicated in the spectrum.

The FWHM of the peaks in the Q-value spectra were verified by GEANT4 simulations [Ago03]. The simulations take into account the resolution of HiRA detectors, angular and energy straggling, kinematics broadening as well as energy resolution of the beam and the finite-size of the beam spot. The resolution of the detection system due to pixelation and detector performance is about 350 keV. Other contributions to energy

resolutions from energy straggling and position resolution on target for each reaction at specific angles are summarized in Table 5.2. The simulated resolutions in center-of-mass frame for $p(^{34,36,46}\mathrm{Ar},d)$ correspond to all the laboratory angles where deuterons do not punch-through the thick silicon detectors. In general, the resolutions obtained from the experiments are consistent with the predicted resolution from simulations. The main contributions to the resolutions were effects due to the target thickness and the kinematic dispersion from the large beam spots. The small discrepancy in energy resolutions between data and simulations for $^{36}\mathrm{Ar}$ case may be attributed to the problems in energy calibrations.

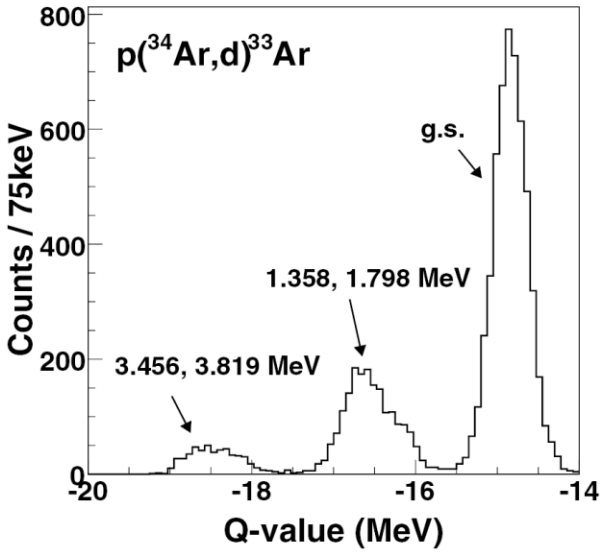

Figure 5.4: $p(^{34}\mathrm{Ar},d)^{33}\mathrm{Ar}$ Q-value spectrum with laboratory angular coverage from 5° to 23°.

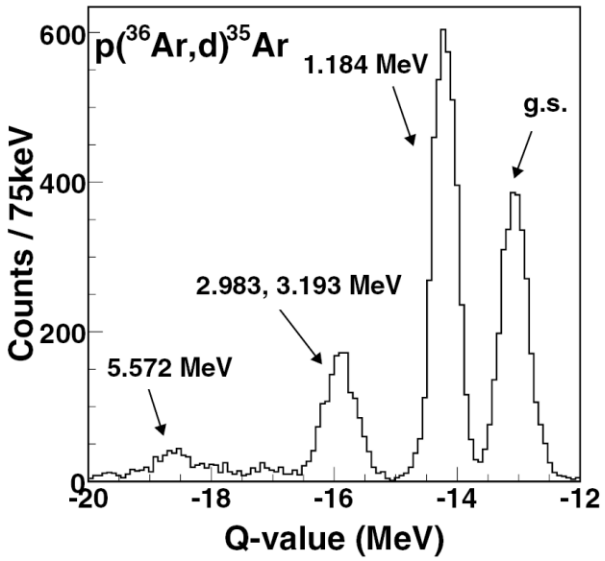

Figure 5.5: $p(^{36}\mathrm{Ar},d)^{35}\mathrm{Ar}$ Q-value spectrum with laboratory angular coverage from 5° to 26°.

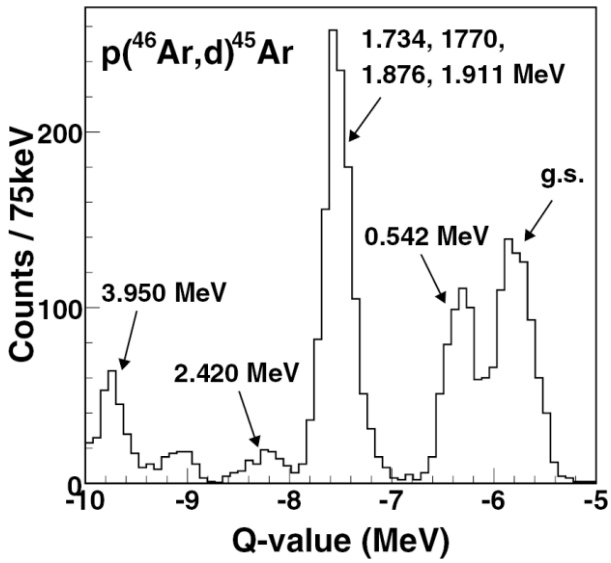

Figure 5.6: $p(^{46}\mathrm{Ar},d)^{45}\mathrm{Ar}$ Q-value spectrum with laboratory angular coverage from 5° to 19°.

Table 5.2: Contributions to the energy resolutions (FWHM) simulated by Geant4 code and comparisons to the FWHM of the peak corresponding to ground-state transitions in the Q-value spectra for the reactions in inverse kinematics.

Reactions (g.s)				**Geant4 Simulations – energy resolutions in keV**				**Data**
	θ_{Lab}	Target thickness	Beam spot (FWHM)	Straggling in Target	Position resolution	Lab. at θ_{Lab}	COM (all angles w/o CsI)	Q-value (keV)
p(^{36}Ar,d)	24°	75 um	3 mm	447	425	650	420	470
p(^{34}Ar,d)	21°	75 um	10 mm	470	750	893	495	500
p(^{46}Ar,d)	30°	25 um	8 mm	397	717	839	377	416

5.3 Background subtraction

The data runs in this experiment were taken with HiRA -S800 coincidence triggers. The deuterons of interest were obtained from the d-^{33}Ar, d-^{35}Ar and d-^{45}Ar coincidence events with the corresponding beam gates. Therefore the main background would mainly be random coincidence. The reaction target was polyethylene $(CH_2)_n$. To assess contributions from the reactions with C nuclei, a 17 mg/cm^2 thick uniform carbon target was employed to evaluate the background. Analyzing the carbon target data in the same way as the normal data runs would directly give the number of deuterons from C background coincidence. Judging from the background in the energy vs. angle spectra in Figures 5.1-5.3, p(^{46}Ar,d) ^{45}Ar reaction has the worse background, probably due to the thin target that was used. The carbon target run was measured using ^{46}Ar beams with HiRA-S800 coincidence trigger. The left panel of Figure 5.7 shows the spectra of the S800 PID gated on ^{46}Ar incoming beam.

Since the number of carbon particles in the target and the duration of runs are different between the carbon target runs and normal data run, normalization in the reaction occurrence is necessary for correct estimate of the background counts. The number of carbon particles on the 17 mg/cm^2 pure carbon target and the 25 *u*m $(CH_2)_n$ target are 8.52x10^{20}/cm^2 and 9.88x10^{19}/cm^2 with the corresponding total beam particles of 2.83x10^9 and 4.15x10^{10} respectively. Therefore the normalization factor is 1.7. The right panel of Figure 5.7 shows the deuteron kinematics spectrum gated on the ^{46}Ar beam particles and ^{45}Ar residues. Multiplying the number of counts in this spectrum by a factor of 1.7 would give the actual background level. From Figure 5.3, it is clear that the random coincidence events could be neglected in ^{46}Ar reaction system. The same conclusion should also be valid for ^{34}Ar and ^{36}Ar as the background problems are much less severe because thicker targets were used. Therefore no background subtraction is included in the analysis discussed here.

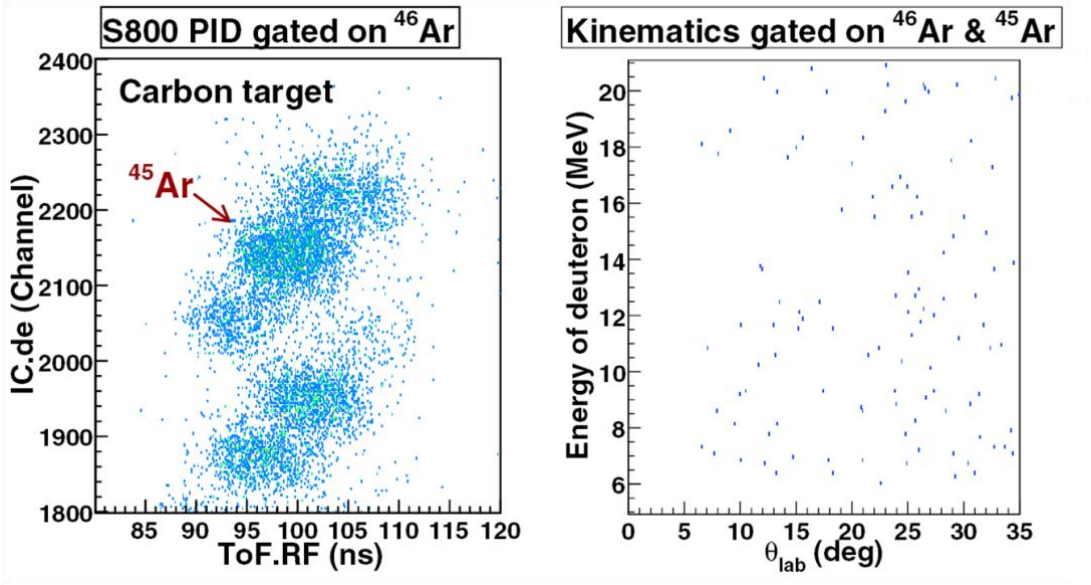

Figure 5.7: Carbon target reaction runs with ^{46}Ar beam. (Left) S800 PID spectrum gated on the incoming ^{46}Ar beam. (Right) Deuteron kinematics spectrum gated on ^{46}Ar beam particle and ^{45}Ar residues.

5.4 Extraction of Cross sections and spectroscopic factors

Normalization analysis is critical in the extractions of absolute cross sections. This section describes the procedures used to obtain absolute normalization and differential cross sections as well as the methods to estimate the measurement uncertainties arising from data acquisition live time and various detector efficiencies. In addition, comparisons of cross section data to reaction model predictions and the extraction of spectroscopic factors are discussed.

5.4.1 Absolute normalization and error analysis

The absolute differential cross sections as a function of angle could be expressed by the following equation 5.3:

$$\left(\frac{d\sigma}{d\Omega}\right)_{\theta_i}^{lab} = \frac{N_d(\theta_i)}{\Delta\Omega(\theta_i) N_{tar} N_{beam}} \qquad (5.3)$$

where N_{beam} is the total beam particles that hit the target for all the runs; N_{tar} is the number of hydrogen nuclei per centimeter square in the reaction target; N_d is the actual number of deuterons from the desired reaction emitted in the i^{th} angular bin of $\pm$ 1° for a given scattering angle in laboratory frame; $\Delta\Omega(\theta_i)$ is the laboratory solid angle subtended by the scattering angle.

By using Jacobian transformation from the laboratory to center-of-mass coordinates for the i^{th} angular bin, the differential cross sections in center-of-mass frame can be obtained using Equations 5.4-5.5:

$$\left(\frac{d\sigma}{d\Omega}\right)_{COM} = \gamma \left(\frac{d\sigma}{d\Omega}\right)_{lab}, \quad \gamma = \frac{\left|1-\rho Cos\theta_i^{COM}\right|}{(1+\rho^2-2\rho Cos\theta_i^{COM})^{3/2}} \qquad (5.4)$$

$$\rho = \frac{m_A\, m_d}{m_B\, m_p} \left(\frac{E_d^{COM}}{E_d^{COM}+Q}\right) \qquad (5.5)$$

where γ is the Jacobian transformation, E_d^{COM} is the center-of-mass kinetic energy of deuteron, Q is the reaction Q-value, m_A, m_B, m_p and m_d are the rest mass of the beam particle, residue, proton and deuteron respectively and θ_i^{COM} is the center-of-mass angle corresponding to the i^{th} angular bin.

The actual number of deuterons, N_d, is determined from the measured recoil-coincident deuterons with consideration of the live time of data acquisition (ϵ_{DAQ}),

A1900 XFP efficiency (ϵ_{XFP}), S800 acceptance and transmission efficiency (ϵ_{S800}), and the HiRA geometric efficiency ($\epsilon(\theta_i)_{HiRA}$) corrected for $N_d^{Det}(\theta_i)$ using Equation5.6.

$$N_d(\theta_i) = \sum_{run}\left(\frac{N_d^{Det}(\theta_i)/\varepsilon(\theta_i)_{HiRA}}{\varepsilon_{DAQ}\,\varepsilon_{XFP}\,\varepsilon_{S800}}\right)_{run} \qquad (5.6)$$

As seen in Equation 5.3, the absolute normalization of the cross sections requires direct continuous measurement of beam intensities N_{beam} which was achieved by the Multi-Channel Plates (MCP) detection system placed 10 cm in front of the reaction target. Since the number of beam particle was determined from MCP, the MCP efficiency is required in order to obtain the actual beam particles on target.

The statistical uncertainty in cross sections is $1/\sqrt{N_d^{Det}}$. Weighing several pieces of target foils suggests less than 1% uncertainty in the target thickness which was neglected in the analysis. Other uncertainties stemming from the determinations of beam intensities, detector efficiencies and live time of DAQ system are considered as systematic uncertainties. In this subsection, the detection efficiencies and the overall normalization uncertainties are discussed.

Detection efficiencies

A. Live time of data acquisition

The live time of the data acquisition is the period when the data acquisition system is accepting the arriving events. The counting rates of events as a function of time were

recorded by electronic scaler modules. By comparing the live to raw (total) rates of trigger events, the DAQ live time can be evaluated. Figure 5.8 shows the ratios of the live to raw rates from MCP0, MCP1 and the clock in the $p(^{34,36,46}\mathrm{Ar},d)$ reactions. The drop in the live time in $p(^{34}\mathrm{Ar},d)\ ^{33}\mathrm{Ar}$ measurement is correlated to the beam rate. The MCP1 live time, which is similar to the MCP0 and the clock live time, was used as DAQ live time in this experiment.

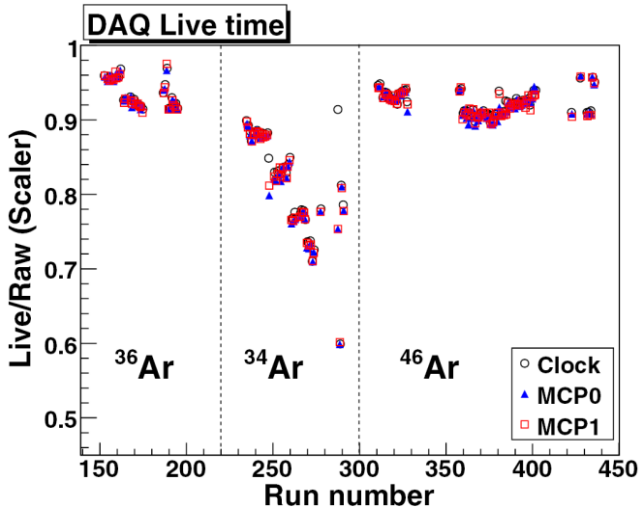

Figure 5.8: Live time of data acquisition determined by the ratios of live to raw rate of MCP0, MCP1 and the clock in the $p(^{34,36,46}\mathrm{Ar},d)$ reactions

B. MCP efficiency

The efficiency of MCP is determined by taking the ratio of the number of registered MCP time events gated on S800 E1 signal to the E1 time events. Since MCP1 time signal was used for MCP-OR input in the DAQ system, MCP1 efficiency is assumed to be 100% relative to MCP0. Figure 5.9 plots the MCP1 efficiency for the reaction runs. The central part of the MCP1 is intensely exposed from the secondary electrons, because the beam

was focused at the reaction target which is 10 cm downstream from MCP1. Therefore the MCP efficiency generally deteriorates with time. To recover the efficiency, bias voltage was raised from 2290V to 2450V at run 398.

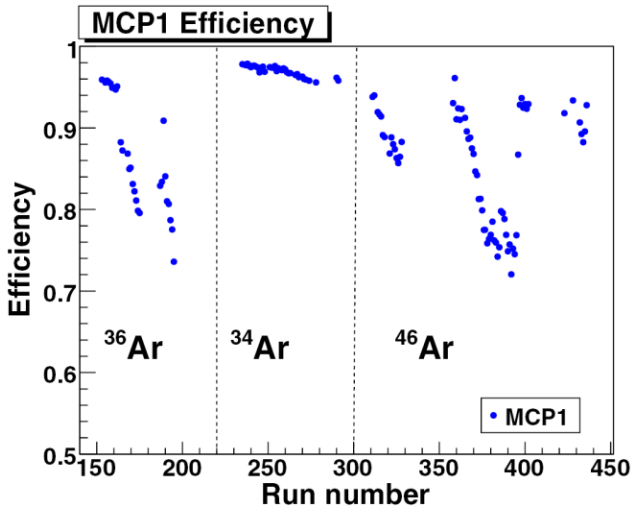

Figure 5.9: MCP1 efficiency of the $p(^{34,36,46}\mathrm{Ar},d)$ reactions.

C. A1900 extended focal plane efficiency

The A1900 extended focal plane (XFP) efficiency was monitored during the experiment. The performance of the scintillator is affected by radiation damage. For slight deterioration, the XFP scintillator bias was simply raised or the XFP scintillator would be moved so that the incoming beam would hit a fresh spot on the scintillator. If the efficiency dropped significantly, the XFP scintillator is replaced. Since beam gates imposed in the analysis were constructed with the ToF-XFP, XFP efficiency needs to be included for absolute cross section determination. The RF and XFP signals for the same data run are shown in the left and right spectrum in Figure 5.10. The total number of RF and XFP event recorded are listed in the spectra. The XFP efficiency for each run is then determined from the ratio of the total event number of XFP to RF based on the fact that

there is no efficiency problem in RF. Figure 5.11 summarizes the XFP efficiency for each data run. Same XFP efficiency is obtained by taking the ratio of the total event number of XFP to E1 of S800 spectrometer.

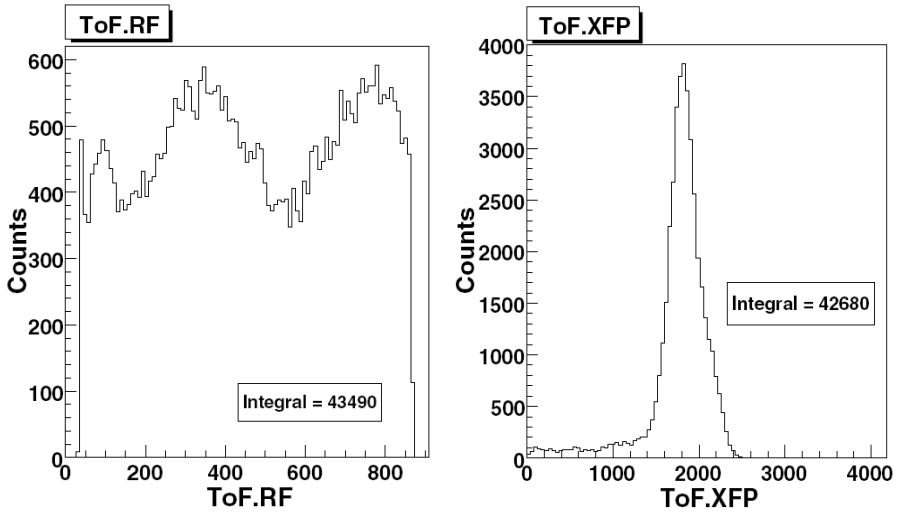

Figure 5.10: The RF (left) and XFP (right) signals for the same data run of $p(^{34}\mathrm{Ar},d)$ reaction. The total number of RF and XFP event recorded are listed in the figure.

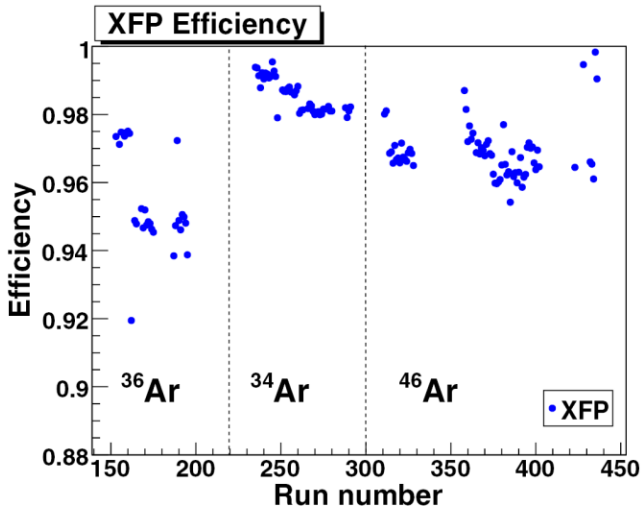

Figure 5.11: A1900 XFP efficiency of the $p(^{34,36,46}\mathrm{Ar},d)$ reactions.

D. S800 acceptance and transmission efficiency

In the present experiment, a tungsten beam blocker was inserted on the low rigidity side of the S800 magnet in order to block the high-momentum tail of the unreacted beam to protect the focal plane detectors. To ensure that the residues of interest were not blocked by the blocker, we investigated the fragments of interest in CRDC dispersive positions with and without being gated on deuterons detected in HiRA. We found that all the fragments corresponding to the reactions of interest are within S800 acceptance. Thus no correction is needed in the normalization factor. Unfortunately, there is no reliable method to obtain the S800 transmission efficiency in this experiment. We assumed the efficiency to be 100%.

E. HiRA geometric efficiency

In the experiment, 16 HiRA telescopes were placed at 35 cm downstream from the center of reaction target. The actual positions of pixels obtained from LBAS measurement as discussed in Section 3.6.3 were used to calculate the actual HiRA geometric efficiency. One CsI crystal in telescope 15 and a total of 38 silicon strips (17 DE, 13 EF and 8 EB) did not work. In addition, strip 15 and 16 are not used in the data analysis because of the gaps between CsI crystals. All these non-functioning crystal and strips have to be taken into account to determine the correct HiRA geometric efficiency. For ^{46}Ar reaction, some of the deuterons completely stopped in EF silicon detector in telescope 5 and 6 without being identified because no DE detector was mounted. Geometric efficiency for the angular regions covered by these two telescopes was corrected.

F. Beam Purity

Degraded ^{36}Ar beam and secondary ^{46}Ar beam were obtained in this experiment. Secondary beam ^{34}Ar with main contaminant ^{33}Cl was identified by time of flight from cyclotron to the A1900 focal plane, using the radio-frequency (RF) of cyclotron and a scintillator at the extended focal plane at the end of the A1900 spectrometer. Since momentum acceptance at image 2 of A1900 was adjusted from 0.5% to 1% to increase the beam intensity on target, the purity of ^{34}Ar changed accordingly. Figure 5.12 displays the purity of ^{34}Ar beam for each data run.

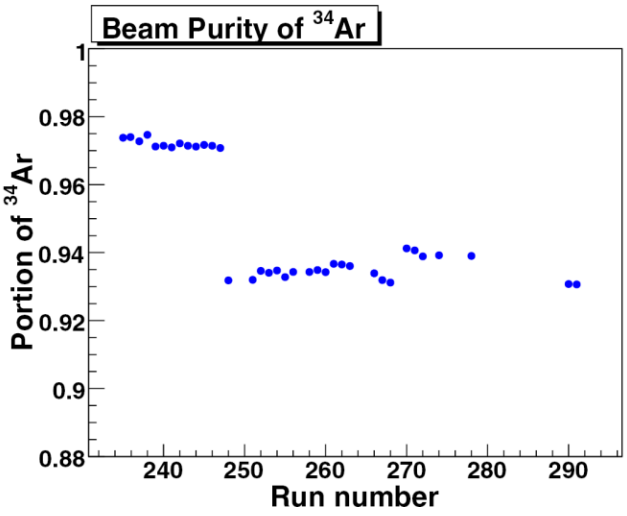

Figure 5.12: Proportion of ^{34}Ar in the incoming secondary beams for the $p(^{34}\mathrm{Ar},d)$ reactions.

Overall normalization uncertainties

In our analysis, the cross sections presented in Table 5.3 were extracted from all the data available. To estimate the overall normalization uncertainties arising from detection efficiencies and systematics uncertainties, we divided the whole set of data for each (p,d) reaction into several groups and extracted the cross sections from each data groups individually. By examining the consistency of the absolute cross sections extracted from different data groups, we can estimate the overall normalization uncertainty.

We grouped approximately every 100 counts in 2-degree bin size and analyzed the cross section using the data in each group individually. The extracted cross sections from each group at deuteron angles θ_{lab}=9° for $p(^{34}\mathrm{Ar},d)$, θ_{lab}=23° for $p(^{36}\mathrm{Ar},d)$ and θ_{lab}= 15° for $p(^{46}\mathrm{Ar},d)$ are presented in Figure 5.13. The solid lines indicate the cross sections at the same corresponding angles extracted using all available data in the experiments. Fluctuations between different times of data-taking are found, but the overall normalization uncertainties are better than 10% indicated by the corresponding dashed lines. The large deviations in the second and third data group of $p(^{46}\mathrm{Ar},d)$ can be explained by the instability of MCP.

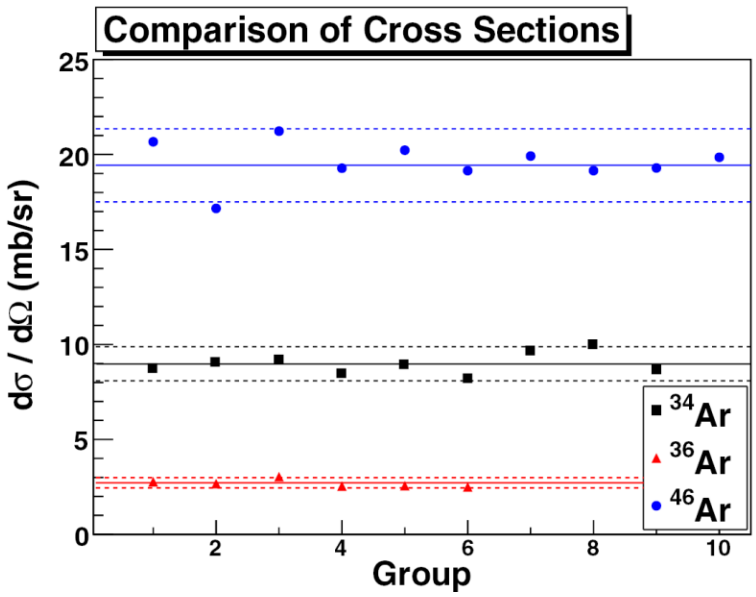

Figure 5.13 Comparisons of absolute differential cross sections at certain angles for p($^{34, 36, 46}$Ar,d) reactions respectively over the entire experiment. The symbols represent the cross sections deduced from about every 100 counts. The solid lines indicate the cross sections extracted using all the available data, while the dashed lines are ±10% of the solid line.

5.4.2 Differential cross sections and spectroscopic factors

After properly determine the normalization for each reaction, the experimental differential cross sections in center-of-mass and the associated statistical errors for *p*(^{34,36,46}Ar,*d*) reactions at 33 MeV/nucleon leading to the ground state, first excited state and groups of excited states are extracted and listed in Table 5.3. The data are also plotted in solid circles with purely statistical uncertainties as shown in Figures 5.14-5.19, 5.21, 5.23-5.26. For the ground states, differential cross sections determined from the present measurements are compared to calculations in the framework of the ADWA using two different prescriptions: (I) CH89 global optical-model potentials and transferred neutron orbital with Woods-Saxon potential of fixed radius 1.25 fm (discussed in section 2.2.1);

(II) JLM potential geometries and single-particle parameters constrained by Hartree-Fock calculations (discussed in section 2.5). For clarity and simplicity, we labeled these two approaches as “CH89” and “JLM+HF”. It should be noted that JLM+ HF descriptions are not available for excited states here because they require HF calculations of the nucleon densities and radii of transferred nucleons for excited-states. Calculations plotted in Figures 5.14-5.19, 5.21, 5.23-5.26 are normalized to the data around the first maximum. Blue and purple lines represent the CH89 and JLM+HF calculations respectively. The normalization factors are the SF values with the associated uncertainties. They are listed in Table 5.4.

Table 5.3: Differential cross sections in center-of-mass frame for $p(^{34,36,46}\mathrm{Ar},d)$ populating to ground-state and excited states of ^{33,35,45}Ar. The uncertainties presented here are purely statistical.

$p(^{34}\mathrm{Ar},d)^{33}\mathrm{Ar}$, Ex=0 MeV		
θ_{COM} (deg.)	$d\sigma/d\Omega$ (mb/sr)	$\Delta d\sigma/d\Omega$ (mb/sr)
6.9	11.75	0.52
9.0	8.97	0.30
11.1	5.47	0.18
13.4	3.00	0.11
15.7	1.45	0.08
18.3	1.11	0.07
21.0	1.53	0.07
23.7	2.09	0.09
28.6	2.10	0.09
31.7	1.54	0.05
37.0	0.60	0.02

$p(^{34}\mathrm{Ar},d)^{33}\mathrm{Ar}$, Ex=1.359+1.798 MeV		
θ_{COM} (deg.)	$d\sigma/d\Omega$ (mb/sr)	$\Delta d\sigma/d\Omega$ (mb/sr)
7.8	0.90	0.13
10.1	0.90	0.08
12.5	0.93	0.07
15.1	1.07	0.06
17.8	1.29	0.07
20.7	1.40	0.06
28.7	1.15	0.07
32.0	0.99	0.04
37.5	0.70	0.02

$p(^{34}\mathrm{Ar},d)^{33}\mathrm{Ar}$, Ex=3.456+3.819MeV		
θ_{COM} (deg.)	$d\sigma/d\Omega$ (mb/sr)	$\Delta d\sigma/d\Omega$ (mb/sr)
8.94	0.52	0.09
11.64	0.54	0.06
14.47	0.68	0.05
16.33	0.70	0.09
20.71	0.96	0.07
24.27	0.83	0.04
28.29	0.88	0.04
33.03	0.61	0.03
39.03	0.44	0.02

$p(^{36}\mathrm{Ar},d)^{35}\mathrm{Ar}$, Ex=0 MeV		
θ_{COM} (deg.)	$d\sigma/d\Omega$ (mb/sr)	$\Delta d\sigma/d\Omega$ (mb/sr)
6.2	1.98	0.31
8.0	2.06	0.21
9.9	1.55	0.14
11.8	1.92	0.13
13.9	2.04	0.14
16.1	2.42	0.14
18.5	2.69	0.14
21.1	2.75	0.13
23.9	2.68	0.11
26.4	2.18	0.13
31.2	0.82	0.04

$p(^{36}\mathrm{Ar},d)^{35}\mathrm{Ar}$, Ex=1.184 MeV		
θ_{COM} (deg.)	$d\sigma/d\Omega$ (mb/sr)	$\Delta d\sigma/d\Omega$ (mb/sr)
6.6	14.04	0.76
8.6	12.01	0.47
10.6	6.58	0.27
12.7	3.80	0.17
15.0	1.87	0.12
17.4	1.24	0.09
20.0	1.69	0.10
22.8	2.41	0.11
25.2	2.80	0.16
29.8	2.19	0.08
34.5	1.04	0.04

Table 5.3 (cont'd)

p(^{46}Ar,d)^{45}Ar, Ex=0+0.542 MeV		
θ_{COM} (deg.)	dσ/dΩ (mb/sr)	Δdσ/dΩ (mb/sr)
4.1	19.34	1.31
5.3	19.97	0.89
6.5	20.30	0.69
7.8	19.26	0.58
9.1	19.41	0.59
10.4	18.72	0.60
11.9	16.89	0.64
13.4	16.29	0.69
15.0	14.12	0.52
16.8	14.15	0.44
18.7	13.25	0.35
20.9	12.95	0.33
23.3	11.24	0.28
26.3	8.75	0.21

p(^{46}Ar,d)^{45}Ar, Ex=0 MeV		
θ_{COM} (deg.)	dσ/dΩ (mb/sr)	Δdσ/dΩ (mb/sr)
4.1	11.47	0.98
5.3	12.09	0.67
6.5	11.59	0.51
7.8	10.75	0.41
20.9	12.95	0.33
23.3	11.24	0.28
26.3	8.75	0.21

p(^{46}Ar,d)^{45}Ar, Ex=1.734-1.911 MeV		
θ_{COM} (deg.)	dσ/dΩ (mb/sr)	Δdσ/dΩ (mb/sr)
4.5	19.45	1.19
5.8	18.74	0.78
7.2	15.03	0.54
8.6	11.07	0.39
10.0	8.92	0.36
11.6	6.14	0.31
13.2	5.24	0.32
14.9	5.33	0.35
16.7	6.10	0.31

p(^{46}Ar,d)^{45}Ar, Ex ~ 3.950 MeV		
θ_{COM} (deg.)	dσ/dΩ (mb/sr)	Δdσ/dΩ (mb/sr)
5.02	4.25	0.50
6.51	3.58	0.31
8.03	2.67	0.20
9.61	2.13	0.15

$p(^{34}Ar,d)^{33}Ar$

For $p(^{34}Ar,d)^{33}Ar$, the shapes of the predicted angular distributions from CH89 (solid curve) and JLM+HF (dashed curve) are in good agreement to the data for the ground-state transition shown in Figure 5.14. The angular distribution clearly characterizes the l=0 angular momentum transfer in the reaction. SF(CH89) = 1.10 and SF(JLM+HF) = 0.85 listed in Table 5.7 were extracted by using the first three data points.

The spectroscopic factors for excited states use only the CH89 algorithms. JLM+HF calculations are not available to describe the excited states. The first two low-lying states, $1d_{3/2}$ at 1.358 MeV and $1d_{5/2}$ at 1.795 MeV, cannot be resolved. Unfortunately these two states have the same orbital angular momentum l=2 and distinguishing the individual contributions of these two states using angular distributions cannot be achieved. The total cross sections are presented in Figure 5.15. CH89 calculations reproduce the experimental data well. Since the calculations of angular distributions for transfer reactions are not sensitive to the spin value (J). Fitting the data around the peak gives normalization of 2.34. Large-basis shell-model calculations suggest a 3/2+ and 5/2+ states at 1.46 and 1.96 MeV respectively. Their corresponding SF values are 0.517 and 1 respectively.

There is another distinct group at excitation energies of 3.456 and 3.819 MeV as shown in the Q-value spectrum in Figure 5.4. The total differential cross sections are extracted and plotted in Figure 5.16. According to NNDC database, the tentative spin assignments of 3.456 MeV and 3.819 MeV states are $(7/2^+)$ and $(5/2^+)$ respectively. Large-basis shell-model calculations suggest a $5/2^+$ state at 4.08 MeV with SF value of

1.407 as shown in Table 5.4. Since the model space used in the calculations is restricted in *sd*-shell, no prediction of $7/2^-$ state is available. The l =2 in the CH89 calculations, which is the dash blue line in Figure 5.16, reasonably reproduce the data and give SF(CH89) = 1.98. Attempt to associate the peak to the $J^\pi=7/2^-$ state has been made. The black line in the figure is the total contribution of j=7/2 and j=5/2 transition, where the blue dotted and dashed lines represent the individual calculated angular distributions multiplied by the respective SF values. Using the combined fit for all the points except the most forward angle point, the SF(CH89) for the $J^\pi=5/2^+$ and $J^\pi=7/2^-$ are 1.49 and 0.43 respectively. Based on the present data, however, no firm conclusion can be drawn on whether the single-particle strength of $J^\pi=7/2^-$ is significant around this region of energy levels. However, the extracted SF values in good agreement with the LB-SM predictions strengthens the tentative assignment of $J^\pi=5/2^+$ for the 3.819 MeV states

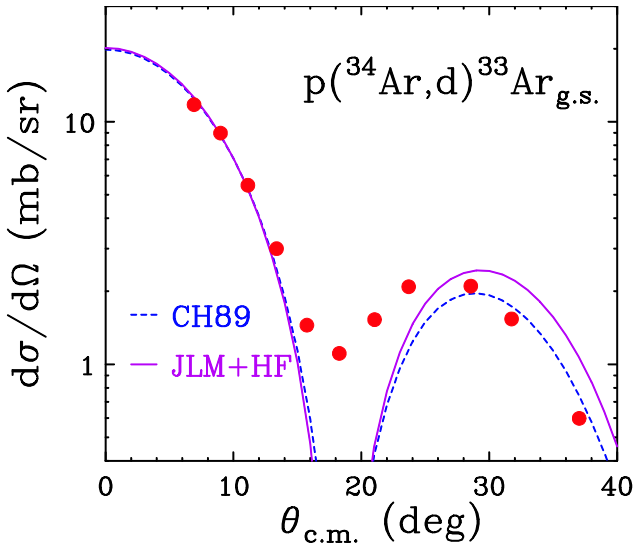

Figure 5.14: Differential cross sections for $p(^{34}\mathrm{Ar},d)^{33}\mathrm{Ar}$ in the center-of-mass frame for the ground-state transition. The red solid circles are the data from the present experiment. The solid and dashed curves are the calculations using CH89 and JLM sets of parameters respectively. The calculations are normalized to the data.

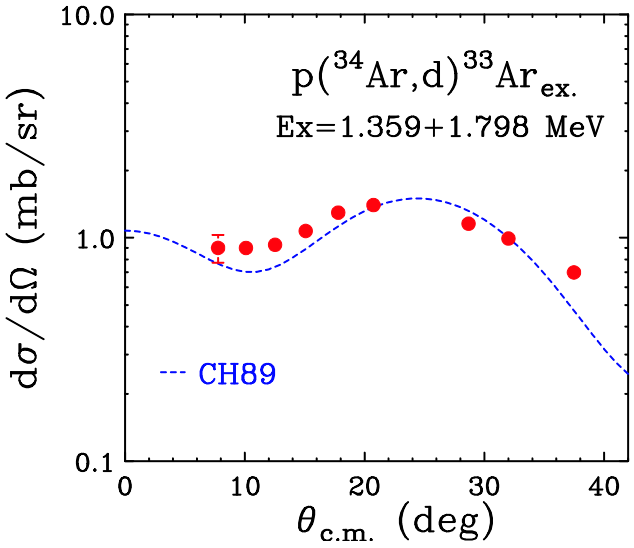

Figure 5.15: Differential cross sections for $p(^{34}\mathrm{Ar},d)^{33}\mathrm{Ar}$ in the center-of-mass frame for transitions to the 1.359 and 1.798 MeV excited states of ^{33}Ar. The red solid circles are the data from the present experiment. The solid curve is the calculation using the CH89 parameters normalized to the data.

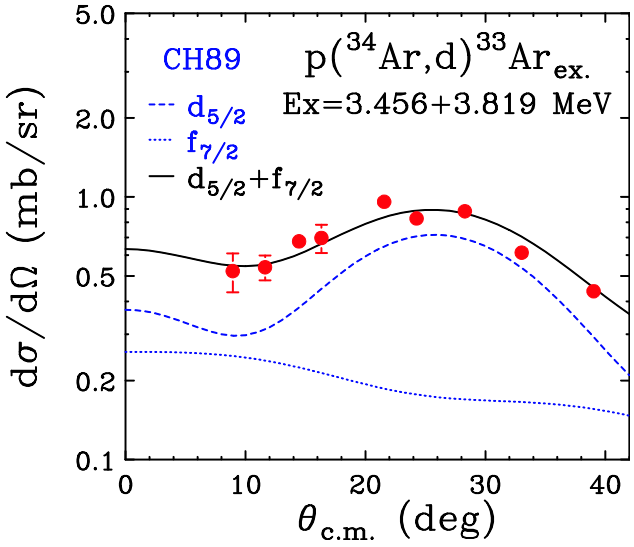

Figure 5.16: Differential cross sections for $p(^{34}\mathrm{Ar},d)^{33}\mathrm{Ar}$ in center-of-mass frame for transitions to the 3.456 and 3.819 MeV excited states. The red solid circles are the data from the present experiment. The black line is the total contribution of j=7/2 and j=5/2 transitions, where the blue dashed and blue dotted lines represent the individual calculated angular distributions multiplied by the respective SF values. Curves are calculations using the CH89 parameters normalized to the data.

$p(^{36}Ar,d)^{35}Ar$

The angular distributions of $p(^{36}Ar,d)^{35}Ar$ obtained from present measurements at 33 MeV/nucleon for transitions to ground-state (Figure 5.17) and first-excited state (Figure 5.18) are compared to the previous work of Kozub et al [Koz68] on the same reaction performed at 33.6 MeV/nucleon in normal kinematics. Our data and the results of Kozub et al are denoted by red closed circles and open squares respectively. The error bars shown in Figure 5.18 of Ref. [Koz68] are smaller than the size of the symbols presented here. The differential cross sections from Kozub et al and the present measurement are in reasonable agreement.

As shown in Figures 5.17-5.18, the calculated distributions using CH89 and JLM+HF approaches give good descriptions for the $p(^{36}Ar,d)^{35}Ar$ reactions, leading to the ground state transitions of ^{35}Ar. The CH89 method reproduces the cross sections of ground-state transition better at the very forward angles. For ground state transition, the six points in the first peak were used to obtain spectroscopic factors and the extracted values are SF(CH89) = 2.29 and SF(JLM+HF) = 1.60. For the first excited state, the first three points were used to obtain SF(CH89) = 1.23. No JLM+HF calculation was done for excited states.

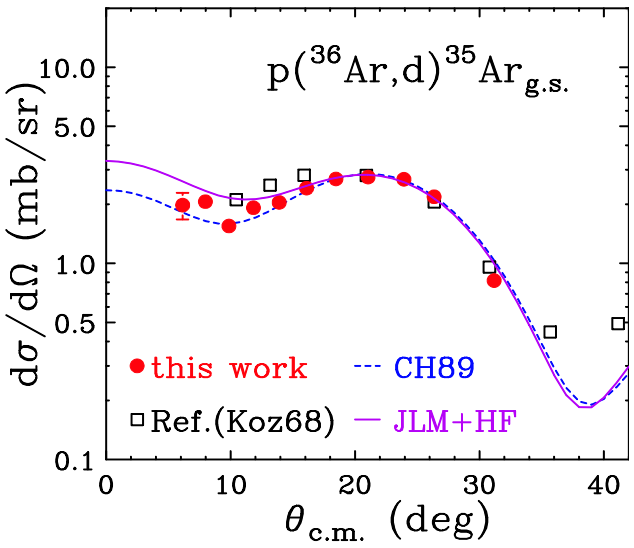

Figure 5.17: Differential cross sections for $p(^{36}\mathrm{Ar},d)^{35}\mathrm{Ar}$ in the center-of-mass frame for the ground-state transition. The red solid circles represent the data from present experiment in inverse kinematics and the black open squares represent results of the (*p*,*d*) reaction at 33.6 MeV/nucleon in normal kinematics from Kozub et al [Koz68]. The dashed and solid curves are the calculations using CH89 and JLM sets of parameters respectively. The calculations are normalized to the data.

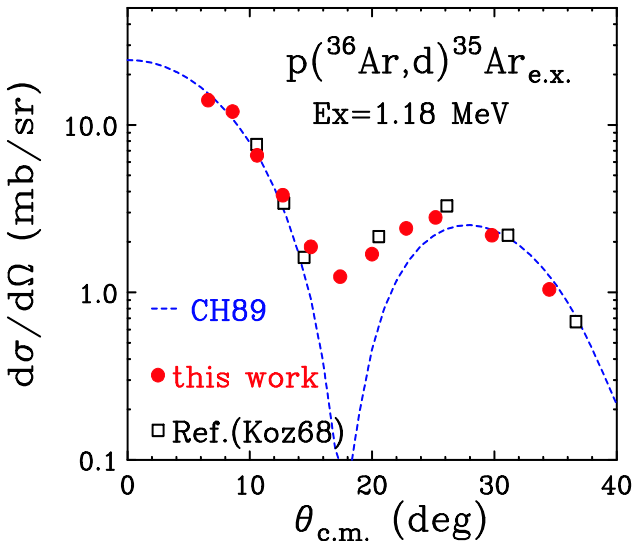

Figure 5.18: Differential cross sections for $p(^{36}\mathrm{Ar},d)^{35}\mathrm{Ar}$ in the center-of-mass frame for the transition to first excited state (1.18 MeV). The red solid circles represent the data from the present experiment in inverse kinematics and the black open squares represent results for the (*p*,*d*) reaction at 33.6 MeV/nucleon in normal kinematics from Kozub et al [Koz68]. The dashed curve is the calculation using CH89 set of parameters. The calculations are normalized to the data.

$p(^{46}Ar,d)^{45}Ar$

For $p(^{46}Ar,d)^{45}Ar$ reaction, the ground state and first excited state of ^{45}Ar are separated by 0.542 MeV. Due to the severe kinematics broadening and inefficiency of the MCP detection system in the experiment, we did not completely resolve the ground-state and first-excited state transitions at all angles. Figure 5.19 shows the experimental data contributed by both the ground and first excited state transitions. The respective l=3 and l=1characteristics for the ground and first excited state transition allows us to determine their individual contributions to the differential cross sections. At forward angles where kinematic broadening has the least effects, we could distinguish the peaks of the ground and first excited states at the small angles up to 13°. Figure 5.20 plots the Q-value spectra at laboratory angle of 12.5° ± 0.5°, which corresponds to center-of-mass angle of ~7.5°. For angles less than 13°, we can extract differential cross sections for ground and first excite states using double-Gaussian fitting. These cross sections are presented in Figure 5.21. The SF values of 5.28 and 0.51 for ground-state and first-excited state obtained by normalizing the calculations to the data points at forward angles would be used to guide the two-l value fitting for composite angular distributions. The dashed and dotted lines in Figure 5.19 represent the angular distributions of l=3 ground-state and l=1 first excited-state transitions and the solid line is the total angular distributions. All the data points are used for two-l value fitting constrained by the respective SF extracted at small angles. In general the shape of the experimental data is reasonably reproduced and the resulting SF(CH89) for ground-state and first-excited state are 5.08 and 0.51 respectively.

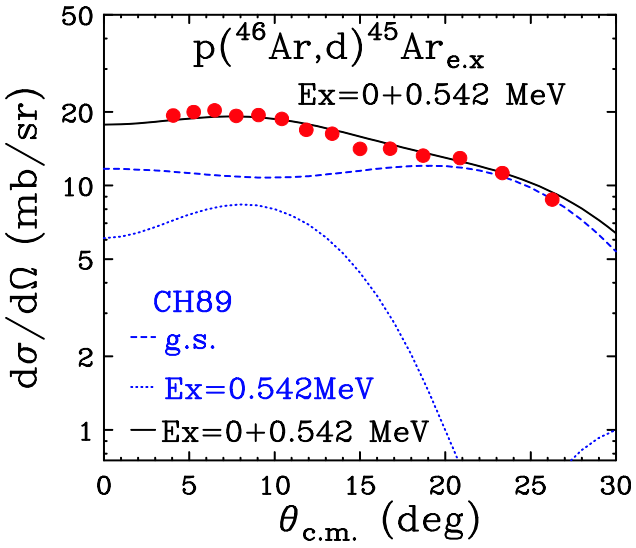

Figure 5.19: Differential cross sections of $p(^{46}\mathrm{Ar},d)^{45}\mathrm{Ar}$ in center-of-mass frame for transitions to ground state and first excited state. The red solid circles are the data from present experiment. The dashed and dotted curves are the calculations using CH89 for ground-state ($1f_{7/2}$-) and first excited state ($2p_{3/2}$-) multiplied by the corresponding SF respectively. The solid curve is the total contributions of these two transitions.

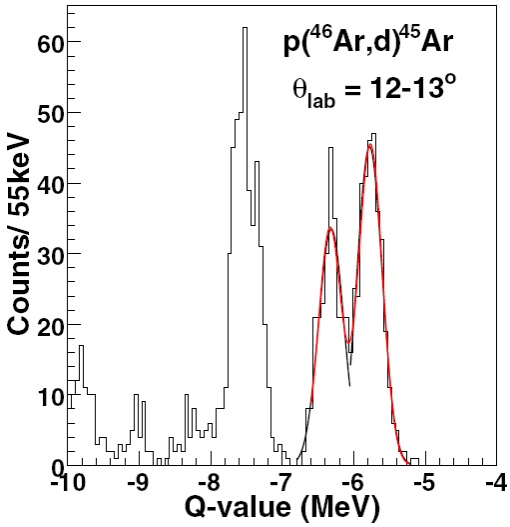

Figure 5.20: Q-value spectrum of $p(^{46}\mathrm{Ar},d)^{45}\mathrm{Ar}$ at θ_{lab}=12.5 ± 0.5° (θ_{COM}~7.5). The red curve is the Double-Gaussian fits to extract cross-sections corresponding to the ground- and first excited-state transitions.

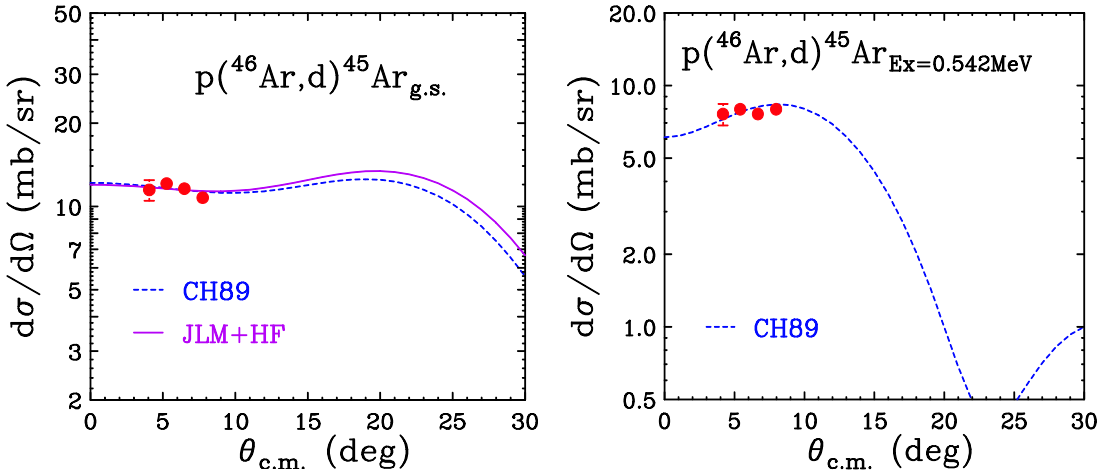

Figure 5.21: Differential cross sections of $p(^{46}\mathrm{Ar},d)^{45}\mathrm{Ar}$ in center-of-mass frame for group of transitions to ground state (left) and first excited state (right) at forward angles.

The different l values for the ground state (l=3) and first excited states (l=1) result in very different angular distributions as shown in Figure 5.19. Specifically between θ_{COM} =20-28°, the angular distributions for the excited state exhibit a deep minimum, suggesting that the data points at θ_{COM} =20.9°, 23.3° and 26.3° (corresponding θ_{lab} =29°, 31° and 33°) reflect mainly the cross-sections from the ground state. To verify this, the Q-value spectrum of $p(^{46}\mathrm{Ar},d)^{45}\mathrm{Ar}$ at θ_{lab}=28-29° (θ_{COM}~21°) is investigated as shown in Figure 5.22. The Gaussian fit for the peak at the lowest excitation energy gives a centroid of -5.75 MeV with FWHM ~550 keV. The adopted Q-value for ground-state transition is -5.80 MeV. The GEANT4 simulations suggest the resolution of the ground-state peak in this angular range to be ~520 keV. The reasonable agreement between the data and simulations suggests the cross sections within the angular range of θ_{COM} =20.9°-26.3° shown in Figure 5.19 can be regarded as pure contribution from ground-state transitions. As displayed in Figure 5.23, we therefore fitted these three data points plus the other four

points obtained at forward angles (shown in the left panel in Figure 5.21) using CH89 calculations and deduced SF(CH89) = 5.29 which is consistent with the ground-state SF of 5.08 deduced from the constrained two-*l* value fitting to within 4%. Similar analysis with JLM +HF approach is performed for this data set and gives SF(JLM+HF) of 3.93.

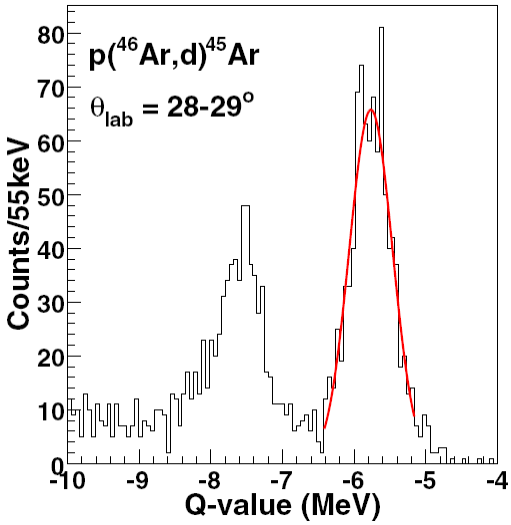

Figure 5.22: Q-value spectrum of $p(^{46}\mathrm{Ar},d)^{45}\mathrm{Ar}$ at θ_{lab}=28-29° (θ_{COM}~21°).

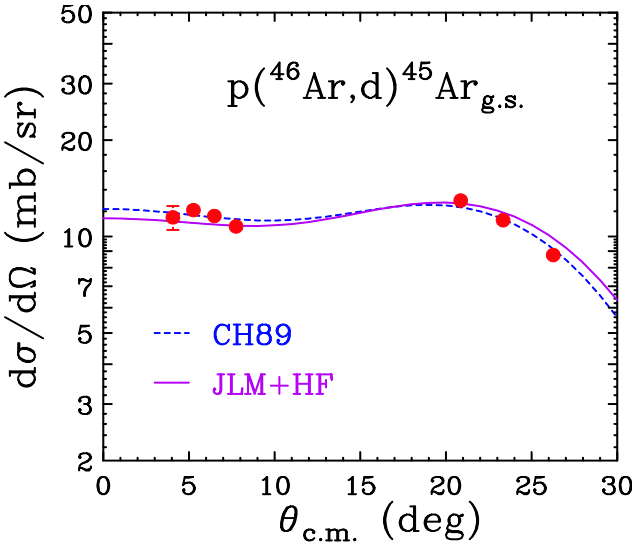

Figure 5.23: Differential cross sections of $p(^{46}\mathrm{Ar},d)^{45}\mathrm{Ar}$ in center-of-mass frame for ground-state transition.

The above discussion shows that the CH89 calculations reasonably describe the experimental ground-state angular distributions. The cross sections from the first excited-state transition can be deduced by subtracting the ground-state contributions from the data presented in Figure 5.19, where the ground-state contribution is the calculated angular distributions multiplied by the deduced SF value. The points in Figure 5.24 represent the deduced cross sections and associated statistical uncertainties for the first excited state. The l=1 calculations nicely reproduce the maximum regions at θ_{COM}<10°. Fitting the calculations to those five points around the peak gives SF(CH89) = 0.53. However the predicted angular distribution could not reproduce the shape of the first peak, where the predictions drop less rapidly compared to the data. The discrepancies in these angles are also reflected in the two-l fitting in Figure. 5.19.

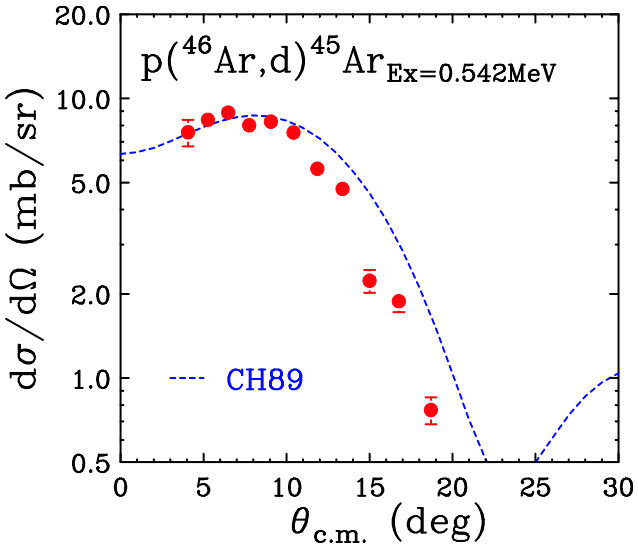

Figure 5.24: Deduced differential cross sections of $p(^{46}\mathrm{Ar},d)^{45}\mathrm{Ar}$ in center-of-mass frame for the first excited-state transition.

A peak with significant statistics around Q value of -7.5 MeV is clearly seen in Figure 5.6. The Q-value spectrum includes data with θ_{lab} up to19°. This peak results from the contributions of the transitions leading to four different states with excitation energies 1.734, 1.770, 1.876 and 1.911 MeV (see Table 5.1). The angular distribution for this group of states was extracted and shown in Figure 5.25. Apart from the spin assignment for the 1.876 state which are $1/2^-$, and $3/2^-$ listed in NNDC, the structural information for these states is unknown as presented in Table 5.1. From the present data, it is found that the angular momentum transfers of l=0, 2 (s, d) orbits need to be included in order to reproduce the angular distribution in Figure 5.25. The extracted SF values are 0.41 and 0.49 for the s- and d-transfer respectively. The solid curve is the total contributions with each distribution multiplied by the corresponding SF value.

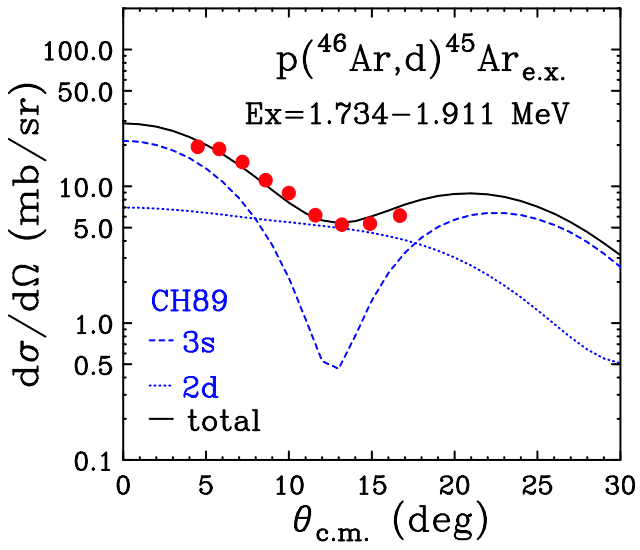

Figure 5.25: Differential cross sections of $p(^{46}Ar,d)^{45}Ar$ in center-of-mass frame for group of transitions to 1.734-1.911 MeV. The red solid circles are the data from present experiment. The dashed and dotted curves are the calculations using CH89 for 3s and 2d transitions respectively. The solid curve is the total contributions.

Another group of states is found at approximate excitation energy of 3.95 MeV, where no information about orbital configuration is available according to NNDC. The corresponding forward angle differential cross sections can be clearly identified and are plotted in Figure 5.26. The shape of the present angular distributions are consistent with the l=0 calculations using CH89, suggesting the existence of l=0 strength for the state at 3.95 MeV. The SF(CH89) deduced is 0.15. Predictions for l=0 is not available in the *pf*-shell model calculations for ^{46}Ar.

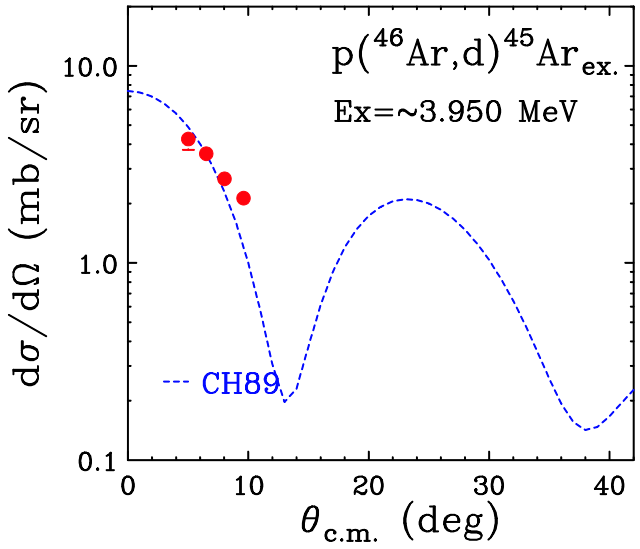

Figure 5.26: Differential cross sections of $p(^{46}\mathrm{Ar},d)^{45}\mathrm{Ar}$ in center-of-mass frame for group of transitions at about 3.950 MeV.

5.5 Theoretical spectroscopic factors and reduction factors

Experimental spectroscopic factor is extracted by taking the ratio of the measured cross-sections to the cross sections calculated with a reaction model. As discussed in section 5.4, the statistical uncertainty was determined better than 10%. The main uncertainty in the measured data is the absolute normalization of the cross-sections which is determined to about 10%. Therefore we assign 10% uncertainty to the experimental SFs summarized in .Table 5.7. No uncertainty arising from the choice of optical mode parameters associated to the deduced SF values is assigned.

The Large-basis shell-model (LB-SM) calculations were performed using the code Oxbash [Bro04] in sd-shell model space with USDB effective interaction [Bro06] for ^{33,35}Ar, where the calculated SFs for excitation energy less than 10 MeV are listed in Tables 5.4 and 5.5. For ^{46}Ar, interaction of Nummela in sd-pf model space et al. is used [Sig07]. The results for energy level less than 5 MeV are presented in Table 5.6.

The LB-SM predictions and the reduction factors which are the ratios of the experimental spectroscopic strengths with respect to LB-SM predictions are listed in Table 5.7. The values of the ground-state SF(CH89) for neutron-rich ^{46}Ar and stable ^{36}Ar isotopes and the first excited-state of ^{36}Ar obtained in the present experiments are in good agreement with the LB-SM predictions, which follow the systematics and benchmarks established by our extensive studies on a wide range of stable nuclei as discussed in Chapter 2. The experimental ground-state SF(CH89) for proton-rich ^{34}Ar is about 15-20% smaller than predictions. If the approach with JLM potential and HF constraints is

adopted to analyze the ground states, an approximately 30% reductions in the experimental SF(JLM) are obtained for ^{34}Ar, ^{36}Ar and ^{46}Ar relative to LB-SM prediction. This is also consistent with our previous results of ~30% systematic reduction as discussed in section 2.5. Such consistent suppression in SFs for ^{34}Ar and ^{46}Ar in the transfer reaction analysis verifies the applicability of a systematic framework with consistent input parameters to extract reliable relative SFs.

Table 5.4: Theoretical spectroscopic factors of ^{34}Ar for energy levels less than 10 MeV using USDB interaction in sd-shell model space.

Ex (MeV)	Jπ	SF(LB-SM)	Ex (MeV)	Jπ	SF(LB-SM)	Ex (MeV)	Jπ	SF(LB-SM)
0.00	1/2+	1.311	5.70	1/2+	0.017	7.61	3/2+	0.008
1.46	3/2+	0.517	6.26	1/2+	0.214	7.64	5/2+	0.214
1.96	5/2+	1.000	6.54	3/2+	0.002	7.93	1/2+	0.008
2.63	3/2+	0.000	6.59	5/2+	0.046	7.94	3/2+	0.004
3.44	3/2+	0.021	6.71	3/2+	0.007	8.22	1/2+	0.003
3.65	5/2+	0.270	6.91	3/2+	0.041	8.37	5/2+	0.020
4.08	5/2+	1.407	6.99	1/2+	0.008	8.86	5/2+	0.058
4.35	1/2+	0.069	7.00	5/2+	0.416	8.96	1/2+	0.004
4.99	3/2+	0.001	7.19	5/2+	0.030	9.21	1/2+	0.005
5.13	5/2+	1.715	7.28	3/2+	0.003	9.55	1/2+	0.005

Table 5.5: Theoretical spectroscopic factors of ^{36}Ar for energy levels less than 10MeV using USDB interaction in sd-shell model space.

Ex (MeV)	Jπ	SF(LB-SM)	Ex (MeV)	Jπ	SF(LB-SM)	Ex (MeV)	Jπ	SF(LB-SM)
0.00	3/2+	2.104	5.71	5/2+	1.358	7.85	3/2+	0.011
1.23	1/2+	1.368	5.80	3/2+	0.000	8.05	5/2+	0.009
1.68	5/2+	0.001	5.83	5/2+	0.050	8.17	3/2+	0.000
2.63	3/2+	0.291	6.41	5/2+	1.587	8.25	5/2+	0.046
3.10	5/2+	1.108	6.86	3/2+	0.001	8.68	3/2+	0.000
3.95	3/2+	0.004	6.97	5/2+	0.152	8.82	5/2+	0.519
3.98	1/2+	0.005	7.11	1/2+	0.052	9.26	1/2+	0.000
4.61	5/2+	0.027	7.31	1/2+	0.175	9.43	1/2+	0.000
4.77	3/2+	0.002	7.37	3/2+	0.015	9.72	1/2+	0.004
4.93	1/2+	0.054	7.83	1/2+	0.058			

Table 5.6: Theoretical spectroscopic factors of ^{46}Ar for energy levels less than 5 MeV using interaction of Nummela et al in sd-pf model space [Sig07].

Ex (MeV)	Jπ	SF(LB-SM)
0.00	7/2-	5.161
0.42	3/2-	0.776
1.24	3/2-	0.005
1.33	5/2-	0.057
1.79	1/2-	0.001
2.14	1/2-	0.037
2.26	7/2-	0.097
2.37	7/2-	1.073
2.42	5/2-	0.006
2.71	3/2-	0.007
2.87	5/2-	0.004
2.87	3/2-	0.013
2.95	5/2-	0.001
2.96	7/2-	0.065
3.27	7/2-	0.071
3.50	3/2-	0.001
3.51	7/2-	0.033
3.75	1/2-	0.011
3.76	5/2-	0.000
3.79	5/2-	0.001
4.03	5/2-	0.000
4.05	7/2-	0.058
4.15	5/2-	0.006
4.18	3/2-	0.000
4.20	7/2-	0.136
4.20	5/2-	0.004
4.28	3/2-	0.002
4.34	1/2-	0.001
4.43	3/2-	0.000
4.46	7/2-	0.060
4.55	3/2-	0.001
4.62	5/2-	0.002
4.68	5/2-	0.044
4.76	7/2-	0.010
4.81	7/2-	0.001
4.85	3/2-	0.000
4.91	5/2-	0.000
4.98	3/2-	0.000
4.98	7/2-	0.001
5.00	5/2-	0.001

Table 5.7: Extracted SF values.

Ground-state neutron spectroscopic factor

Isotopes	lj^{π}	Sn-Sp (MeV)	SF(LB-SM)	SF(CH89)	Rs(CH89)	SF(JLM)	*R*s(JLM)
^{34}Ar	$s_{1/2}^{+}$	12.41	1.31	1.10 ± 0.11	0.84 ± 0.08	0.85 ± 0.09	0.65 ± 0.07
^{36}Ar	$d_{3/2}^{+}$	6.75	2.10	2.29 ± 0.23	1.09 ± 0.11	1.60 ± 0.16	0.76 ± 0.08
^{46}Ar	$f_{7/2}^{-}$	-10.03	5.16	5.29 ± 0.53	1.02 ± 0.10	3.93 ± 0.39	0.76 ± 0.08

First excited-state neutron spectroscopic factor

	NNDC		LB-SM		Present work	
Isotopes	Ex(MeV)	lj^{π}	Ex(LB-SM)	SF(LB-SM)	SF(CH89)	*R*s(CH89)
^{36}Ar	1.184	$s_{1/2}^{+}$	1.23	1.37	1.23 ± 0.12	0.90 ± 0.09
^{46}Ar	0.542	$p_{3/2}^{-}$	0.42	0.78	0.49 ± 0.05	0.63 ± 0.06

Table 5.7 (cont'd)

Normalization value of calculation to data for a group of excited states

	NNDC		LB-SM		Present work	
Isotopes	**Ex(MeV)**	lj^{π}	**Ex(LB-SM)**	**SF(LB-SM)**	**SF(CH89)**	***Rs*(CH89)**
^{34}Ar	1.359+1.798	$d(_{3/2}-, _{5/2}-)$	1.46 (3/2+)	0.52	2.34± 0.23	
			1.9 (5/2+)	1.00		
^{34}Ar	3.456	$1f_{7/2}-$	--	--	0.40 ± 0.04	
^{34}Ar	3.819	$2d_{5/2}+$	4.08	1.407	1.49 ± 0.15	1.06 ± 0.12
^{46}Ar	1.734-1.911	$2d(_{3/2}-)$	--	--	0.49 ± 0.05	
^{46}Ar	1.734-1.911	$3s_{1/2}+$	--	--	0.41 ± 0.04	
^{46}Ar	~3.950	$3s_{1/2}+$	--	--	0.15 ± 0.02	

5.6 Asymmetry dependence of reduction factors

The error bars listed in Table 5.7 reflect the uncertainties in the absolute cross-section determination of 10%. The values of *Rs* deduced using CH89 or JLM+HF for symmetric ^{36}Ar and neutron-rich ^{46}Ar are similar. This is consistent with the previous systematic studies with stable nuclei [Tsa05, Lee07]. The extracted value of *Rs* for proton-rich ^{34}Ar is about 15-20% smaller.

To show the asymmetry dependence for the chain of Ar isotopes, reduction factors of proton-rich ^{34}Ar and neutron-rich ^{46}Ar and stable ^{36}Ar nuclei obtained from the present experiments are plotted in closed symbols and the reduction factors of the stable $^{37-41}$Ar isotopes deduced from previous measurements [Lee07] are plotted in open symbols as a function of ΔS (defined as the difference in the neutron and proton separation energy [Lee06]) in Figure 5.27. The difference of neutron and proton separation energies, ΔS, of ^{46}Ar and ^{34}Ar are -10.03 and 12.41 MeV, significantly

increasing the span of the separation difference from isotopes $^{36\text{-}41}$Ar near stability which have ΔS from -6.70 MeV to 6.57 MeV. The *Rs* deduced from CH89 and JLM+HF are plotted in top and bottom panels of Figure 5.27, respectively.

There are two sets of measurements for ^{40}Ar, but the extracted SFs are different by about a factor of 2. Such inconsistency may be attributed to the inconsistency of absolute normalization in cross sections between two experiments [Joh68,Ton77]. Based on the consistency check as explained in Ref. [Lee06], the SF for ^{40}Ar shown in Figure 5.27 is extracted using data in Ref. [Joh68]. Furthermore, there is only one measurement available for ^{38}Ar and no other independent measurement exists for consistency check [Goo75]. The theoretical and the experimental SFs from transfer reactions for stable Ar isotopes are listed in Table 5.8, where LB-SM calculations use USDB interactions in *sd* model space for $^{37\text{-}38}$Ar isotope and SDPFNOW interaction in *sdpf* model space for $^{39\text{-}41}$Ar. Within experimental uncertainties, little suppression in the reduction factor is found for proton-rich ^{34}Ar compared to the well-bound nuclei or neutron-rich ^{46}Ar.

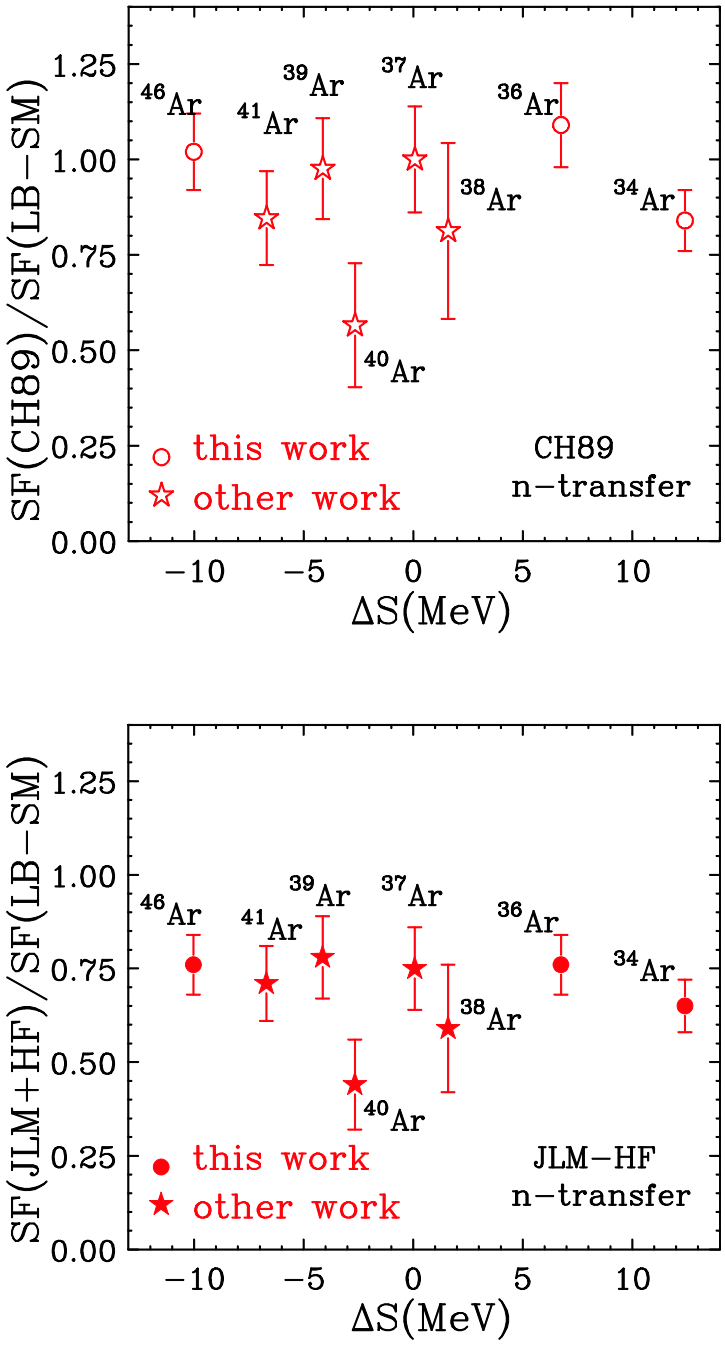

Figure 5.27: (top) Reduction factors deduced using CH89 approach SF(CH89)/SF(LB-SM) of the proton-rich ^{34}Ar and neutron rich ^{46}Ar, together with the well bound $^{36\text{-}41}$Ar isotopes. (Bottom) Same as top panel, except the calculations use JLM+HF method.

Recent dispersive-optical model (DOM) analysis of elastic-scattering and bound-level data on Ca isotopes ($^{40-48}$Ca) suggests that proton correlations exhibit weak dependence on the asymmetry where the proton SF magnitude from ^{40}Ca to ^{48}Ca changes by about 10% [Cha06, Cha07]. Based on the principle of isospin asymmetry, about 2% reduction in neutron SF value for ^{34}Ar relative to ^{36}Ar is predicted [Cha-priv]. The weak dependence of reduction factors on the asymmetry of the three Ar isotopes in this experiment is similar to the trends obtained from the recent Dispersive-Optical-Model analysis of elastic-scattering and bound-level data for $^{40-49}$Ca isotopes [Cha06, Cha07].

However, there are not enough existing data to constrain the asymmetry dependence for neutrons in the DOM analysis. Using no asymmetry term for neutrons, the asymmetry dependence of neutron occupation probabilities in Ca isotopes from the DOM result is plotted as solid line in Figure 5.28. Such results describe the trend of neutron reduction factors for Ca isotopes in transfer reactions [Cha07]. Here the SF values in transfer reactions were deduced using JLM+HF approaches [Lee06] and SF (LB-SM) values of Ca isotopes were calculated in *fp*-shell model space with GXPF1A interactions [GXPF1A]. The shell-model and the experimental SF values are listed in Table 5.8.

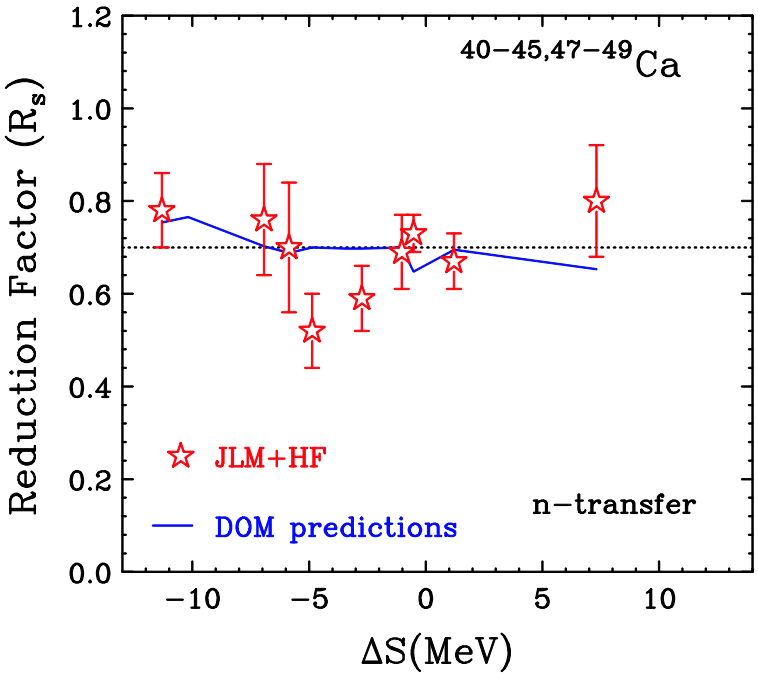

Figure 5.28: Reduction factors of Ca isotopes obtained from the dispersive optical-model (DOM) calculation (solid line) and from neutron (*d*,*p*) and (*p*,*d*) transfer reactions analyzed using JLM+HF approach.

Table 5.8: Extracted ground-state SFs for stable Ar and Ca isotopes.

Isotopes	l j^{π}	Sn-Sp (MeV)	SF(LB-SM)	SF(CH89)	Rs(CH89)	SF(JLM+HF)	Rs(JLM+HF)
^{37}Ar	$d_{3/2}^{+}$	0.07	0.36	0.36 ± 0.05	1.00 ± 0.14	0.27 ± 0.04	0.75 ± 0.11
^{38}Ar	$d_{3/2}^{+}$	1.60	3.04	2.47 ± 0.70	0.81 ± 0.23	1.78 ± 0.50	0.59 ± 0.17
^{39}Ar	$f_{7/2}^{-}$	-4.13	0.83	0.81 ± 0.11	0.98 ± 0.13	0.65 ± 0.09	0.78 ± 0.11
^{40}Ar	$f_{7/2}^{-}$	-2.66	1.91	1.08 ± 0.31	0.57 ± 0.16	0.84 ± 0.24	0.44 ± 0.12
^{41}Ar	$f_{7/2}^{-}$	-6.70	0.65	0.55 ± 0.08	0.85 ± 0.12	0.46 ± 0.07	0.71 ± 0.10
^{40}Ca	$d_{3/2}^{+}$	7.31	4.00	4.35 ± 0.62	1.09 ± 0.16	3.20 ± 0.46	0.80 ± 0.12
^{41}Ca	$f_{7/2}^{-}$	-0.53	1.00	1.01 ± 0.06	1.01 ± 0.06	0.73 ± 0.04	0.73 ± 0.04
^{42}Ca	$f_{7/2}^{-}$	1.20	1.95	1.93 ± 0.17	0.99 ± 0.09	1.31 ± 0.12	0.67 ± 0.06
^{43}Ca	$f_{7/2}^{-}$	-2.74	0.75	0.63 ± 0.07	0.84 ± 0.09	0.44 ± 0.05	0.59 ± 0.07
^{44}Ca	$f_{7/2}^{-}$	-1.03	3.86	3.93 ± 1.08	1.02 ± 0.28	2.67 ± 0.31	0.69 ± 0.08
^{45}Ca	$f_{7/2}^{-}$	-4.88	0.50	0.37 ± 0.05	0.74 ± 0.10	0.26 ± 0.04	0.52 ± 0.08
^{47}Ca	$f_{7/2}^{-}$	-6.93	0.25	0.26 ± 0.04	1.04 ± 0.16	0.19 ± 0.03	0.76 ± 0.12
^{48}Ca	$f_{7/2}^{-}$	-5.86	7.70	7.35 ± 1.42	0.95 ± 0.18	5.41 ± 1.05	0.70 ± 0.14
^{49}Ca	$p_{3/2}^{-}$	-11.31	0.95	0.69 ± 0.07	0.73 ± 0.07	0.74 ± 0.08	0.78 ± 0.08

The weak dependence of reduction factors on the asymmetry observed from the present transfer reaction experiments are, however, in contradiction to the strong systematic suppression in SFs obtained using the intermediate-energy nucleon knockout reactions [Gad08]. Figure 5.29 compares the asymmetry dependence ΔS of reduction factors (*Rs*) for the transfer (closed and open circles) and knockout (open triangles) reactions. For transfer reaction data, the open circles represent *Rs*(CH89)= SF(CH89)/SF(LB-SM)) and the closed circles represent (*Rs*(JLM+HF)= SF(JLM+HF)/SF(LB-SM). For knockout reaction data, the dashed line is the best fit of *Rs* of ^{32,34,46}Ar from knockout reactions.

The ^{34}Ar ΔS values from the present work and ref [Gad04-2,Gad08] are different. In this work, spectroscopic factor of the ground-state is determined. In knockout reactions, ground-state *Rs* are obtained for ^{46}Ar [Gad05] and ^{32}Ar [Gad04-1]; while inclusive cross sections including contributions from the excited states to the ground states were measured for ^{34}Ar [Gad04-2]. Thus the ^{34}Ar ΔS value in Ref. [Gad04-2] is weighted by the nucleon separation energy of the excited states. In principle, the knockout value would give the upper limit of the ^{34}Ar ground-state *Rs* value as contributions from excited states should increase the reduction factor values.

As shown by the open triangles in Figure 5.29, the neutron *Rs* extracted from knockout reactions for ^{34}Ar is approximately a factor of two smaller than that for ^{46}Ar [Gad08]. Even larger reductions have been observed for neutron knockout from ^{32}Ar [Gad08], a nucleus for which transfer data is not available. Within experimental uncertainties of ±10% in the present transfer reaction measurements, the reductions in the spectroscopic factors, deduced using both CH89 and JLM+HF analysis, for ^{34}Ar relative

to ^{46}Ar of 0-35% are possible but much larger reductions are excluded. This suggests that there is a systematic difference between the conclusions drawn from these two probes for the spectroscopic factors of strongly bound particles. Thus a reexamination of the reaction theory description of transfer reactions or knockout reactions including the input parameters used in these analyses may be needed.

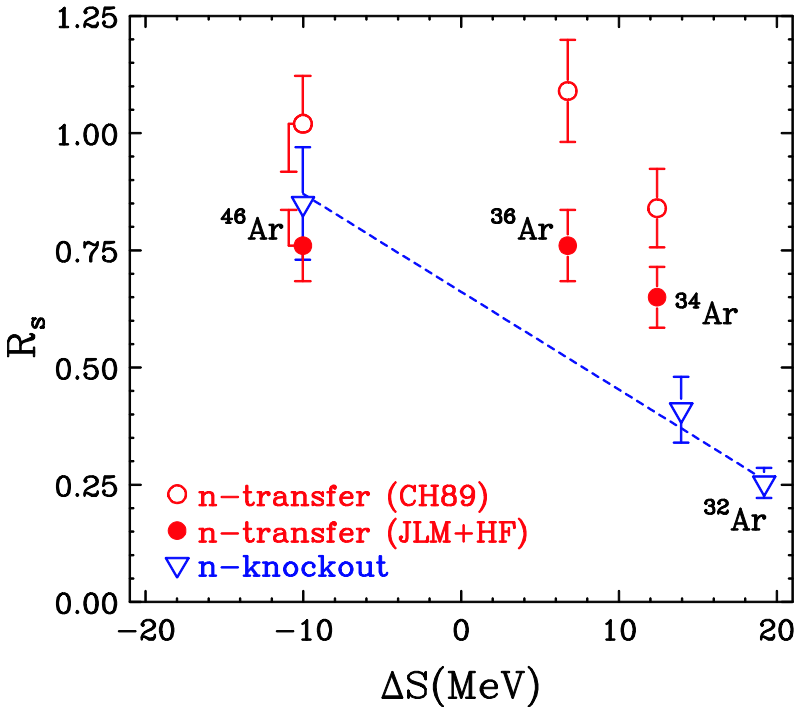

Figure 5.29: Reduction factors *Rs*=SF(expt)/SF(LB-SM) as a function of the difference between neutron and proton separation energies, ΔS. The solid and open circles represent *Rs* deduced in JLM+HF and CH89 approach using the present transfer reaction data respectively. The open triangles denote the *Rs* from knockout reactions [Gad08]. The dashed line is the best fit of *Rs* of ^{32,34,46}Ar from knockout reactions. The use of different ΔS values from the present work and knockout reactions in Ref. [Gad08] is explained in text.

Chapter 6

Summary and conclusions

In this thesis, we investigate the asymmetry dependence of neutron correlations in nuclei over a large span of Ar isotopes. Such correlations govern the nuclear properties of the drip line nuclei. The experimental spectroscopic factor (SF), defined as the ratio of the measured cross sections divided by the cross sections calculated with a reaction model for transfer of a nucleon between the initial and final states, plays a special role in linking the microscopic theory of nuclear structure to the reaction model. The calculated cross sections depend on the wave functions of the nuclei involved and the transferred nucleon. Transfer reactions comprise the preponderance of determining experimental spectroscopic factors in the literature and provide an important technique to study the properties of rare isotopes. In addition to performing a survey of the experimental neutron SF for nuclei $Z \leq 28$ and comparing the results to the shell model, this thesis also describes the first (*p,d*) transfer reaction measurement with Ar isotopes performed at the NSCL using the High Resolution Array (HiRA) and the S800 spectrometer.

In the first part of the thesis, we survey the neutron spectroscopic factors extracted from the available (*p,d*) and (*d,p*) angular distribution data on nuclei with $Z \leq 28$. Utilizing global optical-model potentials and consistent sets of parameters systematically, the long-standing inconsistency and ambiguities in the nucleon-nucleus potentials as well as single-particle parameters can be resolved. As a result, relative spectroscopic factors can be determined over a wide range of nuclei. We re-analyze the past measurements of

(*p*,*d*) and (*d*,*p*) transfer reaction data using nucleon-nucleus global optical-model potential, Chapel-Hill 89 (CH89) and the neutron potential of Wood-Saxon shape with conventional radius of r_o=1.25 fm and diffuseness a_o=0.65 fm in the framework of Adiabatic Distorted Wave approximation (ADWA). The extracted ground-state neutron spectroscopic factors for 88 nuclei ranging in Z=3-28 are in agreement with the large-basis shell-model (LB-SM) calculations to within 20%. The results illustrate the success of the approach for providing systematic and consistent spectroscopic factor values with minimum assumptions.

The excited-state spectroscopic factors are of particular interest because they are needed in astrophysical network calculations. Based on the same methodology, we have extracted 565 neutron spectroscopic factors of *sd*- and *fp*-shell nuclei. We are able to compare 125 of the extracted spectroscopic factors to values predicted by large-basis-shell-model (LB-SM) calculations and evaluate the accuracies of spectroscopic factors predicted by different interactions. For $Z \leq 24$ nuclei far away from closed shells with SF values larger than 0.005, the agreement between the extracted SF and shell-model predictions are better than 30%. Immediately outside the ^{40}Ca core, especially for light Ca isotopes near the closed *sd* shell, the shell model predicts pure single-particle states with much larger spectroscopic factors than experimental values. This is a further indication that a large *sd-fp* model space may be needed due to the effects of core excitations and particle-hole collective states. For Ni isotopes, the agreement is poor and the result suggests that the effective interactions in this region need improvements.

The survey of neutron spectroscopic factors provides important benchmarks for the neutron-transfer reaction studies and a stringent means to test the residual interactions and Hilbert spaces used in the current nuclear structure calculations. Beyond the *sd*-shell, better effective interactions and larger valence spaces should be accommodated in the current large-basis shell-model calculations. Both directions require more efficient shell-model codes/algorithms and larger computational facilities, which is becoming available in the forthcoming years. The good agreement for small spectroscopic factors in the *sd*-shell nuclei suggests that experiments can be reliably performed to extract spectroscopic factor values down to 0.005. The ability to measure and calculate small spectroscopic factor values is important for network calculations of astrophysical interest.

Since the shell model includes the effects of correlations within the model basis, but not those outside the model basis, the shell model spectroscopic factors represent the upper limit. Reduction of the spectroscopic factors is one signature of the correlations experienced by the valence nucleon. This is evidenced in the smaller SF values predicted by the large-basis shell-model compared to those predicted by the Independent Particle Model. Constant quenching (~30-40%) of the proton spectroscopic factor values are observed in the studies of (*e,e'p*) reactions for nuclei near the closed shell compared to the independent particle model (IPM) expectations. For nuclei near the closed shell, the LB-SM calculations give similar predictions as the IPM model. The suppression of the proton spectroscopic factors extracted in the (*e,e'p*) study has been attributed to insufficient treatment of nucleon-nucleon correlations including both short- and long-range correlations in the current shell models. More intriguing is the large (up to 75%)

suppression in the spectroscopic factor values for the strongly bound nucleon of rare isotopes compared to shell model predictions obtained using the intermediate-energy nucleon knockout reactions. Currently, no theory is able to account for the large reduction of the spectroscopic strength.

We study the suppression of the spectroscopic factors in transfer reactions over a range of nuclei using the microscopic potentials with constraints based on physics input. We use the Jeukenne, Lejeune and Mahaux (JLM) nucleon optical interactions and constrain the density of the potential as well as the transferred neutron orbital rms radii with the Hartree-Fock (HF) calculations. With the JLM+HF method, an overall ~30% suppression in SF values for most nuclei is obtained. Similar quenching of the proton SF values have been observed in the studies of (*e,e'p*) reactions. However, unlike the knockout results, the reduction factors *Rs* (the ratio of experimental spectroscopic factors to LB-SM predictions) obtained from the comprehensive transfer reactions data have no dependence on the neutron binding energy within experimental error. Similarly, reduction factors obtained from the studies of (*e,e'p*) reactions are constant.

The survey data include very few extremely neutron-rich or neutron-deficient nuclei. Furthermore, systematic uncertainties inherent in comparing spectroscopic factors from different experiments performed over four decades are large. To reduce the uncertainties and to extend the region of study to more extreme *N/Z* nuclei, we extract the experimental neutron spectroscopic factors for ^{34}Ar and ^{46}Ar using (*p,d*) neutron transfer reactions with proton-rich ^{34}Ar and neutron-rich ^{46}Ar beams in inverse kinematics. The experiments of $p(^{34}\mathrm{Ar},d)^{33}\mathrm{Ar}$ and $p(^{46}\mathrm{Ar},d)^{45}\mathrm{Ar}$ were performed at the National

Superconducting Cyclotron Laboratory at Michigan State University at beam energy of 33 MeV per nucleon. The kinematically complete measurements were achieved by using the high resolution silicon array, HiRA, to detect deuterons in coincidence with the recoil residues detected in the S800 mass spectrometer. The success of the current experiment demonstrates the techniques of transfer reactions in inverse kinematics using radioactive beams to study single-nucleon properties of exotic nuclei. The experience learned from this experiment is essential for future HiRA transfer reaction measurements, especially for those which require excellent energy and angular resolution.

The deuteron differential cross sections obtained in the experiments are compared to cross sections calculated using both JLM+HF and CH89 methods. Consistent with previous systematic studies with stable nuclei, the values of *Rs* for symmetric ^{36}Ar and neutron-rich ^{46}Ar are similar. The extracted value of *Rs* for proton-rich ^{34}Ar is about 15-20% smaller. With the experimental uncertainties of ±10% in the measured differential cross-sections, reductions in the spectroscopic factors for proton-rich ^{34}Ar relative to neutron-rich ^{46}Ar of 0-35% are possible but much larger reductions are excluded. The weak dependence of reduction factors on the asymmetry of the Ar isotopes (including other Ar isotopes obtained in the survey) is similar to the trends obtained from the recent Dispersive-Optical-Model analysis of elastic-scattering and bound-level data for $^{40\text{-}49}$Ca isotopes. In the latter study, calculations using the dispersive-optical model suggest that the proton spectroscopic factors from ^{40}Ca to ^{48}Ca have a weak (10%) dependence on the asymmetry. The experimental trend is consistent with weak asymmetry dependence in the neutron correlations for N>Z Ca isotopes.

In single nucleon knockout reactions in intermediate energy, the deficient nucleon species have stronger reductions in spectroscopic factors than the weakly bound excess species, in particular the neutron reduction factor, *Rs*, of ^{34}Ar is smaller by a factor of two compared to ^{46}Ar. Unlike the trends observed for knockout reactions, comparison of the extracted spectroscopic factors for proton-rich ^{34}Ar and neutron-rich ^{46}Ar using transfer reactions suggests a weak dependence of correlations on neutron-proton asymmetry in this isotope region. The origin of such discrepancy between the spectroscopic factors extracted from transfer and knockout reactions is not clear. The new results pose an intriguing question about the reaction mechanisms of transfer and knockout reactions as well as the nature of neutron correlations in nuclei with extreme isospin asymmetry. Further theoretical study would be needed to resolve the inconsistency in the reaction mechanisms and better describe the asymmetry dependence of nucleon correlations when approaching to the drip lines.

Bibliography

[Acuit] http://www.acuitylaser.com/AR600/index.shtml

[Ago03] S. Agostinelli et al., Nucl. Instrum. Meth. A, 506, 250 (2003).
http://www.geant4.org/geant4/

[Akm98] A. Akmal et cl., Phys. Rev. C58, 1804 (1998).

[Alf78] W. P. Alford et al., Nucl. Phys. A302, 12 (1978).

[And68] S. A. Andersen and Ole Hansen, Nucl. Phys. A120, 421 (1968).

[Aue67] N. Auerbach, Phys. Rev 163, 1203 (1967).

[Aus70] N. Austern, *Direct Nuclear Reaction Theories*, John Wiley & Sons, New York, 1970.

[Bar09-1] C. Barbieri., Phys. Rev. Lett 103, 202502 (2009).

[Bar09-2] C. Barbieri et al., [nucl-th] arXiv:0901.1920v1.

[Bar09-3] C. Barbieri et al., Nucl. Phys. A834 (2010) 788.

[Bau96] E. Bauge et. al., Proceedings of the Specialists' Meeting on the Nucleon Nucleus Optical Model up to 200 MeV, 1996. www.nea.fr/html/science/om200/bauge.pdf

[Baz03] D. Bazin et al., Nucl. Instrum. Methods Phys. Res. B 204, 629 (2003).
[Ber09] J. Berryman et al., Phys. Rev. C 79, 064305 (2009).

[Bje67] J. H. Bjerregaard and Ole Hansen, Phys. Rev. 155, 1229 (1967).

[Bob06] R.J. Charity et al., Phys. Rev. Lett. 97, 162503 (2006).

[Bob07] R.J. Charity et al., Phys. Rev. C76, 044314 (2007).

[Boh75] A. Bohr and B. R. Mottleson, *Nuclear Structure* (Benjamin, New York, 1975),Vol. I

[Boy76] R. N. Boyd et al., Phys. Rev. C 14, 946 (1976).

[Bro00] B. A. Brown, W. A. Richter, and R. Lindsay, Phys. Lett. B483, 49 (2000).

[Bro01] B. A. Brown, Prog. Part. Nucl. Phys. 47, 517 (2001).

[Bro01-1] B.A. Brown, Progress in Particle and Nuclear Physics, 47, 517 (2001).

[Bro01-2] B. A. Brown, S. Typel, and A. Richter, Phys. Rev. C 65, 014612 (2001).

[Bro02] B. A. Brown, P. G. Hansen, B. M. Sherrill, and J. A. Tostevin, Phys. Rev. C 65, 061601(R) (2002).

[Bro04] B. A. Brown et al., Computer program, http://www.nscl.msu.edu/~brown/resources/oxbash-augsut-2004.pdf.

[Bro05] B. A. Brown, http://www.nscl.msu.edu/~brown/Jina-workshop/BAB-lecture-notes.pdf, 2005.

[Bro06] B. A. Brown and W.A. Richter, Phys. Rev. C 74, 034315 (2006).

[Bro74] G. Brown, A. Denning and J. G. B. Haigh, Nucl. Phys. A225, 267 (1974).

[Bro98] B. A. Brown, Phys. Rev. C 58, 220 (1998).

[Bro99] B.A. Brown, J. Phys. G: Nucl. Part. Phys. 25, 623 (1999).

[But64] P. J. A. Buttle and L. J. B. Goldfarb, Proc. Phys. Soc. London 83, 701 (1964).

[Cam06] C. Campbell et al., Phys. Rev. Lett. 97, 112501 (2006).

[Cas90] R.F. Casten, *Nuclear structure from a simple perspective* (Oxford University Press Inc., New York, 1990).

[Cau05] E. Caurier et al., Rev. Mod. Phys. 77, 427 (2005).

[Cau05] E. Caurier, G. Martinez-Pinedo, F. Nowacki, A. Poves, A.P. Zuker, Rev. Mod. Phys. 77, 427 (2005).

[Cau99] E. Caurier, shell model code ANTOINE, IRES, Strasbourg 1989-2004, E. Caurier and F. Nowacki, Acta Physica Polonica 30, 705 (1999).

[Cha06] R.J. Charity et al., Phys. Rev. Lett. 97, 162503 (2006).

[Cha07] R.J. Charity et al., Phys. Rev. C76, 044314 (2007).

[Cow91] J.J. Cowan, F.-K. Thielemann and J.W. Truran, Phys. Rep.208, 267 (1991).

[Daq] http://sourceforge.net/projects/nscldaq/

[Dau63] C.Daum, Nucl. Phys. 45, 273 (1963).

[Del05] F. Delaunay, F. M. Nunes, W.G. Lynch, M.B. Tsang, Phys. Rev. C 72, 014610 (2005).

[deL67] M. E. de López et al., Nucl. Phys. A94, 673 (1967).

[Des00] P. Descouvemont, The Astrophysical Journal, 543,425 (2000).

[Dic04] W.H. Dickoff and C. Barbieri, Prog. Part. Nucl. Phys. 52, 377 (2004).

[Dic08] W. H. Dickhoff and D. V. Neck, *Many-body theory exposed*, World Scientific, Singapore (2008).

[End03] J. Enders *et al.*, Phys. Rev. C 67, 064301 (2003).

[End77] P. M. Endt, Atonic Data and Nuclear Data Tables 19, 23 (1977).

[ENDSF] http://www.nndc.bnl.gov/ensdf/

[Eng07] G. L. Engel et al., Nucl. Instrum. Meth. 573, 418 (2007).

[Expt03045] M. Kilburn, http://groups.nscl.msu.edu/hira/03045/index.htm

[Expt06035] A. Sanetullaev, http://groups.nscl.msu.edu/hira/06035/index.htm

[Fic74] D.Fick, J,NUK,19,693 (1974), http://www.nndc.bnl.gov/exfor/servlet/X4sGetSubent?subID=150326002&master=ND

[Fos69] C. C. Foster, W. E. Maddox, and D. W. Miller, Phys. Rev. 181, 1529 (1969).

[Ful63] R.H.Fulmer and A.L.McCarthy, Phys. Rev. 131, 2133 (1963).

[Gad04-1] A. Gade et al., Phys. Rev. Lett. 93, 042501 (2004).

[Gad04-2] A. Gade *et al.*, Phys. Rev. C 69, 034311 (2004).

[Gad05] A. Gade *et al.*, Phys. Rev. C 71, 051301(R) (2005).

[Gad08] A. Gade et al., Phys. Rev. C77, 044306 (2008) and reference therein.

[Gau06] L. Gaudefroy et al., Phys. Rev. Lett. 97, 092501 (2006).

[Gle04] Norman K Glendenning, *Direct Nuclear Reactions*, World Scientific Publishing, 2004.

[Gol99] G. Golò, P.F. Bortignon, and R.A. Broglia, Nucl. Phys. A649, 335 (1999).

[Goo75] D. R. Goosman, P. D. Parker, and A. J. Howard, Nucl. Phys. A250, 309 (1975).

[Han03] P.G. Hansen and J.A. Tostevin, Annu. Rev. Nucl. Part. Sci. 53, 219 (2003).

[Han75] O. Hansen et al., Nucl. Phys. A243, 100 (1975).

[Hef77] E. F. Hefter, E. T. Boschitz, V. Heidt and Ch. Weddigen, Nucl. Phys. A275, 212 (1977).

[Hen08] V. Henlz, private communication.

[Hjo65] Sven A. Hjorth, J. X. Saladin and G. R. Satchler, Phys. Rev. 138, B1425 (1965).

[Hon02] M. Honma, T. Otsuka, B.A. Brown and T. Mizusaki, Phys. Rev. C 65, 061301(R) (2002).

[Hon04] M. Honma, T. Otsuka, B.A. Brown and T. Mizusaki, Phys. Rev. C 69, 034335 (2004).

[Hon05] M. Honma, T. Otsuka, B.A. Brown and T. Mizusaki, Eur. Phys. J. A 25, Suppl. 1, 499 (2005).

[Hor06] M. Horoi et al., Phys. Rev. C 73, 061305(R) (2006).

[Iga] M. Igarashi et al., Computer Program TWOFNR (Surrey University version).

[ISF] https://intra.nscl.msu.edu/illustrations/gallery.php?id=34

[IU] Electronic Instrument Services, Department of Chemistry, Indiana University, Bloomington.

[Jac70] D.F. Jackson *et al.*, Nuclear Reactions, Methuen, London, 1970.

[Jeu77] J.-P. Jeukenne, A. Lejeune, and C. Mahaux, Phys. Rev. C 15, 10 (1977); 16, 80 (1977).

[Joh70] R.C. Johnson and P.J.R. Soper, Phys. Rev. C 1, 976 (1970).

[Joh68] R. R. Johnson and R. J.Griffiths, Nucl. Phys. A108, 113 (1968).

[Joh89] R.C. Johnson, E.J. Stephenson and J.A. Tostevin, Nucl. Phys. A505, 26 (1989).

[Jon68] R.R. Johnson et al., Nucl. Phys. A108, 113 (1968).

[Kat65] Syohei Kato et al., Nucl. Phys. 64, 241 (1965).

[Kee04] N. Keely et al., Phys. Pev. C69, 064604 (2004).

[Knu75] L. D. Knutson, J. A. Thomson, and H. O. Meyer, Nucl. Phys. A241, 36 (1975).

[Koc71] D. C. Kocher and W. Haeberli, Nucl. Phys. A172, 652 (1971).

[Koz68] R.L. Kozub, Phys. Rev. 172, 1078 (1968).

[Kra01] G. J. Kramer, H. P. Blok, and L. Lapik´as, Nucl. Phys. A679, 267 (2001), and references therein.

[Kra01] G.J. Kramer et. al., Nucl. Phys. A. 679, 267 (2001) and references therein.

[Kra93] K.L. Kratz et al., Ap. J. 403, 216 (1993).

[Kra94] G.Kraus et al., Phys. Rev. Lett. 73, 1773 (1994).

[Lal99] G. A. Lalazissis *et al.*, Phys. Rev. C 60, 014310 (1999).

[Lan88] J. Lang et al., Nucl. Phys. A477, 77 (1988).

[Lee06] Jenny Lee, J.A. Tostevin, B.A. Brown, F. Delaunay, W.G. Lynch, M.J. Saelim, and M.B. Tsang, Phys. Rev. C 73, 044608 (2006).

[Lee07] Jenny Lee, M. B. Tsang and W. G. Lynch, Phys. Rev. C 75, 064320 (2007) and references therein.

[Lee09] Jenny Lee, M.B. Tsang, W.G. Lynch, M. Horoi, S.C. Su, Phys. Rev. C 79, 054611 (2009).

[Lee10] J. Lee et al., Phys. Rev. Lett. 104, 112701 (2010).

[Lee64] L. L. Lee et al., Phys. Rev. 136, B971 (1964).

[Lis04] A. Lisetskiy et al., Phys. Rev. C 70, 044314 (2004).

[LISE] http://groups.nscl.msu.edu/lise/lise.html

[Liu01] Z. H. Liu et al., Phys. Rev. C 64, 034312 (2001).

[Liu04] X. D. Liu et. al., Phys. Rev. C 69, 064313 (2004).

[Liu05] X.D. Liu, PhD thesis, Michigan State University, (2005).
http://groups.nscl.msu.edu/nscl_library/Thesis/Liu,%20Xiaodong.pdf

[Liu-priv] Z.H. Liu, private communications.

[Mar72] P. Martin, M. Buenerd, Y. Dupont and M. Chabre, Nucl. Phys. A185, 465 (1972).

[May60] M.G. Mayer and J. H. D. Jensen, *Elementary Theory of Nuclear Shell Structure* (John Wiley and Sons, London, 1960).

[Min06] K. Minamisono et al, Phys. Rev. Lett. 96, 102501 (2006).

[Mor03] D.J. Morrisey et al., Nucl. Instrum. Methods B 204, 90 (2003).

[Mor97] D. J. Morrissey. The Coupled Cyclotron Project at the NSCL. *Nuclear Physics A*, 616:45c–55c, 1997.

[Mye66] D. Myers et al., Nucl. Phys. 81,1 (1966).

[Nie66] H. Niewodniczanski et al., Phys. Rev. 146, 799 (1966).

[NNDC] Richard B. Firestone, Virginia S. Shirley, Table of Isotopes, Wiley-Interscience; 2 Vols. 8th edition (December 4, 1998), http://www.nndc.bnl.gov/

[NSCL94] The *K*500+*K*1200, A coupled cyclotron facility at the National Superconducting Cyclotron Laboratory. NSCL Report MSUCL-939, July 1994.

[NSR] http://www.nndc.bnl.gov/nsr

[Nun08] F. Nunes, Private communications.

[Ohl63] G.G. Ohlsen and R.E. Shamu, Nucl. Phys. 45, 523 (1963).

[OWIS] http://www.owis-staufen.com

[Pan97] V. R. Pandharipande et al., Rev. Mod. Phys. 69, 981 (1997).

[Per62] F. Perey and B. Buck, Nucl. Phys. 32, 353 (1962).

[Per76] C.M. Perey et al., At. Data Nucl. Data Tables 17, 1 (1976).

[Pet85] J. S. Petler, M. S. Islam, R. W. Finlay, and F. S. Dietrich, Phys. Rev. C 32, 673 (1985).

[Pov01] A. Poves et al., Nucl. Phys. A694, 157 (2001).

[Pre93] M.A. Preston and R.K. Bhaduri, *Structure of The Nucleus* (Westview Press, 1993).

[Ric03] W. A. Richter and B. A. Brown, Phys. Rev. C 67, 034317 (2003).

[Rog09] A. Rogers, PhD thesis, Michigan State University, (2009).

[Rog10-1] A. Rogers, in preparations

[Rog10-2] A. Rogers, in preparations

[ROOT] http://root.cern.ch/drupal/

[S800] http://groups.nscl.msu.edu/s800/Technical/Electronics/Electronics_frameset.htm

[San06] D.P. Sanderson, http://www.slac.stanford.edu/econf/C06092511/papers/WEPO23.PDF, (2006)

[Sat80] G.R. Satchler, Introduction to Nuclear Reactions, Macmillan, London, 1980.

[Sch05] H. Schatz et al., Phys. Rev. C 72, 065804 (2005).

[Sch09] J. Schiffer, lecture notes of the 8th Summer School on Exotic Beam Physics, Berkerly, 2009.

[Sch64] U.Schmidt-rohr, R.Stock and P. Turek, Nucl. Phys. 53, 77 (1964).

[Sch67] J. P. Schiffer et al., Phys. Rev. 164, 1274 (1967).

[Sch98] H. Schatz *et al.*, Phys. Rep. 294, 167 (1998).

[Set70] Kamal K. Seth, J. Picard, G.R. Satchler, Nucl. Phys. A140, 577 (1970).

[Sha00-1] D. Shapira et al., Nucl. Inst. and Meth. A. 449, 396 (2000).

[Sha00-2] D. Shapira et al., Nucl. Inst. and Meth. A. 454, 409 (2000).

[She02] B. M. Sherrill. Scientific opportunities with the nscl coupled cyclotron facility. *Prog. Theor. Physics*, 146:60–69, 2002.

[Sig07] A. Signoracci et al., Phys. Rev. Lett. 99, 099201 (2007).

[Sky67] D. J. Skyrme, Nucl. Instrum. Meth. 57, 61 (1967)

[Sor08] O.Sorlin and M.-G. Porquet, Prog. Part. Nucl. Phys. 61, 602 (2008) and reference therein.

[Spectcl] http://docs.nscl.msu.edu/daq/spectcl/

[Ste06] I. Stetcu et al., Phys. Rev. C 73, 037307 (2006).

[Suz09] D. Suzuki *et al.* Phys. Rev. Lett. 97, 092501 (2006).

[Tan08] I. Tanihata *et al.*, Phys. Rev. Lett. 100, 192502 (2008).

[Ter04] J. R. Terry *et al.*, Phys. Rev. C 69, 054306 (2004).
[Ton77] J. F. Tonn *et al.*, Phys. Rev. C 16, 1357 (1977).

[Tos04] J. Tostevin et al., Nuc. Phy. A746, 166 (2004).

[Tsa05] M. B. Tsang, Jenny Lee and W. G. Lynch, Phys. Rev. Lett. 95, 222501(2005).

[Tsa09] M.B. Tsang, Jenny Lee, S.C. Su, J.Y. Dai, M. Horoi, H. Liu, W.G. Lynch, S. Warren, Phys. Rev. Lett. 102, 062501 (2009).

[Var91] R.L.Varner et al., Phys. Rep. 201, 57 (1991).

[Ver07] D. Verney et al., Phys. Rev. C 76, 054312 (2007).

[Ver94] J. Vernotte et al., Nucl. Phys. A571, 1 (1994).

[Wal05] M.S. Wallace, PhD thesis, Michigan State University, (2005).

[Wal09] M.S. Wallace et al., Nucl. Instrum. Methods Phys. Res. A583, 302 (2007).

[Wal81] R. K. Wallace and S. E. Woosley, Astrophys. J. Suppl. 45, 389 (1981).

[Wes92] J. Wesseling *et al.*, Nucl. Phys. A547, 519 (1992).

[Win01] J. S. Winfield et al., Nucl. Phys. A683, 48 (2001).

[Yur04] K.L. Yurkewicz et al., Phys. Rev. C 70, 054319 (2004).

[Yur06] K.L. Yurkewicz et al,. Phys. Rev. C 74, 024304 (2006).

[Yur99] J. Yurkon et al., Nucl. Instrum. Methods Phys. Res. A 422, 291 (1999).